PATTERN RECOGNITION ANALYSIS OF ORGANISED EDDY STRUCTURES IN A NUMERICALLY SIMULATED TURBULENT PLANE JET

SING HON LO

Thesis submitted to
the University of London
for the degree of
Doctor of Philosophy

Department of Aeronautical Engineering
Queen Mary and Westfield College
University of London

1993

To my mother, sisters, Novella and
in memory of my father.

Declaration

This work is solely that of the author and has not been submitted in any form for another degree.

Abstract

By applying pattern recognition analysis, the organised eddy structures in the near and intermediate fields (10~40 jet diameters) of a numerically simulated turbulent plane jet have been investigated. The Reynolds number based on the jet width is 1,600. The results of the nearly full simulation show good agreement with the experimental measurements in the near and intermediate regions (<40 diameters) of the jet. Patterns of organised eddy structures have been extracted from the three-dimensional simulation databases. Ensemble averaged fields of three velocity components and pressure in the spanwise and transverse planes suggest the existence of inclined vortex pairs. These highly three-dimensional vortical structures are confined to one side of the jet centreplane and approximately align with the principal axis of rate-of-strain. Some of the topological features of these averaged eddy structures have been examined.

Acknowledgements

The author is greatly indebted to Dr. Peter Voke for his three years of guidance and help. He has read my drafts with great patience and offered many valuable comments. I wish to thank my former tutors Dr. H. Horton and Dr. L. Bernstein for their help during my six years in Queen Mary and Westfield College. I wish to express my gratitude to Dr. Glyn Thomas and Anna Down, who have been wonderfully supportive. Personal thanks must include my friends Professor W.R.C. Phillips and Denis Gill. Finally, I would like to thank Novella De Gregori for her warm-heartedness and love during my difficult years of hardship. I take this opportunity to apologise for my English. For any mistake in the thesis, it is entirely the author's responsibilty.

CONTENTS

List of Symbols

a_n	random coefficient.
a_{ij}	velocity gradient tensor.
A	velocity gradient matrix.
A_{out}	area of the outflow plane.
b	half width of the jet.
C()	cross-correlation coefficient.
E	energy.
G	search area.
G′	subdata.
h_i	viscous and convective terms.
J	momentum per unit length.
K	kinematic momentum.
K_z	effective wavenumber.
l	half-width.
M	mean momentum flux.
M_1	length of the template.
M_2	width of the template.
N_1	length of the search area.
N_2	width of the search area.
N_{max}	current number of positively correlated samples.
N_{min}	current number of negatively correlated samples.
$\underline{n}^{\alpha}$, $\underline{n}^{\beta}$	orthonormal vectors.
p	projection in Hilbert space or pressure.
p_o	static pressure.
Q	rate of flow per unit length.
Q_{total}	total entrainment mass flux.
r	expansion factor.
R()	covariance.
R_{ij}	velocity correlation tensor.
R-S	phase-space.
S	scaling factor.
S_x, S_z	scaling factors.
S	strain rate matrix.
$\underline{\underline{S}}$	second-rank strain tensor.
S_{ij}	strain rate tensor.
T	time.
T	template.

T_{eddy} large eddy turn over time.

u streamwise velocity.

U_o jet velocity.

U_{in} inflow velocity.

U_m centreline velocity.

U_s characteristic velocity.

v cross-stream velocity.

v_e entrainment velocity.

w spanwise velocity.

x streamwise coordinate.

y cross-stream coordinate.

z spanwise coordinate.

α Kolmogorov constant.

χ empirical constant.

δ_{mn} Kronecker delta.

Δt time step.

ε viscous dissipation.

$\phi^{(n)}()$ characteristic functions.

Φ characteristic function.

η Kolmogorov microscale

ψ threshold or stream function.

Λ event limit duration.

λ eigenvalue.

$\lambda^{(n)}$ eigenvalues.

λ_x, λ_z wavelengths.

$\underline{\hat{\lambda}}$ unit vector.

μ viscosity.

ν_e subgrid eddy viscosity.

ν_m molecular viscosity.

ν_t eddy viscosity.

θ angle of rotation.

ρ density.

σ arbritrary constant.

τ time delay or no. of iterations.

τ_t turbulent shear stress.

τ_l laminar shear stress.

φ wavelet family.

ω vorticity.

Ω_{ij} rigid body rotation tensor.

ζ_{min} minimum scale ratio of the template.

ζ_{max} maximum scale ratio of the template.

$\xi^{(n)}$ random coefficients of the orthogonal decomposition.

ζ similarity transformation or noise-to-signal ratio.

Introduction

The concept of the organised eddy structures became popular only some 20 years ago. An older generation of fluid dynamists viewed turbulence as a purely stochastic phenomenon. In recent years, it has been increasing evident that turbulent shear flows contain deterministic, identifiable and important structures. These orderly structures are superimposed on the random, background turbulence. The absence of a satisfactory theory of turbulent flow leads to many costs and delays in a variety of activities in engineering industries. The development and investigation of eduction methods of coherent structures are important components of a general move towards more structural descriptions of turbulence.

Townsend (1956) and Grant (1958) first proposed that turbulent plane wakes contain large-scale structures called "double-roller eddies" in the fully developed, far field turbulence. Over the past three decades, Townsend's large eddy hypothesis has been generally accepted and contributed greatly to our understanding of the physical processes in turbulence. The existence of double-roller eddies in the far wake is strongly supported by numerous studies.

The identification and eduction of the unexcited, organised eddy structures has been challenging area. The experimental approaches are undoubtedly very important but suffer from many limitations which hamper the progress of our understanding. Large eddy and full numerical simulations of the Navier-Stokes equations have become an increasingly important tool for elucidating the dynamical and topological information of the organised eddy structures. In numerical simulations, we can obtain as many flow quantities as we like, simultaneously in any direction. Of course, we have limitations, such as Reynolds number constraints, costs, memory and speed of the supercomputers. Although numerical simulations only produce appproximate solutions of the Navier-Stokes equations, the essential physics of turbulence

can be realistically captured. The richness of the simulation databases demands an eddy structure identification and qualification technique which can take full advantages of the available information. Pattern Recognition Analysis (PRA) is one of the most appealing and powerful techniques.

The problem of pattern recognition generally concerns a discrimination or classification of a set of events. One of the simplest approach is called template-matching. A prototype pattern or template is pre-selected. The subset of patterns from the random vector fields is projected on the template by computing their inner products, in order to measure their parallelism in the pattern space. In fact, the inner product is equivalent to the convolution. We are not interested in the intensities of the structures, but the similarity between the input pattern and the template instead. The ensemble averages of the structures are formed by gathering the sets of patterns which satisfy some proper matching criteria.

The present study is an extension of the pattern recognition technique of Mumford (1982, 1983). A nearly full simulation of a turbulent plane jet (up to 60 diameters) has been carried out, using a finite volume code. The Reynolds number based on the jet width is 1,600. In Mumford's experimental study (1982), the Reynolds number was 10,000 and his analysis was performed in the far jet region (160 diameters). We have performed pattern recognition analysis with the spatial-temporal simulation databases gathered in the near to intermediate fields of the jet. The three components of velocity and pressure patterns of the educed structures in three dimensions have been examined.

The main objectives of our study can be summarised as the following:

1) to generate realistic three-dimensional flow databases by numerical simulation of the turbulent plane jet at low

Reynolds number.

2) to develop and apply the pattern recognition code for the eduction of the organised structures in the near and intermediate fields of the jet.

3) to extract qualitative information about the structural topology in three dimensions and investigate their dynamical significance in turbulence.

Outlines of the Thesis

Chapter 2 Review and Background is essentially devoted to the historical development of the eduction and identification of the organised eddy structures in the wakes and jets. Particular emphasis is placed on the pattern recognition analyses. A broad overview of other eduction techniques is included. It covers a very brief review of the numerical simulations. The background materials contain the fundamental concepts of the coherent structures, vorticity dynamics and topological description of the flow patterns. As the scope of the subject is quite broad, it is not possible to be comprehensive.

Chapter 3 Theory and Method (Part I) develops the theory of the turbulent plane jet. It covers the similarity analysis and the theoretical solution of the two-dimensional turbulent jet. In the method section, the numerical schemes, geometry and the boundary conditions of the plane jet simulation are discussed.

Chapter 4 Method (Part II) is devoted to the methodology of the pattern recognition analysis. It assumes that the reader does not have knowledge of pattern recognition, and hence the use of the jargon and formalism of classical pattern recognition are avoided. The template matching technique and the ensemble averaging in three dimensions are discussed.

Chapter 5 Results and Discussion (Part I) presents the results of the numerical simulations, and the comparisons with the experimental results.

Chapter 6 Results and Discussion (Part II) presents the results of the pattern recognition analysis. An account of the features of the educed patterns is reported. The speculated topology of the structures is discussed in detail.

Chapter 7 Conclusions contain the conclusions of the plane jet simulation and PRA.

Appendices: give the classical form of the Karhunen-Loéve theorem and the proof. The principal axes of strain rate and topological classification of flow patterns are described.

CHAPTER TWO

Review

2.1 The Structures and Dynamics of the Coherent Motions in Plane Turbulent Jets and Wakes

Townsend (1950, 1956, 1976 and 1979) postulated the existence of a double roller eddy structure in the plane wake; large scale motions that contributed to the turbulent kinetic energy and the Reynolds stresses. In the measurements of the double velocity correlations in the turbulent plane wake (Townsend 1956), a physical model of the large eddies was constructed to account for the observed correlations. The double-roller eddy was described as a pair of counter-rotating vortical structures, having axes aligned with the direction of shear. The spectra of the velocity components along the principal axes of rate-of-strain were measured by Townsend (1950); he showed that the intensity of the low wavenumber component was strongest for the spectrum of the velocity perpendicular to the positive rate-of-strain (hence the vorticity of the large eddies tended to align with the axis of positive rate-of-strain). The roller eddy was postulated to be in energy equilibrium, extracting energy from the mean flow at the same rate as losing energy through the action of Reynolds stresses of the more disorganised turbulence. They had a growth, quasi-equilibrium and decay cycle. Based on the fitting coefficient for an eddy pattern, Townsend (1979) estimated that the contribution of groups of roller eddies to the turbulent energy was between 15 and 20% in a plane wake.

However, it can be misleading and confusing to construct a unique model eddy from the profiles of the double velocity correlations alone, because much of the detailed structural and phase information is smeared in the long time-averaged correlations. The proposed model was inconsistent with some of the observed correlation profiles and some components of the tensor could not be measured accurately because of the experimental limitations.

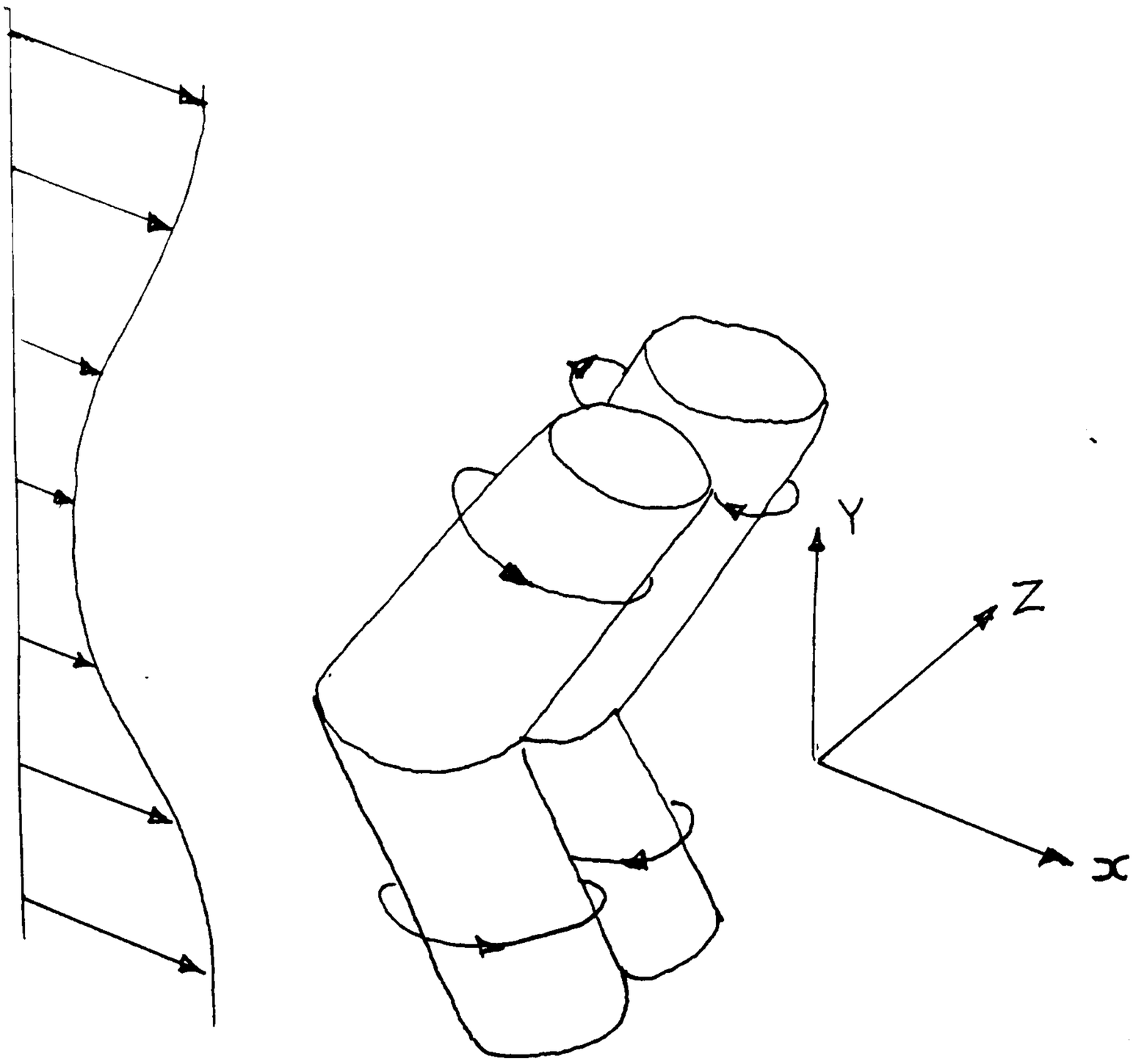

Fig. 2.1 Double roller eddy in the plane wake suggested by Grant (1957).

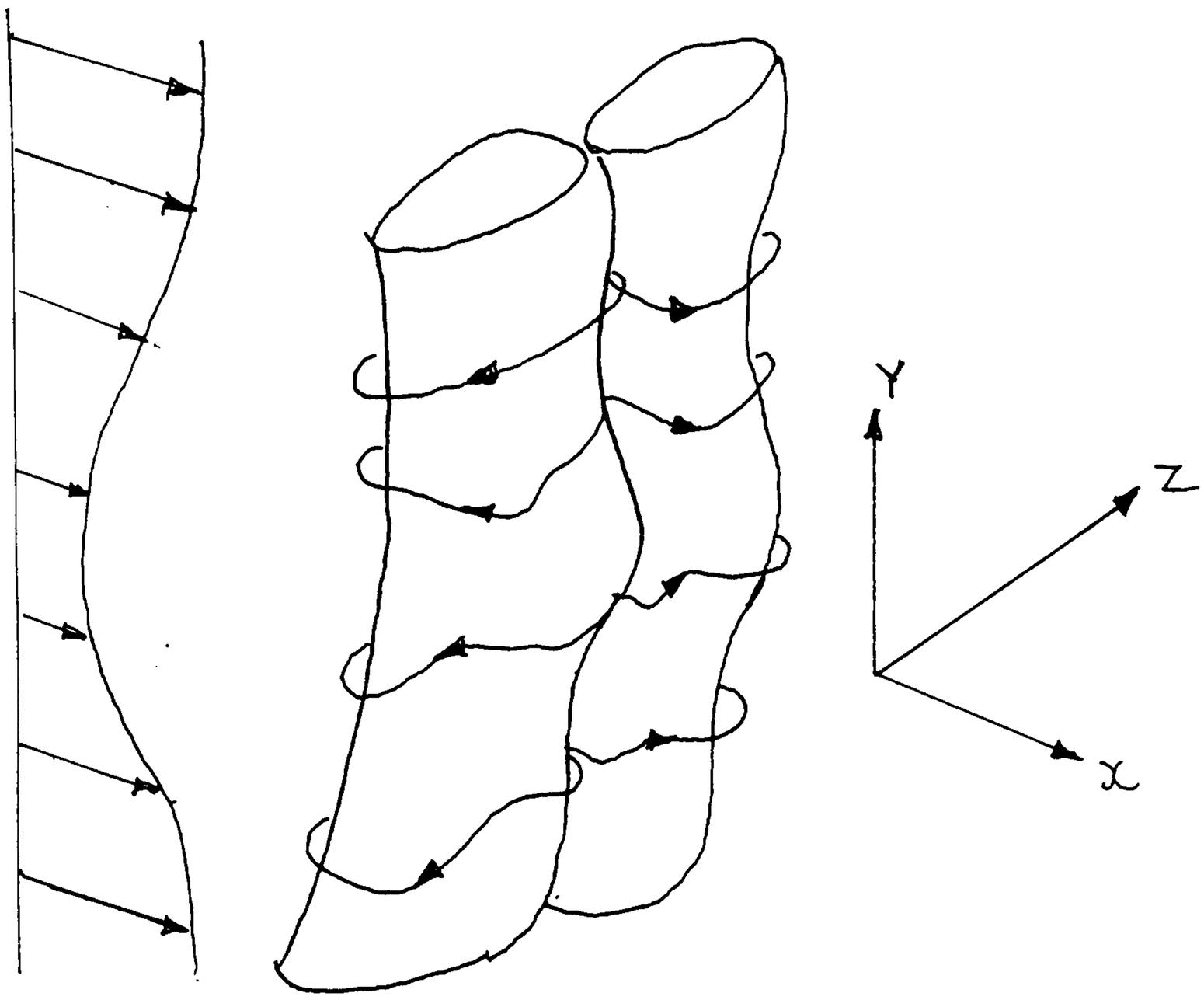

Fig. 2.2 Eddy structure inferred from the results of orthogonal decomposition by Payne and Lumley (1967).

Grant (1957) measured the nine components of the double velocity correlation tensor in the far wake at a Reynolds numbers of 1300. He suggested a slightly modified model of the roller eddy (figure 2.1) and described the mechanism of the mixing jets in relation to the entrainment.

Lumley and Payne (1967) applied the orthogonal decomposition technique to Grant's correlation measurements of the wake behind a circular cylinder. The most energetic eigenfunction was identified as a counter-rotating eddy pair, as shown in figure 2.2. Although this technique offered the most objective and elegant way of extracting the organised eddies, some difficulties were encountered. For example, the complete correlation tensor had to be constructed from an incomplete set of correlation measurements by using the continuity equation and the mixing length assumption. As a result, it is not clear whether the structural information can be fully retained in the incomplete time-averaged correlation tensor. Some abnormalities of their results were observed; the roller eddy structures oriented normally to the wake centreplane and inclined slightly near the centre.

A detailed discussion of the Rapid Distortion Theory (RDT) and the double roller eddies in the plane wake was given by Savill (1979,1987). Any turbulent shear flow was proposed to be composed of basic building blocks of eddy structures; namely the roller eddies, small isotropic eddies and the Large Anisotropic Swirling Motions (LASMOS). The LASMOS were two-dimensional transverse vortices associated with the bulges on the turbulent/non-turbulent interfaces and the entrainment process. The modelling of RDT could possibly offer a description of the production of the roller eddies and their distortion with time by the mean shear. Moreover Savill suggested that the longitudinal eddies could be produced by the highly elongated and rotated double roller eddies. Following the pioneering work of Townsend (1978), Savill (1979) applied a correlation matching PRA technique to analyse the streamwise velocity data of a plane wake. He found that the roller eddies inclined at approximately $\pm 45^{\circ}$

to the direction of the mean flow, and often linked across the wake centreplane as shown in figure 2.3. Their packing density was high enough that they interacted with one another. His results also showed that the roller eddies occurred in groups of three to five.

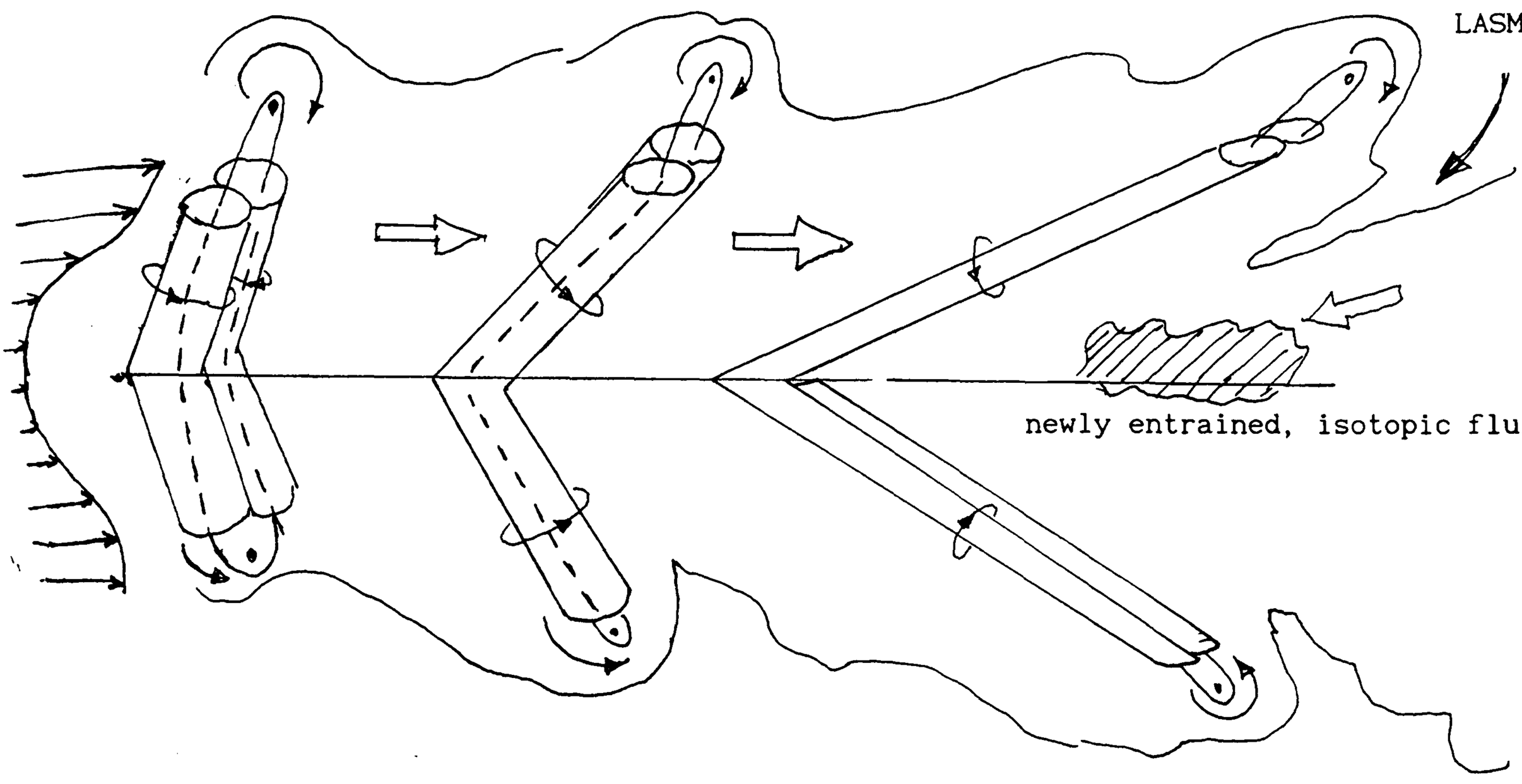

Fig. 2.3 The distortion of a double roller eddy from Savill (1979).

Oler (1980) studied the anti-symmetric vortex street of a plane jet experimentally, with the evaluation of a vortex street numerical model. The Reynolds number was 174,000. Intermittency, interface crossing frequency were measured in the near-jet region ($10 \leq x/D \leq 60$). The two-point correlation measurement showed the existence of Kármán vortex street type of counter-rotating, periodic vortices on opposite side of the centreline, producing antisymmetric transverse distributions of lateral velocity and intermittency. In the numerical modelling, the vortex street was assumed to be a linear superposition of scaled Rankine

vortices, ignoring the effects of the small scale turbulence. The streamwise variation and vortex center offset were specified by similarity scaling relationships. Oler's vortex street model was capable of reproducing the growth rate, mean velocity profiles and velocity decay rates. But it failed to predict the correct sign of Reynolds stress, intensities, spectra and correlations.

Mumford (1982) performed correlation measurements and pattern recognition analysis in the turbulent plane jet at a Reynolds number of 10,000. His results showed that the large scale structures consisted of strainwise roller eddies in various forms, having axes at ±135 degrees to the streamwise axis as shown in figure 2.4. They were confined to one side of the jet centreplane. Moreover, the roller structures were extracted in the far wake behind a circular cylinder (Mumford 1983). The configurations of the rollers in the plane wake were quite different from those in the plane jet.

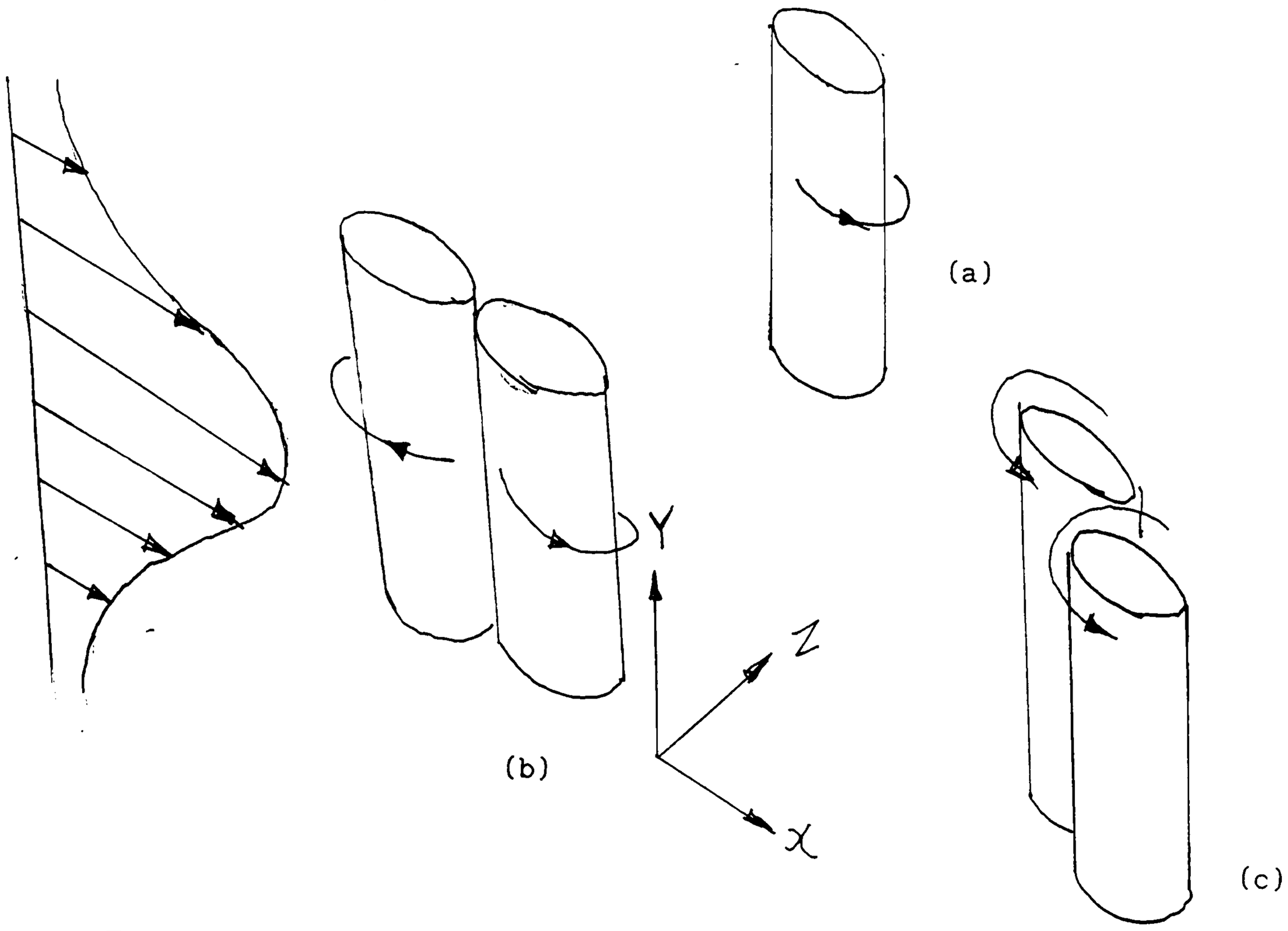

Fig. 2.4 The strainwise roller eddies in a plane jet from Mumford (1982); (a) single roller eddy, (b) double roller eddy separated in the streamwise direction with opposite sign of circulations, (c) double roller eddy separated in both streamwise (x) and spanwise (z) directions with the same sign of circulations.

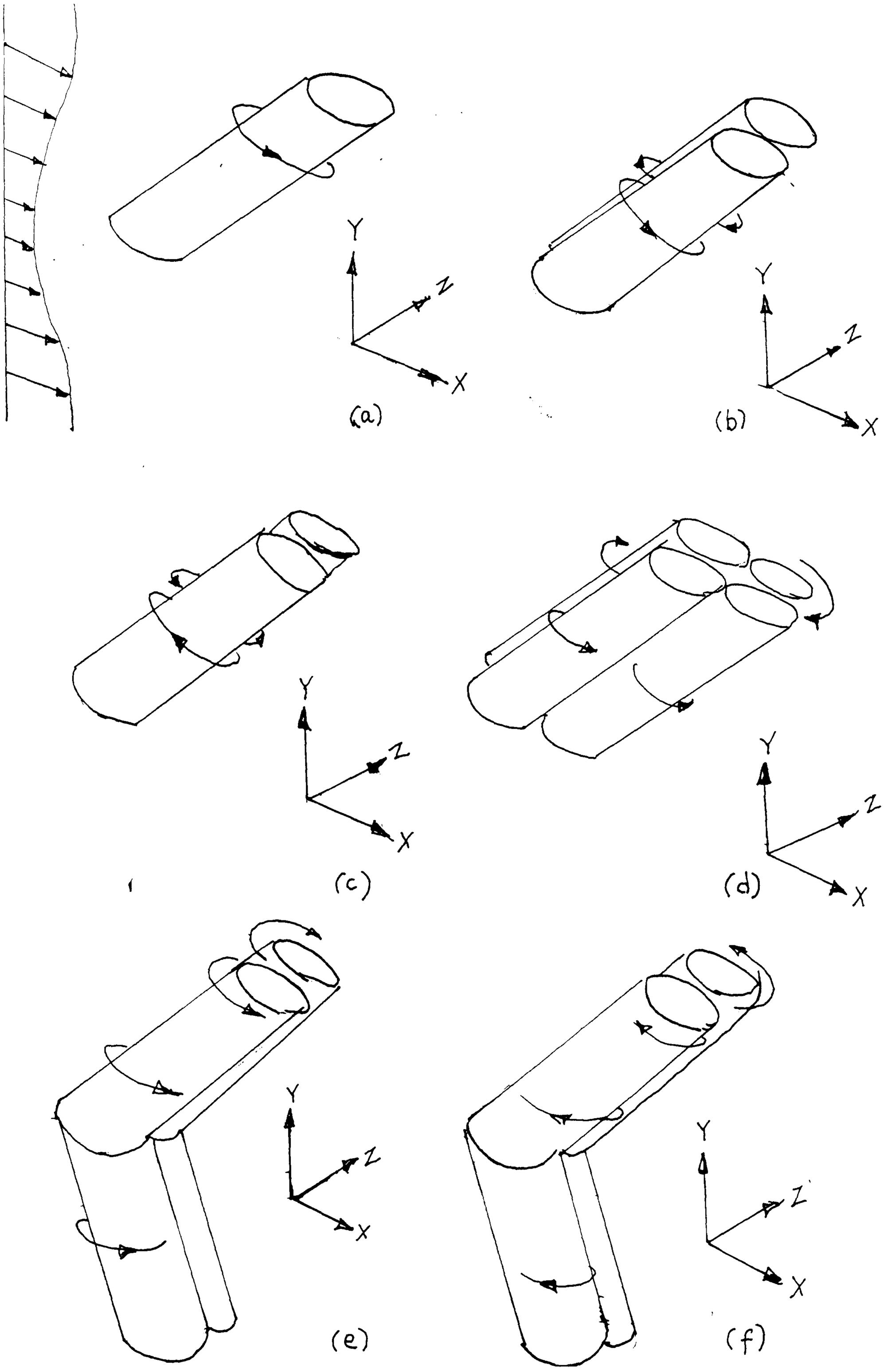

Fig. 2.5 The possible forms of roller eddies in a plane wake from Mumford (1983).

Various possibilities were suggested by Mumford (figure 2.5). He found that a proportion of the rollers were confined to either side of the wake centreplane, rather than extending across the wake. The rollers tended to occur in pairs or in groups.

Further studies of turbulent plane wakes were carried out by Ferré and Giralt (1989,1990), who applied pattern recognition analysis to study the plane wake behind a circular cylinder at a Reynolds number of 9,000. The single and double roller eddies were found to be the dominant structures in the far wake, while the Kármán vortices were detected in the near wake regions. Moreover, they proposed that the double roller eddies were responsible for the entrainment motions by engulfing the external potential flow and the self-preserving property of the wakes. The number of roller eddies active in the wake was suggested to be constant regardless of the streamwise distance.

Antonia & Browne (1983,1986) applied conditional averaging to study the structures in the nearly self preserving region of a heated turbulent plane jet. Their analysis was mainly concentrated on the spanwise organised motions associated with the temperature front, and gave no direct information about the strainwise roller eddies. They identified the temperature front as adjacent vortical structures (with vorticity ω_z in the spanwise direction) connected by a

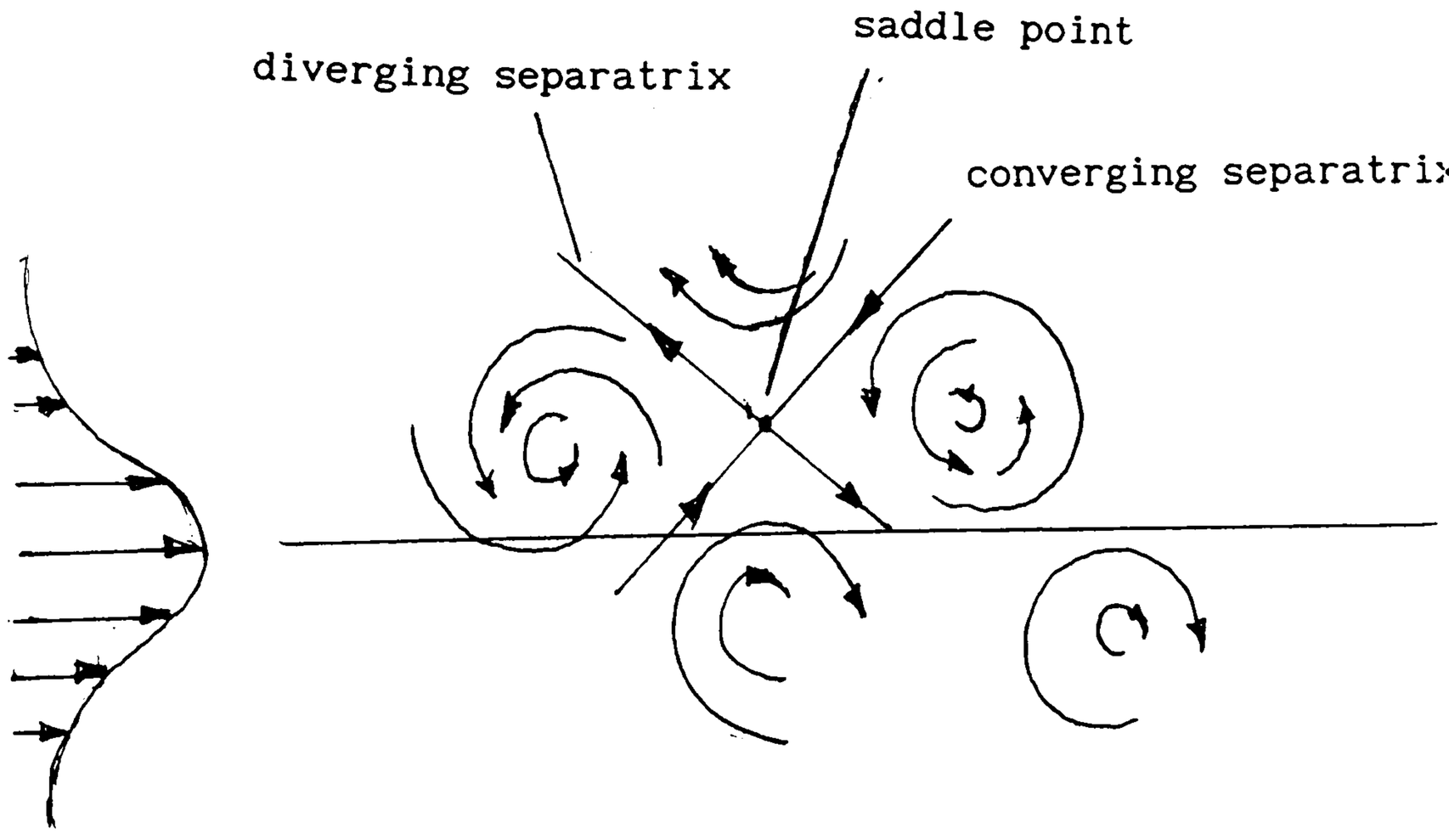

Fig. 2.6 The saddle point, diverging and converging separatrices between the spanwise vortices.

diverging separatrix, the streamline of velocity vectors pointing away from the saddle point, which is located between two adjacent vortices with spanwise vorticity of the same sign as illustrated in figure 2.6. They showed that there is a large concentration of the coherent production terms for the turbulent kinetic energy and temperature variance near the temperature front so that the diverging separatrix may be associated with high turbulent energy dissipation and temperature dissipation. They also observed that the coherent stresses and temperature fluxes are large near the diverging separatrix. Antonia & Browne further suggested that the double-roller eddies could align with the diverging separatrix; the strainwise rollers and the spanwise vortical structures co-exist.

Ferré, Mumford, Savill and Giralt (1990) postulated several hypotheses on the structures of the far wake: a) the tops of the rollers were connected together forming a horseshoe vortical structure as shown in figure 2.7; the "mixing jets" observed by Grant (1958) might be identified as the tops of

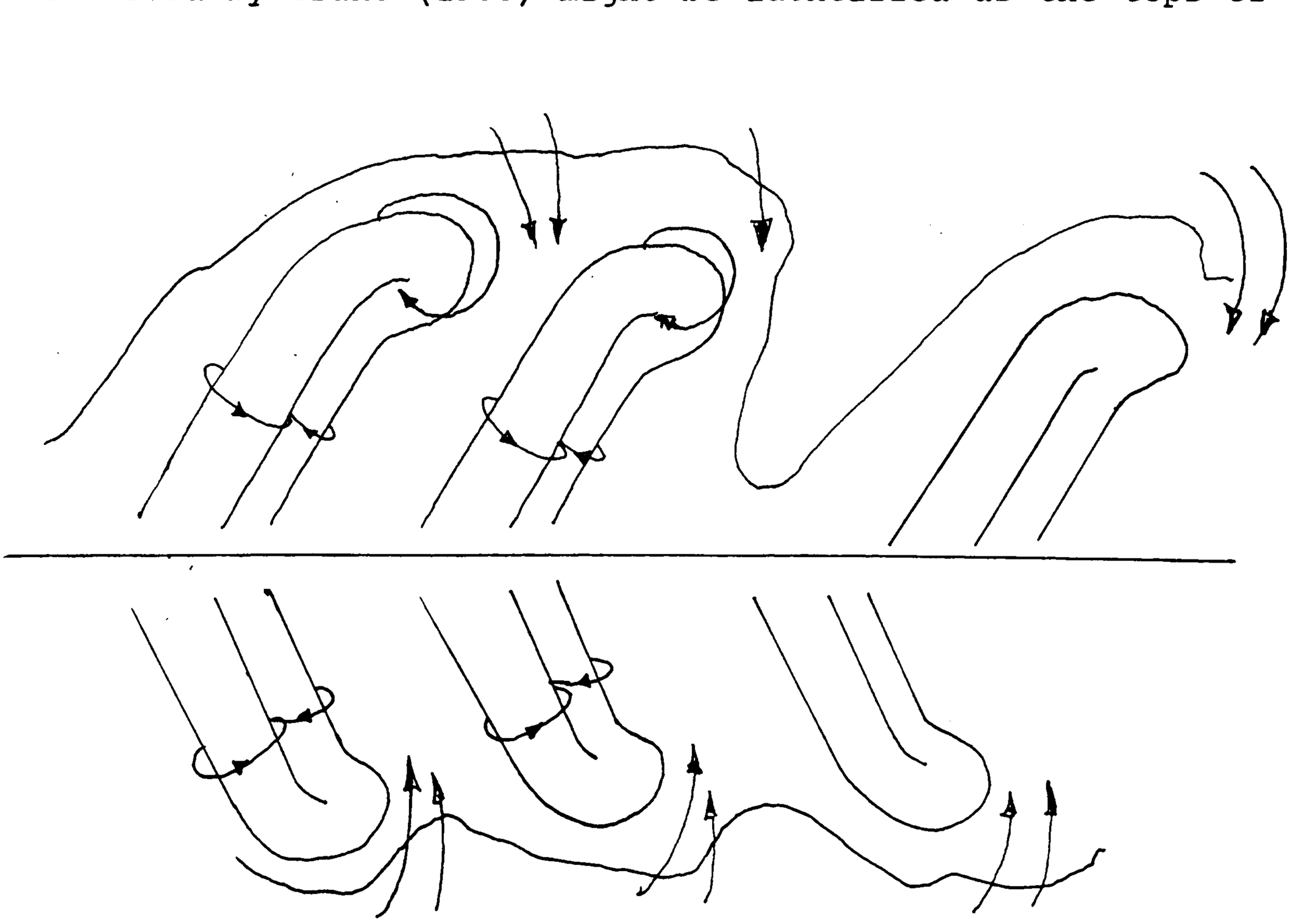

Fig. 2.7 The horseshoe roller structures in the plane wake from Ferré *et al* (1990).

the double-roller eddies. b) the roller eddies contained 40% of the total turbulence energy c) the fine scale motions were the strongest between the rollers.

Hussain and Hayakawa (1987, 1989) studied the organised structures in the intermediate region of an unexcited plane wake by using a vorticity-based sampling and averaging technique. Some of Hussain's viewpoints can be summarised as follows: (a) The structure size does not increase in proportion to the wake width and remains almost constant. The dispersion and three-dimensionality of the structures increase significantly with increasing downstream distance. (b) The turbulence production and the strain rate are maximum at the saddle region. It plays significant role in the dynamics of the flow field. (c) The inclination of the transverse structure or horseshoe-like vortices is about 30° but not 45°. (d) Horseshoe-like vortices with symmetric legs are unlikely to be frequent. They may be predominantly asymmetric with diffused legs or legs of unequal strength. (e) Structures in the intermediate wake region should be similar to those in the far wake. (f) The double roller eddies are formed by outward kinking of the spanwise rolls, being confined to either side of the centreplane. (g) the double-roller eddy (extending over both sides of the centreplane) proposed by Townsend (1956) and Grant (1983) would not be a dominant structure that occurs instantaneously. However, there were some problems associated with Hussain's vorticity eduction technique: for example, his so-called 'objective approach' did require the use of arbritary threshold criteria. The detection of phase coherence of vorticity was simply based on several points surrounding the peak vorticity centre with very limited probe resolution. Moreover, it is hard to justify the use of Taylor's hypothesis in the computations of instantaneous spanwise vorticity.

The inviscid vortex-filament technique was used by Meiburg and Lasheras (1988) to model the three-dimensional, transitional plane wakes combined with experimental flow

visualisations. Such an approach has some limitation; for example the break-up, relinking and viscous diffusion of the vortex tubes have not been taken into account. However, it is quite reasonable to simulate the evolution of the vortex tubes in the three-dimensional transition of the wake, where the initial stages of the flow are essentially laminar. They found that symmetric (under horizontal perturbation) and non-symmetric (under vertical perturbation) modes of vorticity configurations are present. The initial evolution of vorticity is dominated by redistribution, reorientation and stretching. The streamwise and spanwise vortices strongly interact with each other. The horseshoe-like vortices were found to be 180° out of phase on the two sides of the plane wake. A staggered array of closed vortex loops were observed as they started to wrap around the spanwise vortices of the opposite layers. However, their vortex filament technique produced incorrect anti-symmetric pairing of the vortices across the centerplane.

2.2 Relationship between Organised Eddies and Entrainment

In the free planar jet, the fully turbulent fluid is bounded by irregularly distorted surfaces and is intermittent at the mean boundary. The original concept of an entrainment mechanism was based on the idea of small scale nibbling of the interface (Corrsin and Kistler 1954). The large eddies had been thought to be responsible for the formation of bulges and the lateral growth of the turbulence zone in the downstream direction. The propagation of the turbulence front causes the increase of total volume of the turbulent fluid. In the turbulent region the flow is rotational while outside the bounding surfaces the fluid is irrotational. The irrotational fluid is turned into rotational fluid by the viscous shearing actions concentrated at a thin layer of interface. Corrsin and Kistler showed that the thickness of the interface should be the same order of magnitude as the Kolmogoroff length scale.

Grant (1957) described the "mixing jets" as a series of periodic structures in which turbulent fluid is projected outwards from the centre of the wake (The name jet is the terminology constantly used by Grant and Townsend; I feel that it may be more appropriate and less confusing to call it entraining eddy). The "mixing jets" occur in groups of several structures arranged asymmetrically on both sides of the wakes, each of the structures maintaining a nearly regular streamwise spacing. The generation mechanism of mixing jets may be the instability of turbulent shear stress, which is similar to the Helmholtz type instability of a vortex sheet. The fluid surrounding the "jet" is essentially irrotational. A schematic sketch of the structures is given in figure 2.8(a),(b). Townsend (1970)

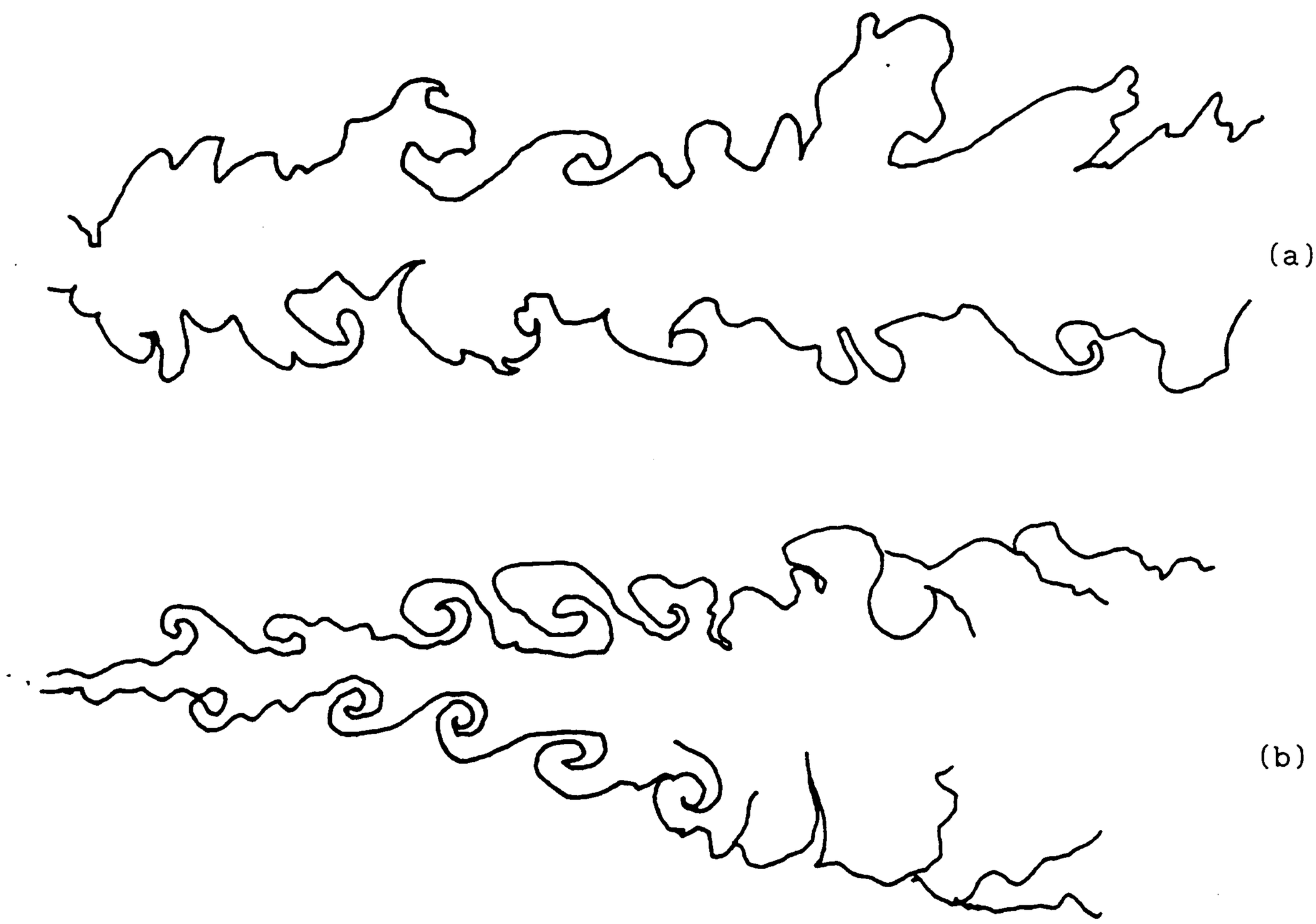

Fig. 2.8 Schematic sketches of (a) the plane wake, (b) the plane jet.

suggested that the entrainment mechanism is a folding in and engulfing of the potential fluid by movements of the interface. The basic origin of the mechanism is the velocity fields of eddies of the main motion. He concluded that rapid entrainment in a plane wake depends on an active instability of the interface.

The entraining eddies can be readily visualised in the photographs of the plane jets taken with stroboscopic lighting at moderately low Reynolds number, but at high Reynolds number the large structures are obscured by the fine grained turbulence. Brown (1935) observed from flow visualisation of a plane jet that vortices are produced on alternate sides of the jet. These structures normally appear as cylindrical vortices alternatively on opposite sides of the jet, but simultaneously on opposite sides in some cases. These vortices may be the same kind of structures as the mixing jets observed in the two dimensional wake by Grant, but the orientation of the vortex structures is opposite to those in the plane jets.

Freymuth (1966) studied the stability of a symmetric shear layer formed at a jet orifice. The unstable wave motion is initiated by the velocity difference between the fluid inside and outside the jet, producing *jelly rolls* (Rodi 1982); a surface that rolls up. The vortex motion induces a velocity field in the non-turbulent fluid, which in turn rolls into the jet; the entraining fluid is engulfed and carried downstream by the mean flow.

LaRue and Libby (1973) examined the intermittency and interface structure of a heated plane wake. By using the Fast Fourier Transforms of the digital data measured with one or two probes, they obtained the power spectrum, coherence, phase and cross covariance of the temperature and intermittency signals. No evidence of periodicity of interface structure was shown by the autocovariance coefficient. The transverse axis of the large scale structures was about 31° deduced from quantitative

measurement. They suggested that the interface structures are related to the large scale structures. The symmetric structure could correspond to the vortex pair of Grant (1958) with its vertex at the centreplane while the antisymmetric structure (or the mixing jet described by Grant) may corresponds to a vortex pair with its vertex displaced away from the centreplane.

The connection between entrainment and the large eddies was described by Bevilaqua and Lykudis (1977), who showed that the large eddies corrugated the interface between the turbulent flow and the potential flow by engulfment or folding.

In the pattern recognition analysis of the heated turbulent wake, Ferré and Giralt (1989) suggested that the intermittent bulges were the double-roller eddies emerging towards the edges of the wake which occured mainly at the front edges of the bulges. The double-roller eddies were suggested to exist in groups of three to five, and in a staggered arrangement (Ferré *et al* 1990). The entrainment of the potential flow could be induced by the top of the rollers.

2.3 Coherent Structures of Jets and Wakes in Flow Visualisations

The phenomena of complex smoke patterns produced by jets are commonly seen in our daily experience. The buoyant jet produced from the smoke of a cigarette is one example. One can appreciate the complexity of these smoke patterns by performing a simple experiment in a sunny room with still air. If we hold the cigarette in an upright position without any external disturbances, the buoyant jet is laminar near the cigarette end and becomes turbulent as it moves upwards (figure 2.9a). It is not difficult to produce a train of orderly vortex rings by jerky movement of the cigarette along the axial direction (figure 2.9b). If the cigarette is oscillated laterally, an array of interlocking vortex loops

can be observed (figure 2.9c). Careful observation of the vortex ring can give us a very rough idea about the evolution and break-up of the structure. The diameter of the ring is growing, as it travels upwards. The waviness of the loop starts to occur, then it becomes highly distorted. The closed vortex loop cuts and links itself, and finally breaks into randomly orientated or sphagetti-like, diffused vortex filaments.

Although pictures of smoke patterns can be sometimes confusing or even misleading, some of the most convincing evidence for the existence of highly organised structures have been inferred from flow visualisations. The Schmidt number (defined as the ratio of kinematic viscosity to smoke diffusivity) can be important for the interpretation of the pictures, depending on the types of visualization methods. Normally a fluid tracer with relatively high Schmidt number is desirable for the visualization of the streamlines; the diffusivity should be low in order to avoid the rapid spreading of the tracer by molecular diffusion in the flow.

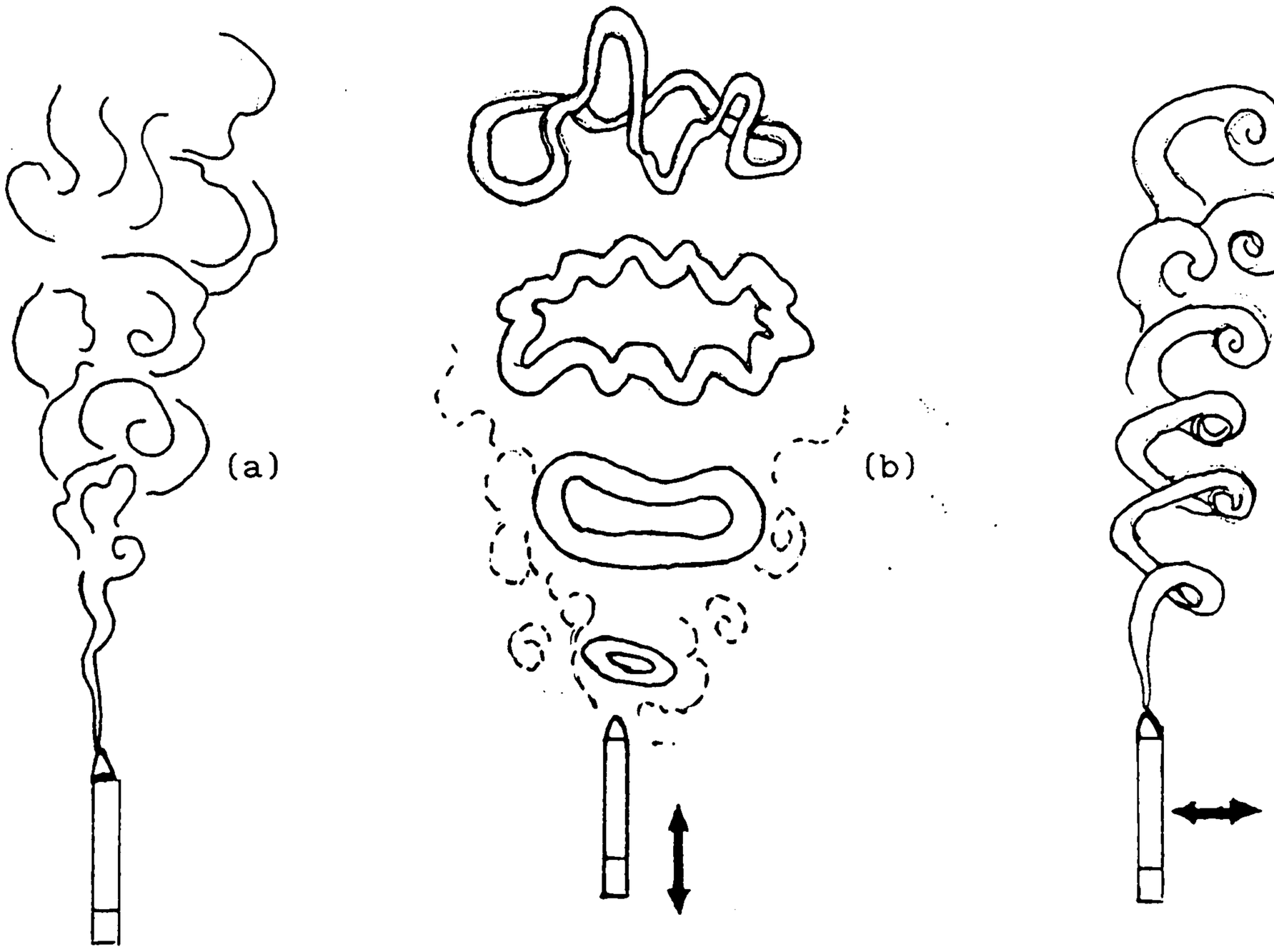

Fig. 2.9 Buoyant jet produced from the smoke of a cigarette. (a) no perturbation, (b) vertical oscillation, (c) lateral oscillation.

Figure 2.10(a) to 2.10(f) show some fine examples of these structures in the jets and wakes (Breidenthal 1980, Perry and Tan 1984, Williamson 1988, Cimbala *et al* 1988, Soria *et al* 1992. It should be noted that the Schmidt numbers of the photographs were not mentioned in the original sources). Figure 2.11 shows the intuitive interpretation of the visualised structures. Even though the flows are at relatively low Reynolds numbers, they help us to understand the generation and evolution mechanisms of the large scale structures at higher Reynolds. The significance of these pictures will be discussed later.

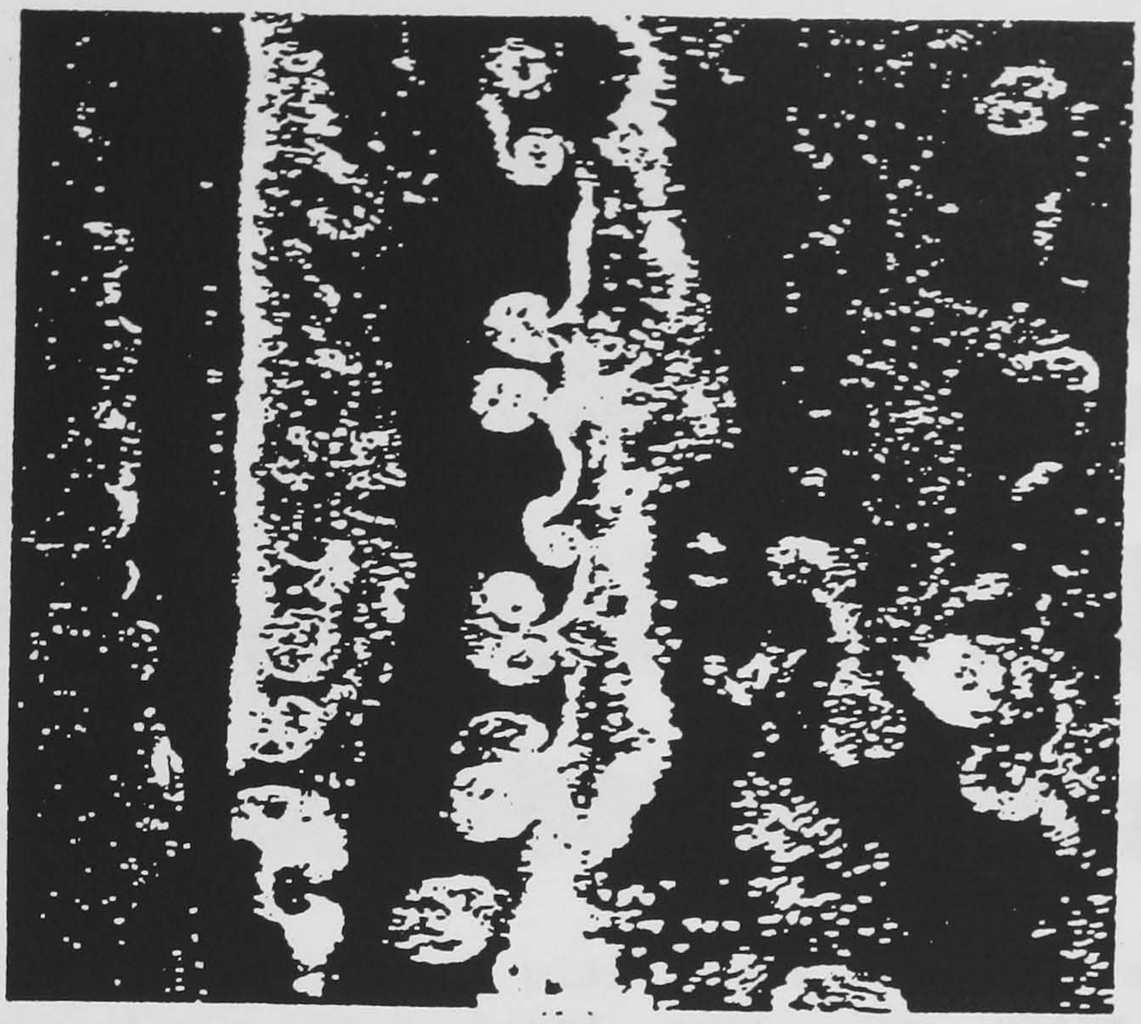

Fig. 2.10(a) Plan view of the mushroom-like streamwise vortices in the near wake region of a circular cylinder. Re = 901 (photograph by Soria (1992)).

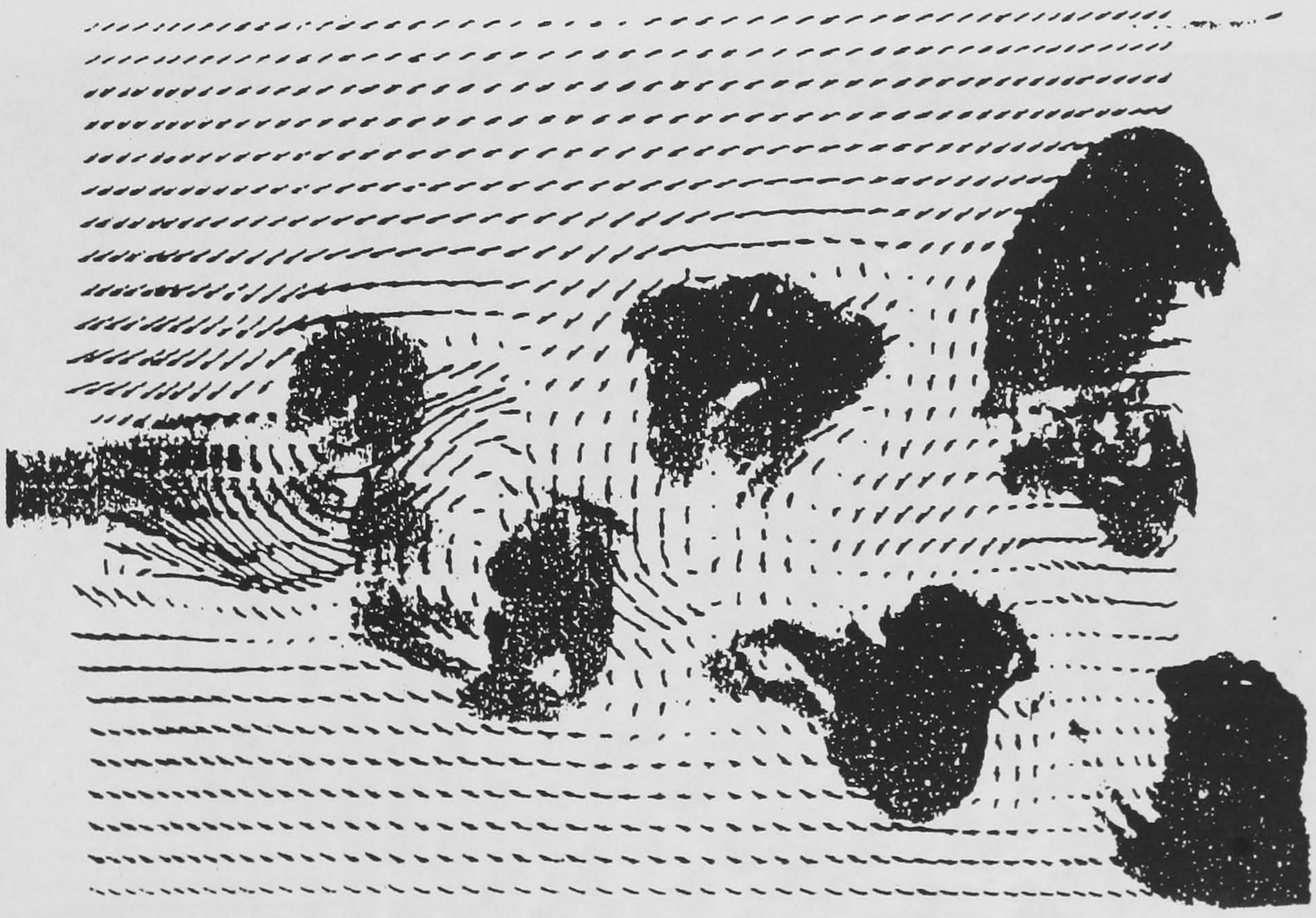

Fig. 2.10(b) Vector field superimposed on smoke photograph of a double-sided three dimensional co-flowing jet. (photograph by Perry and Tan (1984)).

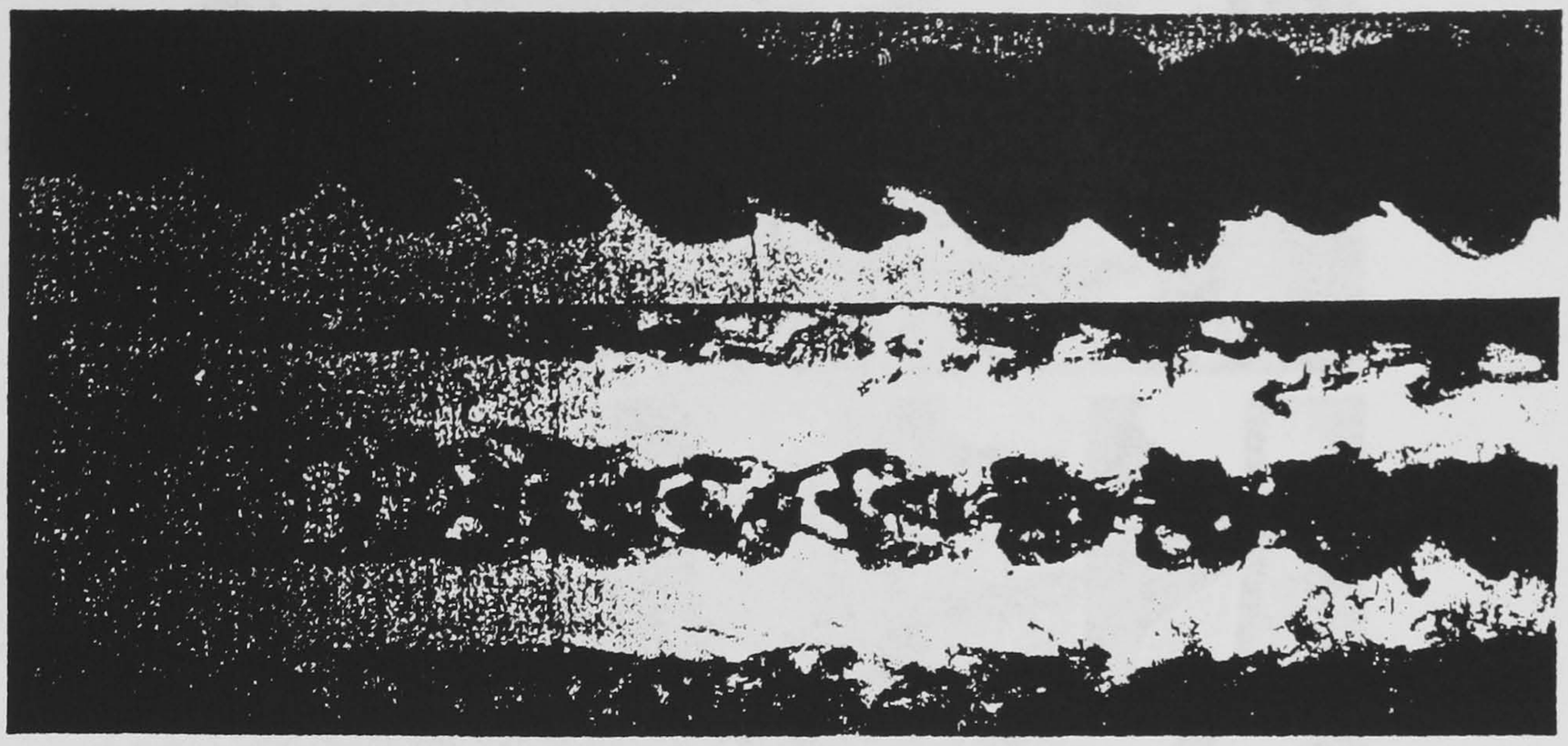

Fig. 2.10(c) Side and plan views of the wakes behind a splitter plate with blunt edge. Two sharp wedges were attached to the end of the splitter plate. (photographs by Breidenthal (1980)).

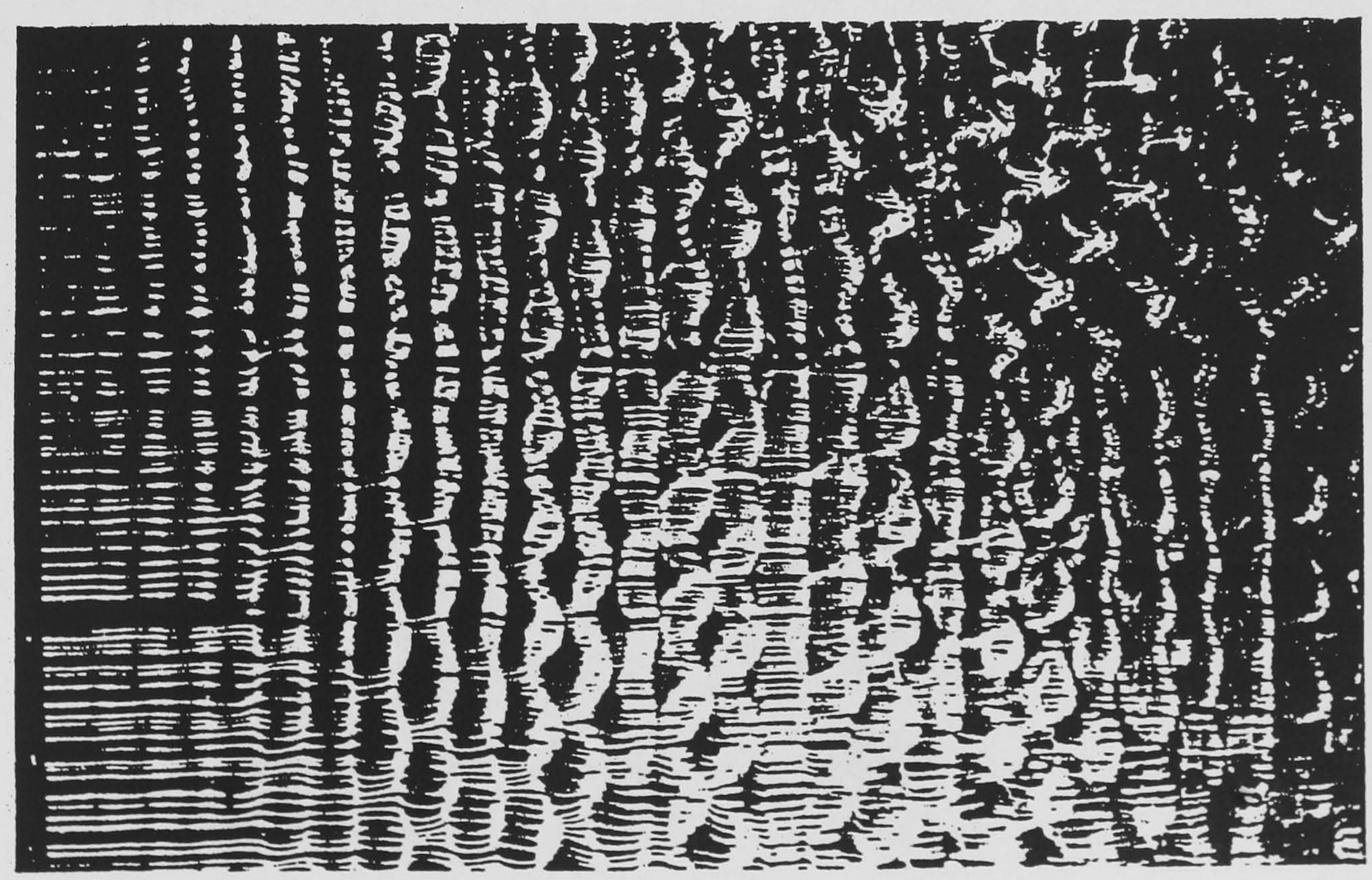

Fig. 2.10(d) Plan view of a plane wake behind a circular cylinder at Re = 150, x/d = 100, y/d = 2. (photographs by Cimbala *et al* (1988)).

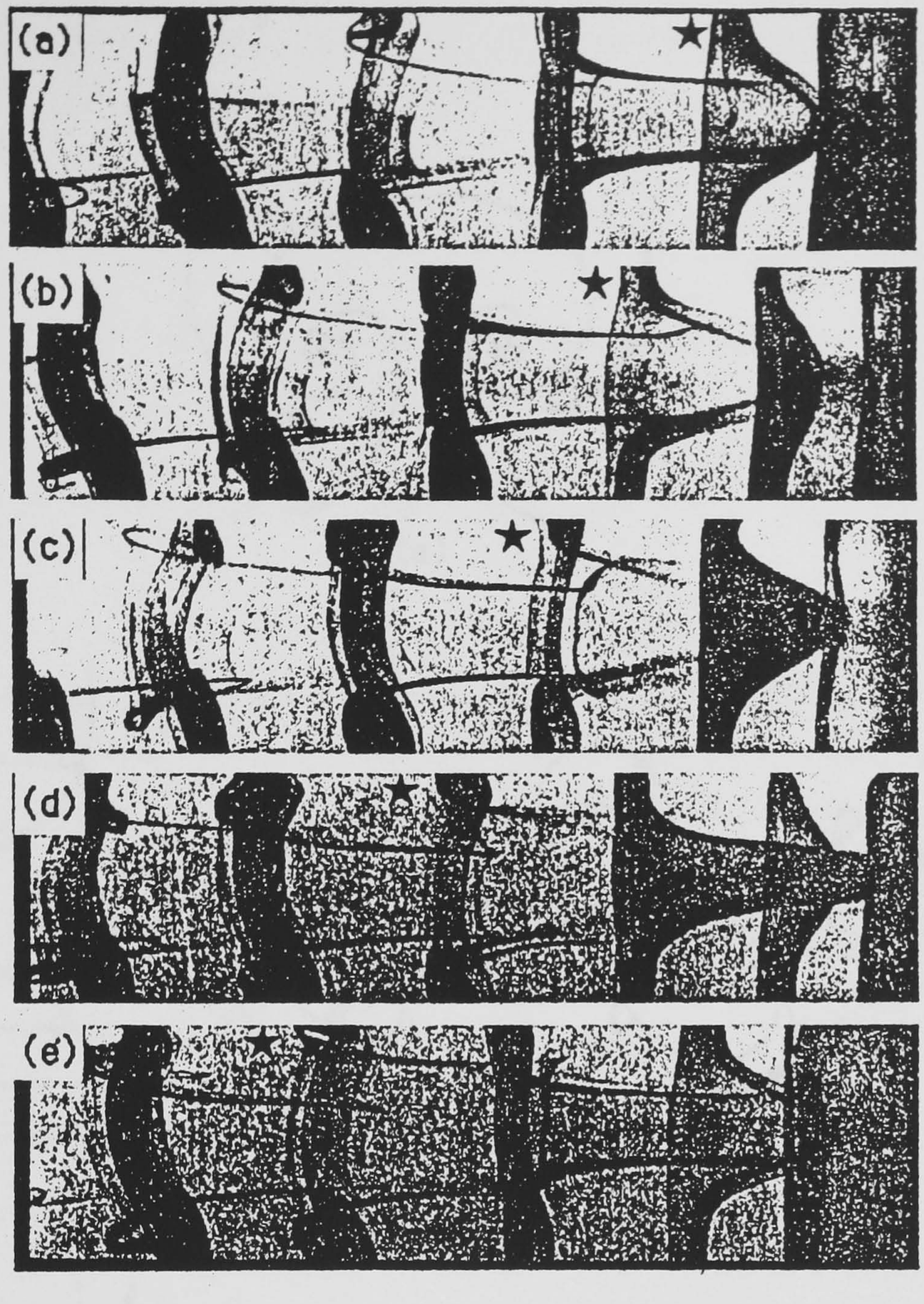

Fig. 2.10(e) Plan view of the cylinder wake at Re = 180; formation of the vortex loops and pairs of streamwise vortices.

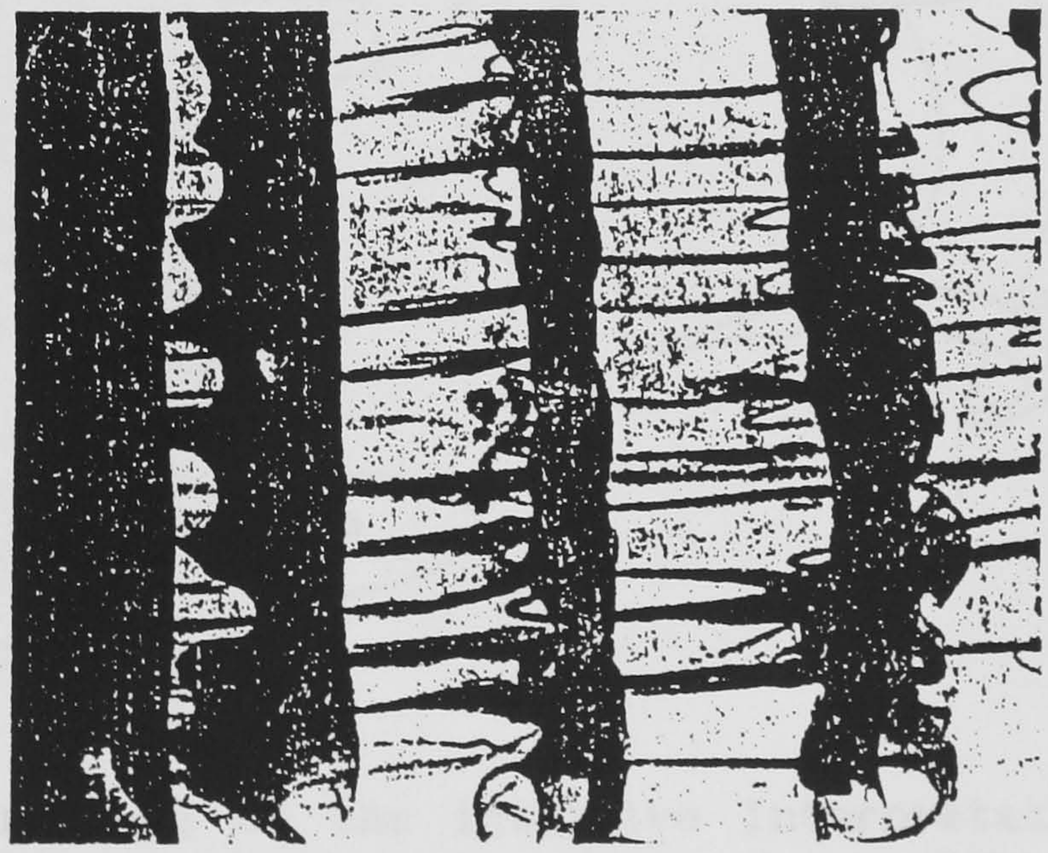

Fig. 2.10(f) Formation of the finer-scale streamwise vortices at Re = 285.

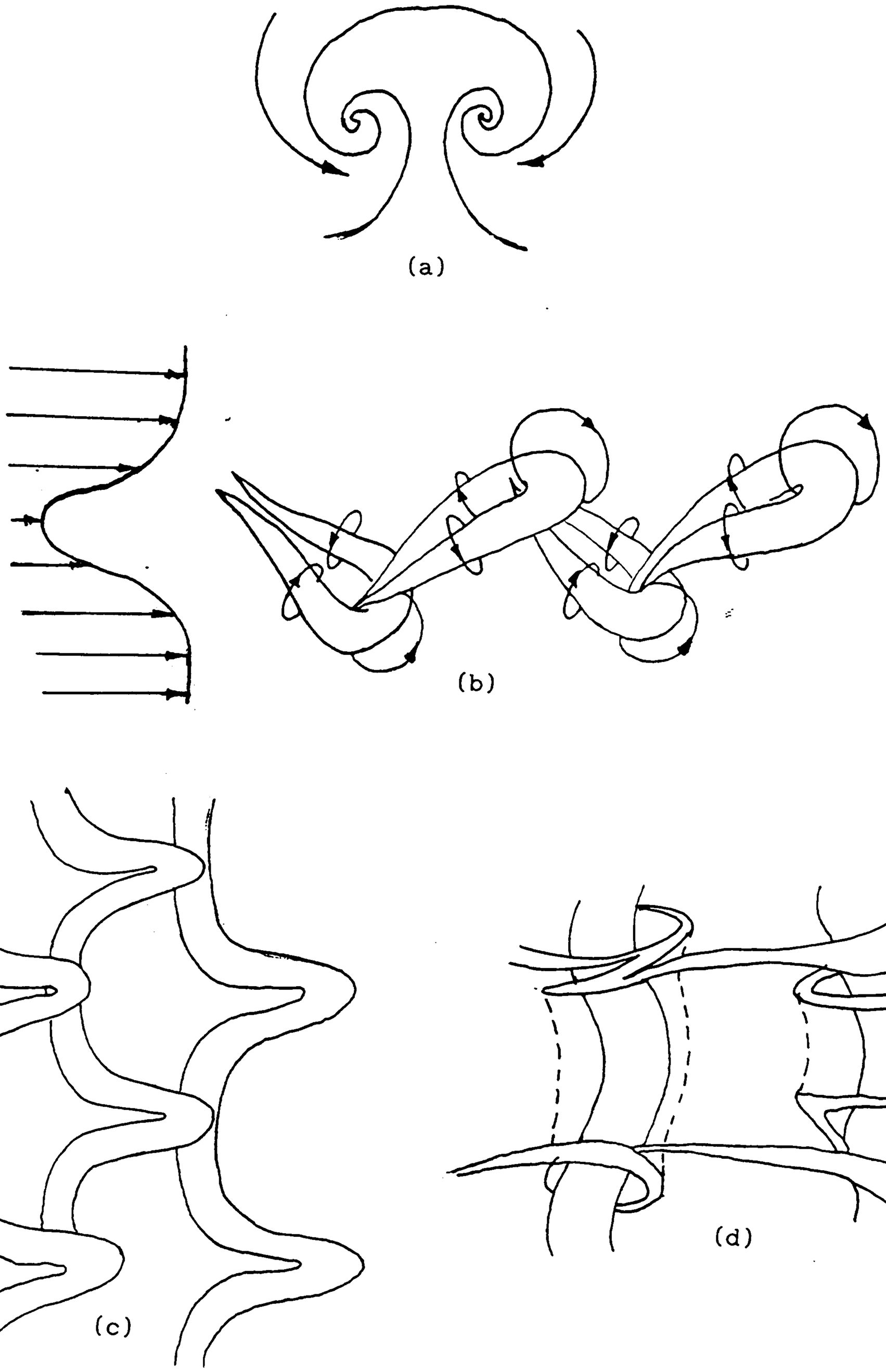

Fig. 2.11 Sketches of the intuitive interpretation of the flow visualisation photographs: (a) mushroom-like streamwise vortices in the plane wake, (b) interlocking loops in the 3-D wake behind a splitter plate, (c) distorted spanwise rolls in the transitional wake, (d) distorted rolls and streamwise vortices in the transitional wake.

2.4 Detection and Quantitative Characterisation Techniques of the Organised Motions in Turbulent Shear Flows

a) Two-point correlations

The general form of the *double velocity correlation* can be written as:

$$R_{ij}(\mathbf{x};\mathbf{r},\tau) = \overline{u_i(\mathbf{x},t)\ u_j(\mathbf{x}+\mathbf{r},t+\tau)} \qquad (2.1)$$

In most experimental studies, the time delay τ is zero so that the velocity components are measured simultaneously at two separated points. R_{ij} should tend to zero for separation larger than the characteristic length scale of the largest eddies, since correlation between velocities at two separated points should not be affected by fine scale motions. The principal correlation tensors can provide qualitative information about the structure of the large organised eddies and it is possible to fit a model eddy in order to account for a set of correlations (Grant 1957, Townsend 1976).

The nine principal correlation functions are:

$$R_{ii}(r,0,0) \qquad R_{ii}(0,r,0) \qquad R_{ii}(0,0,r) \quad i = 1,\ 2,\ 3 \qquad (2.2)$$

The velocity components can be either parallel (transverse correlation) or perpendicular (longitudinal correlation) to the separation r.

The addition of the time delay increases the complexity of the experimental measurements. Usually the space-correlation function for a single velocity component and spatial separation in the direction of the mean flow is measured.

b) Conditional Sampling

Conditional sampling generally means that we sample a data

set according to some predetermined criterion; we average some fluctuating property of the flow only if the criterion is satisfied. Conditional sampling with one probe or two probes has been applied for the detection and quantitative analysis of many different kinds of flows. At the outer edge of a boundary layer or jet, the flow is intermittent. With one probe at a fixed point, an intermittency function is defined such that the criterion is the inclusion or non-inclusion of the data (whether the probe is within or outside the boundary of the turbulent flow). We can define an intermittency function as:

$$I(\mathbf{x},t) = \begin{cases} 1 & \text{(if the flow is turbulent at } \mathbf{x}\text{)} \\ 0 & \text{(if the flow is non-turbulent at } \mathbf{x}\text{)} \end{cases} \qquad (2.3)$$

Zone averages are then determined by time averaging of the products between the signal and the intermittency function

$$< f > = \lim_{T\to\infty} \frac{1}{T} \int_{t}^{t+T} f(t')\ I(t')\ dt' \qquad (2.4)$$

It is possible to use two probes; one of them is fixed in space for the triggering, the other one is variable for the spatial sampling. Multiprobe conditional sampling in the jet flows has been described by Yule (1980), who also discussed the problem of *phase scrambling effects* associated with the measurements: difficulties are encountered in the conditional sampling as there are variations of the size, strength and shift positions (relative to the sampling probes) of the structures.

c) VITA

The Variable Interval Time Average (VITA) technique of Blackwelder and Kaplan (1976) uses a detector probe to detect the occurrence of bursts in the wall-bounded turbulent shear flows. The VITA average of the streamwise velocity $U(x_i,t)$ is defined as:

$$\hat{U}(x_i,t,T) = \frac{1}{T}\int_{t-T/2}^{t+T/2} U(x_i,t)\,dt \qquad (2.5)$$

T is the averaging time and is variable. The VITA average of the squared streamwise velocity minus the local squared mean is used as a measure of the local turbulent kinetic energy:

$$\hat{var}(x_i,t,T) = \hat{u}^2(x_i,t,T) - (\hat{U}(x_i,t,T))^2 \qquad (2.6)$$

The velocity signals are ensemble averaged if $\hat{var}$ exceeds the threshold value; the threshold value is usually defined as the r.m.s. of the turbulent intensity multiplied by an arbitrary constant.

d) Stochastic Estimation

In this technique, first developed by Adrian (1974), the *conditional* velocity field is estimated by the *unconditional* statistics. An estimate of the conditional average of the velocity vector **u** at the position **x** + **r** and time t + τ can be written as:

$$\hat{\mathbf{u}}(\mathbf{x}, t; \mathbf{r}, \tau) = \langle \mathbf{u}(\mathbf{x}+\mathbf{r}, t+\tau) \mid \mathbf{u}(\mathbf{x},t) \rangle \qquad (2.7)$$

The conditional average is expressed as a power series of $u_j(\mathbf{x},t)$ with unknown coefficients $A_{ij}(\mathbf{r},\tau)$ which are functions of separation **r** and time separation τ:

$$\hat{u}_i(\mathbf{x}, t; \mathbf{r}, \tau) = A_{ij}(\mathbf{r},\tau)\, u_j(\mathbf{x},t) + O[u^2(\mathbf{x},t)] \qquad (2.8)$$

The coefficients are determined by the least square method to minimize the error between the velocity at point **x** + **r**, time t + τ and the estimate, leading to a system of equations. The two-point, second-order space time correlation tensor is required to determine the coefficients. The underlying mathematical principals are

complicated; the reader should be referred to Adrian (1979,1978,1988) and Guezennec (1987,1992).

d) Proper Orthogonal Decomposition

This technique was first proposed by Lumley (1967). The method consists of extracting the dominant eddy structure which is the best correlated in a statistical sense. The structures are identified with the orthogonal eigenfunctions of the Karhunen-Loêve decomposition theorem (see Appendix A1,2,3 for the classical form and proof of the theorem). The proper orthogonal decomposition was independently introduced by several Soviet scientists for geophysical and meteorological applications. The method is also applicable to the analyses of signals in radio communications and in radar. This is by far the most objective method of extracting the eddy signature with minimum a priori knowledge required. The author personally finds the proper orthogonal decomposition (POD) fascinating because of its elegance and objectivity. Therefore, we shall discuss the method in detail.

Briefly, the orthogonal decomposition represents a random field by a set of deterministic functions which are in turn determined by the field itself. The velocity field is decomposed into a sum of orthogonal functions, the functions being optimally determined in such a way that the energy in the lowest order term is maximum. The determination of the function is reduced to an eigenvalue problem, the dominant eddy having the same velocity pattern as the first eigenfunction. This technique requires a knowledge of the two-point correlation tensor possibly with separation in space and time, and it is particularly favourable for the analysis of numerically simulated flows.

Given an ensemble of realisations of the random field $u(x)$, we are looking for the candidate $\Phi(x)$ that is best correlated with the elements of the ensemble; the

deterministic function $\Phi(x)$ has a structure typical of the ensemble of the elements. The inner product in the Hilbert space is defined as:

$$(u(x),\Phi(x)) = \int u_i(x)\ \phi_i^*(x)\ dx \qquad (2.9)$$

where * denotes the complex conjugate.
The projection is given by:

$$p = \frac{(u(x),\Phi(x))}{\|\Phi(x)\|} \quad . \qquad (2.10)$$

The statistical mean square of the projection $\overline{|p|^2}$ is maximized. In other words, the random vector field $u(x)$ is projected onto the candidate vector $\Phi(x)$, in order to measure the degree of parallelism between these two vectors in Hilbert space.

Suppose $\Phi(x)$ is square integrable, i.e. $(\Phi(x)\cdot\Phi(x))$ exists. We wish to maximise the ensemble average of the square of the projection:

$$\overline{|p|^2} = \frac{\overline{(\Phi(x),u(x))\ (\Phi(x),u(x))^*}}{(\Phi(x),\Phi(x))} = \lambda \geq 0 \qquad (2.11)$$

Note that $u(x)$ and $\Phi(x)$ can be complex in general.

By using the kernel theorem, we have

$$\frac{(\ R(x,x'),\Phi(x)\ \Phi^*(x')\ )}{(\Phi(x),\Phi(x))} = \lambda \qquad (2.12)$$

where $R(x,x') = \overline{u(x)\ u^*(x')}$.

It can be shown by the calculus of variation that λ is maximum when

$$(\ R(x,x'),\Phi^*(x')\ ) = \overline{|p|^2}\Phi(x)$$

or

$$\int R(x,x')\ \Phi(x')\ dx' = \lambda\ \Phi(x) \qquad (2.13)$$

This is the Fredholm integral equation of the first kind, (see Lovitt 1950) which can be solved by various numerical schemes. Alternatively, it can be written as:

$$\int R_{ij}(x,x')\ \phi_j^{(n)}(x')\ dx' = \lambda^{(n)}\phi_i^{(n)}(x) \qquad (2.14)$$

where $R_{ij}(x,x') = \overline{u_i(x)\ u_j(x')}$.

The random field is constructed by the sum of different modes:

$$u_i(x) = \sum_{n=1}^{\infty} a^{(n)}\ \phi_i^{(n)}(x). \qquad (2.15)$$

where $a^{(n)} = (\ u(x), \Phi^{(n)}(x)) = \int u_i(x)\ \phi^{(n)*}(x)\ dx$

The set of characteristic functions or eigenfunctions is an orthonormal basis:

$$(\Phi^{(n)}, \Phi^{(m)}) = \begin{cases} 0 & n \neq m \\ 1 & n = m \end{cases} \qquad (2.16)$$

The coefficients are uncorrelated with one another so that the ensemble average of $a^{(n)}a^{(m)}$ is zero,

$$\overline{a^{(n)}a^{(m)}} = \begin{cases} 0 & n \neq m \\ \lambda^{(n)} & n = m \end{cases}. \qquad (2.17)$$

Any function u in the Hilbert space can be expanded in terms of the orthonormal basis $\Phi^{(n)}$:

$$u = \sum_{n=1}^{\infty} (u,\Phi^{(n)})\Phi^{(n)} \text{ and } (u,u) = \sum_{n=1}^{\infty} |(u,\Phi^{(n)})|^2 \qquad (2.18)$$

which is a convergent series.

The turbulence kinetic energy is the sum of the eigenvalues, because

$$E = \overline{(u,u)} = \int R(x,x)dx$$

$$= \sum_{n=1}^{\infty} \overline{|(u,\Phi^{(n)})|^2}$$

$$= \sum_{n=1}^{\infty} \lambda^{(n)} < \infty \qquad (2.19)$$

and $\lambda^{(n)} \geq 0$.

The general form of the four dimensional POD has been proposed by Glauser (1992),

$$\iiint R_{ij}(\mathbf{x},\mathbf{x}',t,t')\ \phi_j^{(n)}(\mathbf{x}',t')\ d\mathbf{x}'dt' = \lambda^{(n)}\phi_i(\mathbf{x},t) \qquad (2.20)$$

The random coefficient a_n is defined as the integral of the projection of the original field over the eigenfunction:

$$a_n = \int_{\mathbf{x},t} u(\mathbf{x},t)\ \phi^{(n)}(\mathbf{x},t)\ d\mathbf{x}\ dt \qquad (2.21)$$

The velocity field is reconstructed by the summation of the modes:

$$u(\mathbf{x},t) = \sum_{n=1}^{\infty} a_n\ \phi^{(n)}(\mathbf{x},t) \qquad (2.22)$$

So far the 4-D POD (three dimensions in space and one dimension in time) has not been done because of the complexity of the mathematics and the difficulties of measuring the time-dependent 3-D spatial correlation tensor in the experiments. Taylor's hypothesis cannot be used because of the overlapping of the information in time with that of the streamwise direction.

If the random field is homogeneous in two dimensions, say x and z, the eigenfunctions become Fourier modes so that the POD reduces to harmonic orthogonal decomposition. The inhomogeneous direction y and t are treated by the POD:

$$\int\int_{ty} R_{ij}(y,y',k_1,k_3,t)\ \phi_j^{(n)}(y',k_1,k_3,t')\ dy'dt'$$

$$= \lambda^{(n)}(k_1,k_3,t)\ \phi_i^{(n)}(y,k_1,k_3,t) \qquad (2.23)$$

The POD has been applied by Moin and Moser (1989) in the numerical simulation of a channel flow. More recently, Manhart and Wengle (1992) have applied the POD to the free shear layers above a 3D obstacle in a high Reynolds number large eddy simulation.

Another method is called the snapshot-POD (Sirovich *et al* 1987), the integral equation can be written as:

$$\int\int\int_{xyz} R_{ij}(\mathbf{x},\mathbf{x}',t,t')\ \phi_j^{(n)}(\mathbf{x}')d\mathbf{x}' = \lambda\ \phi_i(\mathbf{x}) \qquad (2.24)$$

The coefficients are functions of time,

$$a_n(t) = \int_{\mathbf{x}} u(\mathbf{x},t)\ \phi^{(n)}(\mathbf{x})\ d\mathbf{x} \qquad (2.25)$$

The snapshot is given by the reconstruction of the velocity field:

$$u(\mathbf{x},t) = \sum_{n=1}^{\infty} a_n(t)\ \phi^{(n)}(\mathbf{x}) \qquad (2.26)$$

This method has been used by Hilberg (1992) in the turbulent shear layer with small sidewalls and Rajaee *et al* (1992) in free shear layers.

e) <u>Spectral Analysis</u>

Spectra are the decompositions of the measured function into waves of different frequencies. The spectrum tensor Φ_{ij} is defined as the Fourier transform of the correlation tensor R_{ij}:

$$\Phi_{ij}(\mathbf{k}) = \frac{1}{(2\pi)^3} \int_{-\infty}^{\infty}\int\int \exp(-i\mathbf{k}\ .\ \mathbf{r})\ R_{ij}(\mathbf{r})\ d\mathbf{r} \qquad (2.27)$$

where **r** is the separation vector, and **k** is the wave-number vector. The two commonly used spectra are the

one-dimensional Fourier transform of $R_{11}(r_1,0,0,)$ and $R_{22}(r_1,0,0)$:

$$\Phi_{11}(k_1) = \int_{-\infty}^{\infty} \exp(-ik_1 r_1)\ R_{11}(r_1,0,0)\ dr_1$$

$$\Phi_{22}(k_1) = \int_{-\infty}^{\infty} \exp(-ik_1 r_1)\ R_{22}(r_1,0,0)\ dr_1. \qquad (2.28)$$

The space-time spectrum function can be defined as:

$$\Phi_{11}(k_1,\omega) = \frac{1}{(2\pi)^2} \int\int \exp[-i(k_1 r_1+\omega\tau)]\ R_{11}(r_1,0,0,\tau)dr_1d\tau.$$

f) Wavelet Transforms

The first application of the wavelet transform to turbulence was by Farge and Rabreau (1988). They used the Morlet wavelet to analyse the homogeneous turbulent flows from numerical simulations. This is a fast growing technique, which can be a useful tool to study coherent structures. The wavelet transform consists of the decomposition of the field into both space and scale. The scale decomposition is obtained by the dilation of the wavelet function before convolving with the signal. In the continuous wavelet transform, the set of the convolution products between the signal and the family of continuously translated, dilated and rotated wavelets are computed. The wavelet transform is the inner product between the signal f and the wavelet family $\varphi_{l,x',r}$. l and $\mathbf{x}'$ are the scale dilation parameter and translation parameter respectively. r is the rotation parameter. The wavelet coefficients are:

$$\hat{f}(l,\mathbf{x}',\theta) = \langle \varphi_{l,x',r} | f \rangle = \int_{\mathbf{R}^n} f(\mathbf{x})\ \varphi^*_{l,x',r}(\mathbf{x})\ d^n\mathbf{x} \qquad (2.29)$$

$\mathbf{x}' \in \mathbf{R}^n,\ l \in \mathbf{R}^+$

where * denotes the complex conjugate.

The Morlet wavelet is a plane wave of wavevector k modulated

by the Gaussian envelope:

$$\varphi(x) = e^{ik.x}\, e^{-(|x|^2/2)} \qquad (2.30)$$

The wavelets can be used to obtain spatial information of the flow structure, but not the frequency content. The local wavelet energy spectrum can be only understood in terms of the scales rather than the wavenumbers. A comprehensive review of the wavelet transform is given by Farge (1992).

2.5 Pattern Recognition Analyses of the Organised Structures

One of the earliest applications of pattern recognition analysis for the study of turbulent structures can be dated back to Wallace and Eckelmann (1977), who used a pattern recognition technique to detect the near-wall structures such as sweep and ejection events during *bursting*. A burst is an event in which a streaky structure moves out from the wall, oscillates and finally breaks up. A one-dimensional pattern in the time function of the streamwise velocity was sought: a gradual deceleration immediately followed by a strong acceleration. The pattern recognition technique was iterative, the wave forms of different time scales being normalised to obtain the ensemble average.

A similar development was undertaken by Ziberman, Wygnanski and Kaplan (1977), in which transitional boundary layer spots were initiated and marked by spark discharges in the laminar region of the flow. The boundary layer was tripped by a row of small spheres. An iterative pattern recognition scheme was used to align the time traces of the velocity history, each individual realisation being cross correlated with a test pattern. The cross-correlation was computed by fast Fourier transform. (The complex transform of the test pattern was multiplied by the complex conjugate of the transform of the time trace, and the product was inversely Fourier transformed to yield the correlation). The educed average was written to the disk and it was used as the new test pattern for the subsequent passes.

Townsend (1978) developed a correlation-function fitting method which was the backbone of the later development by Mumford and other workers. Velocity fluctuations in a wake and turbulent boundary layer were measured by arrays of sensors and the correlations were computed by the mean values of the velocity products as well as products weighted by the turbulent intensity or Reynolds stress within the spatial-temporal volume of data. A simple eddy model with unknown parameters was used and the corresponding

correlation function was constructed with the assumption that the turbulence consisted entirely of a superposition of simple eddies. The correlation functions were also computed from the experimental data. A similarity measure between the correlation function from the experimentally measured data and that from the eddy model was computed by the *matching coefficient*, which is the cross-correlation coefficient between the correlation functions. Then the parameters of the eddy model were systematically varied to yield the maximum matching coefficient.

Perhaps the most significant refinement of the pattern recognition technique was by Mumford (1982, 1983). He further developed Townsend (1978) and Savill's (1979) idea to extract the two- dimensional streamwise velocity patterns of the roller structures in a turbulent plane jet and wake. In his experimental studies, an array of eight probes was used to sample the streamwise velocity signals. A test pattern based on Townsend's eddy stream function model was cross-correlated with the velocity data field. The ensemble average was formed by adding the samples which satisfied the threshold criteria.

Ferré and Giralt (1989) developed a pattern recognition algorithm which was primarily an extension of Mumford's work. Their analysis was more statistically orientated, significance tests of the ensemble averages being carried out to assess the level of significance of the ensemble averages and the contribution to the turbulence intensity. A double classification procedure was applied to separate the single-rollers from the double-rollers as there is a lack of orthogonality between these two types of structures. Ferré, Mumford, Savill and Giralt (1990) investigated the relationship between the fine scale activity and the large scale structures. They described what they called a *fine-scale activity indicator function*, which is the envelope of the second time derivatives of the velocity signals. It had been argued that the dissipation term in the transport equation for the turbulent kinetic energy in

isotropic turbulence is proportional to the time average of the square of the first time derivative of the velocity (Ferré 1990). This would be a crude assumption for anisotropic turbulence, so they used the envelope of the second time derivatives of the velocity signals as the fine-scale indicator function.

Smith and Lu (1988) combined template matching and image processing to study the turbulent boundary layer velocity data obtained from hydrogen bubble flow visualisation. The bubble lines were captured with a video system synchronised with strobes lights, the video frames being converted to digitized, enhanced images. The velocity profiles were determined by a time-of-flight technique. They employed experimentally generated hairpin vortex template patterns and varied the dimensions of the space-time window to optimise the cross-correlation.

Savill and Ferré (1989) applied pattern recognition analysis to the multi-point hot-wire data of a highly curved wake, plane boundary layer and manipulated boundary layer. They showed that the stable side of the curved wake was mainly composed of single rollers. In the unstable side, there was evidence of the longitudinal vortices with circulation predominantly in the cross-stream plane. On the other hand, the centreplane structures consisted of a mixture of both weak single and double rollers. In their boundary layer analysis, they showed that even very simple template patterns were sufficient to extract the dominant inclined eddy structures, and the repeated applications of PRA technique together with the double classification procedure (Ferré *et al* 1989) allowed the detection of asymmetric structures. More recently, Savill, Klein and Friedrich (1993) have applied pattern recognition analysis to the Large Eddy Simulation data of manipulated channel flows.

Voke (1993) applied *flip matching* and *affine matching* pattern recognition analyses to conditionally sampled velocity fields from the direct simulation of a numerically

tripped boundary layer. The conditional averaging was based on the single-point triggering signal, second and fourth quadrant events being detected within a subvolume of the computational domain. A database was formed by storing the surrounding flow fields characterised by high shear stress. The idea of the flip matching is to eliminate the symmetry of the averaging. Each of the conditional sampled velocity field and its corresponding reflected field are cross-correlated with the running average, the better correlated field being added into the average. Therefore the running average may be regarded as a self-constructing template; it is constantly updated during the first scan of the database. The final average is then used as a fixed template for the subsequent iterations until the average converges. Voke (1993) also employed the affine matching technique to improve the average: a sequence of geometric transformations are applied to each sampled field in order to find the transformation which yields maximum cross-correlation with the running average.

2.6 Numerical Simulation of Turbulence

In Direct Numerical Simulation (DNS), the Navier-Stokes equations are solved without any modelling; all scales of motions are resolved. However it is limited to low Reynolds numbers and flows in simple geometries. As the computations are necessarily three-dimensional and time-dependent, the computational cost is extremely high. They are only feasible with powerful supercomputers such as the Cray series. The pioneering direct simulation was by Orszag and Patterson (1972); the simulation of decaying isotropic turbulence. Among the more notable work was the direct simulation of a fully developed channel flow by Kim, Moin and Moser (1986). With increasing computer power, direct simulation has become a popular tool for the study of coherent structures in turbulence (Moin and Rogers 1985, Moin and Kim 1986, Kim and Spalart 1987, Moin and Moser 1989).

In direct simulations, the total number of mesh points N is estimated to be the cubed ratio between the largest turbulence scale L and the dissipation length scale η (the smallest resolved scale)

$$N \approx \left(\frac{L}{\eta}\right)^3$$

The largest length scale can be determined from the two-point correlation measurements. The number of mesh points increases drastically with Reynolds number and hence the computer storage capacity and speed becomes a critical factor.

As the direct simulation places overwhelming demand on computer memory and speed, the *nearly full simulation* (Voke 1990) has become an appealing alternative. In the nearly full simulation, most essential scales are resolved on the computational grid except the scales at highest wavenumbers, a subgrid model being used to avoid energy pile-up of the spectra at high wavenumbers.

2.7 Large Eddy Simulation

In Large Eddy Simulation (LES), the grid scale eddies are simulated while the effects of the subgrid scale eddies on the large eddies are modelled. The fundamental assumptions of LES are that the small eddies are nearly isotropic and hence universal. The sub-grid scale model (SGM) of eddy viscosity type is based on the assumption that the energy production equals the dissipation, ignoring the diffusion, convection and other terms in the subgrid turbulence budget. The model must be dissipative because the net energy transfer from the large scales to the small eddies is in the form of dissipation and not reversible. Kolmogorov (1941) showed that at high Reynolds numbers, the smaller eddies must be in a state of equilibrium, in which the rate of energy received from the larger eddies is nearly equal to the total rate of loss to smaller eddies by energy

cascading, and the small eddies lose energy by viscous dissipation. If the grid scale is assumed to be much larger than the Kolmogorov length scale, the grid scale cutoff (the cutoff between the large and small scales) lies in the inertial subrange of the equilibrium spectrum (see figure 2.12).

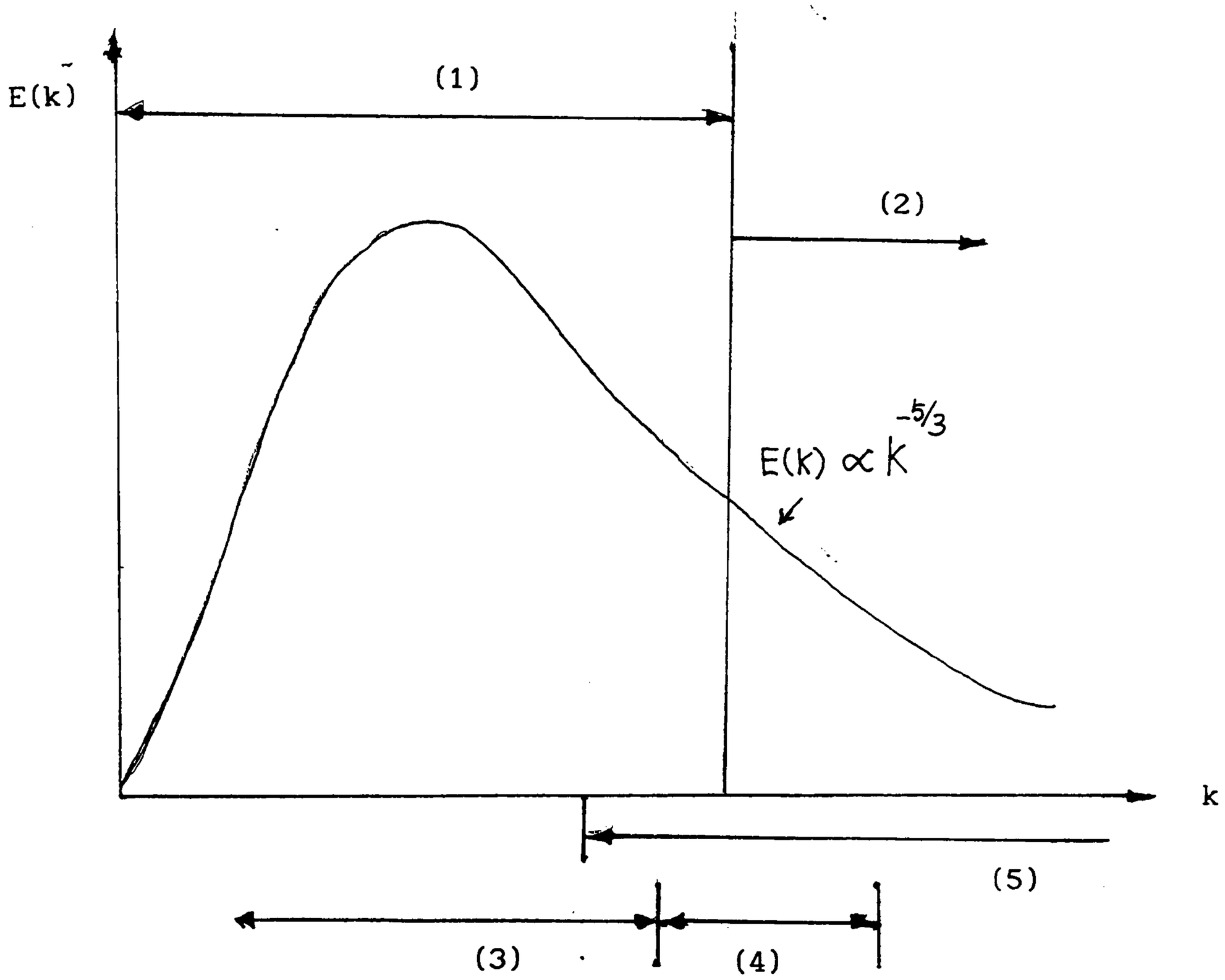

Fig 2.12 The resolved scales and subgrid scales in the energy spectrum. (1) resolved scales, (2) subgrid scales, (3) energy containing eddies, (4) inertial subrange, (5) universal equilibrium range.

Historically, the most important work in large eddy simulations were made by Smagorinsky (1963), Deardorff (1970) and Schumann (1973). A profound theoretical study of the subgrid scale models was carried out by Leslie *et al.* (1976).

2.8 Numerical Simulations of Free Shear Flows

The mixing layer is one of the simplest kinds of free shear flow. The evolution of the mixing layer is strongly sensitive to the initial condition. Numerical simulations were made by numerous researchers such as Mansour *et al* (1978), Cain *et al* (1981), Metcalfe and Riley (1980). A majority of the mixing layer simulations were concerned with the initial roll-up stages and the vortex pairing.

The first direct numerical simulation of the wake behind a self-propelled body was performed by Orszag and Pao (1974), however only a subvolume of the entire flow field was stimulated because of the resolution problem. More recent works include the large eddy simulation of a plane wake behind a flat plate by Potamitis and Voke (1992).

The interaction of the hot and cold jets was simulated by Tsai *et al* (1988) with periodicity assumed in the cross-stream inhomogeneous direction of the jets, but the existence of image flows above and below the computational domain affected the dynamics of the jets. Large eddy simulation of the buoyant thermal jet discharged from the bottom of the free surface channel has been attempted by Thomas and Williams (1992). The large eddy simulation of the heat transfer from an impinging jet has been studied by Gao and Voke (1992). To date, there has not been any three-dimensional large eddy or full simulation of the plane jet apart from the present study. The major difficulties in the simulation of a free jet are the treatment of the turbulent outflow boundary conditions and the boundary conditions of the potential part of the flow. The outflow boundary conditions are normally applied with the frozen turbulence approximation. The boundary conditions of the irrotational flow have been a troublesome and untouched problem.

2.9 Definition of Coherent Structure

Here are some terminologies commonly used in the language of turbulence structure eduction:

Large/big eddy
Organised/coherent structure
Characteristic eddy
Conditional eddy

'Large eddy' is the oldest terminology, being popularly used in 50's to 60's. Its meaning is self-explanatory but it lacks a precise definition. The term 'coherent' is very well defined for electromagnetic waves and has been long used in physics, e.g. laser is coherent light; the earliest radio detector was called the coherer. But it is very difficult to define 'coherent structure' in turbulence.

Lumley (1967) attempted to provide an objective definition of the large eddies (the terminology 'coherent structure' had not been used in fluid mechanics at that time): the characteristic eddy is identified as the lowest order eigenfunction (the most energetic eddy is defined to be the eigenfunction with largest eigenvalue) resulting from the orthogonal decomposition of the turbulence random field.

Hussain (1980) suggested a definition of the coherent structure as: "a connected turbulent fluid mass with instantaneously phase-correlated vorticity over its spatial extent". He claims that vorticity is the best quantity for the detection of the coherent structures inferred by his own definition and velocity would be a poor quantity. He also strongly emphasized that coherent structures do not have to be highly energetic. Hussain's definition of the coherent structure is very different from the coherent eddy structures extracted in the PRA and lacks any statistical content.

Robinson, Kline and Spalart (1988) defined coherent structures or vortical structures as "identifiable vortices, usually with segments of varying orientation in space". They also suggested a specific definition for the vortical structures in a zero pressure gradient boundary layer: "A vortex exists when instantaneous streamlines mapped onto the cross-stream plane display a roughly circular or spiral pattern". In their numerical simulation, regions of low pressure were used to identify vortex cores. The low-pressure region is a necessary condition for the existence of a vortex in the flow, but it is not necessarily a sufficient condition.

The definition of conditional eddy was better summed up by Adrian (1992): "It is absolutely essential to distinguish conceptually between the structure of any particular conditional average and the structure of coherent elements of the flow, should they exist. There is no *a priori* guarantee that any conditional average (or, the structure extracted by any other pattern recognition procedure) must coincide with individual, random realisations of portions of the flow field". He added "To avoid confusing conditional averages with realisations of the random field (and to avoid the problem of defining 'coherent structure') the flow fields described by conditional averages have been referred to as 'conditional eddies'". Conditional eddies are defined by event and there is no single event that is of universal importance (Adrian 1988). Stochastic estimation does not require conditional sampling but it links conditional sampling and two-point correlation functions together. On the other hand, the proper orthogonal decomposition is statistically unconditional. In fact, Lumley's characteristic eddies can be mathematically related to the stochastic estimate (Adrian 1988).

Furthermore, Fiedler (1988) proposed a more generalised definition of the coherent structure: "a connected non-stationary dynamic system, 'connected' in the sense of a

correlated and concentrated dynamic quantity". Nevertheless, it seems fruitless to seek a universal definition. In spite of the fact that the coherent structures can be deterministic, they often appear to be indeterminate. The question of defining coherent structures remains for open debate.

Finally, it should be noted that Tsinober and Levich (1983) suggested the universal property and significance of helicity (the helicity tensor is defined as $h_{ij} = u_i\omega_j$; the normalized helicity density is $h = \mathbf{v}\cdot\omega/(|\mathbf{v}|\ |\omega|)$) in three-dimensional coherent structures, particularly regarding the nonlinear dynamics or three dimensional instabilities of turbulence. They argued that the three-dimensional coherent structures possessed coherent helicity.

2.10 Vortex Stretching Mechanism and Energy Cascade

The energy transfer mechanism for the organised eddies is associated with vortex stretching, the three dimensional, large scale eddies being stretched by the mean strain rate. In order to conserve angular momentum, the vorticity component aligned with the direction of stretching is amplified while its cross-sectional area and moment of inertia are decreased. The dominant eddies are those that can extract energy from the mean flow, and maintain the correlation between the velocity fluctuations u′ and v′, through the production of Reynolds stress. Such large eddies have their axes aligned with that of the mean strain rate and tend to be *anisotropic.*

The vorticity fluctuations play an important role in the dynamics of turbulence, particularly the energy transfer from the large scale coherent eddies to the small eddies. We will show that vorticity subjected to a strain rate can be amplified by stretching. The vorticity equation can be derived by applying the curl operator to the Navier-Stokes equation (Tennekes and Lumley 1972). It can be written as:

$$\frac{\partial \tilde{\omega}_i}{\partial t} + \tilde{u}_j \frac{\partial \tilde{\omega}_i}{\partial x_j} = \tilde{\omega}_j \tilde{S}_{ij} + \nu \frac{\partial^2 \tilde{\omega}_i}{\partial x_j \partial x_j}$$

where ~ denotes instantaneous quantity.

$\tilde{S}_{ij}$ is the strain rate tensor.

The term $\tilde{\omega}_j \tilde{S}_{ij}$ represents the amplification and rotation of the vorticity vector by the strain rate (Lumley and Tennekes 1972) If the effect of the viscosity is ignored and the observer is moving with the flow at the velocity $\tilde{u}_j$ (in the Lagrangian frame), then the terms $\tilde{u}_j \partial\tilde{\omega}_i/\partial x_j$ and $\nu\partial^2\tilde{\omega}_i/\partial x_j\partial x_j$ can be omitted

$$\frac{\partial\tilde{\omega}_i}{\partial t} = \tilde{\omega}_j \tilde{S}_{ij}$$

Considering a three-dimensional vortex element under the two-dimensional strain-rate field $s_{11} = -s_{22} = s > 0$ and $s_{12} = 0$ as shown in figure 2.13, then we have

$$\omega_1 = \omega_o e^{st}, \quad \omega_2 = \omega_o e^{-st}$$

and $\omega_1^2 + \omega_2^2 = 2\omega_o \cosh 2st$

If a vortex element is stretched by the positive strain rate s_{11}, the component of vorticity ω_1 in this direction increases at all times. On the other hand, that in the direction of squeezing decreases slowly with time. In the absence of viscosity, the angular momentum of the vortex is conserved. The total energy of the vortices increases due to the work done by the strain rate. The energy exchange rate is

$$E = s(u_2^2 - u_1^2)$$

When ω_1 is increased then u_2 and u_3 increase; when ω_2 is decreased, u_1 and u_3 decrease. Therefore E is positive, energy being extracted from the strain-rate field. Moreover, the stretching also produce an additional strain field,

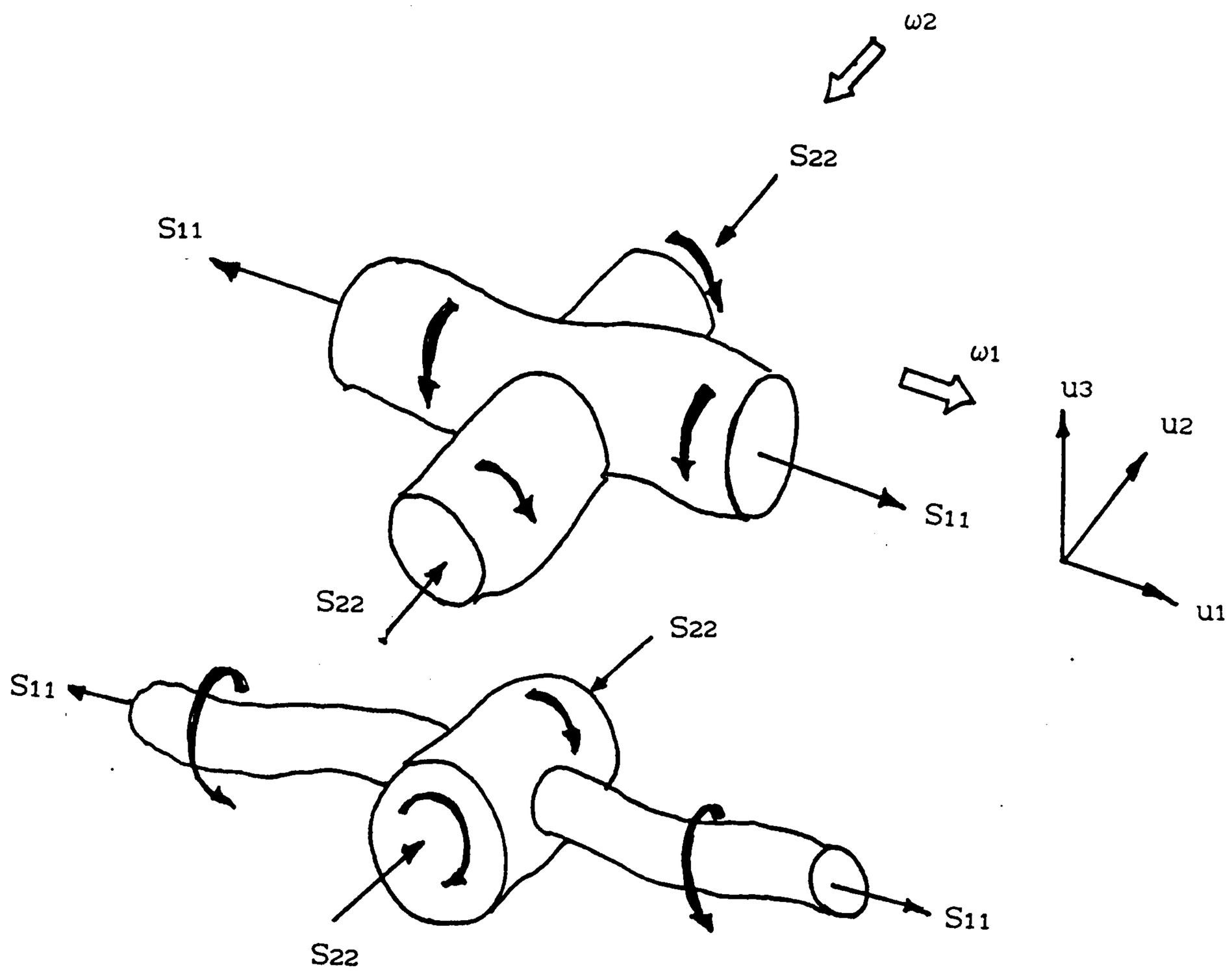

Fig 2.13 A vortex element under a two-dimensional strain-rate field.

which in turn stretches other vortices, the scale of the motion getting smaller and smaller. Hence, the energy of the smaller eddies increases at the expense of the energy of the larger eddies.

At high Reynolds numbers, the vorticity budget equation can be simplified by ignoring the turbulent vorticity transport and production terms (Taylor 1938).

$$\overline{\omega_i \omega_j \, s_{ij}} = \nu \, \overline{\frac{\partial \omega_i}{\partial x_j} \frac{\partial \omega_i}{\partial x_j}} > 0$$

The right hand side is the viscous dissipation of $\overline{\omega_i \omega_i}$, and the left hand side represents the vorticity production. As the terms on both side are positive: on the average there is more vortex stretching than squeezing (Lumley and Tennekes 1972). Vortex stretching transfers turbulent vorticity from large scale eddies to small scale turbulence.

The smallest eddies lose their energy through viscous

dissipation. Through the so-called *energy cascade*, large eddies split and split again to become smaller eddies down to the Kolmogorov microscale η:

$$\eta \sim (\nu^3/\varepsilon)^{1/2}$$

The small scale structure tends to be independent of the mean strain rate and lacks orientation; this is often referred as *local isotropy*. (The concept of local isotropy has been recently challenged by some modern thinking; the fine-scale structures are believed to have preferred orientation with respect to the large eddies in a shear flow. A more controversial concept has been suggested by Hussain (1992): he proposed the fractal scenario of vorticity cascade from the largest scale to the smallest scales at very high Reynolds numbers.) At high wave numbers of the spectrum, the time scales of the small eddies are short compared with that of the mean flow, and they respond rapidly to the changes of local conditions. The small eddies are said to be in statistical equilibrium so that the rate of energy supply is equal to the rate of dissipation by viscosity.

2.11 Generation Mechanism of the Strainwise Vortex Pairs

We may speculate that the strainwise vortex pairs in the plane wakes or jets are formed from undulation of the spanwise vortex tubes through secondary instability (similar to the Kelvin-Helmholtz instability). As shown in figure (2.14), the disturbances introduce waviness of the vortex from a straight filament, the vortex being pulled and rotated. Then the vorticity of the vortex is amplified and stretched by the shear, resulting in a horseshoe type of structure aligned in the direction of the mean rate of strain.

An analogy can be drawn between the generation mechanism of the hairpin vortex in the wall turbulence and the vortex pairs in the plane wake or jet: Moin and Rogers (1985) studied the direct simulation database of a homogeneous turbulent flow with an imposed mean shear. They found that the hairpin vortices or Ω-shaped vortices were formed from the rolling-up of sheets of spanwise vorticity. The inclination of the vorticity vector to the direction of the mean flow was shown to be 45 and -135 degrees. Moin and Rogers also showed that the hairpin structures would only develop in the presence of mean shear.

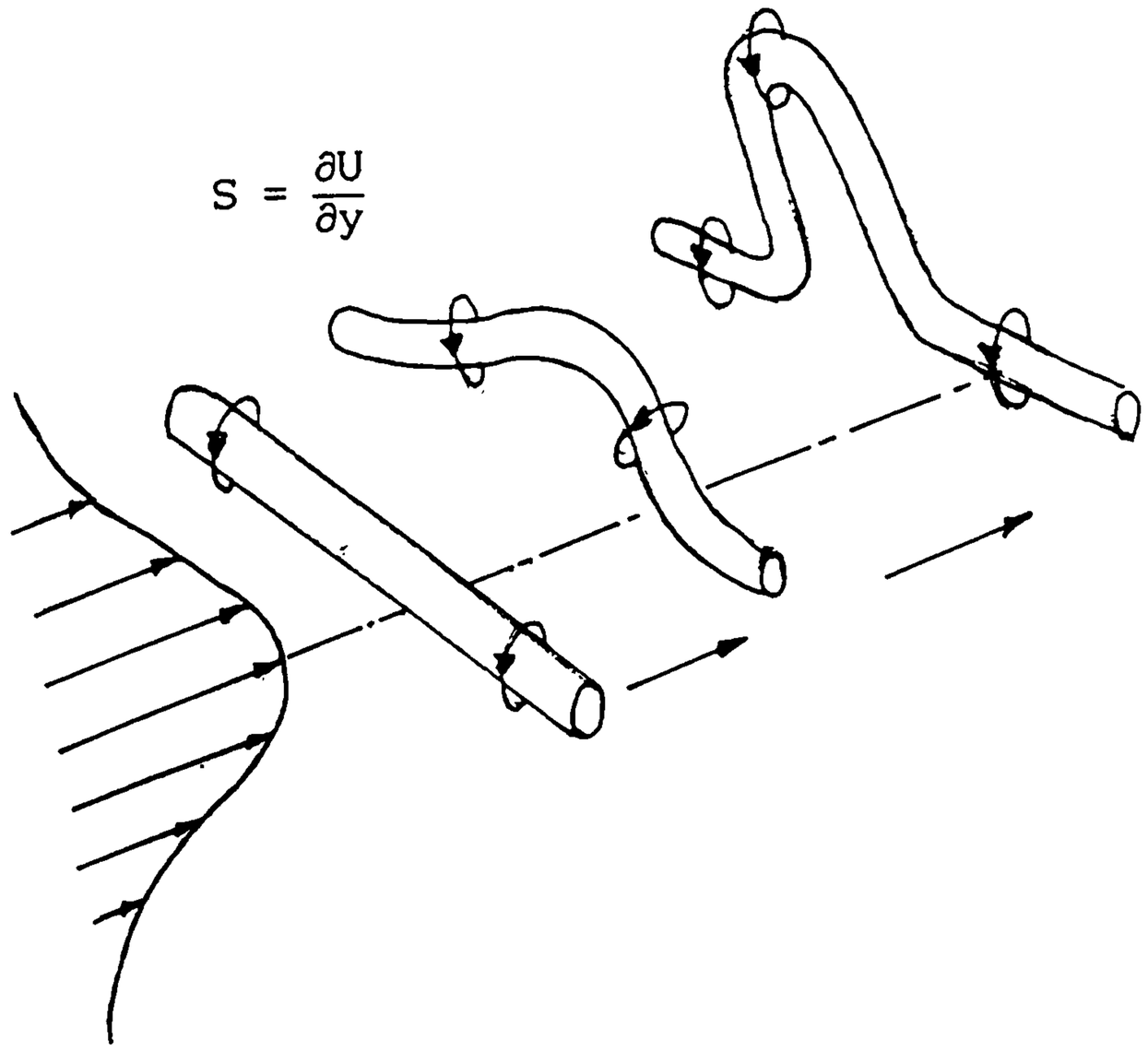

Fig. 2.14 Rolling up of a vortex filament.

2.12 Proposed Topology of the Eddy Structures

Here we label the counter-rotating vortices as vortex pairs but it is very likely that they are part of a vortex loop. Seemingly, the open-ended double-roller eddy appears to be inconsistent to both our intuitive and perceptual picture of the spanwise vortices with axes parallel to the cylinder, which are frequently observed in the near and intermediate fields of the plane wakes. Several possible configurations of the vortex pair are sketched in figure 2.15. Of course, these are speculative suggestions. It seems plausible to speculate that the vortex pair is just part of a distorted spanwise vortex tube or roll. The initially straight vortex tube is pulled by the mean shear. Then the velocity gradient of the mean flow causes the deformed loop to align with the

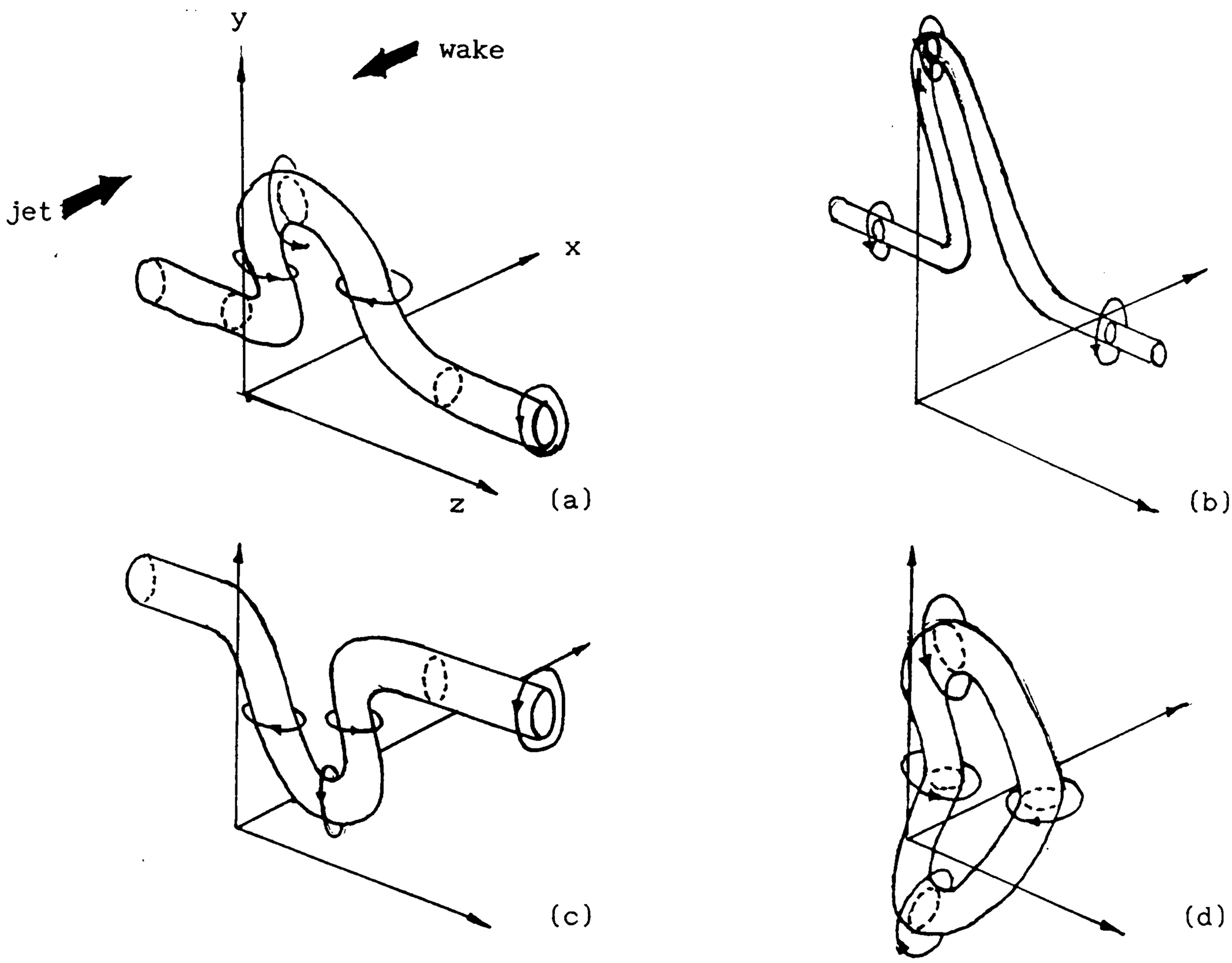

Fig.2.15 Speculated topology of the vortical structures in the plane wakes and jets : (a) outward kinking roll, (b) distorted roll at higher Reynolds number, (c) inward kinking roll, (d) closed vortex loop.

direction of the principal rate-of-strain. This results in the strengthening of vorticity in the direction of stretching. The distorted spanwise rolls are very much similar to the hairpin vortices found in the turbulent boundary layer (Head and Bandyopadhyay 1980) and in homogeneous flows with imposed mean shear (Rogers and Moin 1985). The vortex pairs extracted in the pattern recognition analysis may be the legs of distorted and stretched vortex loops. Head *et al* (1980) suggested that the hairpin might maintain the fixed inclination (45 degrees) by the induced velocity of its limbs in order to counteract rotation due to the plane shearing of the velocity gradient $\partial U/\partial y$. On the other hand, the single roller eddy described by Mumford (1983) may not be the dominant structure and they cannot occur in an isolated form. Mumford's single-roller eddies are possibly the legs of the undulated, spanwise rolls or parts of the vortex loops with diffused legs.

Some idea about the generation mechanism of the vortex loops can be revealed in the flow visualisations by Williamson (1988), as well as Cimbala, Nagib and Roshko (1988). Williamson (1988) observed the three-dimensional transition of the near wake of a circular cylinder. He found that the three-dimensional vortex loops start to evolve from periodic, laminar vortex shedding at very low Reynolds numbers (170~180). The vortex loops are formed by the rolling up and deformation of the primary vortices during the vortex shedding. A whole string of vortex loops are generated at the same spanwise position, one loop followed by another. At higher Reynolds numbers (230-260), there is a change of the structures from the vortex loops to finer-scale streamwise vortices. The streamwise vortices originate from the highly stretched vortex loops, the two legs of the loop evolving into a pair of contrarotating streamwise vortices. However, it is not clear how these transitional structures are related to the structures at much higher Reynolds numbers. Besides, there has been strong debate on whether the structures of the near field are the same as those in the fully developed, far field of the

flows.

Apart from the horseshoe-like vortex loop, the vortex pair may occur in a form of the closed vortex loop which is tilted and symmetric about centreplane (figure 2.15(d)). Roshko (1976) suggested that the plane jets or wakes consist of two rows of spanwise vortices of opposite sign; the vortex loop may be formed by pinching off and joining together of vortices from opposite sides of the street. Experimental evidence for closed vortex loops in plane wakes was shown by Breidenthal (1980), who obtained photographs of the vortex loops in the plane wakes of the splitter plates. The splitter plate produced several side-by-side three-dimensional wakes. The geometry of the flow is different from a plane wake behind an infinitely long circular cylinders. We have to be cautious when we compare the topology of the structures in the plane wakes with those of the three-dimensional wakes, since the three-dimensional effects of the obstacles can strongly affect the generation mechanism and the topology of these vortex loops. Careful examination of Breidenthal's photographs makes it clear that the structures in three-dimensional wakes cannot simply be described as closed loops; they are very similar to the interlocking loops observed by Perry and Lim (1978) in three-dimensional coflowing jets and wakes, instead of the symmetric closed loop.

More recently, the existence of the closed vortex loop in the plane wake has also been suggested by Guezennec and Gieseke (1992). They applied multipoint stochastic estimation to study the structures of the fully developed far wake behind a circular cylinder (Re = 5000, x/d = 100). The conditional structures were found to be closed vortex loops aligned at ±45 degrees to the mean flow. The pesudo-dynamical reconstruction of the velocity field showed that the vortex structures appeared in a staggered arrangement. But we have to emphasize that it is a conditional structure; it is not clear whether such symmetric structure is caused by the symmetry of the

statistics. The symmetric, closed vortex loops may not occur frequently, because the two rows of spanwise vortices often appear on alternative sides (anti-symmetric mode) of the wakes/jets (although LaRue and Libby(1973) argued that the vertex of the structure could be displaced away from the centreplane). However, they probably occur in symmetric mode in some flows. Furthermore, Hussain *et al* (1989) also suggested that the closed vortex loop would not be the probable dominant structure. The closed loop vortex may be produced by crosslinking between two horseshoe-type vortex tubes of opposite sign from opposite sides of the centreplane. He also believed that the horseshoe vortices would not frequently occur in a symmetric arrangement across the centreplane of the wake.

A speculative arrangement of the structures in the near field of a plane jet is shown in figure 2.16(a) and (b). It consists of two rows of spanwise vortices in staggered positions. Figure 2.16(a) shows the streamline pattern of the flow. Similar patterns were observed by Perry and Tan (1983) in the three-dimensional coflowing jets. The saddle point is located at the interception between the diverging separatrix and the converging separatrix.

In the plane wake, the diverging separatrix or braid connects the top of a roll to the bottom of an adjacent roll (Antonia (1992), Hussian and Hayakawa (1987), Lasheras and Merbury (1987)). The braid may consist of streamwise vortex filaments which are smaller than the spanwise vortices and under expansive strain as shown in figure 2.17. They are often called longitudinal vortices or ribs. They also orient in the direction of the principal axis of strain field induced by the velocity field of the spanwise vortices. (The angle of inclination is about ±50 degrees. (Antonia (1992)). The spanwise vortices or rolls are not straight but they appear to be wavy and strongly three-dimensional. In fact, the streamwise and spanwise vortices interact with each other. The wavy undulation of the rolls is caused by the induced velocity field of the counter-rotating streamwise

vortices; they lift the roll up and push it down in an alternating arrangement. The orientation of the distorted rolls should align with the direction of the principal rate-of-strain (roughly ±45°in the wakes, ±135°in the jets), but it is quite possible that the angle may be altered by the induced strain field of the streamwise vortices. The spatial relationship between the two rows of rolls on both sides of the centerplane is not clear. They could be possibly either in phase or 180°out of phase in the spanwise direction. Moreover, very little information is known about the detailed configurations of the ribs.

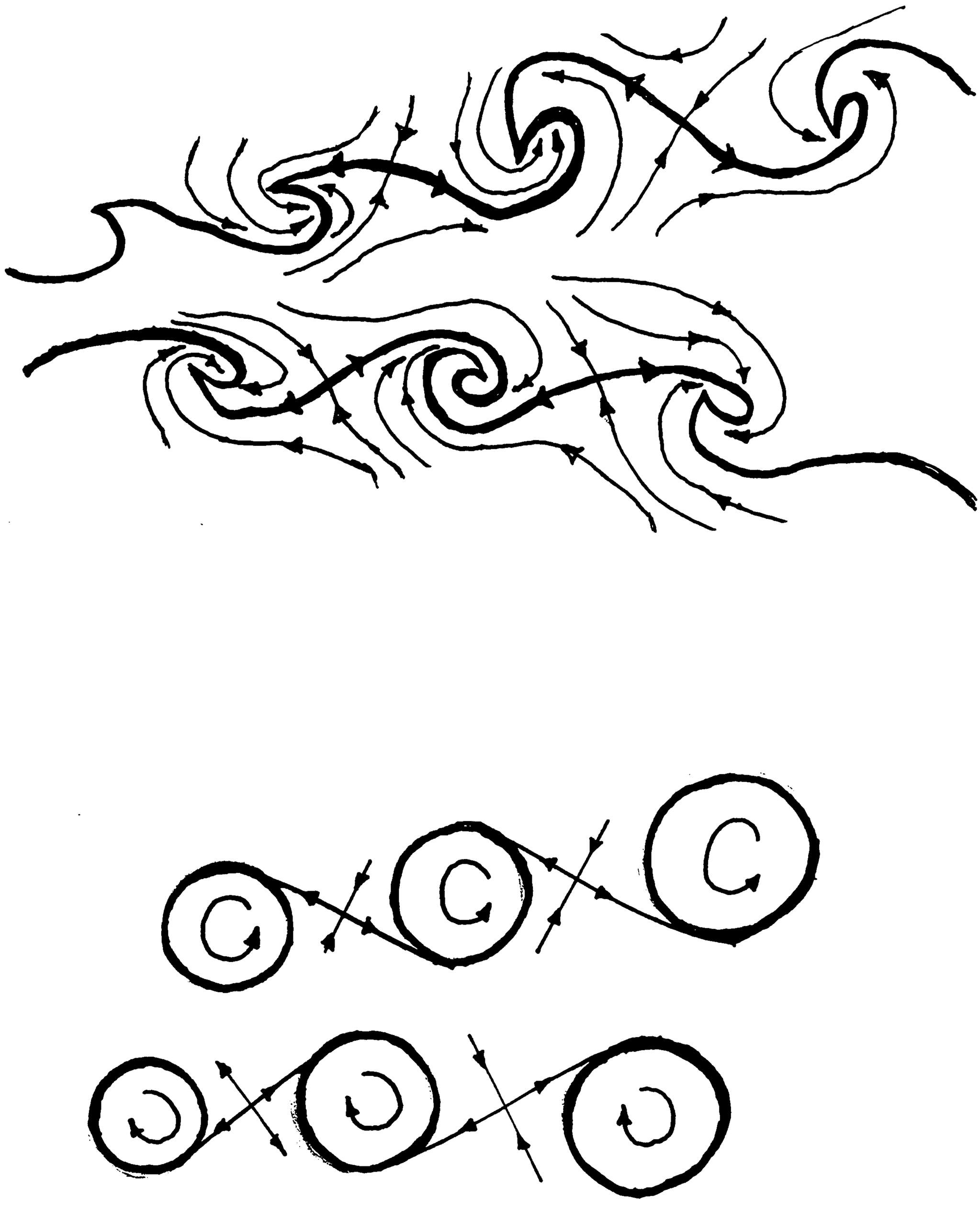

Fig.2.16 Speculated arrangement of the structures in the plane jet(a) streamline pattern, (b) spanwise rolls.

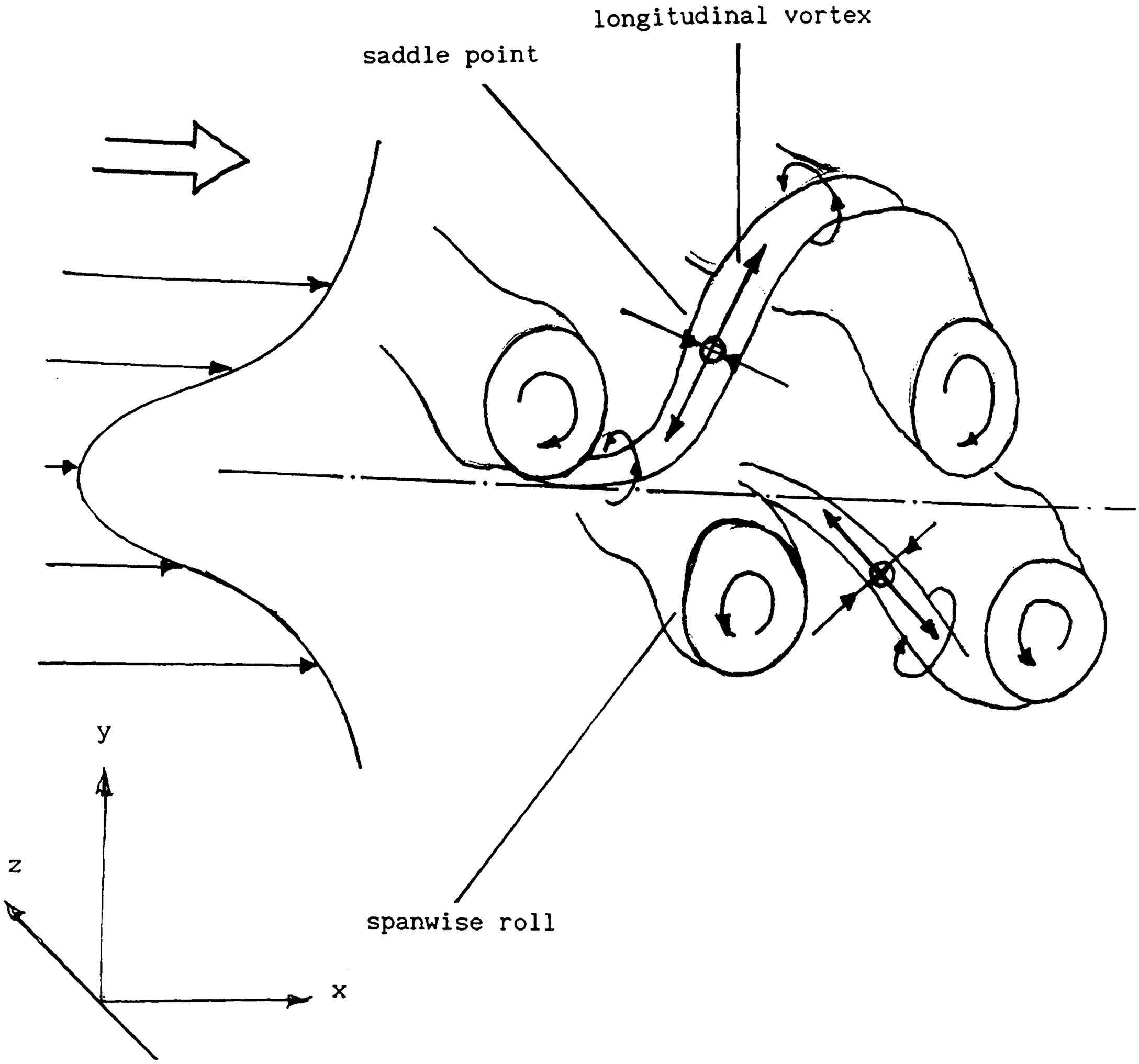

Fig.2.17 Speculated arrangement of the spanwise rolls and longitudinal vortices in a plane wake.

CHAPTER THREE
Theory and Method (Part One)

Theory of the Turbulent Plane Jet

3.1 Equations of Motions

The Reynolds-averaged Navier-Stokes equations can be written as:

$$\bar{u}\frac{\partial\bar{u}}{\partial x} + \bar{v}\frac{\partial\bar{u}}{\partial y} + \bar{w}\frac{\partial\bar{u}}{\partial z} = -\frac{1}{\rho}\frac{\partial\bar{p}}{\partial x} + \frac{\mu}{\rho}\nabla^2\bar{u} - \left[\frac{\partial\bar{u}'^2}{\partial x} + \frac{\partial\overline{u'v'}}{\partial y} + \frac{\partial\overline{u'w'}}{\partial z}\right] \quad (3.1)$$

$$\bar{u}\frac{\partial\bar{v}}{\partial x} + \bar{v}\frac{\partial\bar{v}}{\partial y} + \bar{w}\frac{\partial\bar{v}}{\partial z} = -\frac{1}{\rho}\frac{\partial\bar{p}}{\partial y} + \frac{\mu}{\rho}\nabla^2\bar{v} - \left[\frac{\partial\bar{v}'^2}{\partial y} + \frac{\partial\overline{u'v'}}{\partial x} + \frac{\partial\overline{v'w'}}{\partial z}\right] \quad (3.2)$$

$$\bar{u}\frac{\partial w}{\partial x} + \bar{v}\frac{\partial\bar{w}}{\partial y} + \bar{w}\frac{\partial\bar{w}}{\partial z} = -\frac{1}{\rho}\frac{\partial\bar{p}}{\partial z} + \frac{\mu}{\rho}\nabla^2\bar{w} - \left[\frac{\partial\bar{w}'^2}{\partial z} + \frac{\partial\overline{u'w'}}{\partial x} + \frac{\partial\overline{v'w'}}{\partial y}\right] \quad (3.3)$$

For two-dimensional flow, $\bar{w} = 0$ and the terms involving $\partial/\partial z = 0$. The transverse gradients are large compared with those in the streamwise direction; the equations of motion can be greatly simplified by the boundary layer approximations.

The streamwise momentum equation reads:

$$\bar{u}\frac{\partial\bar{u}}{\partial x} + \bar{v}\frac{\partial\bar{u}}{\partial y} = -\frac{1}{\rho}\frac{\partial\bar{p}}{\partial x} + \nu\frac{\partial^2\bar{u}}{\partial y^2} - \frac{\partial\overline{u'v'}}{\partial y} - \frac{\partial\bar{u}'^2}{\partial x} \quad (3.4)$$

From order of magnitude considerations, the cross-stream momentum equation can be approximated as:

$$\frac{\partial\bar{v}'^2}{\partial y} = -\frac{1}{\rho}\frac{\partial\bar{p}}{\partial y} \quad (3.5)$$

Integration of (3.5) yields

$$\frac{\bar{p}}{\rho} + \bar{v}'^2 = \frac{p_o}{\rho} \quad (3.6)$$

where p_o is the pressure outside the turbulent region of the jet.

Differentiating the above equation and using the fact that $\partial p_o/\partial x = 0$, we obtain

$$\frac{1}{\rho}\frac{\partial p}{\partial x} + \frac{\partial \overline{v}'^2}{\partial x} = 0 \qquad (3.7)$$

Substituting in (3.4)

$$\overline{u}\frac{\partial \overline{u}}{\partial x} + \overline{v}\frac{\partial \overline{u}}{\partial y} = \nu\frac{\partial^2 \overline{u}}{\partial y^2} - \frac{\partial \overline{u'v'}}{\partial y} - \frac{\partial \overline{u}'^2}{\partial x} - \frac{\partial \overline{v}'^2}{\partial x} \qquad (3.8)$$

Since the last two terms are negligible, we write the equation as:

$$\overline{u}\frac{\partial \overline{u}}{\partial x} + \overline{v}\frac{\partial \overline{u}}{\partial y} = \frac{1}{\rho}\frac{\partial}{\partial y}(\tau_l + \tau_t)$$

where

$$\mu = \rho\nu$$

$$\tau_l = \mu\frac{\partial u}{\partial y}$$

$$\tau_t = -\rho\,\overline{u'v'}$$

τ_l, τ_t are called the laminar and turbulent shear stresses respectively. In free turbulent flows $\tau_t >> \tau_l$; τ_l can be neglected:

$$\overline{u}\frac{\partial \overline{u}}{\partial x} + \overline{v}\frac{\partial \overline{u}}{\partial y} = \frac{1}{\rho}\frac{\partial \tau_t}{\partial y} \qquad (3.9)\ .$$

3.2 Integral Momentum Equation

Integrating equation (3.9) from y = 0 to y = ∞ (the overbars are omitted for convenience):

$$\rho\int_0^\infty u\frac{\partial u}{\partial x}\,dy + \rho\int_0^\infty v\frac{\partial u}{\partial y}\,dy = \int_0^\infty \frac{\partial \tau_t}{\partial y}dy \qquad (3.10)$$

and using Liebnitz rule, the first term of equation (3.10)

becomes

$$\rho \int_0^\infty u\frac{\partial u}{\partial x}\, dy = \frac{1}{2}\,\frac{d}{dx}\int_0^\infty \rho u^2 dy$$

and the second term,

$$\rho \int_0^\infty v\frac{\partial u}{\partial y}\, dy = \rho\Big(uv\Big|_0^\infty - \int_0^\infty u\frac{\partial v}{\partial y}dy \Big)$$

$$= \rho\Big(\int_0^\infty u\frac{\partial u}{\partial x}\, dy \Big)$$

$$= \frac{1}{2}\,\frac{d}{dx}\int_0^\infty \rho u^2 dy \quad .$$

The right-hand side of equation (3.10)

$$\int_0^\infty \frac{\partial \tau_t}{\partial y} dy = \tau_t\Big|_0^\infty = 0,$$

since the flow is symmetric about y = 0 and τ_t vanishes at large values of y.

Equation (3.10) becomes

$$\frac{d}{dx}\int_0^\infty \rho u^2 dy = 0. \qquad (3.11)$$

Therefore

$$\rho \int_0^\infty u^2\, dy = M, \qquad (3.12)$$

where M, the mean momentum flux in the x-direction, is constant.

3.3 Similarity Analysis

The jet is self-preserving in the fully developed region and the velocity distributions are similar. Then we can assume that the non-dimensionalised velocity u/U_m is a function of y/b only:

$$\frac{u}{U_m} = f(\frac{y}{b}) \qquad (3.13)$$

where U_m is the velocity along the centre of the jet and b is the half-width; defined as the value of y at which u = 1/2 U_m. (Note that b is a function of x.)

Moreover, the turbulent shear stress can be assumed to be self-similar:

$$\frac{\tau t}{\rho U_m^2} = \frac{-\overline{u'v'}}{U_m^2} = g(\frac{y}{b}) \qquad (3.14)$$

Equations (3.13) and (3.14) are known as the self-preservation hypothesis: the velocity profile and the turbulent shear stress are independent of x if they are expressed in terms of the local length scale b and the velocity scale U_m.

Denote η = y/b and assume

$$b \propto x^m \qquad (3.15)$$

$$U_m \propto x^n \qquad (3.16)$$

From equation (3.12) and (3.13):

$$\frac{d}{dx}\left(\rho b U_m^2 \int_0^\infty f^2 d\eta\right) = 0 \quad .$$

Since $\int_0^\infty f^2 d\eta$ is constant, we get

$$\frac{d}{dx}(bU_m^2) = 0 \qquad (3.17)$$

Substituting equation (3.15) and (3.16) into (3.17):

$$\frac{d}{dx}(x^m\, x^{2n}) = 0$$

Consequently,

$$m + 2n = 0 \qquad (3.18)$$

If we substitute(3.13) and (3.14) into (3.9), we may write (the overbars are omitted for convenience):

$$\frac{\partial u}{\partial x} = - \frac{U_m f' y}{b^2} \frac{db}{dx} + f \frac{dU_m}{dx}$$

$$\frac{\partial u}{\partial y} = \frac{U_m}{b} f'$$

By integrating the continuity equation,

$$v = \int_0^y \frac{\partial u}{\partial x} dy$$

$$= U_m \int_0^\eta \eta f' d\eta \frac{db}{dx} - b \int_0^\eta f d\eta \frac{dU_m}{dx}$$

$$\frac{\partial \tau_t}{\partial y} = \frac{\rho U_m^2}{b} g'$$

where $f' = df/d\eta$ and $g' = dg/d\eta$.

Then equation (3.9) becomes:

$$\frac{b}{U_m} \frac{dU_m}{dx} \left(f^2 - f' \int_0^\eta f \, d\eta\right) - \frac{db}{dx} \left(\eta f' - \eta f f' + f' \int_0^\eta f d\eta\right) = g' \qquad (3.19)$$

Since g′ is a function of η only and independent of x, we require both

$\frac{b}{U_m} \frac{dU_m}{dx}$ and $\frac{db}{dx}$ terms to be invariant with respect to x.

Since

$$\frac{b}{U_m} \frac{dU_m}{dx} \propto x^m \; x^{n-1-n} = x^{m-1}$$

$$\frac{db}{dx} \propto x^{m-1}$$

Thus m = 1 and from equation (3.18) n =-1/2.

Therefore,

$$U_m \propto \frac{1}{\sqrt{x}} \qquad (3.20)$$

$$b \propto x \qquad (3.21)$$

3.4 Goertler Solution of the Two-dimensional Turbulent Jet

The solution of the velocity distribution was first derived by Tollmien (1926), who used Prandtl's mixing length hypothesis and solved the equation numerically. Goertler and Reichardt (1942) also obtained the solution with Prandtl's second hypothesis. For detailed discussion of the theoretical analysis, the reader should be referred to the excellent text "Boundary-Layer Theory" by Schlichting (1955).

We have shown that (equation (3.9), the overbars are again omitted for convenience):

$$u\frac{\partial u}{\partial x} + v\frac{\partial u}{\partial y} = \frac{1}{\rho}\frac{\partial \tau_t}{\partial y}$$

where τ_t denotes the turbulent shear stress, which is

$$\tau_t = \rho\, \nu_t \frac{\partial u}{\partial y} \qquad (3.22)$$

Then

$$u\frac{\partial u}{\partial x} + v\frac{\partial u}{\partial y} = \nu_t \frac{\partial^2 u}{\partial y^2} \qquad (3.23)$$

The kinematic eddy viscosity ν_t is determined by Prandtl's second hypothesis: ν_t is assumed to be proportional to the maximum difference in mean velocities $(U_{max}-U_{min})$ and the width of the mixing zone b

$$\nu_t = \chi\, b(x)\, (U_{max}-U_{min}) = \chi\, b(x)\, U_m(x) \qquad (3.24)$$

where χ is an empirical constant determined by experiment.

Denoting U_s, b_s and ν_s as the centreline velocity, half-width and kinematic eddy viscosity respectively at a characteristic distance x = s, we have

$$\nu_s = \chi\, b_s\, U_s$$

Suppose the velocity profiles U(x,y) of the jet are affine at all values of x, then the similarity solutions of equation (3.23) exist.

The stream function ψ may be assumed to be of the form

$$\Psi \sim x^{1/2} f(y/b) \qquad (3.25)$$

The partial differential equation (3.23) can be transformed into a third order, non-linear ordinary differential equation with the stream function and the similarity transformation

$$\zeta = \sigma \frac{y}{x} \qquad (3.26)$$

where σ is an arbitary constant.

The stream function is given by Schlichting (1979):

$$\Psi = \left(\frac{U_s\, s^{1/3}}{\sigma} \right) x^{1/2} f(\zeta) \qquad (3.27)$$

Hence

$$u = \frac{\partial \Psi}{\partial y} = U_m \left(\frac{x}{s}\right)^{-1/2} f'$$

$$v = - \frac{\partial \Psi}{\partial x} = \left(\frac{U_s\, s^{1/2}}{\sigma} \right) x^{-1/2} \left(\zeta\, f' - \frac{1}{2}\, f \right) .$$

By subsituting into equation (3.23) and choosing to put

$$\sigma = \frac{1}{2}\sqrt{\frac{U_s\ s}{\nu_s}} \quad , \qquad (3.28)$$

we have the third order differential equation:

$$2f' + 2f\ f'' + f''' = 0 \ . \qquad (3.29)$$

The boundary conditions are:

$$f = 0,\ f' = 1 \quad \text{at } \zeta = 0$$

$$(u = U_m,\ v = 0 \text{ at } y = 0)$$

and

$$f' = 0 \text{ at } \zeta = \infty$$

$$(u = 0 \text{ at } y = \infty)$$

The solution can be obtained by integrating equation (3.29) twice:

$$u(x,y) = \frac{\sqrt{3}}{2}\sqrt{\frac{K\sigma}{x}}\ (1-\tanh^2\zeta) \qquad (3.30)$$

$$v(x,y) = \frac{\sqrt{3}}{4}\ \sqrt{\frac{K}{\sigma\ x}}\ \left[\ 2\zeta\ (1-\tanh^2\zeta) - \tanh\zeta\right] \ . \qquad (3.31)$$

where K is the kinematic momentum.

3.5 Entrainment

The lateral boundary conditions for the jet can be described as

$$y \to \infty \quad u = w = 0 \quad v = v_e(x) \qquad (3.32)$$

where $v_e(x)$ is the entrainment velocity.

Suppose Q(x) is the rate of flow per unit length at any section of the jet, then

$$Q(x) = 2 \int_0^\infty u(x,y)\ dy \qquad (3.33)$$
$$= \int_{-\infty}^{\infty} u(x,y)\ dy$$

Note that the integral is meaningful only within the jet, although the upper and lower limits are { ∞,-∞ }. The turbulent jet draws a large amount of fluid from the surroundings. The mass of the fluid carried by the jet increases with downstream distance.

By differentiating equation (3.33) with respect to x:

$$\frac{d\ Q(x)}{d\ x} = 2\ \frac{d}{dx} \int_0^\infty u(x,y)\ dy$$
$$= 2\ v_e(x) \qquad (3.34)$$

Substituting equation (3.13) into (3.34) :

$$v_e(x) = \frac{d \int_0^\infty u(x,y)\ dy}{dx}$$

$$= \frac{d \int_0^\infty U_m(x)\ b(x)\ f(\eta)\ d\eta}{dx}$$

$$= \frac{d\ U_m(x)\ b(x)}{dx} \left(\int_0^\infty f(\eta) d\eta \right)$$

Then $$v_e(x) \propto \frac{d\ U_m(x)\ b(x)}{dx} \qquad (3.35)$$

According to equation (3.20) and (3.21)

$$v_e(x) \propto \frac{d(x^{-1/2 \cdot}\ x)}{dx}$$
$$v_e(x) \propto x^{-1/2} \qquad (3.36)$$

So it can be seen that:

$$v_e(x) = \alpha_e \, U_m(x), \tag{3.37}$$

where α_e is defined as the entrainment coefficient.

3.6 The Estimation of the Entrainment Coefficient α_e

The entrainment velocity is obtained by letting $y \to \infty$ in equation (3.31):

$$v_e(x) = \lim_{y\to\infty} \frac{\sqrt{3}}{4} \sqrt{\frac{K}{\sigma x}} \left[2\sigma\left(\frac{y}{x}\right) \left(1-\tanh^2\left(\frac{\sigma y}{x}\right)\right) - \tanh\left(\frac{\sigma y}{x}\right) \right]$$

$$= -\frac{\sqrt{3}}{4} \sqrt{\frac{K}{\sigma}} \, x^{-1/2} \tag{3.38}$$

K is related to the momentum per unit length J by:

$$K = \frac{J}{\rho} \tag{3.39}$$

$$J = \rho \int_{-\infty}^{+\infty} u^2(x) \, dy = \frac{4}{3}\rho \, U_s^2 \, s/\sigma \tag{3.40}$$

The experimental value of σ determined by Reichardt and Goertler (1942) is 7.67.

By using equations (3.38), (3.39) and (3.40) , we get:

$$v_e(x) = -\frac{U_s}{2\sigma}\sqrt{s} \; x^{-1/2} \tag{3.41}$$

Note that $U_s\sqrt{s} = U_m(x)\sqrt{x}$ = constant

Then

$$v_e(x) = -\frac{1}{2\sigma} \, U_m(x) \tag{3.42}$$

Hence

$$\alpha_e = -1/2\sigma = -0.065.$$

If Q_o is the mass flux from the inlet per unit span, we can determine $Q(x)/Q_o$:

$$Q(x) = 2 \int v_e(x)\, dx = 2\alpha_e U_s\sqrt{s} \int x^{-1/2} dx = 4\alpha_e U_s\sqrt{sx}$$

$$Q_o = U_o D$$

Therefore,

$$\frac{Q(x)}{Q_o} = \frac{4\alpha_e U_s\sqrt{sx}}{U_o D} \qquad (3.43)$$

3.7 Simulation Code

The source code used in the plane jet simulation is a modified version of DUCT, which was originally written by S. Gavrilakis (1992), and later developed by P.R. Voke and S.G. Potamitis in the Turbulence Unit of Queen Mary and Westfield College. DUCT was originally designed for studying flow through a square duct. This 2nd-order finite difference code has inflow and outflow boundary conditions with two statistically inhomogeneous coordinates (streamwise and cross-stream), which allow the simulations of spatially developing flows. The spanwise direction is periodic. The discretisation of the continuity and Navier-Stokes equations is obtained by the 2nd-order finite volume method applied to the staggered grid. The standard Smagorinsky (1965) and Schumann (1975) subgrid scale models are both available in the code. The boundary conditions in the side walls are optional; either stress free (free slip) or solid wall (no slip), but no inflow or outflow is allowed in the side boundaries. A "guard ring" or fictitious cells are placed outside the computational domain in order to enforce the boundary conditions. The original boundary conditions for the side boundaries are modified for the free jet simulation.

The integration of the Navier-Stokes equations is achieved by the Adams-Bashforth time advancement scheme. The pressure solver involves the Fourier transform of the discretised Poisson equation in the direction of periodicity, and a cyclic reduction algorithm (Swarztrauber (1974)) is required for the solution of the resulting block-tridiagonal system. Parts of the Fortran 77 source code are vectorized to increase the speed of computations on the Cray supercomputers. All the units in the code are non-dimensional or arbritary units.

3.8 Time Advancement

Adams-Bashford and Crank-Nicolson Schemes

The explicit Adams-Bashford scheme is based on the idea that the time advancement of a function can be extrapolated by the slope at the mid-point between two time levels. Let f_n be a continous function at the n-th time level. It is given as:

$$f^{n+1} = f^n + \Delta t \; \dot{f}^{n+1/2} \qquad (3.44)$$

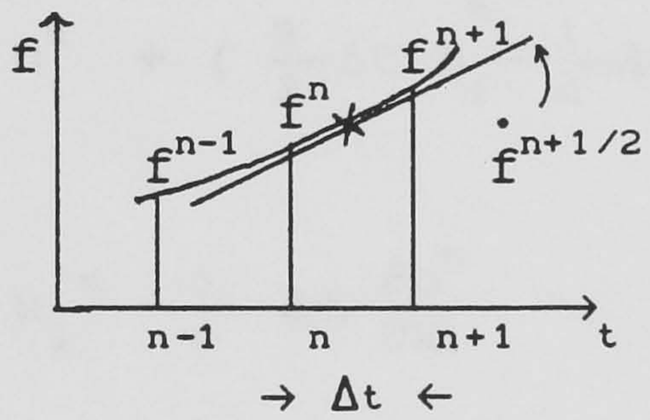

Fig. 3.1(a)

where $\dot{f}^{n+1/2}$ is the gradient of the function midway between time level n and (n+1) as shown in the diagram (3.1a). The gradient is simply obtained by linear extrapolation (see diagram (3.1b)):

$$\dot{f}^{n+1/2} = \dot{f}^{n-1} + \frac{3}{2}\left(\dot{f}^{n} - \dot{f}^{n-1}\right)$$

$$= \frac{3}{2}\dot{f}_n - \frac{1}{2}\dot{f}_{n-1} \qquad (3.45)$$

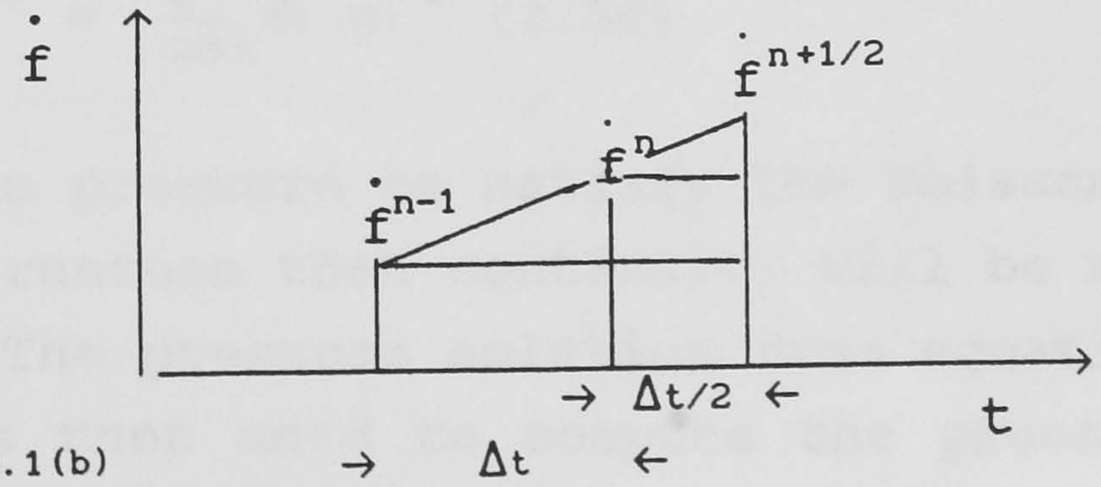

Fig.3.1(b)

Substitute equation (3.45) into (3.44)

$$f^{n+1} = f^n + \Delta t \left(\frac{3}{2} \dot{f}^n - \frac{1}{2} \dot{f}^{n-1} \right) \qquad (3.46)$$

The Navier-Stokes equations can be written in the form:

$$\frac{\partial u_i}{\partial t} = \frac{-\partial p}{\partial x_i} + h_i \qquad (3.47)$$

where h_i includes the viscous and convective terms.

Then from equation (3.45) and (3.47) :

$$u_i^{n+1} = u_i^n + \Delta t \left(\frac{3}{2} \dot{u}_i^n - \frac{1}{2} \dot{u}_i^{n-1} \right)$$

$$= u_i^n + \left(\frac{3}{2}\Delta t\, h_i^n - \frac{1}{2}\Delta t\, h_i^{n-1} - \frac{3}{2}\Delta t \frac{\partial p^n}{\partial x_i} + \frac{1}{2}\Delta t \frac{\partial p^{n-1}}{\partial x_i} \right)$$

$$= u_i^{*n} - \frac{3}{2} \Delta t \frac{\partial p^n}{\partial x_i} \qquad (3.48)$$

where $u_i^{*n} = \frac{3}{2}\Delta t\, h_i^n - \frac{1}{2} \Delta t\, h_i^{n-1} + \frac{1}{2} \Delta t \frac{\partial p^{n-1}}{\partial x_i} + u_i^n$

In equation (3.48), u_i^{*n} is computed first ignoring the pressure gradient term at time level n.

The continuity equation can be written as:

$$\partial_i\, u_i^{n+1} = 0 \qquad (3.49)$$

By applying the divergence operator to equation (3.48):

$$\partial_i\, u_i^{*n} - \frac{3}{2} \Delta t\, \nabla^2 p^n = 0$$

We obtain the Poisson equation:

$$\nabla^2 p^n = \frac{2}{3\Delta t} \partial_i\, u_i^{*n} \qquad (3.50)$$

Forcing the pressure to satisfy the Poisson equation at time step n guarantees that continuity will be maintained at time step n+1. The pressure solution from equation (3.50) at time level n is then used to compute the pressure gradient term in (3.48) and hence the velocity at the (n+1)th time level. With the use of the Adams-Bashford scheme for both viscous

and convective terms, the pressure field advancement is always one step lagged behind the velocity field, which is not very convenient. In order to solve this problem, the pressure gradient term in equation (3.47) can be treated implicitly with Crank-Nicolson scheme, while h_i is formulated with Adams-Bashford scheme in the manner described.

The Crank-Nicolson scheme approximates $\dot{f}^{n+1/2}$ in equation (3.44) by:

$$\dot{f}^{n+1/2} = \frac{1}{2}(\dot{f}^{n} + \dot{f}^{n+1}) \qquad (3.51)$$

i.e. the function $\dot{f}$ at time level $n+1/2$ is simply the average of those values at step n and n+1. It is implicit because $\dot{f}^{n+1}$ is unknown at step n.

Equation (3.47) is then written as:

$$u_i^{n+1} = u_i^{n} + (\frac{3}{2}\Delta t\, h_i^{n} - \frac{1}{2}\Delta t\, h_i^{n-1}) - \frac{1}{2}\Delta t\frac{\partial P^{n+1}}{\partial x_i} - \frac{1}{2}\Delta t\frac{\partial P^{n}}{\partial x_i} \qquad (3.52)$$

By putting $u_i^{*} = u_i^{n} + \frac{3}{2}\Delta t\, h_i^{n} - \frac{1}{2}\Delta t\, h_i^{n-1} - \frac{1}{2}\Delta t\frac{\partial P^{n}}{\partial x_i}$

$$u_i^{n+1} = u_i^{*} - \frac{1}{2}\Delta t\, \frac{\partial P^{n+1}}{\partial x_i} \qquad (3.53)$$

The continuity equation :

$$\partial_i\, u_i^{n+1} = \partial\, u_i^{*n} - \frac{1}{2}\Delta t\nabla^2 P^{n+1} = 0$$

gives the Poisson equation:

$$\nabla^2 P^{n+1} = \frac{2}{\Delta t}\partial_i u_i^{*n} \qquad (3.54)$$

Note that the actual interpretation of the pressure in DUCT

is slightly different from above formulation, it uses:

$$p^{n+1/2} = (p^{n+1} + p^{n})/2$$

or $$p^{n+1/2} = \frac{3}{2} p^{n} - \frac{1}{2} p^{n-1}$$

Then equation (3.53) may be written as:

$$u_i^{n+1} = u_i^{*} - \Delta t \left(\frac{\partial p}{\partial x_i}\right)^{n+1/2}$$

The resulting Poisson equation will be similar though with a different coefficient.

The Poisson equation is solved by the block tridiagonal solver with the cyclic reduction algorithm.

3.9 Block Tridiagonal Systems

For elliptic problems that are governed by systems of equations, the use of the three-point differencing approximation often lead to a tridiagonal system of linear equations:

$$\begin{bmatrix} \underline{b}_1 & \underline{c}_1 & & & & & \\ \underline{a}_2 & \underline{b}_2 & \underline{c}_2 & & & & \\ & \ddots & \ddots & \ddots & & & \\ & & \underline{a}_i & \underline{b}_i & \underline{c}_i & & \\ & & & \ddots & \ddots & \ddots & \\ & & & & \underline{a}_{N-1} & \underline{b}_{N-1} & \underline{c}_{N-1} \\ & & & & & \underline{a}_N & \underline{b}_N \end{bmatrix} \begin{bmatrix} V_1 \\ V_2 \\ \\ V_i \\ \\ \\ V_{N-1} \\ V_N \end{bmatrix} = \begin{bmatrix} d_1 \\ d_2 \\ \\ d_i \\ \\ \\ d_{N-1} \\ d_N \end{bmatrix} \qquad (3.55)$$

where $\underline{a}_i$, $\underline{b}_i$, $\underline{c}_i$ are M x M submatrices and V_i and d_i are M-component subvectors. Equation(3.55) can be manipulated into the upper triangular form :

$$\begin{bmatrix} \underline{I} & \underline{c}_1' & & & & & \\ & \underline{I} & \underline{c}_2' & & & & \\ & & \cdot & \cdot & \cdot & & \\ & & & \underline{I} & \underline{c}_i' & & \\ & & & & \cdot & \cdot & \cdot \\ & & & & & \underline{I} & \underline{c}_{N-1}' \\ & & & & & & \underline{I} \end{bmatrix} \begin{bmatrix} V_1 \\ V_2 \\ \\ V_i \\ \\ \\ V_{N-1} \\ V_N \end{bmatrix} = \begin{bmatrix} d_1' \\ d_2' \\ \\ d_i' \\ \\ \\ d_{N-1} \\ d_N' \end{bmatrix}$$

(3.56)

The submatrix $\underline{a}_i$ is eliminated and $\underline{b}_i$ is replaced by the unit matrix $\underline{I}$.
For the first block of equations:

$$\underline{c}_1' = (\underline{b}_1)^{-1}\underline{c}_1 \qquad \text{and} \qquad d_1' = (\underline{b}_1)^{-1} d_1 \qquad (3.57)$$

The equations are subjected to the forward sweep, the general block of equations being given by:

$$\begin{aligned} \underline{b}_i' &= \underline{b}_i - \underline{a}_i \underline{c}_i' \quad , \\ \underline{c}_i' &= (\underline{b}_i')^{-1}\underline{c}_i \quad , \\ d_i' &= (\underline{b}_i')\,(d_i - \underline{a}_i d_{i-1}') \end{aligned} \qquad (3.58)$$

Then the subvectors $\underline{V}_i$ are solved by back subsitution:

$$V_N = d'_N \ ,$$

$$V_i = d_i' - c'_i V_{i+1} \qquad (3.59)$$

3.10 Direct Pressure Solver

The central difference representation of the second derivative $\partial^2 f/\partial z^2$ is:

$$\frac{\partial^2 f}{\partial z^2} = \frac{f_{k-1} - 2f_k + f_{k+1}}{\Delta z^2} \qquad (3.60)$$

If the function f_k is represented by waves:

$$f_k = R\ \{\ e^{i\ k_z\ z_k}\} = \cos[\ k_z\ z_k\ ] \qquad (3.61)$$

where $R\ \{\ \}$ is the real part of the function, k_z is the wave number, then the *analytic* second derivative is:

$$\frac{\partial^2 f}{\partial z^2} = -\ k_z^2 \cos(k_z\ z_k) \qquad (3.62)$$

Substitution of (3.61) into (3.60) gives:

$$\frac{f_{k-1} - 2f_k + f_{k+1}}{\Delta z^2} = \frac{1}{\Delta z^2}\left[\ \cos[k_z(z_k - \Delta z)] - 2\cos[k_z\ z_k] + \cos[k_z(z_k + \Delta z)]\ \right]$$

$$= -k_z^2 \left[\ \frac{\{\ \sin(\ \frac{k_z\ \Delta z}{2}\ )\}}{(\ \frac{k_z\ \Delta z}{2}\ )}\ \right]^2 \cos[\ k_z\ z_k\ ]$$

$$= -K_z^2\ f_k \qquad (3.63)$$

$$\text{where } K_z = \frac{2\sin(\ \frac{k_z\ \Delta z}{2}\ )}{\Delta z} \qquad (3.64)$$

K_z is called the *effective wavenumber*.

The finite difference approximation introduces a change in the amplitude and phase shift of the derivative by comparing with equation (3.62), the errors will disappear as $\Delta z \to 0$. Equation(3.54) can be Fourier transformed in the z-direction(assumed periodic):

$$\frac{\partial P(x,y,k_z)}{\partial x} + \frac{\partial P(x,y,k_z)}{\partial y} - \left[\ \frac{2\sin(k_z\Delta z/2)}{\Delta z}\ \right] P(x,y,k_z) = s(x,y,k_z) \qquad (3.65)$$

where $s(x,y,k_z)$ is the source term (Fourier transform of the right hand side of equation(3.54)) and $P(x,y,k_z)$ is the

pressure p in Fourier domain.

Two techniques, cyclic reduction and Fourier series representation are used in solving the Poisson equation. The algorithm is given by Swarztrauber(1970,1977). The cyclic reduction consists of three phases: preprocessing, reduction and back-substitution. In the reduction phase, half of the unknown subvectors $\mathbf{V}_i$ are eliminated and the resulting system has a block order half of the preceding system. For the detailed discussions of the direct solutions for the Poisson equation and the fast Fourier transform the reader is referred to Swartztrauber(1977).

3.11 Staggered Grid

A staggered grid is used for the computational mesh. The velocity components are stored at locations staggered with respect to those at which the pressure are stored; the velocity components are defined on the cell surface while the pressure is at the centre as shown in figure 3.2(a),(b). A staggered grid is much better than a non-staggered grid because it avoids the problem of decoupling of adjacent pressure nodes, which is associated with the central finite-difference discretisation of the momentum equations. Moreover, staggered meshes eliminate the need for boundary conditions on pressure, since the domain boundaries can be chosen to fall on velocity nodes.

Discretisation of the continuity equation on the staggered grid gives:

$$\frac{u_{i,j,k} - u_{i-1,j,k}}{\Delta x} + \frac{v_{i,j,k} - v_{i,j-1,k}}{\Delta y} + \frac{w_{i,j,k} - w_{i,j,k-1}}{\Delta z} = 0$$

which is the discrete form of the global mass conservation,

$$\int_c \mathbf{v}.\mathbf{n}\, ds = 0. \qquad (3.66)$$

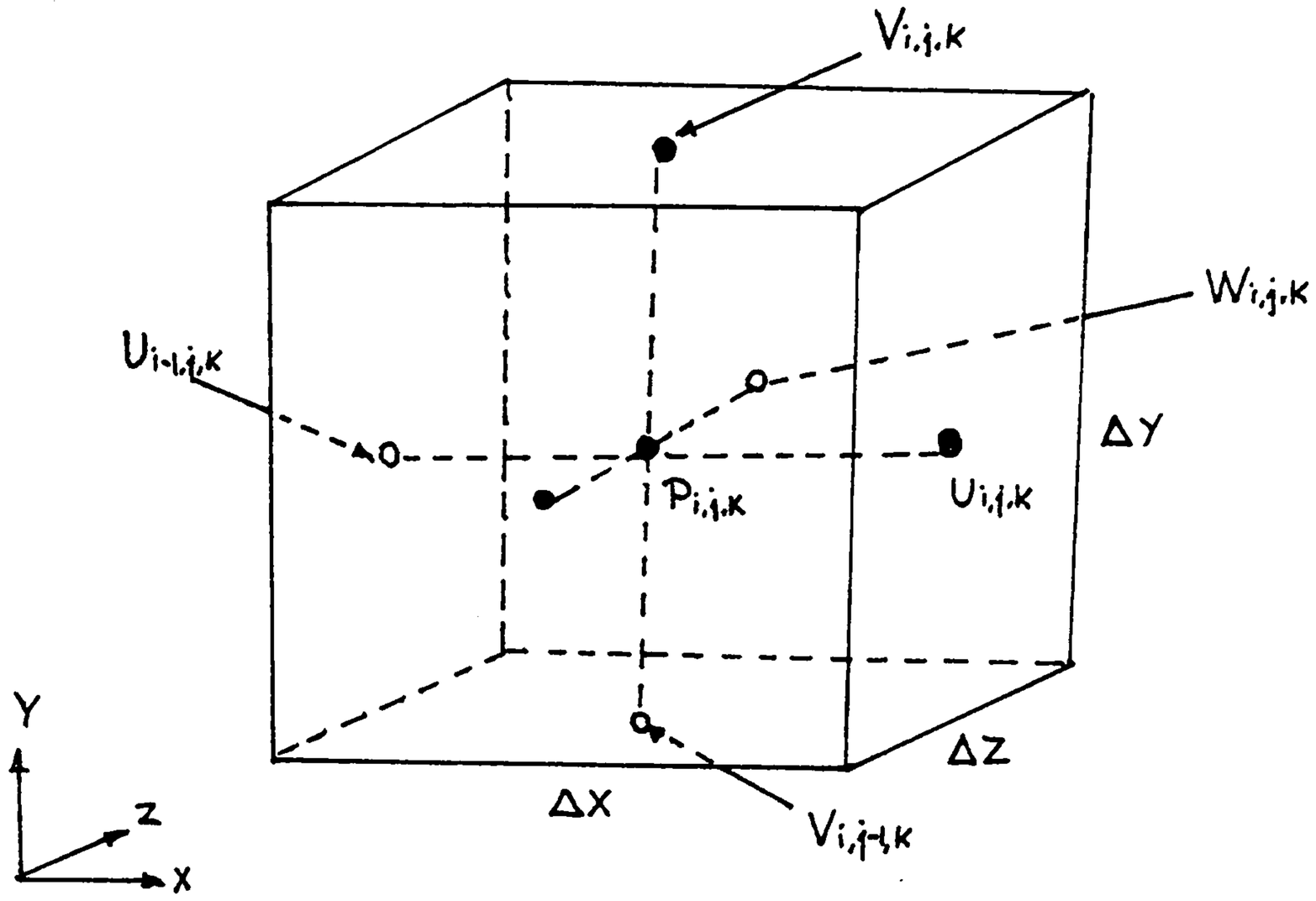

Fig. 3.2(a) Staggered grid in three dimensions.

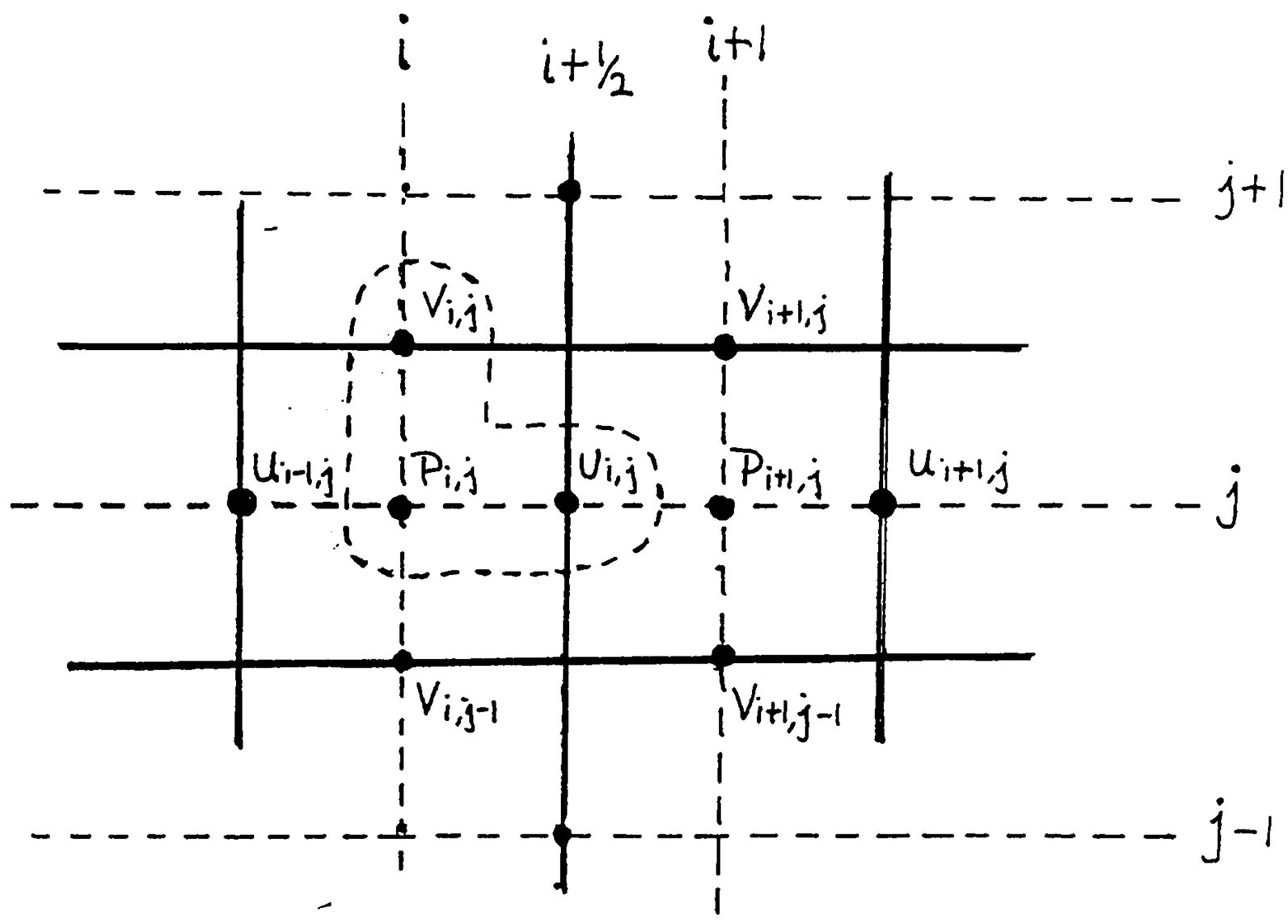

Fig. 3.2(b) Staggered grid in two dimensions.

3.12 Configurations and Geometry of the Simulation

The geometry and coordinates of the simulation are shown in figure 3.3. The Reynolds number based on the jet width is 1,600 (the inlet velocity U_o = 16, molecular viscosity ν_m = 0.01). Both the streamwise (x) and the cross-stream (y) directions are inhomogeneous. Periodic boundary conditions are used in the spanwise (z) direction. One of the problems with the spatially developing free jet is the lateral spreading of the flow. As a result, the jet width must be as narrow as possible compared with the width of the computational box. The dimensions are 60dx50dx10d in

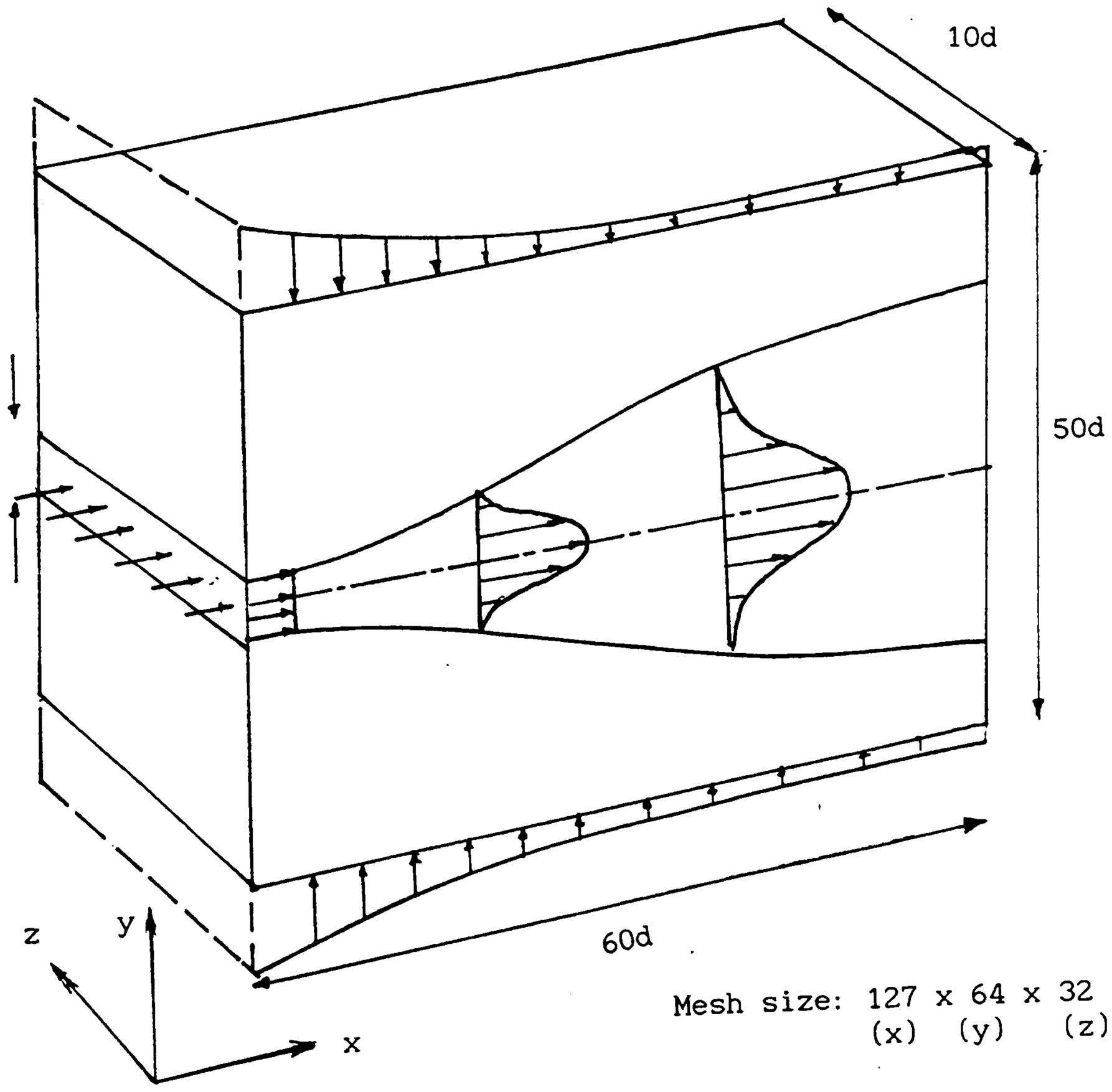

Fig. 3.3 The geometry and coordinates of the simulation.

the x, y and z directions respectively. This geometry should allow plenty of clearance for the spreading of the jet. The limitations of the computation time allocation restricted us to a 127x64x32 mesh, which requires 3Mwords buffer memory

for the velocity and pressure fields. It can be fitted into a 6.5 Mwords medium-size job of the Cray XMP 4/16. The mesh is uniform in x and z directions with $\Delta x = 0.472$ and $\Delta z = 0.3125$. The y-mesh is stretched from the jet centreplane to provide fine resolution within the turbulent region of the jet, an arbritary expansion factor r of 1.068355 being used:

$$y_j = y_{j-1} + \Delta y_o \, r^{j-1}$$

$$\Delta y_o = 0.25.$$

The computation time allocation of this project has been very limited, therefore the cost of the simulation must be taken into account in the consideration of computational box dimensions. The spanwise width of 10 jet diameters should be adequate and sufficently wider than the length of the largest structures, although it is difficult to validate without the time-averaged, spanwise two-point correlations being available.

3.13 Inflow Boundary Conditions

The jet inlet velocity is a uniform profile with random numbers as initial disturbances. The magnitude of the random disturbances is 1/16 of the inlet velocity U_o. The random disturbances were removed, when the flow became turbulent. On both sides of the inlet, the boundary condition is set to be no-slip or solid (see figure 3.4):

$$v_{1j} = - v_{2j}, \quad w_{1j} = - w_{2j}, \quad u_{1j} = u_{2j} = 0 \qquad (3.67)$$

or it could be set to free-slip (impermeable wall):

$$v_{1j} = v_{2j}, \quad w_{1j} = w_{2j}, \quad u_{1j} = u_{2j} = 0 \; . \qquad (3.68)$$

The use of (3.67) should be avoided, if the entrainment boundary condition is implemented.

3.14 Side Boundary Conditions

The y-wall boundary conditions of DUCT were originally set to:

$$u_{i1} = u_{i2}, \qquad w_{i1} = w_{i2}, \qquad v_{i1} = v_{i2} = 0 \quad (3.69)$$

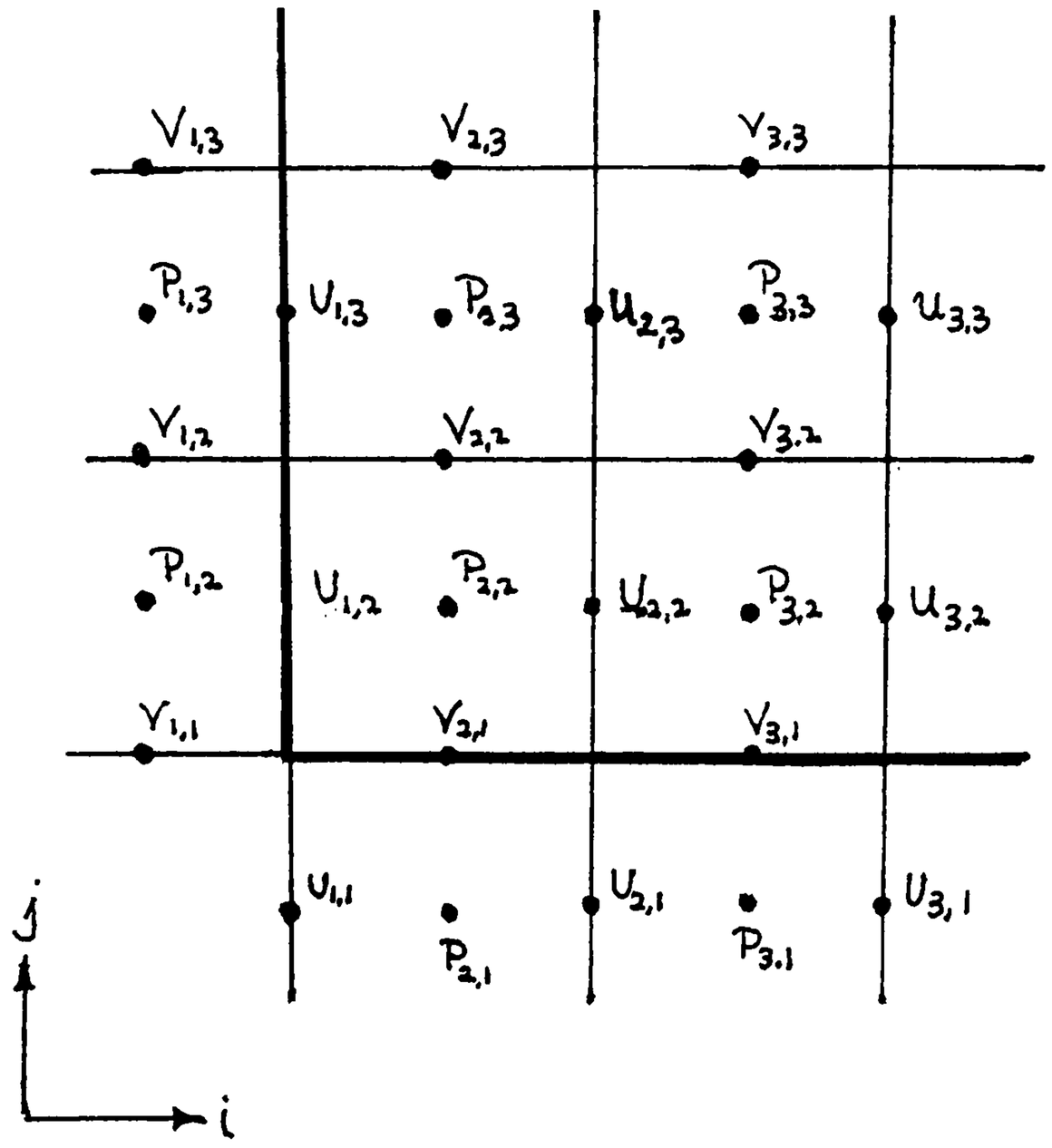

Fig. 3.4 Inflow and lateral boundary conditions.

Hence fluid is not allowed to flow in and it behaves as a free slip impermeable surface. This does not work well in the simulation of a free jet because the flow in the downstream region recirculates back to the upstream and entrains into the jet. The situation is very similar to a jet discharging into a confined space.

The boundary condition for velocity v in (3.69) can be modified :

$$v_{i1} = v_{i2} = V_c$$

where V_c is a constant velocity. This imposes a uniform velocity stream to allow entrainment of the irrotational

flow. This should work well in the kind of the flows where entrainment rate is very low, such as boundary layers. However, we have shown that the rate of entrainment in a fully developed plane jet varies with the streamwise distance. The use of a uniform entrainment velocity would force the jet to behave in an unrealistic way, especially if V_c is large. In attempt to tackle this problem, free slip boundary condition was used in the early phase of the simulation. When the flow has become fully turbulent, an entrainment velocity profile (equation 3.37) is imposed. The ratio of the total entrainment to the jet inlet mass flux Q_{total}/Q_o was adjusted accordingly to minimize the recirculation flows. We will discuss this in chapter five.

3.15 Outflow Boundary Conditions

The outflow boundary conditions are based on the assumption that the turbulent flow structures are "frozen" at the outflow plane of the computational box, ie. the structures are simply convected through the outflow plane without any change in shape. This is conceptually very similar to Taylor's hypothesis. The method is called the advective boundary condition. We have:

$$\frac{\partial u}{\partial t} + u_c \frac{\partial u}{\partial x} = 0$$

$$\frac{\partial v}{\partial t} + u_c \frac{\partial v}{\partial x} = 0$$

$$\frac{\partial w}{\partial t} + u_c \frac{\partial w}{\partial x} = 0 \qquad (3.70)$$

In the DUCT code, the local, outflow convection velocity u_c (should not be confused with the usual meaning of 'convection velocity') is approximated by the mean velocity U_{out} over the outflow area A_{out} (figure 3.5), i.e.

$$\frac{\partial u}{\partial t} + U_{out} \frac{\partial u}{\partial x} = 0 \qquad (3.71)$$

and

$$U_{out} = \frac{\int_{A_{out}} u \, dA}{A_{out}} \qquad (3.72)$$

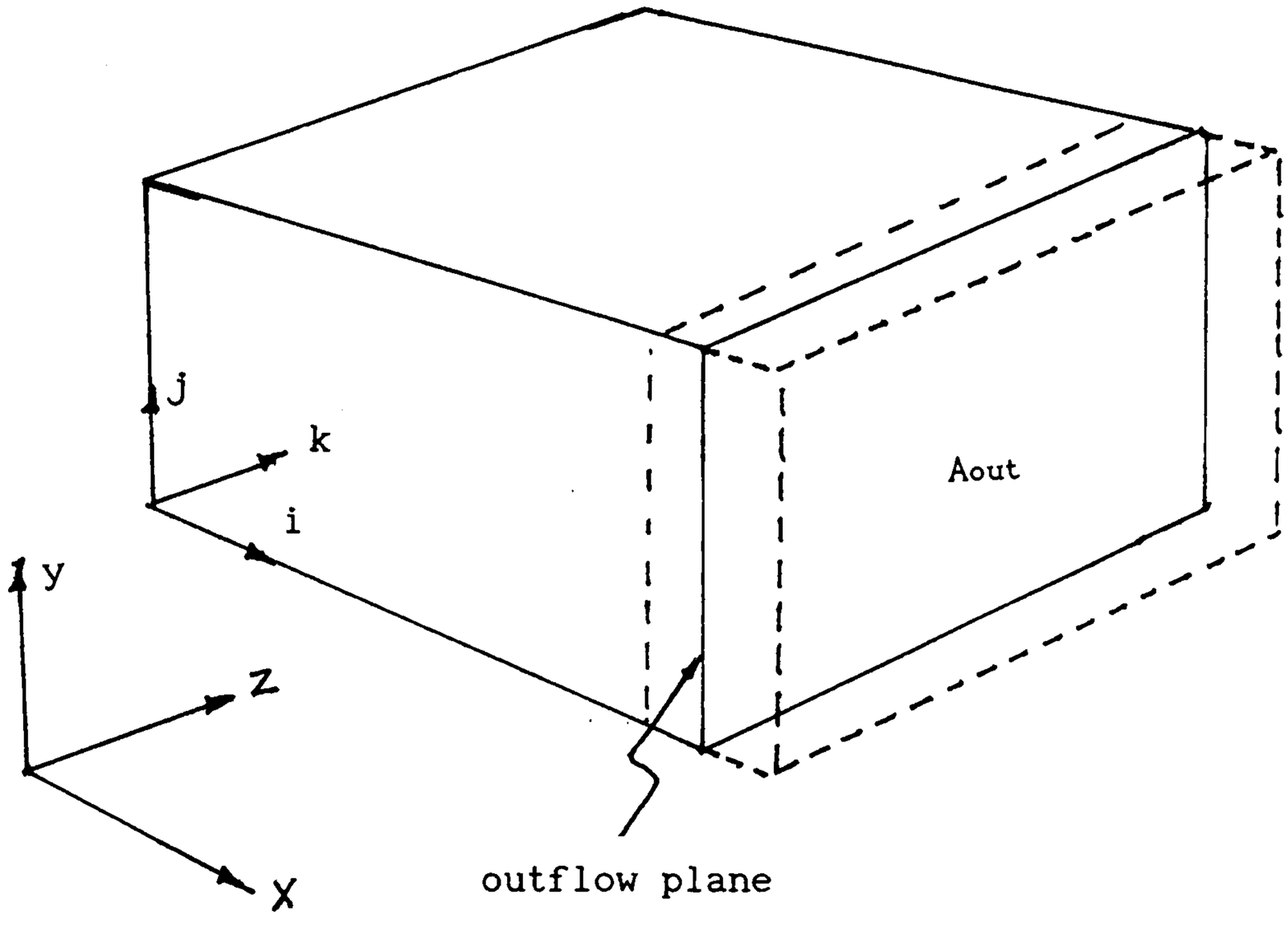

Fig. 3.5 Outflow boundary conditions.

The discretised form of equation (3.72) can be written as:

$$U_{out} = \frac{\sum_{A_{out}} u_{ij}\,\Delta y\,\Delta z}{A_{out}} \qquad (3.73)$$

The velocity gradient $\partial u/\partial x$ can be computed by the explicit Adams-Bashford scheme:

$$\frac{u_{jk}^{n+1}\big|_{ofp} - u_{jk}^{n}\big|_{ofp}}{\Delta t} = -U_{out}\left(\frac{\partial u}{\partial x}\right)_{ofp}^{n+1/2}$$

$$u_{jk}^{n+1} = u_{jk}^{n} - U_{out}\,\Delta t\left(\frac{3}{2}\frac{\partial u_i^{n}}{\partial x} - \frac{1}{2}\frac{\partial u_i^{n-1}}{\partial x}\right)_{ofp} \qquad (3.74)$$

where ofp denotes the velocity at the outflow plane.

The velocity u_{jk}^{n+1} is extrapolated from the velocity u_{jk}^{n+1} at the previous time step and it does not necessarily satisfy the global conservation of mass flux in equation (3.66). Hence, the outflow velocity is scaled by the

factor:

$$\frac{Q_{in}}{Q_{out}} = \frac{U_{out}\ A_{out}}{U_{in}\ A_{out} + 2\int_{A_{xz}} v_e\ dA} \qquad (3.75)$$

Equation (3.71) is a fairly crude assumption, because the local, outflow convection velocity u_c is assumed to be constant and equal to U_{out}. But in fact the mean streamwise velocity is large at the centre and tends to zero near the edge of the jet. This can introduce some errors of the computations, i.e. the velocity profile of the jet will be slightly flattened, and the flow at the centre will be forced to decelerate very near the outflow plane. Although equation (3.70) had been used, it was noted by Potamitis (unpublished private communication) that energy was being reflected from the outflow plane and caused numerical instability. There is no simple solution of this problem. It may be easier to simulate a coflowing jet than a free jet discharging into stationary fluid (in experiments, it is certainly easier to measure the flow quantities accurately in the coflowing jet, as found by experienced experimentalists).

CHAPTER FOUR
METHOD (PART II)

4.1 Template Matching Technique

Template matching is a fundamental operation in image processing and computer vision. It has found wide application in filtering, edge detection and object detection. A *template* or a *mask* (sometimes it is called a window) is a prototype used to detect some regional feature within a data field. It has an identifiable feature into which we are trying to classify a subset of data — *subdata*. The idea of working out the similarity between the prototype and the image is referred to as template matching. The most commonly used measure of similarity is the *cross correlation coefficient* or *convolution*. In local feature detection, the template is shifted into every possible position within a data field and the convolution is computed at every shift.

In the pattern recognition of turbulent flow structures, template matching is used to detect and locate an eddy pattern from the flow data. The organised eddy does not repeat itself exactly in the flow, since it has a variety of different shapes and sizes; moreover it is randomly distributed in the data field. Therefore the present template matching technique incorporates *position-invariant* cross correlation method with variation of the template scale. The scale of the template pattern can be shrunk or expanded in order to optimise the match, normally achieved by the zoom transformation of the template pattern.

A 2-D data field, called the *search area* can be represented by an N_1 by N_2 array or matrix G. Let G(i,j) be the element of the data at the i-th row and j-th column, where $i \in [\ 1, N_1\ ]$, $j \in [\ 1, N_2\ ]$ as shown in figure 4.1.

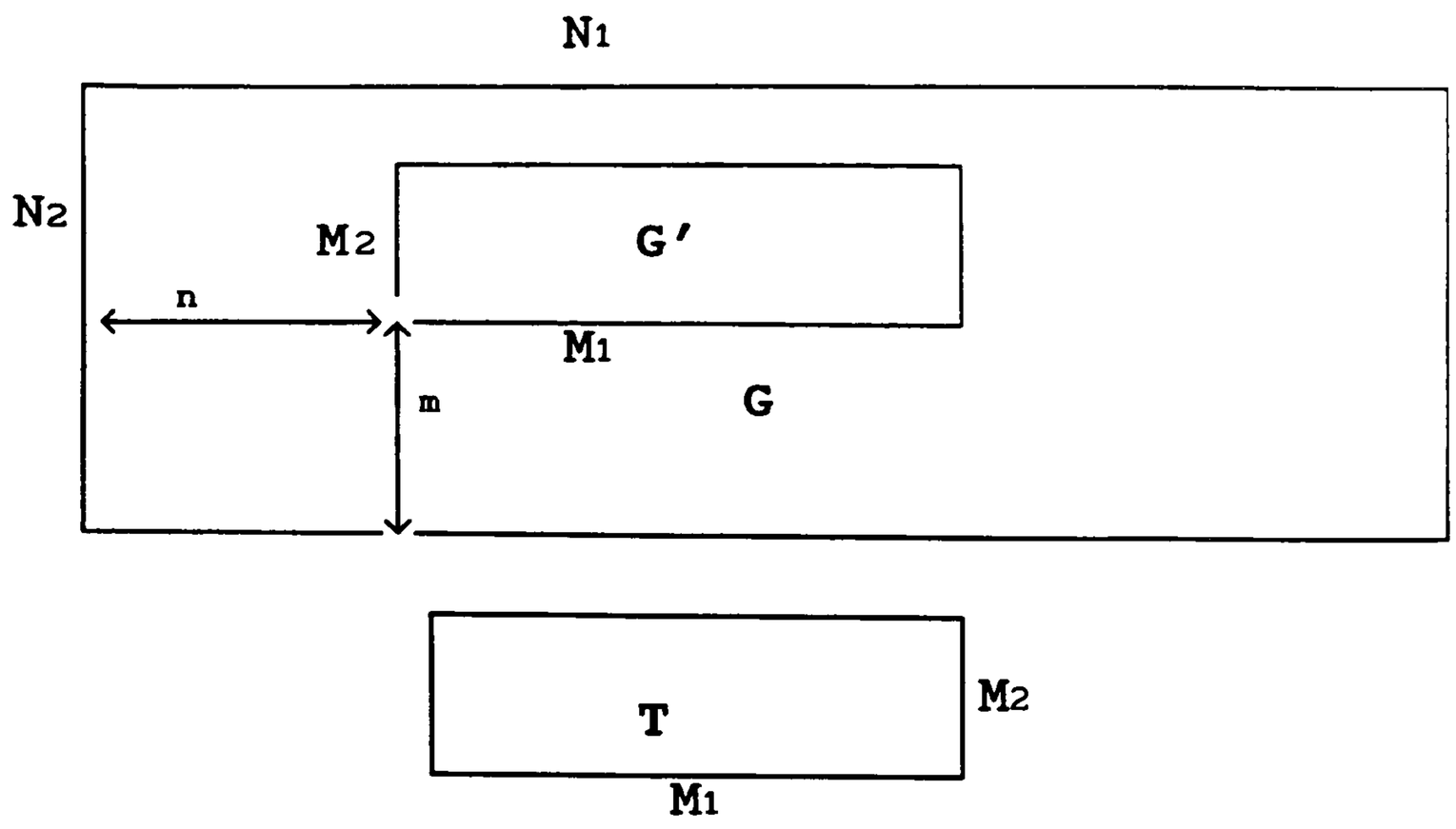

Figure 4.1 N1 by N2 search area G and M1 by M2 template T.

A template is an M_1 by M_2 array or matrix, $T = \{ T(k,l,s) \}$, where $k \in [\ 1,\ M_1\ ]$, $l \in [\ 1,\ M_2\ ]$ and $s \in [\ \zeta_{min}, \zeta_{max}\ ]$; ζ_{min} and ζ_{max} are the lower and upper limits of the zoom factor. The typical dimensions of the template and the data field are 24x12 and 20,000x32 respectively.

It is helpful to imagine the template as a mobile frame lying on the search area. The area the template covers is called the subdata: G'c G. Let m and n be the coordinates of the lower left corner of the subimage. If the frame of G' is not allowed to move beyond the edge of the domain G and M_2 is smaller than N_2, there are (N_2-M_2+1) possible shift positions in the transverse direction and (N_1-M_1+1) shift positions in the longitudinal direction:

$$n \in [\ 1,\ N_1 - M_1 + 1\ ]$$

$$m \in [\ 1,\ N_2 - M_2 + 1\ ] \quad \text{if } N_2 > M_2\ .$$

In some situations, it is possible to shift the template beyond the edge of the data field; this is called *periodic* or *wrap-around template*, which can be implemented in the present study because the boundary condition in the homogeneous direction of the jet is periodic. But this is not essential if the template width is much smaller than that of the data field.

The convolution is defined as :

$$C(m,n,s) = \frac{\sum_{p=1}^{M_2} \sum_{q=1}^{M_1} G(p+m-1,\ q+n-1) * T(p,q,s)}{\sqrt{\sum_{p=1}^{M_2} \sum_{q=1}^{M_1} G(p+m-1,\ q+n-1)^2}\ \sqrt{\sum_{p=1}^{M_2} \sum_{q=1}^{M_1} T(p,q,s)^2}} \qquad (4.2)$$

It is the element-by-element multiplication of a template with the corresponding elements of a subdata, summing the products, the resulting value being divided by the normalising factors so that the convolution is independent of the local intensity of the flow patterns.

Both G' and T can be regarded as (M_1 x M_2)-dimensional vectors in a vector space. The inner product of G' and T is defined as:

$$G'^{t}\ T = ||G'||\ \ ||\ T\ ||\cos\theta$$

so that

$$\cos\theta = \frac{G'^{t}\ T}{||\ G'\ ||\ \ ||\ T\ ||} \qquad (4.3)$$

where G'^{t} is the transpose of G' and

$$||\ G'\ || = \sqrt{G'.G'}$$

So the cross correlation coefficient is conceptually equivalent to the measurement of the direction cosine between two vectors T and G'; we are not concerned with their magnitudes. If both vectors are aligned in the same direction, then $\cos\theta = 1$. In other words, if the template is identical to the subdata then the convolution will be equal to unity.

In the experimental studies by Mumford and Ferré *et al* the number of sensors was inadaquate to cover the whole width of

the flow, so they employed a template which was wider than the data field ($M_2 > N_2$). This is cruder than our approach because each subdata is matched against only a portion of the entire template. The number of subimages for each position n is just *one* as compared with $(N_2 - M_2 + 1)$ subsets of data in our case.

At this point, it is worth mentioning the filtering property of the template. Consider the special case where **T** = **I**, T(p,q) = 1 for all p and q. **I** is called a unit template, and the convolution becomes:

$$\hat{G}'(m,n) = \frac{\sum_{p=1}^{M_2} \sum_{q=1}^{M_1} G'(p+m-1,\ q+n-1)}{M_2 M_1 \sqrt{\sum_{p=1}^{M_2} \sum_{q=1}^{M_1} G'(p+m-1,\ q+n-1)^2}} \qquad (4.4)$$

We may write :

$$\hat{G}' = G'^{t} \cdot \mathbf{I} \qquad (4.5)$$

This is a filtering operation, the unit template being a *low-pass averaging filter*. Eventually each resulting value $\hat{G}(m,n)$ is the unweighted sum of the elements within the subdata divided by the total number of points (M_1 x M_2). The filter removes high frequencies in an image while retaining the low frequencies.*

---

* At first it seems a bit odd that the resulting image $\hat{G}$ is smaller than the original image G. This nevertheless is unimportant for most image processing application as the template is usually much smaller than the image. The unit template is one of the simplest filters, but of course we can perform many different kinds of filtering operation by arranging the weight distribution and signs of the template's elements. The details are beyond the scope of our discussion.

The convolution is in fact equivalent to the cross-correlation. It can be either computed in the Fourier domain or by direct multiplications and additions. The *Discrete Correlation Theorem* says that the discrete correlation of two real functions **T** and **G′** is one member of the discrete Fourier transform pair. It can be written as:

$$\mathrm{corr}(\mathbf{T},\mathbf{G}') \equiv \mathbf{F}^{-1}\ [\ \mathbf{F}[\mathbf{T}]\ \mathbf{F}^{*}[\mathbf{G}']\ ]$$

If N is the length of the data field and M is the length of the template (it is assumed that the data field and the template are both squared for simplicity), then the number of computation steps is $(N - M + 1)^2\ M^2$ in the direct method. The cost ratio of the FFT method to direct method is given by:

$$\frac{\text{Cost of FFT method}}{\text{Cost of direct method}} = \frac{10N^2\log_2 N + 2MN\log_2 N + 4N^2}{(\ N - M + 1\ )^2\ M^2}$$

If M « N, the direct method is much cheaper. On the other hand, as the size of the template becomes large, the convolution is best done in the frequency domain.

4.2 Matching Criteria

In the previous section, we have shown that the cross-correlation C(m,n,s) can be used as a measure of the similarity between the template and the subdata. Suppose we plot the correlation function as an isometric surface, we can imagine the two dimensional correlation function as a rippling landscape of hills and valleys. If we only consider the positive correlation, each of the peaks of the mountains corresponds to the best alignment as well as similarity between the template and the subdata in spatial-temporal coordinates. On the other hand, if we plot the negative correlation only, each of the valleys of the terrain can be regarded as the best alignment between the template and subdata, but the subsets of data are now similar to the mirror image of the template pattern. We name these peaks and valleys the *events.* The difficulty is how to define the events unambiguously and identify them from the irregularly distributed landscape of the two dimensional correlation function. At this point, we shall discuss the use of the threshold criterion.

4.3 Threshold Criterion

Suppose we find the local spanwise (z direction) maxima and minima of the correlation function C(m,n,s) for every temporal position n (sometimes this is referred as longitudinal position). $C_{max}(n,s)$ is defined as the spanwise maximum of C(m,n,s) and $C_{min}(n,s)$ is defined as the spanwise minimum. If we plot $C_{max}(n,s)$ and $C_{min}(n,s)$ against n, our problem is reduced to one dimension. The spanwise maximum and minimum correlation curves give useful information about the temporal behaviour of the matching.

The purpose of setting a threshold value is to separate the apparently well correlated signals from the poorly correlated background noises and fine scale motions. If the spanwise maximum correlation is above the threshold, we may

say that the corresponding flow pattern is significant. The selection of the threshold value is entirely arbitrary. Too high a threshold would miss out many potentially important patterns except a few highly correlated patterns; too low a threshold would pick up too many noisy patterns. The choice of the threshold should be a compromise between these two extremes. A sensible value can be deduced from a typical spanwise maximum correlation curve plotted against the temporal coordinate. The threshold value of ±0.35 is used.

However, the use of a threshold is not sufficient by itself as a detection criterion, since very often those extraneous flow elements or background turbulence give short bursts of high correlation. As a result it is essential to measure the time duration of the burst; if it exceeds the *event duration limit* and is above the threshold, then the pattern is accepted as a sample and included in the ensemble average.

4.4 Event Duration Limit

It is reasonable to assume that the event duration limit has the same order of magnitude as the temporal length of the template pattern. The implementation of the event detection algorithm in the programming language is quite involved. The general idea is illustrated in figure 4.2. The horizontal axis is the time or streamwise coordinate of the pattern. Supposing an event occurs in the time interval A to D, the operation of the algorithm can be summarised as follows:

From A to B:
The *current pattern* is updated, if $C_{max}(n,s)$ is increasing and above the threshold ψ. The current pattern is the instantaneous sample, which is temporarily stored in the buffer memory, and it is constantly replaced by the better correlated frame or pattern.

At B:
Best alignment between the template and the pattern occurs

at this instant, with the correlation reaching a local peak value $C_{max}^*(s)$.

From B to C:
The duration of the event is being counted, when $C_{max}(n,s)$ is decreasing and less than $C_{max}^*(s)$.

At C:
When the number of counts is longer than the event duration limit Λ, the stored pattern at the peak B will be included in the working average.

At D:
The count is reset, whenever the correlation drops below the threshold value.

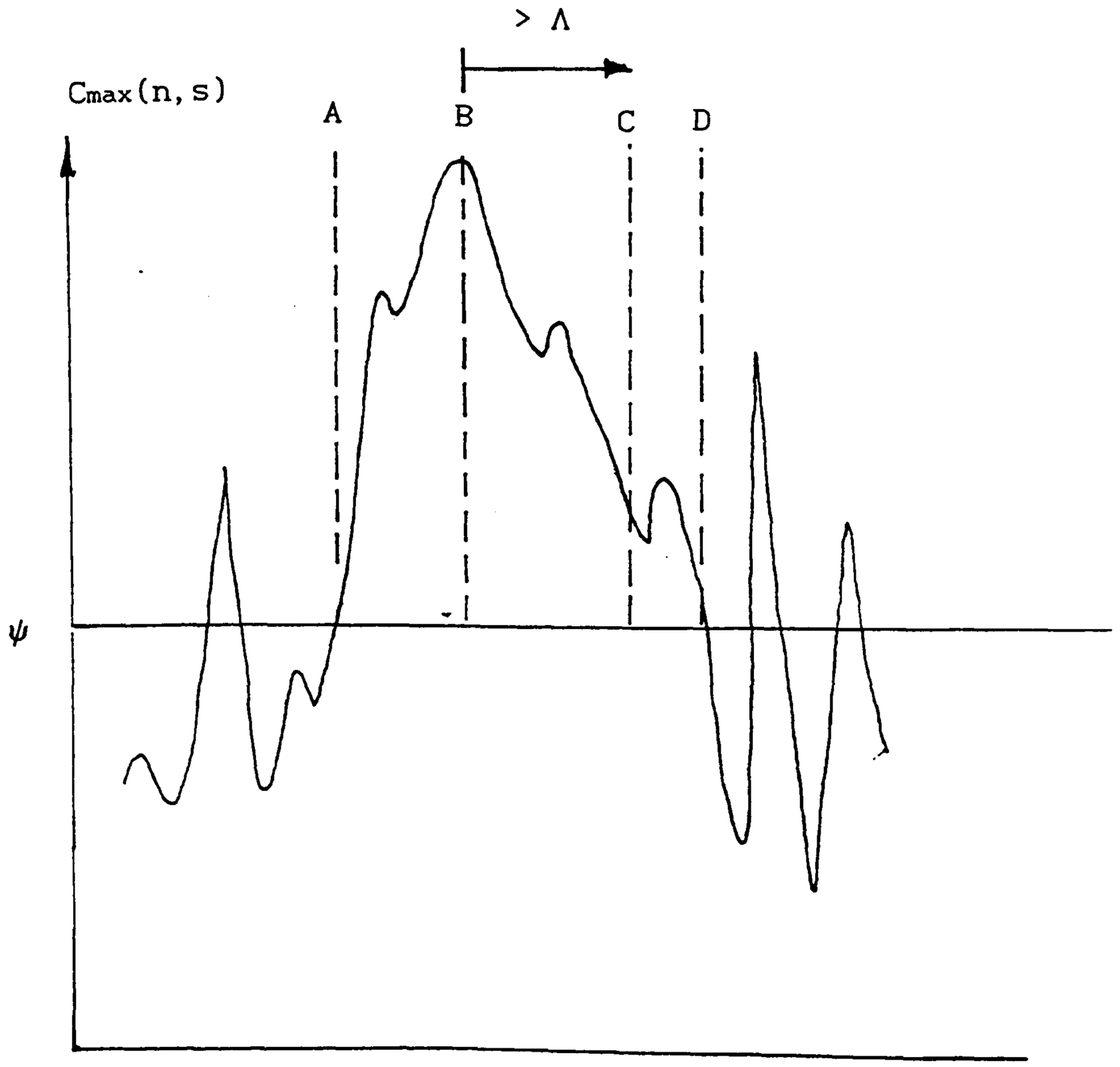

Fig. 4.2 Event duration limit.

The burst detection algorithm is not sensitive to the variation of shapes and noisy ripples of the correlation function.

The event duration limit Λ is set equal to 40 time steps or roughly one fifth of the largest eddy lifetime (see chapter five for the definition of Letot).

4.5 Extension of Averaging to Three Dimensions

Ensemble averaging of the velocity and pressure fields is performed in three perpendicular planes, namely the (x,z) plane (spanwise plane), (x,y) plane (transverse plane), and the (y,z) plane (cross-stream plane). It should be emphasised that all the template matching analyses are performed in the (x,z) plane because the double roller eddies have definite circulation or vorticity patterns in this plane, although it is possible to do the matching in the vertical plane as in the previous studies of Mumford (1982, 1983).

Our method of extracting the patterns in the vertical plane is very different from their approach. The ensemble averaging is split into two stages: in the first stage, the template matching is performed in the horizontal plane and

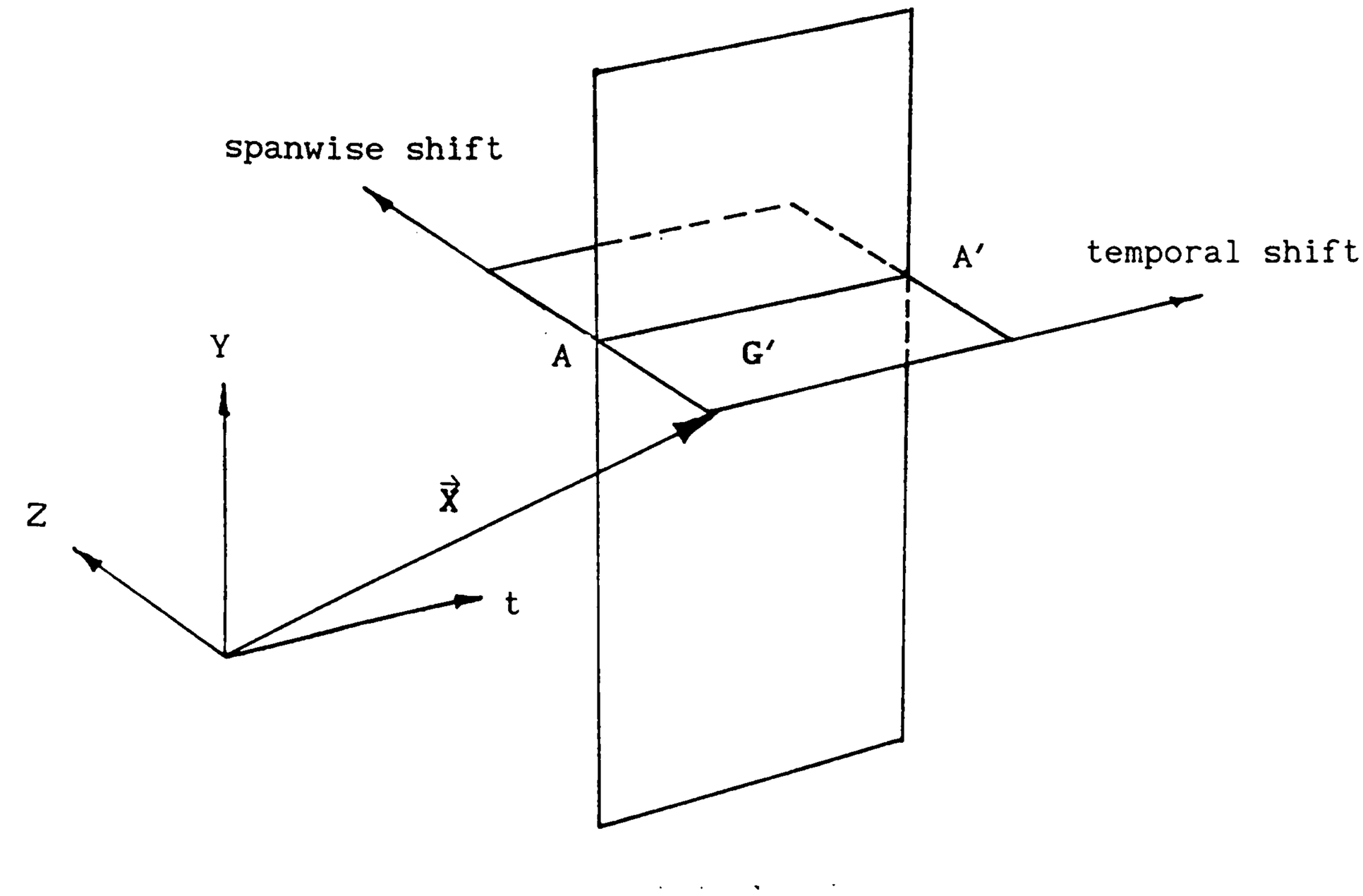

Fig. 4.3 Ensemble averaging in the (y,t) and (z,t) planes.

the ensemble averages $< \mathbf{E} >_{xz}$ (in the (x,z) plane) are formed by adding up all the best matched patterns. The locations of the patterns or *pointers* are then stored on the disc.

Since we are also interested in the surrounding fields in the (x,y) and (y,z) planes, denote $< \mathbf{E} >_{xy}$ and $< \mathbf{E} >_{yz}$ as ensemble averaged patterns in these planes, located at the centre of $< \mathbf{E} >_{xz}$ as illustrated in figure (4.3). In the next stage, we scan the three dimensional (y,z,t) databases and read the pointers from the disc, so that the surrounding fields located by the pointers are added to yield the ensemble averages of the other two planes.

4.6 Data Acquisition and Processing

The spatial-temporal data is gathered in the near and middle jet fields where the self-preserving property of the flow is attained and well away from the effects of the boundary conditions. The flow data in the outflow region, about 10 ~ 20 diameters from the outflow plane should not be used for pattern recognition, because there is some unavoidable influence of both the outflow and entrainment boundary conditions.

Data acquisition was performed in four sampling (y,z) planes at streamwise positions: x/d = 16.5, 18.9, 28.3 and 37.8. The dimensions of the 2-D arrays of sampling fields are 32x28, 32x38, 32x48 and 32x58 respectively (figure 4.4). After the numerical simulation had been run to statistical equilibrium (about 48,000 time steps), three components of velocity and pressure slices were written into four data channels and then dumped onto the Cray disks at every time step. The databases were gathered between time steps from 48,000 to 65,000. As the limit of the Cray Unix disk filespace is 600 Mb, all databases were copied onto 20 magnetic cartridges.

The databases are unformatted binary data. In the Cray Unix system, file compression and packing algorithms are available for ASCII data, the compression efficiency is about 30% of the original file size. However it is not

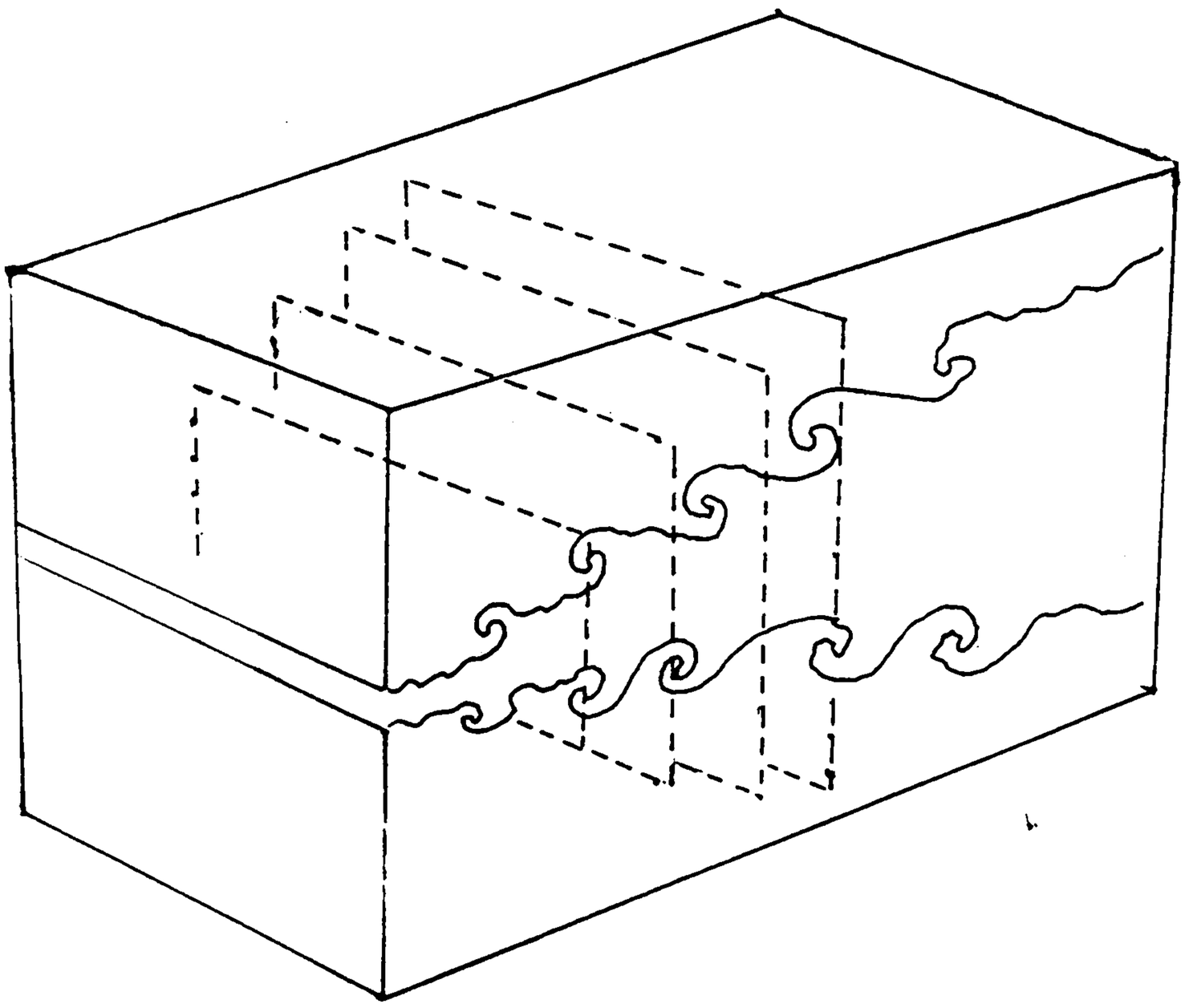

Fig. 4.4 Sampling planes.

necessary to compress binary data because it is already written in very compact form. The size of the databases accumulated is 4.3 Gigabytes. Special data retrievel procedures are required to avoid the need of constant file transfers to and from the C480 magnetic tape library.

A fraction of the databases are then selected and merged to create a long 'ribbon' of spatial-temporal (z-t) data on a single disk file. The data field has the 32 points in the z-direction and temporal length of 20,000 time steps.

4.7 Template Patterns

There are four categories of template patterns:

(1) Eddy stream function model based on experimental

observations of the double-velocity correlations.

(2) Simple step function or Gaussian function.

(3) Experimentally or numerically generated template patterns from the selection of individual flow samples which contain eddy patterns. But it requires a fair amount of time looking at the flow data and selecting the frames of patterns which may be a representative and repetitive structure.

(4) Conditional sampled flow fields.

The selection of the template patterns very much depends upon the nature of the flow and the availability of the flow data (which is often the major restriction in the experimental studies). In the numerical simulation, flow variables such as velocity, pressure, shear stress or vorticity fluctuation fields can be used as template patterns.

Although we could use the pressure pattern alone as flow detection diagnosis in the jet, the low pressure region is a necessary but not sufficient condition for the presence of a double-roller eddy. The lateral flapping motions or any fast speed fluids of the jet can also produce low pressure fluctuations. In theory, a Gaussian distribution of a pressure fluctuation pattern can be used to detect the cores of the vortices. However, such investigation had not been carried because the focus of our project was PRA.

In the present study, a two-dimensional, *velocity vector template* is used in the matching:

$$\mathbf{T} = \{ U_t, W_t \},$$

which is similar to the scalar velocity template used by Mumford (1982,1983) and Ferré *et al* (1986, 1989,1990).

The 3-D template approach of Stretch, Britter and Kim (1990)

in a numerically simulated channel flow is not necessarily superior than the 2-D template matching technique (Savill, Klein and Friedrich (1993)). It is computationally more expensive and the use of very crude 3-D template pattern would produce very low cross-correlation in the matching. Besides, the use of a 3-D roller model template seems unpractical, as the roller structures are inclined, and there are variations in size, shape and orientation of the eddy structures. However, the cost problem of 3-D template matching is surmountable; the speed of computations of the cross-correlation (with a very large 3-D template) can be substantially improved by the Fast Fourier Transform method. The present 2-D template approach appears to be more attractive, which is equally capable of educing 3-D structures. The advantages of the 2-D approach are also discussed by Savill, Klein and Friedrich (1993).

4.8 Model of the Double-Roller Eddy

Townsend(1979) described the model eddy as a pair of inclined, counter-rotating roller eddies. His model was based on the results of extensive correlation measurements and correlation fitting method. By assuming the stream function to be a Gaussian function with parameters a_x, a_y, a_z and a_{xy}, the velocity fields can be written as:

$$u = -(1 - a_z^2 z) \exp -\frac{1}{2}(a_x^2 x^2 + a_y^2 y^2 + a_z^2 z^2 + 2 a_{xy} xy)$$

$$w = -z \left((a_x^2 + \beta a_{xy})x + (\beta a_y^2 + a_{xy})y\right)$$

$$\times \quad \exp -\frac{1}{2}(a_x^2 x^2 + a_y^2 y^2 + a_z^2 z^2 + 2 a_{xy} xy)$$

$$v = \beta u$$

The parameters can be determined by the correlation function fitting method (Townsend 1979) by cyclic variation of the parameters to optimise the fitting coefficient or to give the best fit. But it is not possible to determine all the

parameters because of the experimental limitations.

The equations for the double-roller eddy model in the x-z plane can be simplified by putting $\beta = a_y = a_{xy} = 0$:

$$f(x,z,S) = e^{-1/2\, S^2(a^2x^2 + z^2)}$$

where a is the aspect ratio of the pattern,
S is the scaling factor.

Stream function:

$$\Psi_s(x,z,S) = - z\, f(x,z,S)$$

Velocity:

$$u(x,z,S) = (S^2z^2 - 1)\, f(x,z,S)$$

$$w(x,z,S) = - S^2a^2x\, z\, f(x,z,S)$$

Vorticity:

$$\omega_y(x,z,S) = -z\, ((S^2a^2x)^2 + (S^2z)^2 - S^2(a^2 + 3))f(x,z,S)$$

The velocity and vorticity patterns are shown in figure 4.5.

4.9 Box-eddy Patterns

The *box-eddy pattern* is a very crude representation of the velocity field of a double-roller eddy. It is used as the template in order to test the sensitivity of the results to the choice of template. For example, the two components of velocity fields can be defined in the 12X24 template:

$$\text{If } k \in [3,22],\quad U_t(i,k) = \begin{cases} 1 & i \in [2,4] \\ -1 & i \in [5,8] \\ 1 & i \in [9,11] \end{cases}$$

$$\text{Otherwise,}\quad U_t(i,k) = 0.$$

$$\text{If } k \in [3,12],\quad W_t(i,k) = \begin{cases} -1 & i \in [2,6] \\ 1 & i \in [7,11] \end{cases}$$

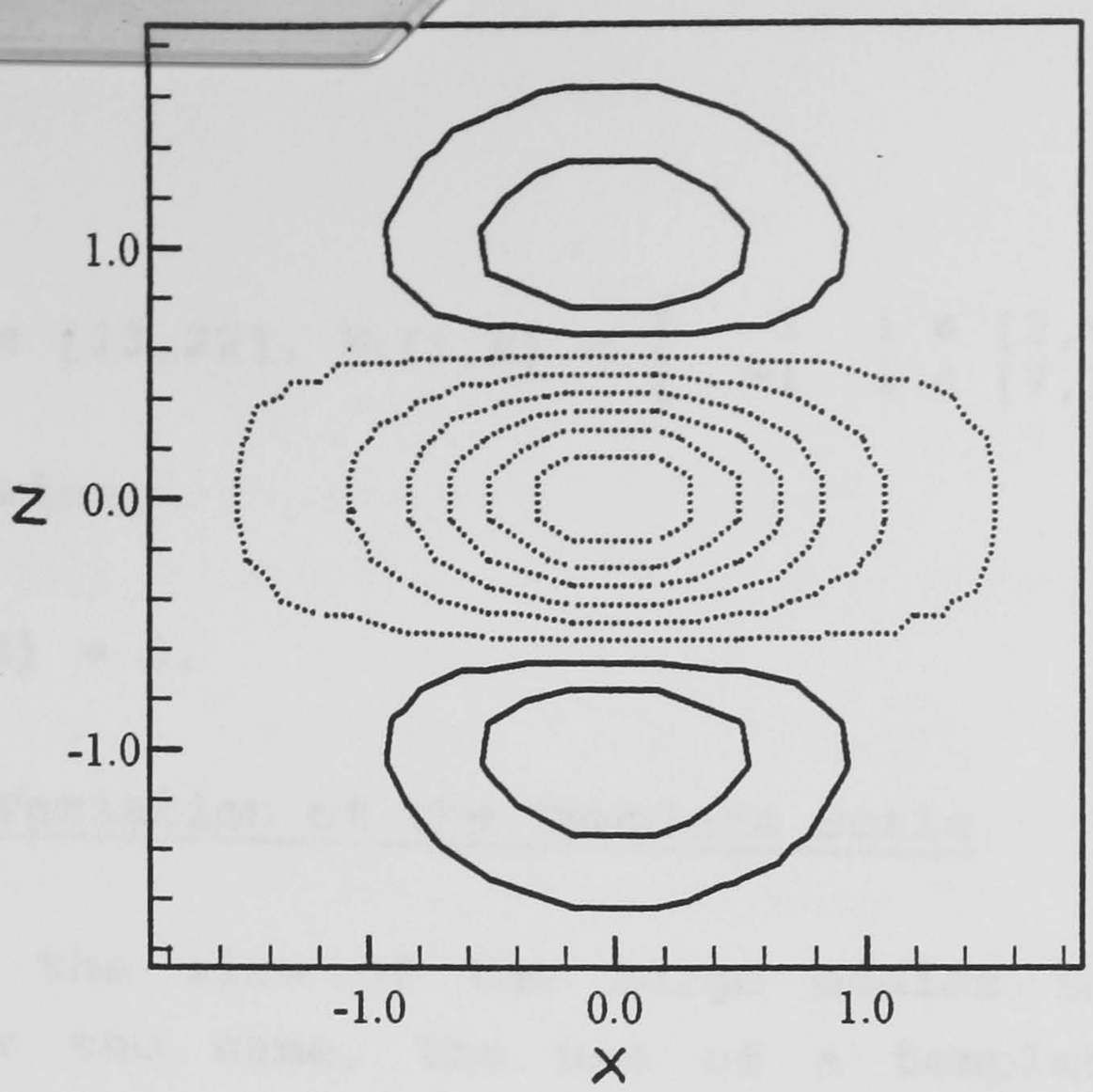

Fig.4.5(a) U-velocity pattern.

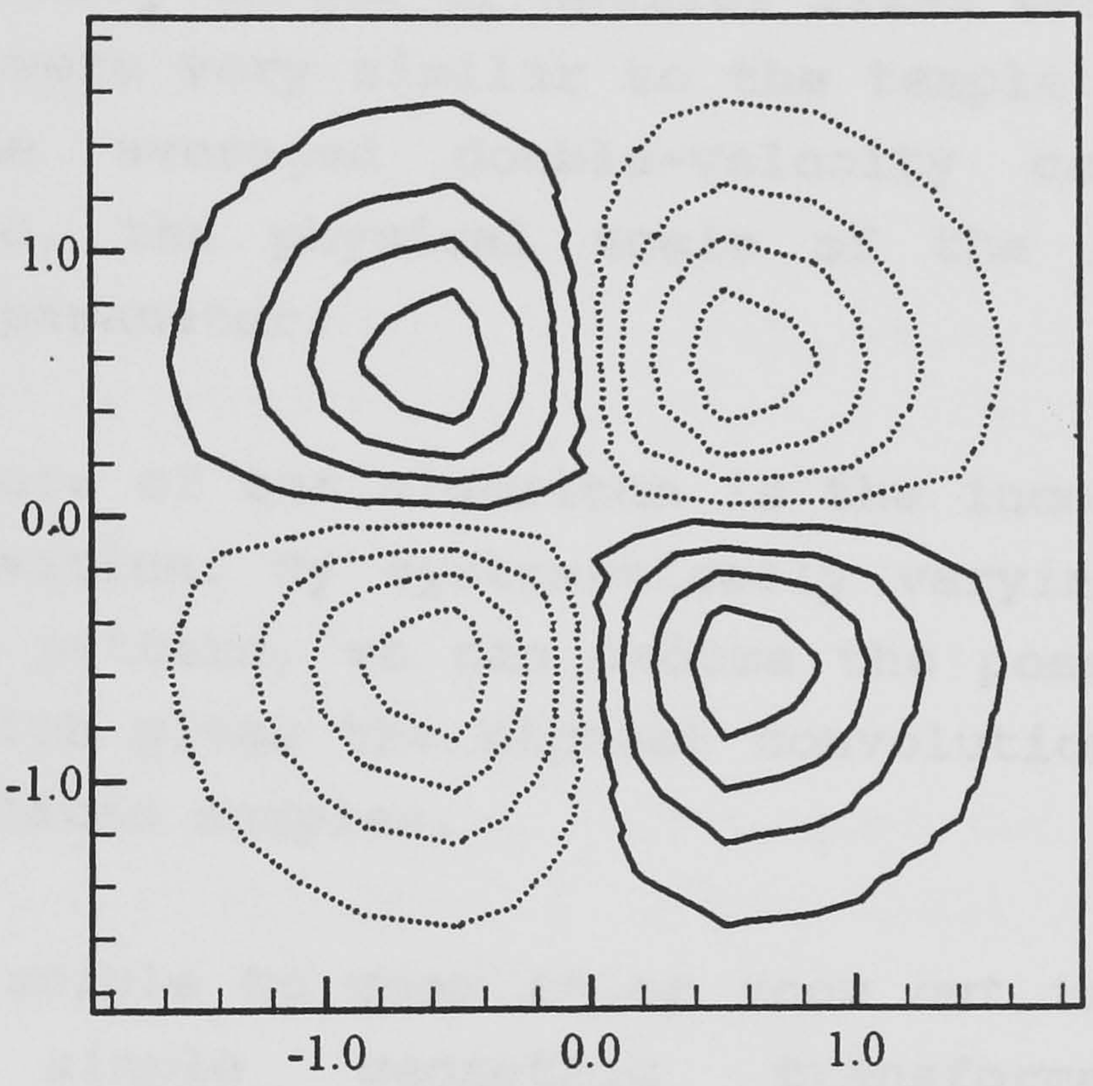

Fig.4.5(b) W-velocity pattern.

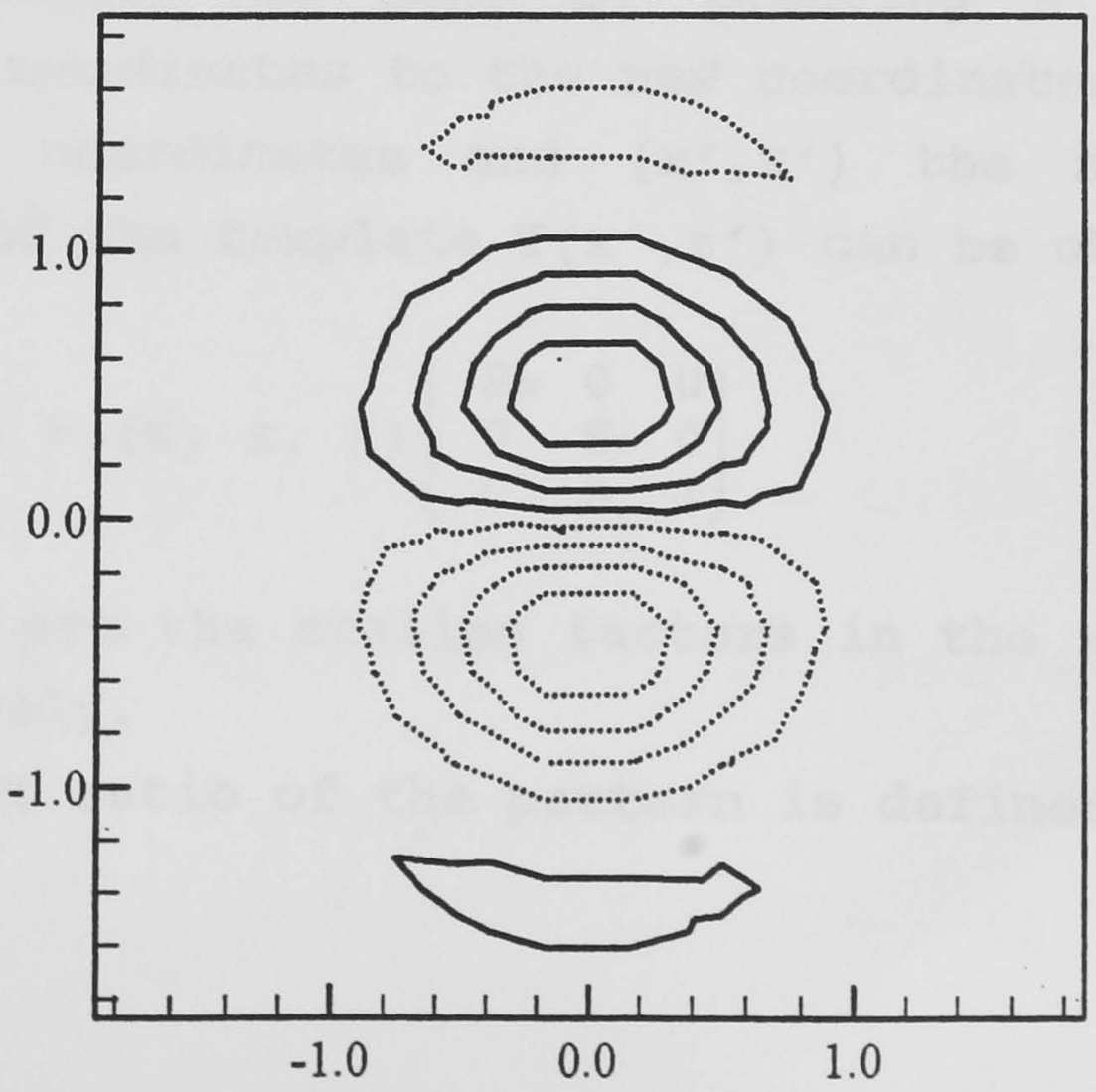

Fig.4.5(c) Vorticity pattern.

If $k \in [13,22]$, $Wt(i,k) = \begin{cases} 1 & i \in [2,6] \\ -1 & i \in [7,11 \end{cases}$

Otherwise,

$Wt(i,k) = 0.$

4.10 Variation of the Template Scale

Since the size of the large eddies in turbulence is not always the same, the use of a template pattern of fixed scale would mean that those organised eddies of substantially larger or smaller sizes were decorrelated even if they were very similar to the template. Moreover, unless the time averaged double-velocity correlation data is available, the physical scale of the large eddies is an unknown parameter.

One feature of our algorithm is the incorporation of a zoom transformation. By systematically varying the scale of the template pattern, we can deduce the possible range of eddy sizes which gives the highest convolution or largest number of correlated samples.

It is possible to *zoom in* or *zoom out* the template pattern by a simple geometric transformation. The zoom transformation is done by creating a mapping from the pattern coordinates to the new coordinates. Let (x,z) be the original coordinates and (x′,z′) the new coordinates. A mapping of the template T(x′,z′) can be obtained by:

$$(x,\ z',1) = (x,\ z,\ 1)\begin{pmatrix} S_x & 0 & 0 \\ 0 & S_z & 0 \\ 0 & 0 & 1 \end{pmatrix}$$

S_x and S_z are the scaling factors in the x and z coordinates respectively.

The aspect ratio of the pattern is defined as:

$$AR = \frac{S_z}{S_x}$$

which is usually set to 0.5 or 1.
The range of scaling ratio used is between 1/8 and 8.

Strictly speaking, the present algorithm is not scale-invariant. The scale of the template pattern remains unchanged throughout the matching for a given dataset. Then the matching is repeated with various values of scaling parameters.

4.11 The Algorithm

Note that the iteration (no.6) is optional and not necessarily essential for the algorithm (this will be discussed in chapter 6.6).

First Stage

1. Initialise the template, threshold and event duration limit. Define **T** to be the normalised template, ψ and Λ to be the threshold and event duration limit respectively. We can either have a scalar template:

$$\mathbf{T} = \{u_T(k, l, s)\}$$

or a vector template:

$$\mathbf{T} = \{u_T(k, l, s), w_T(k, l, s)\}$$

for $k \in [1, M_1]$, $l \in [1, M_2]$ and $s \in [\xi_{min}, \xi_{max}]$.

2. Shift the template **T** over the search area **G**, where

$$\mathbf{G} = \{u'(k, t)\}$$

or

$$\mathbf{G} = \{u'(k, t), w'(k, t)\}$$

for $t \in [1, N_1]$ and $k \in [1, N_2]$.

Compute the normalised cross-correlation $C(m,n,s)$ at every shift position (m,n) for $n \in [1, N_1 - M_1 + 1]$ and $m \in [1, M_2 - N_2 + 1]$.

3. Determine the *translational* (spanwise) shift position m where the maximum or minimum cross-correlation is attained, obtaining the local spanwise maximum and minimum correlation for every temporal location n:

$$C_{max}(n,s) = \max(C(m,n,s))$$
$$C_{min}(n,s) = \min(C(m,n,s))$$

4. Test

If the temporal length of the event exceeds Λ and

$$C_{max}(n,s) \geq \Psi \text{ then } C_{max}^{*}(s) = C_{max}(n,s)$$
$$n = n_{max}^{*}(s), \quad m = m_{max}^{*}(s).$$

OR

$$C_{min}(n,s) \leq -\Psi \text{ then } C_{min}^{*}(s) = C_{min}(n,s)$$
$$n = n_{min}^{*}(s), \quad m = m_{min}^{*}(s).$$

$C_{max}^{*}(s)$ and $C_{min}^{*}(s)$ are the local temporal maxima and minima of $C_{max}(n,s)$ and $C_{min}(n,s)$ respectively.

Store the pointers: $n_{max}^{*}(s)$, $m_{max}^{*}(s)$, $n_{min}^{*}(s)$ and $n_{min}^{*}(s)$.
If temporal length < Λ, go to 2; carry on matching.

5. Normalise and add the best matched pattern G^{*} into the working ensemble average $\mathbf{E}_{xz} = \langle E(s) \rangle_{xz}$ where

$$\mathbf{E}_{xz} = \langle u' \rangle_{xz}, \langle v' \rangle_{xz}, \langle w' \rangle_{xz} \text{ and } \langle p' \rangle_{xz}.$$

The working ensemble averages are updated, whenever a new sample has been detected. The weighting factors of all the samples are equal. In the pattern recognition code, the

working averages are computed as in the following:

$$\langle E(s)\rangle_{xz}^{Nmax} = \frac{\langle E(s)\rangle_{xz}^{Nmax-1}\,(N_{max}-1) + G_{max}(s)^{*}}{N_{max}}$$

$$\langle E(s)\rangle_{xz}^{Nmin} = \frac{\langle E(s)\rangle_{xz}^{Nmin-1}\,(N_{min}-1) + G_{min}(s)^{*}}{N_{min}}$$

N_{max}: current number of positively correlated samples.
N_{min}: current number of negatively correlated samples.
$G^{*}_{max}(s)$: current best matched pattern with positive correlation.
$G^{*}_{min}(s)$: current best matched pattern with negative correlation.
$G^{*}_{max}(s)$ and $G^{*}_{min}(s)$ are normalised by their intensities.

In other words, the ensemble average is equal to the sum of all the best matched patterns divided by the total number of samples.

Note that the ensemble average is a function of the zoom transformation factor s. The patterns of different scales should not be added together.

6.(OPTIONAL)
If iteration is required, rewind the data **G** and replace the old template **T** by the final ensemble average **E**.

Repeat the whole matching process as (1~5), and test convergence of **E**.

Iterate until the ensemble average remains unchanged.
The convergence is tested by:

$$\delta^{\tau}=\sum_{t=1}^{M1}\sum_{k=1}^{M2}\left(\ E_{kt}^{\tau}\ -\ T_{kt}^{\tau}\ \right)^2=\sum_{t=1}^{M1}\sum_{k=1}^{M2}\left(\ E_{kt}^{\tau}-E_{kt}^{\tau-1}\ \right)^2$$

where τ is the number of iteration.

$E_{kt}^{\tau}, T_{kt}^{\tau}$ denote the ensemble average and the template pattern respectively at iteration step τ.

This equation represents the change δ^{τ} in the ensemble average, with respect to the template pattern after every iteration.

If δ^{τ} is decreasing with τ, the ensemble average is converging.
If δ^{τ} is increasing with τ, the ensemble average is diverging from the original template pattern.

2nd Stage

Read the stored pointers $n_{max}^{*}(s)$, $m_{max}^{*}(s)$, $n_{min}^{*}(s)$ and $m_{min}^{*}(s)$ from the disk.

Read the (y,z,t)-database **D** = {u'(j,k,t), v'(j,k,t), w'(j,k,t), p'(j,k,t)}, where **G** ⊂ **D**.

Locate the patterns perpendicular to the plane of the corresponding best-matched pattern $\mathbf{G}^{*}$.

Form the ensemble average: $\mathbf{E}_{yz} = \langle \mathbf{E} \rangle_{yz}$ and $\mathbf{E}_{yz} = \langle \mathbf{E} \rangle_{yz}$ at the centre of $\mathbf{G}^{*}$ on the (y,z) and (x,z) planes respectively,

$\mathbf{E}_{yz} = \{\langle u' \rangle_{yz}, \langle v' \rangle_{yz}, \langle w' \rangle_{yz}, \langle p' \rangle_{yz}\}$

$\mathbf{E}_{xy} = \{\langle u' \rangle_{xy}, \langle v' \rangle_{xy}, \langle w' \rangle_{xy}, \langle p' \rangle_{xy}\}$.

CHAPTER FIVE
RESULTS AND DISCUSSIONS (PART I)

5.1 Results of the Simulations

The simulation is nearly full as the resolution of the meshes is not high enough to reproduce all the small scale turbulence at high wavenumbers, but the subgrid eddy viscosity ν_e is small. In spite of this, the principal advantage of nearly full simulation relative to direct simulation is the much lower computational cost. The subgrid scale model used in the simulation is the Smagorinsky model (1963). Athough the split model by Schumann (1975) was also tested, it appears that the present simulation is not sensitive to the choice of the models. The subgrid model only acts as a sink or energy drain, to model the effects of dissipation by the unresolved eddies. It has been observed that the volume-averaged turbulent kinetic energy increases more rapidly when the subgrid model is switched off. Although the role of the subgrid model in the nearly full simulation is not as important as in the case of the large eddy simulation, it dissipates the energy at high wave numbers and hence maintains stability of the simulation.

The simulation was started with pseudo-random numbers as initial disturbances, the random numbers being injected into the three velocity components at the inflow plane at every time step. Andrade (1939) found that the critical Reynolds number of a plane jet was about 33. In theory the jet should go turbulent by itself without the need of any initial disturbance, if the Reynolds number is above the critical value. But in practice, it takes very long running time and high computational costs to achieve this without random disturbances. It is because the only source of disturbances for triggering turbulence in the simulation are extremely small numerical noises.

The simulations had been run for 17,000 time steps (δt = 0.0001, in non-dimensional time unit) with random numbers

switched on. Since the turbulence then became self-sustaining, the random disturbance was turned off thereafter. The simulation was dumped and restarted every 500 time steps; the vital data such as the instantaneous flow variables (velocity, pressure) simulation specifications (for example, time step, mesh, coordinate information), space-time averages were stored on disk files, the size of each dump file was 18 Mwords. This is essential, since we need to check the statistics and monitor the levels of the Courant number and viscous stability number on a regular basis. The time step is adjusted if necessary to keep these numbers within the limits.

No entrainment inflow boundary condition was imposed during the initial phase of the simulation. The y-wall boundary condition was stress free with v = 0 at the boundaries, because the jet had not become fully turbulent and the rate of entrainment was small. After 40,000 time steps, genuine turbulence started to develop and the volume-averaged turbulence kinetic energy was oscillating about a mean value of 0.886, the Courant number and viscous stability number were about 0.057 and 0.0013 respectively. In order to avoid numerical instablities in the early stage of the simulation, the time step used was extremely conservative. δt was changed from 0.0001 to 0.0008 after 17,000 time steps. It was also changed to larger value (δt=0.0032) during the database acquisition.

It is useful to define a measure of the lifetime of large eddies in the jet. The Large Eddy Turn-Over Time (LETOT) is fairly well-defined in a wall-bounded shear flow. In the boundary layer, it is roughly equal to the boundary layer thickness divided by the wall-friction velocity. In the free jet, the eddy turn over time T_{eddy} can be defined as

$$T_{eddy} \approx \frac{l(s)}{U_m(s)}$$

where l(s) is the half width, and $U_m(s)$ is the centreline velocity at streamwise position s. According to the

definition, the eddy turn over time increases with streamwise distance and should be roughly proportional to $x^{3/2}$ (However this is not always true considering the fact that the size of the large eddy structures does not necessarily scale with the half width of the jet in the fully developed far field). An estimate is given by

$$T_{eddy} \approx 0.594 \text{ (non-dimensional time unit)}.$$

The total number of time steps for the entire simulation including the computation of time-averaged statistics and database aquisition was 56,000, which was roughly 138 eddy lifetimes.

Before the entrainment inflow boundary condition was set, strong recirculating flows appeared in the far downstream region; flow reversals had been observed at the corners of the computational box near the outflow plane. These might be associated with the adverse pressure gradient $\partial P/\partial x$ near the outlet, which was caused by the old stress-free boundary condition that no external fluid was allowed to entrain laterally from the y-boundaries.

As soon as the jet had become fully turbulent, the new entrainment boundary condition was switched on, the amount of entrainment mass flux being increased progressively. As we have discussed before, the source code is designed in such a way that the mean outflow velocity is automatically scaled to ensure the global conservation of mass flux. The recirculating flows diminished considerably but still existed even after a long running time. Nevertheless, they were confined to small regions very near the outflow plane and had negligible effect on the behaviour of the jet upstream.

The theoretical estimation of the ratio Q_{total}/Q_o is 2.013, but the entrainment coefficient from the experimental measurement (section 3.6) was not actually used in the simulation. The total entrainment mass flux was adjusted by

varying the magnitude of the entrainment velocity in an attempt to minimise the adverse pressure gradient previously existing at the outflow plane. This was a time-consuming procedure, since every time the total entraining mass flux was changed, it created discontinuous and transient pressure shocks in the simulations which took a considerable time to smooth out. As a result, the simulation required much longer time to settle down than it ought to take. It had been found that the adverse pressure gradient and recirculating flows were weak when Q_{total}/Q_o was set equal to 2.73.

5.2 Time-Averaged Statistics

The statistics were gathered from time step 38,000 to 48,000 at the rate of every 10 time steps (1,000 samples of data fields were averaged). There is some evidence to suggest that the angle of spread of the jet is a slowly growing linear function of distance along the streamwise direction. Figure (5.1) shows the half width l/d of the mean velocity profile as a function of the streamwise distance. The fitting of the data is given by l = 0.1977 x. The rate of spread obtained by Bradbury(1965) based on the experimental measurement was 0.109, at the Reynolds number of 30,000. Note that the width of the jet is almost constant for x less than ten diameters. The scattering of data points in figure (5.1) may be due to inadequate averaging time of the statistics and the flapping motions (the wave-like lateral motions of the instantaneous velocity profiles) associated with the anti-symmetric vortex street. Such flapping behavior was also observed in the simulation.

Figure 5.2 shows the U-velocity profiles from the simulation (at x/d = 23.6) and an empirical fit to Bradbury's experimental results measured between 13.9~68.5 diameters. The property of partial self-preservation is exhibited.

The distribution of static pressure coefficient across the jet at various streamwise positions (x/d = 10.3, 13.2 and 15.6) is shown in figure 5.3. The static pressure

coefficient is defined as:

$$C_p = (\bar{p} - \bar{p}_o)/ (1/2\ U_m^2)$$

where $\bar{p}_o$ is the stagnation pressure and U_m^2 is the centreline velocity. No self-preservation is observed in the curves, but it is possible that partial self-preservation will be attained further downstream. The numerical prediction is close to experimental results by Miller and Comings (1957) as shown in figure 5.4. The gradual transition of the static pressure with streamwise distance is apparent. A negative relative pressure field appears throughout the turbulent region of the jet.

The isometric plot of the mean streamwise velocity is shown in figure 5.5. Note that the small ripples of the isometric surface are due to the short time averaging.

Figure 5.6 show an isometric plot of the contour plot of the subgrid eddy viscosity ν_e/ν_m x100%. The eddy viscosity of the subgrid model is normalised by the molecular viscosity ν_m and is defined as:

$$\nu_e = (C_e\ \Delta)^2\ (S_{ij}\ S_{ij})^{1/2}$$

where c_e is constant and

$$\Delta = (dx\ dy\ dz)^{1/3}.$$

c_e is given by the equation (Smagorinsky 1963, Lilly 1967):

$$c_e = (\frac{2}{3}\ \alpha)^{3/2}/\ \pi^2\ (= 0.1 \sim 0.2)$$

where α is the Kolmogorov constant ($\simeq$1.5).

The subgrid eddy viscosity depends on the mesh size and the local strain rate, but it is interesting to see how it

varies in the flow. It should not be confused with the eddy viscosity of the Reynold stress and velocity gradient. The subgrid eddy viscosity is generally very small compared with the molecular viscosity except in those regions where the local strain rate is high, its maximum value being approximately equal to 1 or 2 % of the molecular viscosity. This suggests that the simulation is nearly full.

The logarithmic decay curve for squared velocity at the centerplane is plotted in figure 5.7, the horizontal portion of the curve corresponding to the laminar core and transition region of the jet ($x/d < 10$) where the velocity is nearly constant. The jet becomes fully turbulent at $x/d > 10$, the linear portion of the curve having a slope of -1.05, which is very close to the theoretical value of -1. Hence we can deduce the exponents of the decay function from the slope of the curve

$$\frac{U_m}{U_o} \propto \left(\frac{x + x_o}{d}\right)^{-1/2}.$$

U_o is the inlet velocity of the jet; x_o is the virtual origin which is approximately equal to 2.5 ~ 5 jet diameters.

Note that the fit is poorer in the extreme downstream region where the flow is affected by both outflow and the y-wall boundary conditions. As the jet spreads out in the downstream region, the interaction between the y-wall boundary and the jet becomes strong; recall that the entrainment velocity V_∞ is set proportional to $x^{-1/2}$, as x is large (i.e.near the outflow region), V_∞ tends to be zero. The y-wall boundary would in turn behaves more like an impermeable wall in the downstream region. Another source of error may be the particular way of implementating the advective boundary condition. As we have discussed in the previous section, the local convection velocity (referring to the outflow boundary condition) is assumed to be constant and equal to the mean velocity averaged over the outflow plane, but in fact the streamwise velocity of jet at the

centre is much higher than that at the edges. Nevertheless, the agreement with the experimental results is reasonable at streamwise distance less than 40 jet diameters.

The profiles of the turbulence intensities $\overline{u'^2}/ U_m^2$, $\overline{v'^2}/ U_m^2$ and $\overline{w'^2}/ U_m^2$ at x/d = 17.5 are shown in figure 5.8. The overall shape and magnitude of the curves are in good agreement with experimental measurements. Figure 5.9 shows the comparison of the $\overline{u'^2} / U_m^2$ (at x/d = 21.7) with the empirical fit of the experiment at $22 \leq x/d \leq 70$. The profiles of the Reynolds shear stress $\overline{u'v'}/U_m^2$ from the experiment and the simulation are shown in figure 5.10. The agreement between the numerical and the experimental results is reasonable. The maximum magnitude of the Reynolds shear stress from the simulation is about 0.022~0.027, while the experimental value is 0.025.

CHAPTER SIX

RESULTS AND DISCUSSIONS (PART II)

6.1 Noise Test

In order to test the sensitivity of the correlation to noise and the ability of the programme to extract an organised eddy pattern buried in disorganised motions, a noise test with randomly generated signals has been performed. An eddy pattern in a random position is superimposed on a data field which consists of a two-dimensional sinusoidal wave pattern with amplitude modulated by a random number generator :

$$h(x,z) = \zeta\ R(-1,1)\ \sin(\frac{2\pi x}{\lambda x})\ \cos(\frac{2\pi z}{\lambda z})$$

where ζ is the noise to signal amplitude ratio, and R(-1,1) are the random numbers between -1 and +1.

The wavelengths λx, λz are set equal to 1/2L and 1/4L respectively, where L is the length of the eddy pattern. By varying the noise-to-signal ratio (ζ = 0.5, 1, 2), we can determine the effects of the noise as shown in figure 6.1(a),(b) and (c). The programme is capable of extracting the eddy pattern even from high noise-to-signal data. The correlation coefficient decreases slowly with increasing noise amplitude. In figure 6.1(b), the eddy pattern is barely visible in the iso-contour plot with noise-to-signal amplitudes ratio of 2.0, but we can still observe a characteristic peak in the correlation curve. We conclude that the cross-correlation method is not very sensitive to the level of background noise.

6.2 Template Updating

There are two approaches in the updating of the template and both of them have been tested:

a) The template pattern remains unchanged throughout the whole matching whereas iteration is optional. It will be updated only if iteration is required; the original template pattern is replaced by the final ensemble average for the successive iterations, with the database being scanned again. This approach has proved reliable and stable, hence it is used in the present algorithm. It should be noted that the iteration procedure does not significantly improve the averages as indicated by some tests, and hence it is not used in the present study.

b) The template is constantly updated by setting it equal to the current working ensemble average during the matching. The template is said to be adaptive because it is changed according to the current best-matched sample. This method is different from method (a) in the sense that the final average may significantly deviate from the original template. Moreover it seems to be less stable, since the template can be susceptible to corruption or contamination by noisy samples when it is applied to an unconditionally sampled database. Several tests were performed with the simulation data. The results (not shown here) showed that the final ensemble averages did not converge to the expected pattern. A suggestive alternative is that each individual sample can be weighted by its corresponding peak cross-correlation coefficient in the ensemble averaging. This will put less weighting on the noisy, poorly correlated samples. However, this approach has not been fully tested. A successful application of this approach has been reported by Voke (1992) in the affine matching pattern recognition analysis combined with a conditional sampling method. One possible reason why it works well in his study is that the affine matching is performed with a subset of conditional sampled flow data which are more organised and less noisy than the raw data fields.

It should be noted that approach (b) was abandoned in favour of approach (a). Most of the results presented in this thesis are obtained from the velocity vector template

patterns of section 4.8 and 4.9, without updating and iterating the template. The iterated results are not shown here because of their close resemblance to the non-iterative averages.

6.3 Results of Pattern Recognition Analysis

The characteristics of the spanwise maximum convolution against time coordinate give us some insight into the degree of flow organisation. We shall examine the variation of the convolution function particularly with the zoom factors and various types of templates.

Figure 6.2 shows a typical example of the spanwise maximum and minimum cross-correlation curves; the horizontal axis is the temporal coordinate. The result is obtained with a streamwise velocity pattern $T = \langle u \rangle_{xz}$ as the template. The values of the spatial-temporal maxima and minima reach as high as ±0.75 indicating quite good matches. As the temporal resolution of the databases is higher than required, the data are sampled at the rate of every 5 time steps in the template matching, so the total time for the curves in figure 6.2 is 10,000 time steps ($t = 32$). Some events have durations as long as 500~600 time steps ($t \simeq 1.6$). Note that the peaks of the positive correlation and the valleys of the negative correlation are often in phase but of different magnitudes*.

It has been observed that if the threshold criterion is too strict, the number of samples educed would be small and the resulting ensemble averages appear to be less representative. On the contrary, if the criterion is over-relaxed, the structural features may be too smeared to reveal any useful information. The most sensible threshold value is found to be between 0.3 ~0.4.

---

* This observation is related to the transverse (spanwise) alignment of the data frames with the template. As the streamwise velocity pattern of a vortex eddy consists of a central neagtive lobe with two positive lobes on both sides, when the positively correlated pattern is exactly aligned with the template, it will give a local maximum. On the other hand, when the same eddy pattern is offset from the exact alignment, template will partially and negatively correlate with the pattern, and will contribute to a local minimum.

The scale of the organised eddies in the flow is an unknown parameter. The most probable range of scales has been found by varying the zoom factors of the template systematically. Figure 6.3 demonstrates the optimisation of correlations by zoom transformations. In this case, the specific zoom factors are 1/2, 1/3, 1/4 and 1/5. The template is poorly correlated with the flow patterns when the zoom factor is too small (C_{max} ~ 0.25 for zoom factor = 1/5). As the pattern is expanded to larger scales, the correlation increases substantially to a peak value of about ±0.7 at zoom factor equal to 0.5. Therefore, the correlation is highly sensitive to the scale of the template pattern relative to the turbulent flow structures and we are able to deduce the most probable scales of the eddies which produce optimum correlation.

One may pose the question: "Could these correlation curves be solely contributed by some random turbulent flow structures which happen by chance to be correlated?". The answer is that if the turbulent flow data generated by the simulations were truly random, the overall correlation would be very low (of the order of ~ 0.1) and the events would last very short times. Suppose we use a template which is comprised of random numbers and it is matched against the data. The result is shown in the bottom curve of figure 6.4. As we expected the mean peak correlation is less than 0.1 and the curve consists of small ripples. The result with a step function template is compared in figure 6.4; the peak values are between 0.65 up to 0.85.

The finer scale structure of turbulence tends to be more disorganised and has a shorter time scale, while the largest eddies have sizes the order of the shear flow width L and time scale of T ~ L / U_c, where U_c is the convection velocity. When the template pattern is zoomed to smaller scales, the correlation becomes lower and fluctuates at higher frequencies.** In figure 6.5, two correlation curves are obtained with zoom factors of 1 and 1/4 respectively.

The ensemble averaged streamwise velocity of the single vortex at y/l = 0.3, x/d = 18 is shown in figure 6.6(a). The template used is a 12x28 pattern for a single eddy model. An extra negative velocity field is produced on one side of the average; the average may be contributed by a mixture of single and paired structures. The ensemble averaged velocity patterns of the paired eddies of various sizes are shown in figure 6.6(b), 6.6(c) and 6.6(d) with a 18x48 template (zoom factors are 1, 1.5 and 0.5 respectively). They are topologically very similar structures but of different sizes.

If a vorticity (ω_y) pattern for a paired eddy is used as a template, the results are shown in figure 6.7 and 6.8. The educed averages contain a pair of concentrated vorticity lobes of opposite sign. The matching is then repeated with the streamwise velocity pattern as template. The curves of the vorticity and velocity correlation coefficients are compared in figure 6.8, the dots indicating that the peak vorticity and velocity correlations are both in phase; these structures exhibit correlated vorticity as well as velocity.

** Note that the template behaves more like a high-pass filter with decreasing values of zoom factors.

6.4 Pattern Eduction of Three Components of Velocity and Pressure Fields in the (x,z) and (x,y) Planes

In order to examine the three-dimensional topology of the structures, the extracted velocity and pressure fields in the (x,z) and (x,y) planes are compared. The averages in the (x,y) plane are formed by adding those surrounding data fields at the centre of the (x,z) patterns with spatial and temporal coordinates located by the pointers. Therefore, the averages in the (x,z) and (x,y) planes are not independent pattern-recognition averages. The pattern recognition analyses have been performed in various y-positions including the centreplane and the planes of maximum Reynolds shear stress (y/l = 0, 0.3, 0.67 and -0.67 at x/d = 18). A 12x24 template is matched against the velocity vector fields in the (x,z) planes. The zoom factor of the template is 0.8 corresponding to the optimum mean peak correlation (note that the zoom factor is defined as 1 for an arbitary reference scale).

In the present study, the temporal scale of all ensemble averages in the (t,z) plane is converted into a spatial scale by Taylor's frozen turbulence hypothesis, which can be expressed as :

$$\partial f/\partial t = - \bar{U}(y)\ \partial f/\partial x$$

$\bar{U}_{(y)}$ is the *local* mean convection velocity which is a function of y. Since conversion of time scale to x-scale is based on the local convection velocity, the (x,z) averages obtained at different values of y have different scales in the streamwise direction.

The temporal scale of the (t,y) averages is converted to spatial scale with the mean centreplane velocity:

$$\partial f/\partial t = - \bar{U}_c\ \partial f/\partial x.$$

It should be emphasized that the ensemble averages are authentic and not weighted by the initial template in the averaging; the template patterns are not included in the sums of the samples.

The ensemble averages can be divided into two classes: (a) the averages of the detection fields (velocity vector (u,w) fields in (x,z) plane), (b) the averages of the associated fields (all other averages in the (x,z) and (x,y) planes except those of the detection fields in (x,z) plane). The ensemble of realisations are also decomposed into positively and negatively correlated fields together with their associated fields. The ensemble averages of the associated fields are important, because they ascertain the consistency of the pre-assumed template in three-dimensions and reveal unknown features connected with the known detection features.

6.5 Details of the Educed Patterns

Six sets of results are presented in figure 6.9(a-g), 6.10(a-i), 6.11(a-h) and 6.12(a-h) for positively correlated patterns at y = 0, 0.767, 1.68 and -1.68 respectively; figure 6.13(a-h) 6.14(a-h) for negatively correlated patterns at y = 0.767 and 1.68 respectively.

The velocity and pressure averages in the (x,z) planes are denoted as $\langle u \rangle_{xz}$, $\langle v \rangle_{xz}$, $\langle w \rangle_{xz}$ and $\langle p \rangle_{xz}$. These corresponding patterns in the (x,y) planes are $\langle u \rangle_{xy}$, $\langle v \rangle_{xy}$, $\langle w \rangle_{xy}$ and $\langle p \rangle_{xy}$. The vector plots of the velocities $(\langle u \rangle_{xz}, \langle w \rangle_{xz})$ and $(\langle u \rangle_{xy}, \langle v \rangle_{xy})$ are also presented. The velocity vector diagram of each flow pattern can be visualized as the spatial structure of the coherent motion observed from a moving frame at the convection speed. The solid contours represent negative values; the dotted contours are positive. The direction of the mean flow is from the left to right for all the following plots. The line AA' represents the line of interception between the spanwise and transverse planes.

The averages show the cross-sections of the paired vortical structures at different y-values. The ensemble averages $\langle u \rangle_{xz}$, $\langle w \rangle_{xz}$ and the velocity vector plots in the (x,z) planes (e.g. fig. 6.9(a),(b),(c); 6.10(a),(b),(i)) display very obvious patterns of a counter-rotating vortical structure located in a low pressure region (fig 6.10(c),(g); 6.11(c),(g); fig 6.12(d); 6.13(g); 6.14(d)). The $\langle v \rangle_{xz}$ patterns (6.9(d), 6.10(d), 6.11(d), 6.12(c), 6.13(c) and 6.14(c)) show the velocity component pointing towards and away from the reader.

The flow patterns in the transverse or (x,y) plane show the ensemble averaged motions across the central cross-section of the eddy structures. Sometimes the patterns becomes noisy, as the ensemble averages are formed from a finite number of unfiltered, individual realisations. The total number of samples averaged is varied between 60 and 90 for either positively or negatively correlated patterns.

The results can be understood when viewed in the light of the three-dimensional averaged eddy structures. The scale of the large eddies is observed to be comparable to the width of the jet. Their temporal length in the streamwise direction has the same order as the spanwise length divided by the mean convection velocity. The three dimensionality of the structures is also characterised by the velocity fluctuations u', v', and w', which have the same order of magnitude and remain coherent over a three dimensional spatial-temporal domain.

By comparing $\langle u \rangle_{xz}$ with $\langle u \rangle_{xy}$, we can see that the negative u-velocity region of the pattern $\langle u \rangle_{xy}$ directly corresponds to the negative velocity field at the centre of the vortex pair for the positively correlated samples. We can deduce that the negative contours (solid contours in figure 6.9(e), 6.10(e), 6.11(e), 6.12(f);) of the pattern $\langle u \rangle_{xy}$ show a cross-sectional slice of the paired vortical structure while the positive velocity zone (dotted contours) may not be part of the vortex structure and it is probably

associated with the entraining motions and turbulent mixing induced by the structures. The same phenomenon can be found in the averages of the negatively correlated samples, but the sign of the streamwise velocity is reversed (dotted contours in figure 6.13(e) and 6.14(f)).

It is important to visualise that the pattern $\langle v \rangle_{xz}$ shows an upward or downward velocity field normal to the (x,z) plane (moving towards and away from the reader in figure 6.9(d), 6.10(d), 6.11(d), 6.12(c), 6.13(c) and 6.14(c)). This is interesting because the same kind of motions have been observed in the results obtained from different (x,z) planes. In the averages of the positively correlated samples ($y > 0$), the average $\langle v \rangle_{xz}$ is characterised by a definite negative region which is always positively correlated with the streamwise velocity pattern $\langle u \rangle_{xz}$ (negative at the center). Again the signs of the velocity fields $\langle v \rangle_{xy}$ and $\langle v \rangle_{xz}$ are reversed in the averages of the negatively correlated samples (figure 6.13(c),(f); 6.14(c),(g)).

The interpretation of the vertical velocity $\langle v \rangle_{xz}$ (velocity component normal to the xz-plane) is not so straightforward without relating it to the corresponding pattern $\langle v \rangle_{xy}$ in the vertical plane. The vertical velocity pattern $\langle v \rangle_{xz}$ can be explained by the view that the vortex pair has axes of circulation inclined at a certain angle to the streamwise direction.

Note that the boundaries of the negative contours in figure 6.10(e), 6.11(e), 6.12(f) and positive contours in figure 6.14(f) suggests the inclination of the vortex pairs. The vector plots of velocities (figure 6.9(g), 6.10(h), 6.11(h), 6.12(h) and 6.14(h)) in the (x,y) plane also show the inclination of the structures, (since the velocity vectors consistently align at an angle to the horizontal axis). The angle of inclination is about $\pm$ 128°~ 147° degrees to the streamwise direction. This is a very crude estimation because the angle depends on the mean convection velocity used and the shape of the structures is not always clearly

defined in some ensemble averages.

The patterns educed from the (x,z) planes at various y-positions are topologically similar in some aspects. The inclined vortex pairs have been found on either side of the centreplane (y = 0). As shown in figure 6.12, the averaged structure extracted on the plane y = -1.68 has inclination roughly -135° to the streamwise direction (fig.6.12(f), 6.12(h)). Hence the structures on the two sides of the jet are similar but opposite in orientation.

The low pressure region is indistinct in shape (possibly globular) and this is revealed by the ensemble averages $\langle p \rangle_{xz}$, $\langle p \rangle_{xy}$ and $\langle p \rangle_{yz}$. The averaged pressure is found to be minimum at the centre of the structure. It is well known that a simple vortex is always characterised by a low pressure core. But in the case of a three dimensional vortex pair, the situation is more complicated. If the vortex pair is a horseshoe type of structure or part of a distorted spanwise roll, the pressure field should be governed by all three components of velocity which have the same order of magnitude. The pressure is lowest at the centre region of the vortex pair where the induced velocity is the strongest.

There is some reservation regarding the low pressure region appearing in the ensemble averages. The somewhat unexpected patterns of the pressure fluctuations in the averages may be possibly related to the computations of the time-averaged mean pressure, which has been a recently noticed problem in the numerical simulation of a turbulent boundary layer using a very similar code. The calculations of the pressure fluctuations may be affected by the global (the entire computational domain) fluctuations of the pressure solutions with time in the existing simulation code.

The ensemble averages of the negatively correlated structures (positive velocity field at the centre of the rollers) are shown in figure 6.13 (y = 0.767) and 6.14 (y = 1.68). The inclination of the structure is apparent in

figure 6.14(f) and 6.14(h) which is about 135°. But it is not so obvious in figure 6.13(h). The ensemble averages of the velocity fields at y = 1.68 (figure 6.14(f),(h)) closely resemble the experimental results of Mumford (1982,p.263; 1983,p.455) in the far jet and wake at higher Reynolds number (Re=10,000), although the present methodology of extracting the patterns in the (x,y) plane is different; no template matching is necessary in the (x,y) plane.

In the present study, it has been found that the averages of negatively correlated patterns have some subtle features different from the positively correlated patterns, but it is not immediately clear whether they play an equal dynamical role in the process of entrainment and mixing. The positively correlated structures may correspond to the inward kinking spanwise rolls, while the negatively correlated samples may be the outward kinking rolls. However, this is only a speculation.

There is also the possibility that the averages of the positively correlated samples may be contributed by juxtapositions of the negatively correlated samples and vice-versa. In addition, our technique cannot distinguish between the strainwise vortex pairs from the intermmediate-scale substructures or ribs which may exist in the near and intermediate regions of the jet.

The size of the averaging window is insufficient to cover the whole flow field surrounding the structures. Therefore, the ensemble averages of the velocity vectors in the vertical plane only reveal part of the entire cross-section of the structure. It would be very difficult to clarify where are the "tops" or "tails" of the vortex pairs. Moreover, the detection criterion is based on the flow features near the jet centreplane, the fine detailed features at the intermittent turbulent/non-turbulent interfaces or motions associated with the tops of the vortex pairs being smeared out in the ensemble averaging, because of the intermittency and bulgy nature of the jet boundary

surface. Since there is no clear indication of the tops of the vortex pairs (horseshoe-like vortices), our results neither disprove nor support the argument that the counter-rotating vortex pairs are joined together at the tops, or they are just the legs of the distorted spanwise rolls. More evidence will be required in order to elucidate the topology of the structure.

The restrictive time limit and funding of the current project does not allow further investigations such as the pattern matching in (x,y) plane. Hopefully it will be examined in the join MOD/SERC funded project in the future.

6.6 Effects of the Template

It has been found that the analyses performed with a vector template **T** = {u_t, w_t} generally give better and more consistent results than using a single-velocity pattern alone as a template **T** = {u_t}. This is because a highly correlated u'-velocity pattern does not always guarantee that the corresponding w'-velocity pattern is also correlated in the case of a scalar velocity template. Some of the irrelevant structures can happen to produce high correlations. On the other hand, a vector template only correlates well with those structures which have both correlated u'- and w'-velocity patterns. We may say that a vector template is more selective or discriminating than a scalar velocity template. This is supported by the fact that if the vector velocity template is used in place of a scalar velocity template, the total number of samples which satisfies the threshold criteria drops by 30~40%.

Most of the ensemble averages in the horizontal or (x,z) plane are obtained without iteration, because very good results can be produced even when there is no iteration. Some tests were made in order to see the effects of iterations. It was found that the iteration procedure did not significantly improve the ensemble averages. The averages of the subsequent iterations were very similar to

those without any iteration (results not shown here).

In order to test the dependency of the results on the choice of templates, a fairly crude velocity vector template has been employed in the matching. The two components of velocity fields are defined by the box shaped patterns in the 12x24 template (figure 6.15(a),(b)). The results are presented in figure 6.15(c),(d),(e),(f) (positively correlated patterns) and figure 6.16(a),(b),(c) (negatively correlated patterns). The ensemble averages converge to the counter-rotating eddy patterns without iteration. The step function template performs equally as well as the eddy function model; It's advantages include simplicity and minimum assumption about what the real eddy pattern would be like. The results are in good agreement with those obtained with an eddy model template.

6.7 Variation of the Matched Eddy Structures

Figure 6.17 shows the spatial and temporal locations of the positively and negatively correlated events for a given zoom factor of the template. The structures seem to be scattered randomly in space.

There is strong evidence of variation in the scales of the matched eddy patterns. The template matching is performed with a broad range of zoom factors varying from 0.1 to 8. The analysis was then repeated with fine increments of the zoom factors at a narrower range of scales where the number of matches was highest. Figure 6.18 shows the variation of the number of the best-matched patterns (both positively and negatively correlated) with the zoom factor for a given dataset at streamwise position x/d = 18 (the graph should not be misinterpretated as the distribution of the eddy size). The distribution is skewed towards zoom factors less than 3.0. The highest number of matches occurs with zoom factors between 0.6 to 2.0 and hence the probability of occurence of paired eddy structures is largest at these scales. It should be noted that the PRA of Savill (1979)

detected a range of structures sizes covering the scale ratio of roughly 1/4 to 4, which is very close to the scaling factors of the present study. His results showed that, upstream or downstream large rollers were often accompanied by smaller rollers, the typical size being one half or one quarter that of the largest rollers.

There is a sharp drop in the number of samples when the scale is very small and the number decreases slowly with increasing zoom factors. The optimum convolution is also attained when the number of samples is highest. Moreover, the number of positively correlated samples is fairly close to the negatively correlated samples. The probabilities of occurrence of these two types of events may be equal.

The scale of these vortex pairs should depend on the Reynolds number of the mean flow. For example, Head and Bandyopadhyay (1979) found that the hairpin vortices tend to be narrower and elongated at moderate to high Reynolds numbers in turbulent boundary layers, while the vortex loops appear to be fatter and less stretched at very low Reynolds numbers. They are not necessarily scaled with the local half width of the jet. It is also unlikely that they are responsible for the self-preserving property of mean statistics.

6.8 Dynamical Significance of the Structure

Our results agree with the postulation that the inclined vortex pairs may be associated with the production of the coherent Reynolds stresses, the large scale entraining motions and ejections. The velocity fluctuations u' and v' at the centre of the vortex pairs are observed to be positively correlated (if $y > 0$), i.e. positive $u'v'$ is present and hence negative Reynolds stress $-\langle u'v' \rangle$. The entrainment of the surrounding non-turbulent fluid may take place through the interaction with the velocity field of an inclined vortex pair. As shown in the vector plots of the velocities $\langle u \rangle_{xy}$ and $\langle v \rangle_{xy}$, the entraining motions of the

irrotational flow into the turbulent zone are displayed by the fluid motions moving towards the centre of the jet.

If the entraining potential flow is induced by the velocity field of the tops of the vortex loops, then it is equally probable that they may be responsible for the transportation or "ejection" of the turbulent fluid from the centre of the jet towards the potential flow, and hence turbulent mixing. The continous movement of turbulent fluid across the jet away from the centreplane is observed in our v-velocity ensemble averages in the vertical plane. This is consistent with the conditional-sampling analysis of the thermal wake by Fabris(1979), his conditional averaged v-velocities also indicating hot fluid moving away the centre of the wake and cold fluid moving towards the centre. In addition, Guezennec *et al*(1992) showed that the major Reynolds stress contributing events in the plane wake were the entraining and ejecting (sweeping) eddies.

6.9 Topology of the Eddy Structures

The double-roller eddies found in the near jet simulation are different from those of Mumford(1982) in the far field, the roller eddies being paired in the spanwise direction instead of streamwise or other directions. They are somewhat similar to the double-rollers found in the far wakes of Mumford (1983) and Savill (1979) though having opposite orientation. However, the structures are not joined together across the centreplane, which is consistent to the findings of Mumford (1982). It appears that there is a strong link between the near-jet structures and the weaker, less deterministic structures in the far field. Based on the findings of other the studies and the present results, we can tentatively propose a configuration for the roller-eddies in the near jet, as shown in figure 6.19. Such arrangement is somewhat similar to horseshoe vortices suggested by Savill (1979) and Ferré *et al* (1990) in the plane wakes. But the double roller eddies are parts of the distorted spanwise vortices, which are often in alternative

arrangement without crossing the centreplane.

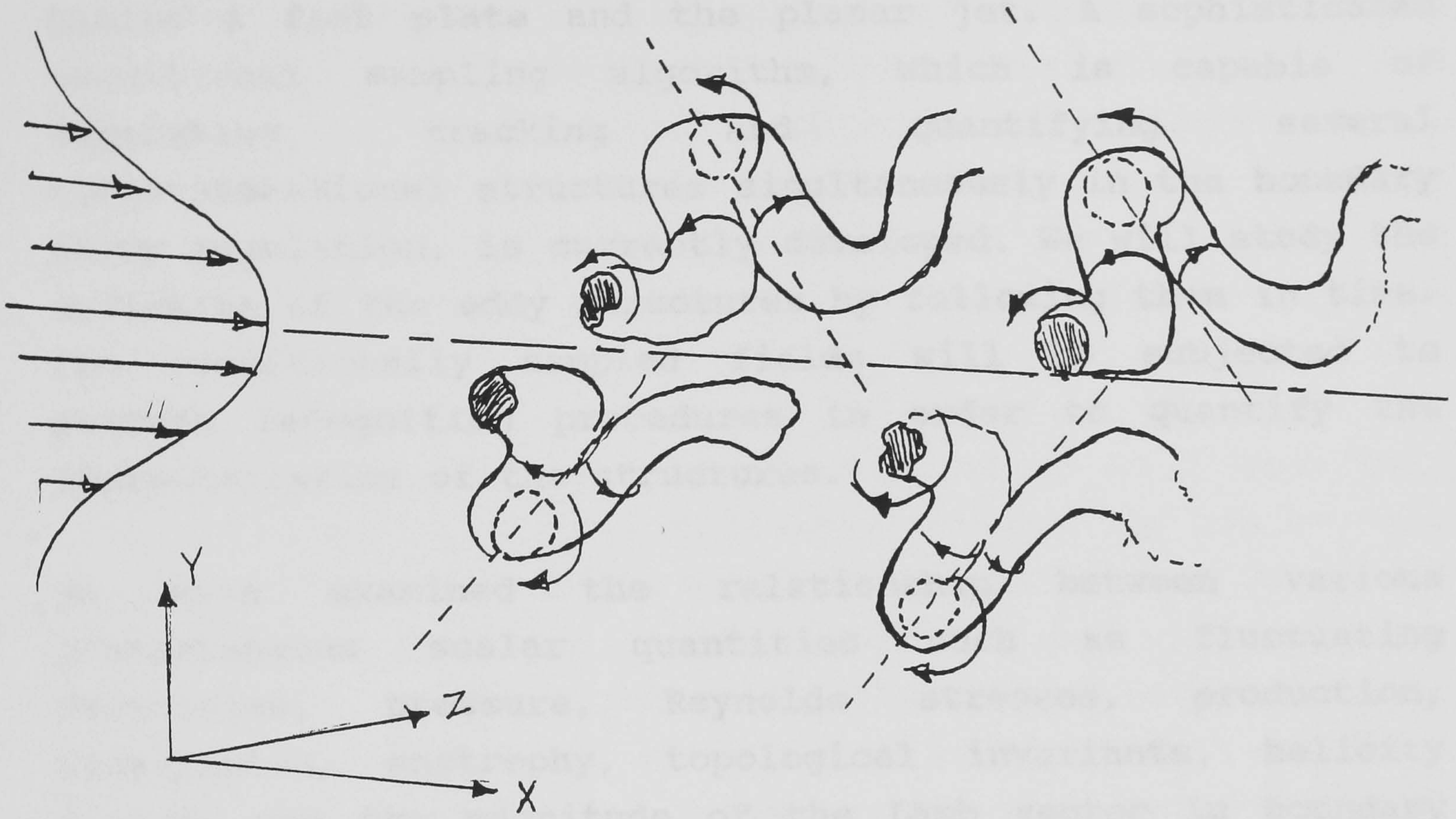

Fig. 6.19 Speculated topology of the vortical structures in plane jets:

6.10 Future Development

A separate project on the application of PRA to conditionally sampled flow fields have been carried out. It includes the analyses of three different numerical simulations: the tripped turbulent boundary layer, the wake behind a flat plate and the planar jet. A sophisticated conditional sampling algorithm, which is capable of separating, tracking and quantifying several three-dimensional structures simultaneously in the boundary layer simulation, is currently developed. We will study the evolution of the eddy structures by following them in time. The conditionally sampled fields will be subjected to pattern recognition procedures in order to quantify the characteristics of the structures.

We have examined the relationship between various instantaneous scalar quantities such as fluctuating velocities, pressure, Reynolds stresses, production, dissipation, enstrophy, topological invariants, helicity density and the magnitude of the Lamb vector in boundary layer simulation. Some of these scalar quantities will be used as triggering signals in conditional sampling.

We will refine our PRA in order to extract full three-dimensional fields in the plane jet simulation. We will further study the topology of the rollers eddies, particularly the connectivity of the tops and the existence of various forms of rollers.

Chapter Seven

CONCLUSIONS

7.1 The Plane Jet Simulation

A plane jet issuing into an open domain has been simulated by a finite volume code, being the first attempt of its kind. An existing simulation code with the standard subgrid scale model, designed for studying flow through a square duct and subsequently modified to allow the simulation of spatially developing flows, was applied to the problem of the plane jet.

Our study demonstrates that the simulation of a spatially developing free jet in a stationary surrounding can be very challenging because of the problems related to the treatment of boundary conditions in the potential part of the flow. Modification of the boundary conditions was necessary, the main technical problems being the side boundaries at which entrainment from the far field is known to take place. It was found to be very difficult to control the inflow through these boundaries in such a way as to produce simultaneously a zero pressure gradient and no recirculation of the mean velocity near the outflow boundary. The entrainment velocities through the side walls had to be included and adjusted, but the theoretically- derived values of the entrainment did not produce the desired behaviour in the simulation. A compromise was finally accepted in which the main part of the jet appeared to be substantially unaffected by these problems. In addition, the use of the advective boundary condition in the outflow appeared to be less satisfactory, however it only affected the solutions of the flow near the outflow region and had minor effect in the principal region of interest.

Nevertheless, the simulation reproduced many statistical characteristics and coherent eddy structures observed experimentally at higher Reynolds numbers. Comparisons with

available experimental data on jet growth rate, centre-line velocity, turbulence intensities, and stresses are reasonably satisfactory in the near-jet. The minor scattering of the time-averaged statistics was caused by inadequate number of samples averaged (the Cray time allocation was limited in this project). It is suggested that the simulation statistics should be averaged over a very long period of time. The resolution of the simulation was adequate, as the subgrid scale eddy viscosity was very small.

7.2 The Organised Eddy Structures

The results of the PRA confirmed the existence of large eddy structures realistically captured in the simulation. The double-roller eddies are present in the near field of the numerically simulated plane jet and appear to be somewhat similar to those detected in the multi-probe experiments by Mumford and Ferré *et al*. However, their measurements were performed in the fully developed far fields of the flows with much higher Reynolds numbers. The results show evidence of the orientation of the roller eddies at roughly ±135 degrees to the flow direction, but no evidence of the rollers joining up or forming groups. We have investigated the change in the double roller structures with distance from the centreplane of the jet, and the effects of changing the scale of the template used. The possible range of structural sizes has been deduced by repeated applications of the template matching to the simulation database, the scaling ratio of roughly 0.6 to 2.0 being obtained.

The educed patterns of the roller eddies are similar at various cross-stream planes from the centreline. The roller structures are found to be not linked across the centreplane of the jet, which is consistent with the findings of Mumford (1982). However, they are paired in the spanwise direction instead of the streamwise direction. They possess characteristics similar to the double roller eddies detected in the far wakes by Savill (1979), Mumford (1983) and Ferré

et al (1986, 1989, 1990). However, they appear to be more organised and stronger in the near jet than those in the far wakes. Some evidence indicates that the roller eddies exist in two types with opposite sign of circulation, which are believed to be sections of the inward and outward kinking rolls respectively. The double roller eddies also appear to be associated with the production of coherent Reynolds stresses, large scale entraining motions and ejections of the turbulent fluid towards the potential flow.

7.3 Numerical Simulation and PRA

The numerical simulation databases provided very rich and detailed information about 3D eddy structures, and pattern recognition analysis is well suited to the eduction of eddy structures from simulation data. Pattern recognition was carried out in a manner similar to that used for the experimental eduction of eddy structures. The extension to averaging in the x-y plane allowed the extraction of important information on the three-dimensional nature of the detected eddy structures. It proved possible to visualise the three-dimensional flow fields associated with the two-dimensional patterns extracted by PRA in the x-z plane. Therefore it is not essential to use 3D template approach of Stretch (1991) in order to educe 3D structures. The use of template patterns with various scaling factors allowed us to study the variation of size of flow samples. It appears that PRA will be a promising tool for quantifying the size, shape, orientation, sign, symmetry and strength of the coherent eddy structures in the future. We consider this project to have been successful in demonstrating that PRA has an important role to play in extracting real understanding of turbulence dynamics from numerical simulations.

FIGURE CAPTIONS

Chapter 2

Fig. 2.1 Double roller eddy in the plane wake suggested by Grant (1957).

Fig. 2.2 Eddy structure inferred from the results of orthogonal decomposition by Payne and Lumley (1967).

Fig. 2.3 The distortion of a double roller eddy from Savill (1979).

Fig. 2.4 The strainwise roller eddies in a plane jet from Mumford (1982); (a) single roller eddy, (b) double roller eddy separated in the streamwise direction with opposite sign of circulations, (c) double roller eddy separated in both streamwise (x) and spanwise (z) directions with the same sign of circulations.

Fig. 2.5 The possible forms of roller eddies in a plane wake from Mumford (1983).

Fig. 2.6 The saddle point, diverging and converging separatrices between the spanwise vortices.

Fig. 2.7 The horseshoe roller structures in the plane wake from Ferré *et al* (1990).

Fig. 2.8 Schematic sketches of (a) the plane wake, (b) the plane jet.

Fig. 2.9 Buoyant jet produced from the smoke of a cigarette. (a) no perturbation, (b) vertical oscillation, (c) lateral oscillation.

Fig. 2.10(a) Plan view of the mushroom-like streamwise vortices in the near wake region of a circular cylinder. Re = 901 (photograph by Soria (1992)).

Fig. 2.10(b) Vector field superimposed on smoke photograph of a double-sided three dimensional co-flowing jet. (photograph by Perry and Tan (1984)).

Fig. 2.10(c) Side and plan views of the wakes behind a splitter plate with blunt edge. Two sharp wedges were attached to the end of the splitter plate. (photographs by Breidenthal (1980)).

Fig. 2.10(d) Plan view of a plane wake behind a circular cylinder at Re = 150, x/d = 100, y/d = 2. (photographs by Cimbala *et al* (1988)).

Fig. 2.10(e) Plan view of the cylinder wake at Re = 180; formation of the vortex loops and pairs of streamwise vortices.

Fig. 2.10(f) Formation of the finer-scale streamwise vortices at Re = 285.

Fig. 2.11 Sketches of the intuitive interpretation of the flow visualisation photographs: (a) mushroom-like streamwise vortices in the plane wake, (b) interlocking loops in the 3-D wake behind a splitter plate, (c) distorted spanwise rolls in the transitional wake, (d) distorted rolls and streamwise vortices in the transitional wake.

Fig 2.12 The resolved scales and subgrid scales in the energy spectrum. (1) resolved scales, (2) subgrid scales, (3) energy containing eddies, (4) inertial subrange, (5) universal equilibrium range.

Fig 2.13 A vortex element under a two-dimensional strain-rate field.

Fig. 2.14 Rolling up of a vortex filament.

Fig.2.15 Speculated topology of the vortical structures in

the plane wakes and jets: (a) outward kinking roll, (b) distorted roll at higher Reynolds, (c) inward kinking roll, (d) closed vortex loop.

Fig.2.16 Speculated arrangement of the structures in the plane jet(a) streamline pattern, (b) spanwise rolls.

Fig.2.17 Speculated arrangement of the spanwise rolls and longitudinal vortices in a plane wake.

Chapter 3

Fig 3.1(a),(b) Adam-Bashford scheme.

Fig 3.2(a) Staggered grid in three dimensions.

Fig 3.2(b) Staggered grid in two dimensions.

Fig 3.3 The geometry and coordinates of the simulation.

Fig 3.4 Inflow and lateral boundary conditions.

Fig 3.5 Outflow boundary conditions.

Chapter 4

Fig 4.1 N_1 by N_2 search area G and M_1 by M_2 template.

Fig 4.2 Event duration limit.

Fig 4.3 Ensemble averaging in the (y,t) and (z,t) planes.

Fig 4.4 Sampling planes.

Chapter 5

Fig 5.1 Mean half-width l/d as a function of streamwise distance. Symbols, simulation; line, l = 0.1977x.

Fig 5.2 Time-averaged mean velocity profiles. Solid line, simulation at x/d = 23.6; dot dash line, Bradbury (1965), empirical fit at 13.9 ≤ x/d ≤ 68.5..

Fig 5.3 Static pressure profiles, numerical simulation; solid line: x/d = 10.3, dot dash line: x/d = 13.2, and dash line: x/d = 15.6.

Fig 5.4 Static pressure profile, Line, simulation at 37.5; symbols, Miller and Comings (1957) at x/d = 40.

Fig 5.5 Isometric plot of the short-time (over 6,000 time steps) averaged streamwise velocity.

Fig 5.6 Contours of the subgrid eddy viscosity ν_e/ν_m x 100%.

Fig 5.7 Decay curve of the mean velocity on the centreline from the simulation.

Fig 5.8 Profiles of the turbulence intensities from numerical simulation at x/d = 17.5. Solid line: $\overline{u'^2}/ U_m^2$; dash dot line: $\overline{w'^2}/ U_m^2$; dash line: $\overline{v'^2}/ U_m^2$.

Fig 5.9 Profiles of $\overline{u'^2}/ U_m^2$. Solid line: simulation at x/d = 21.7; Dash dot line: Bradbury (1965), empirical fit at 22 ≤ x/d ≤ 70.

Fig 5.10 Profiles of the Reynolds shear-stress. Line, simulation at x/d = 21.7; symbols, Bradbury(1965) at x/d = 51.

Chapter 6

Fig. 6.1(a) Noise test. ζ = 0.5.

Fig. 6.1(b) Noise test. ζ = 2.0.

Fig. 6.1(c) Variation of the cross-correlation with

noise-to-signal amplitude ratio.

Fig. 6.2 Spanwise max. and min. cross-correlation.

Fig. 6.3 Variation of cross-correlations with zoom factors.

Fig. 6.4 Comparison between a random template and a step function template. (a) Random template, (b) step function template.

Fig. 6.5 Cross-correlation coefficients.(a) Zoom factor = 1, (b) zoom factor = 1/4.

Fig. 6.6 Ensemble averages of positively correlated streamwise velocity fields, (a) single eddy pattern with 12x28 template; (b) vortex pair, zoom factor = 1, (c) zoom factor = 1.5, (d) zoom factor = 0.5 with a 18x48 template at y/l = 0.3, x/d = 18.

Fig. 6.7 Ensemble averages of vorticity $\langle\omega\rangle_{xz}$, (a) zoom factor = 1, (b) zoom factor = 1.5 with a 12x48 vorticity template at y/l = 0.3, x/d = 18.

Fig. 6.8 Cross-correlation curves of (a) ——— vorticity, (b) ------- streamwise velocity; · the peaks are in phase.

Fig. 6.9 Ensemble averages of (a) velocity vectors in (x,z) plane, (b) $\langle u\rangle_{xz}$, (c) $\langle w\rangle_{xz}$, (d) $\langle v\rangle_{xz}$, (e) $\langle u\rangle_{xy}$, (f) $\langle v\rangle_{xy}$, (g) velocity vectors in (x,y) plane at y/l = 0, x/d = 18. Positively correlated velocity vector field. ····· negative; ——————— positive contours.

Fig. 6.10 Ensemble averages of (a) $\langle u\rangle_{xz}$, (b) $\langle w\rangle_{xz}$, (c) $\langle p\rangle_{xz}$, (d) $\langle v\rangle_{xz}$, (e) $\langle u\rangle_{xy}$, (f) $\langle v\rangle_{xy}$, (g) $\langle p\rangle_{xy}$, (h) velocity vectors in (x,y) plane (i) velocity vectors in (x,z) plane at y/l = 0.3 (y = 0.767) , x/d = 18. Positively correlated velocity vector fields.

Fig. 6.11 Ensemble averages of (a) $\langle u \rangle_{xz}$, (b) $\langle w \rangle_{xz}$, (c) $\langle p \rangle_{xz}$, (d) $\langle v \rangle_{xz}$, (e) $\langle u \rangle_{xy}$,(f) $\langle v \rangle_{xy}$,(g) $\langle p \rangle_{xy}$,(h) velocity vectors in (x,y) plane at y/l = 0.67 (y = 1.68). Positively correlated velocity vector fields

Fig. 6.12 Ensemble averages of (a) $\langle u \rangle_{xz}$,(b) $\langle w \rangle_{xz}$,(c) $\langle v \rangle_{xz}$,(d) $\langle p \rangle_{xz}$,(e) velocity vectors in (x,z) plane (f) $\langle u \rangle_{xy}$,(g) $\langle v \rangle_{xy}$,(h) $\langle p \rangle_{xy}$,(i) velocity vectors in (x,y) plane at y/l = -0.67 (y = -1.68). Positively correlated vector fields.

Fig. 6.13 Ensemble averages of (a) $\langle u \rangle_{xz}$,(b) $\langle w \rangle_{xz}$,(c) $\langle v \rangle_{xz}$,(d) velocity vectors in (x,z) plane (e) $\langle u \rangle_{xy}$,(f) $\langle v \rangle_{xy}$,(g) $\langle p \rangle_{xy}$,(h) velocity vectors in (x,y) plane at y/l = 0.3 (y = 0.767), x/d = 18. Negatively correlated velocity vector fields.

Fig. 6.14 Ensemble averages of (a) $\langle u \rangle_{xz}$,(b) $\langle w \rangle_{xz}$,(c) $\langle v \rangle_{xz}$,(d) $\langle p \rangle_{xz}$,(e) velocity vectors in (x,z) plane (f) $\langle u \rangle_{xy}$,(g) $\langle v \rangle_{xy}$,(h) velocity vectors in (x,y) plane at y/l = 0.67 (y = 1.68), x/d = 18. Negatively correlated velocity vector fields.

Fig. 6.15 (a) and (b): velocity components of a box-eddy template. (c) $\langle u \rangle_{xz}$,(d) $\langle w \rangle_{xz}$,(e) $\langle v \rangle_{xz}$,(f) velocity vectors in (x,z) plane at y/l = 0, x/d = 18. Positively correlated velocity vector fields.

Fig. 6.16 (a) $\langle u \rangle_{xz}$, (b) $\langle w \rangle_{xz}$, (c) $\langle v \rangle_{xz}$ at y/l = 0, x/d = 18, x/d = 0, y/l = 0. Negatively correlated velocity vector fields with a box-eddy template.

Fig. 6.17 Spatial-temporal locations of the events.

Fig. 6.18 The variation of the best correlated samples with

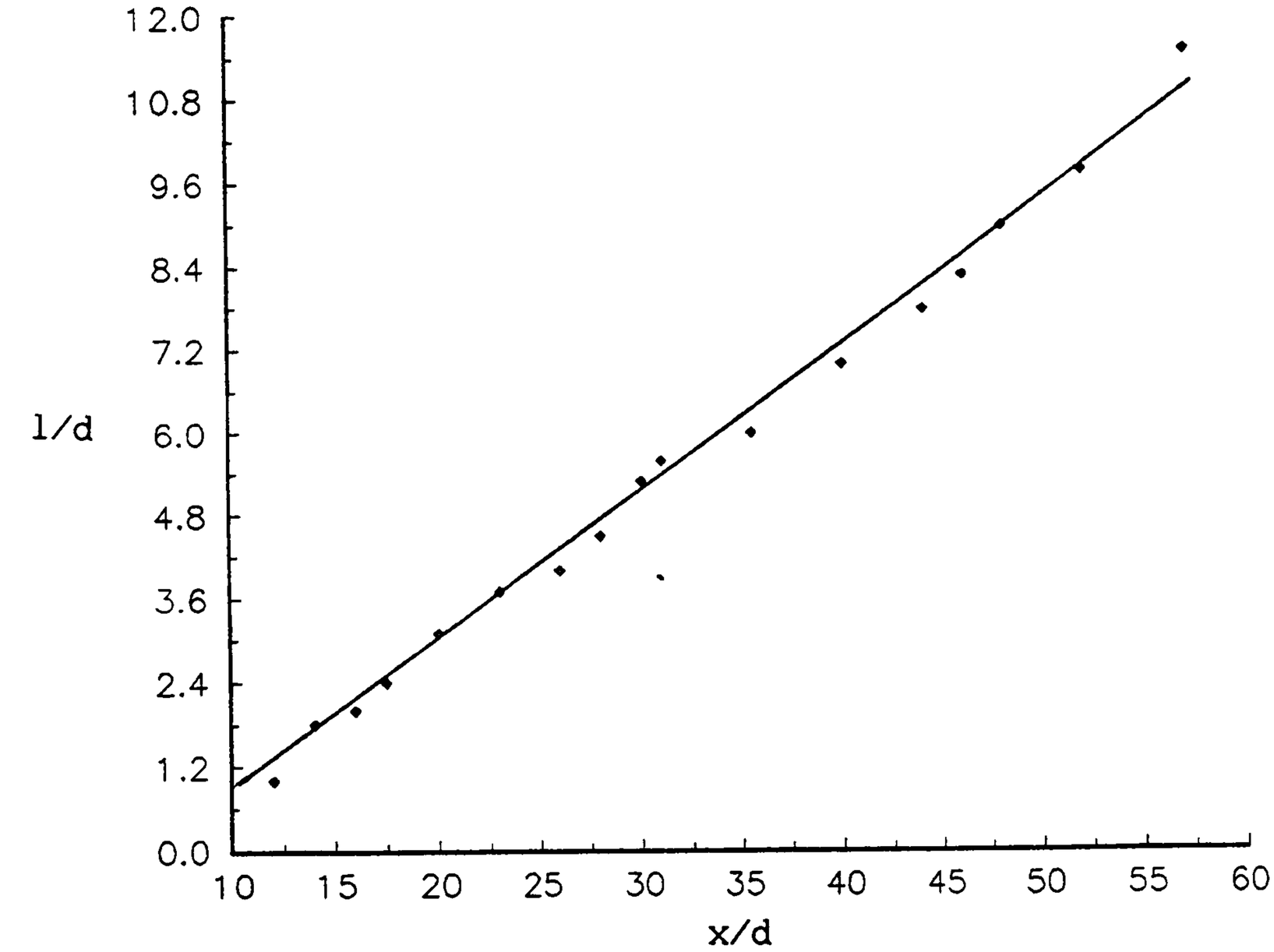

Fig 5.1 Mean half-width l/d as a function of streamwise distance. Symbols, simulation; line, dx/dl = 0.1977.

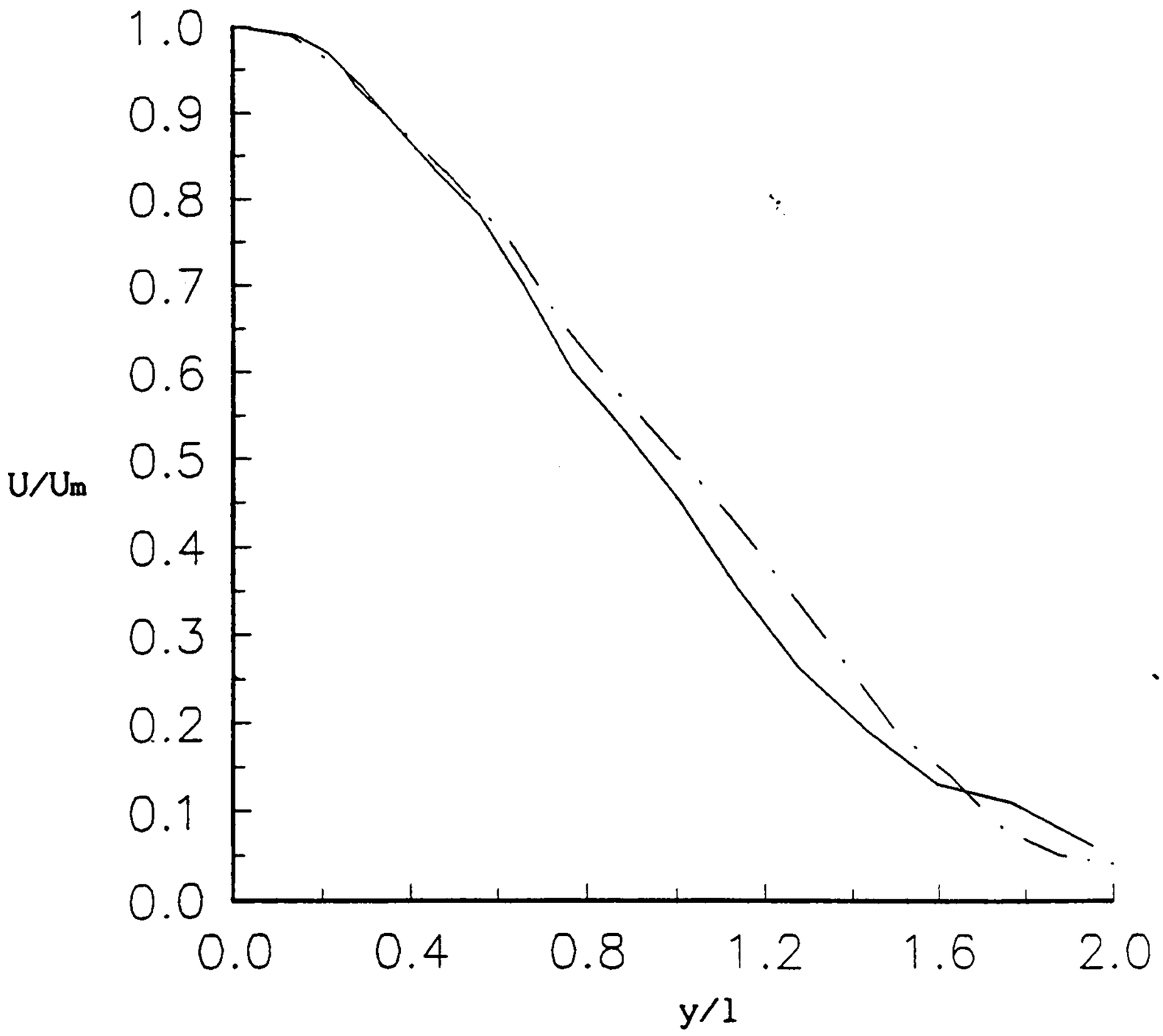

Fig 5.2 Time-averaged mean velocity profiles. Solid line, simulation at x/d = 23.6; dot dash line, Bradbury (1965), empirical fit at 13.9 ≤ x/d ≤ 68.5..

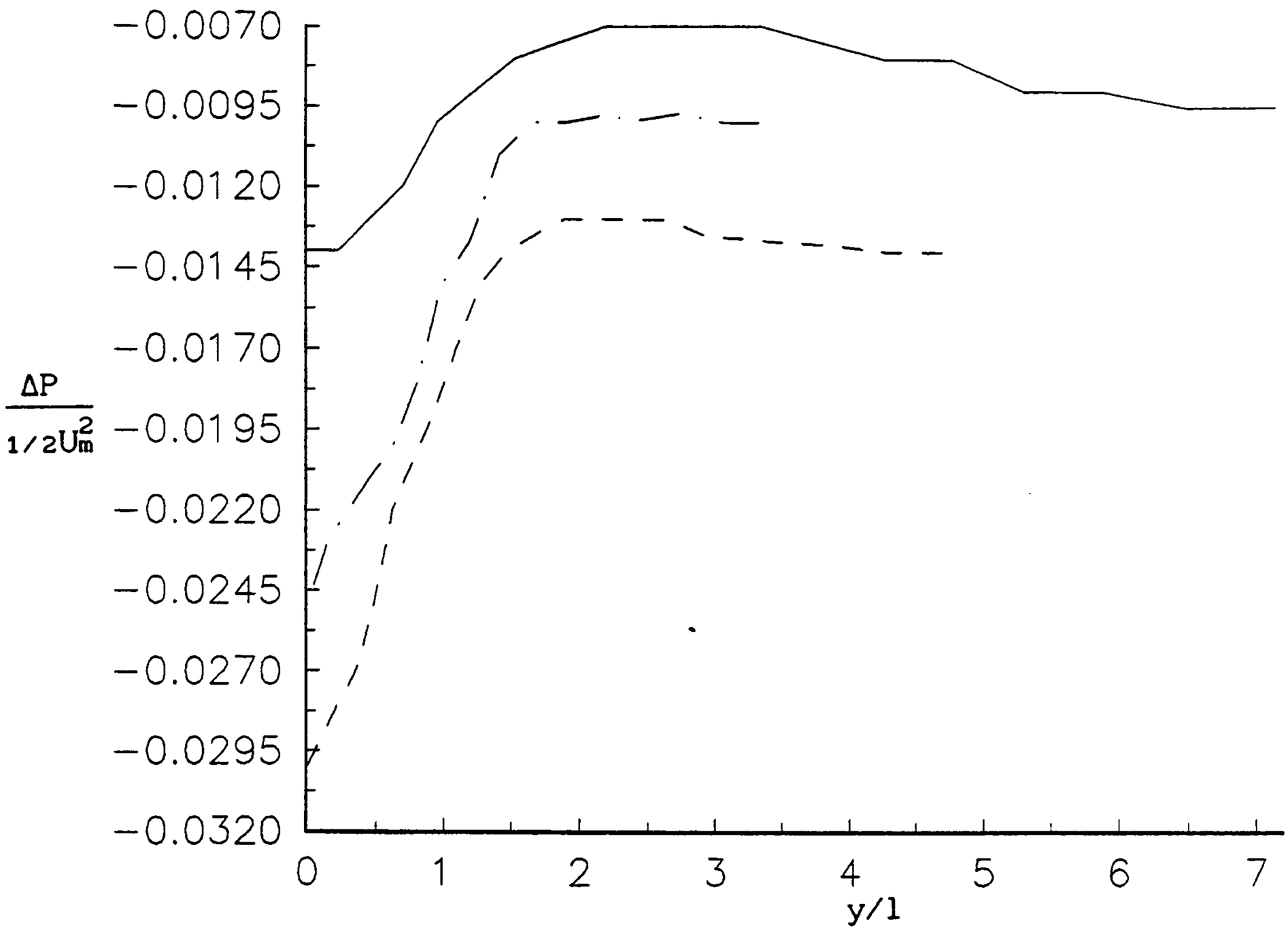

Fig 5.3 Static pressure profiles, numerical simulation; solid line: x/d = 10.3, dot dash line: x/d = 13.2, and dash line: x/d = 15.6.

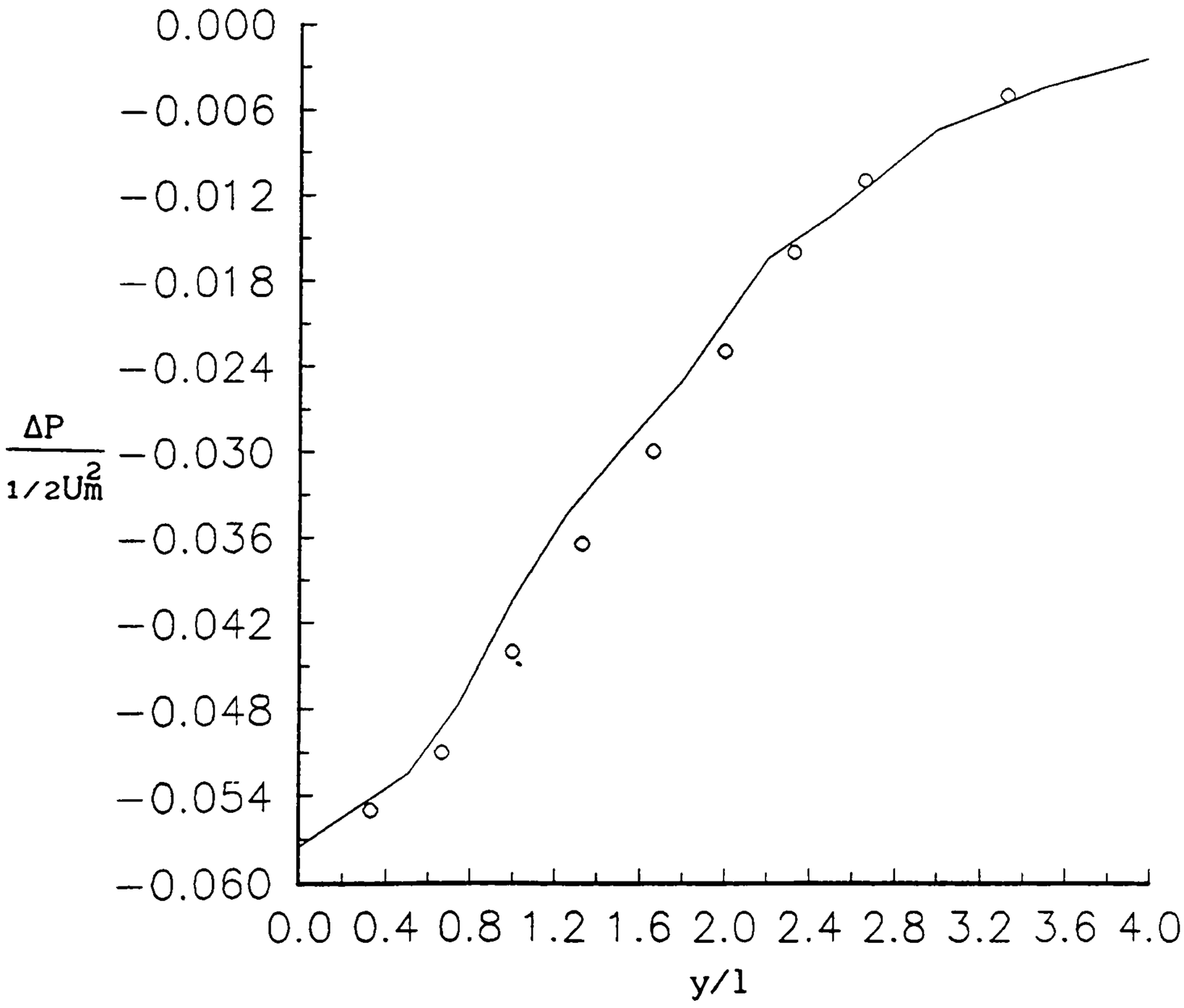

Fig 5.4 Static pressure profile, Line, simulation at 37.5; symbols, Miller and Comings (1957) at x/d = 40.

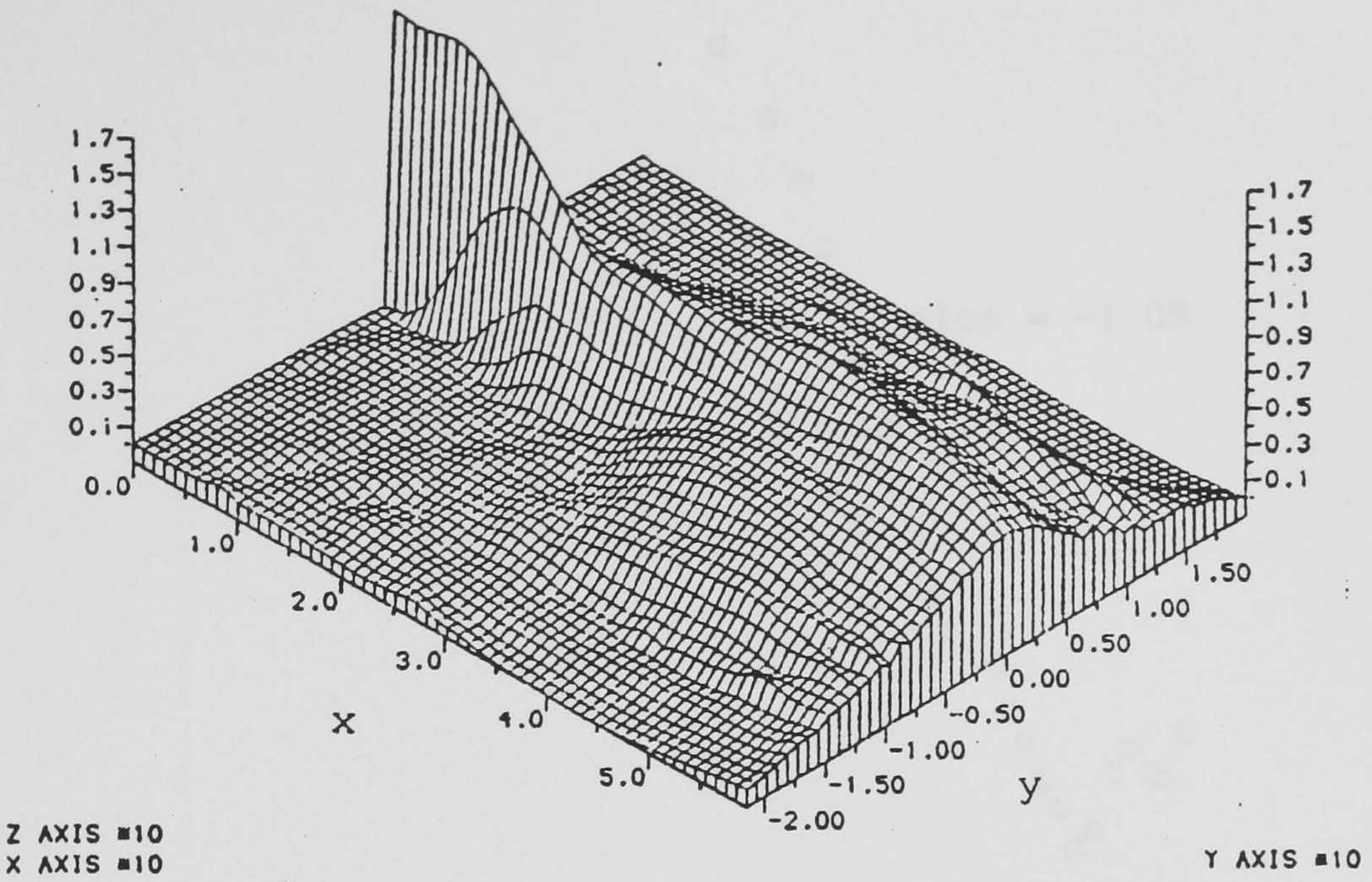

Fig 5.5 Isometric plot of the short-time (over 6,000 time steps) averaged streamwise velocity.

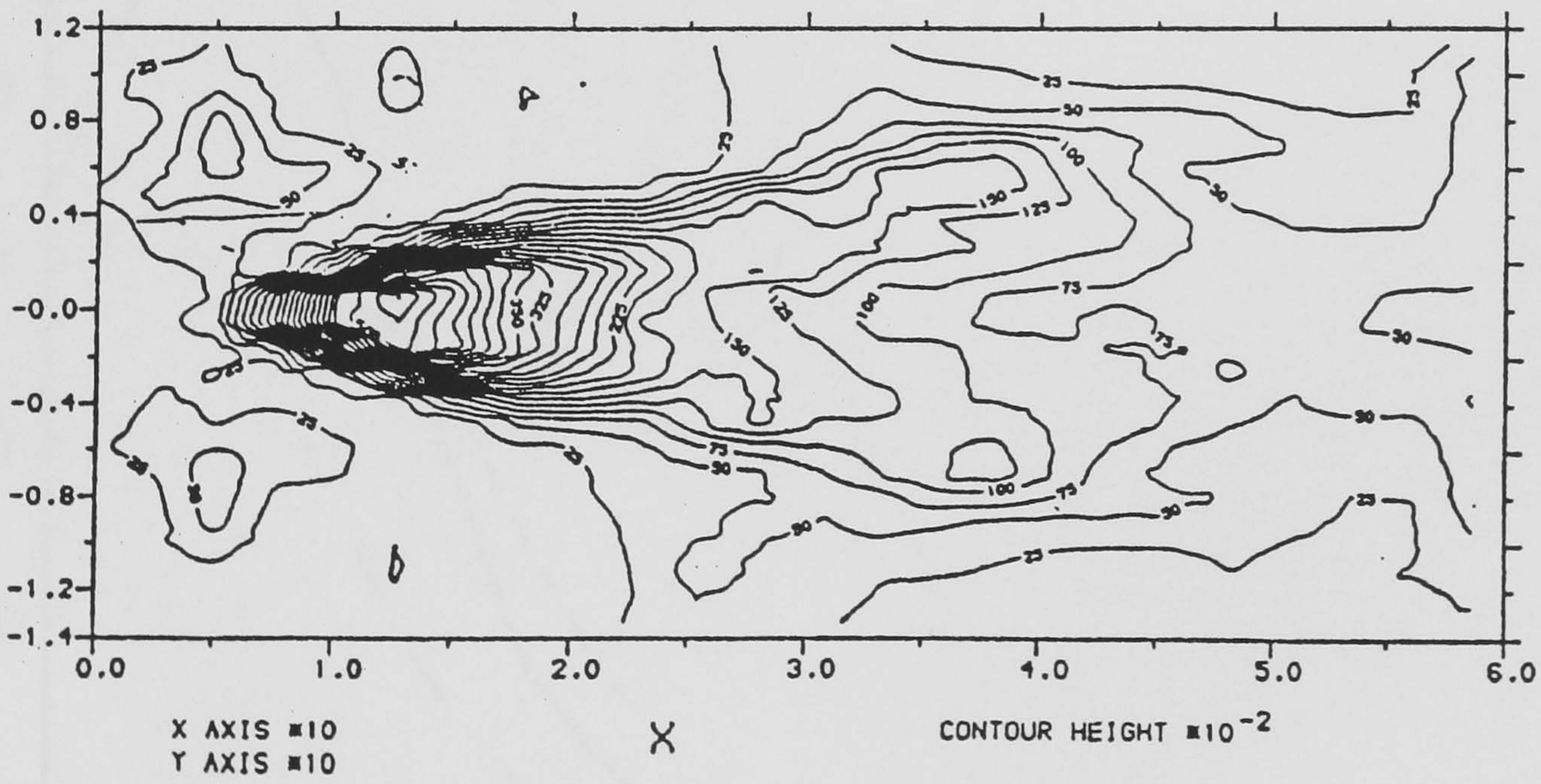

Fig 5.6 Contours of the subgrid eddy viscosity ν_e/ν_m x 100%.

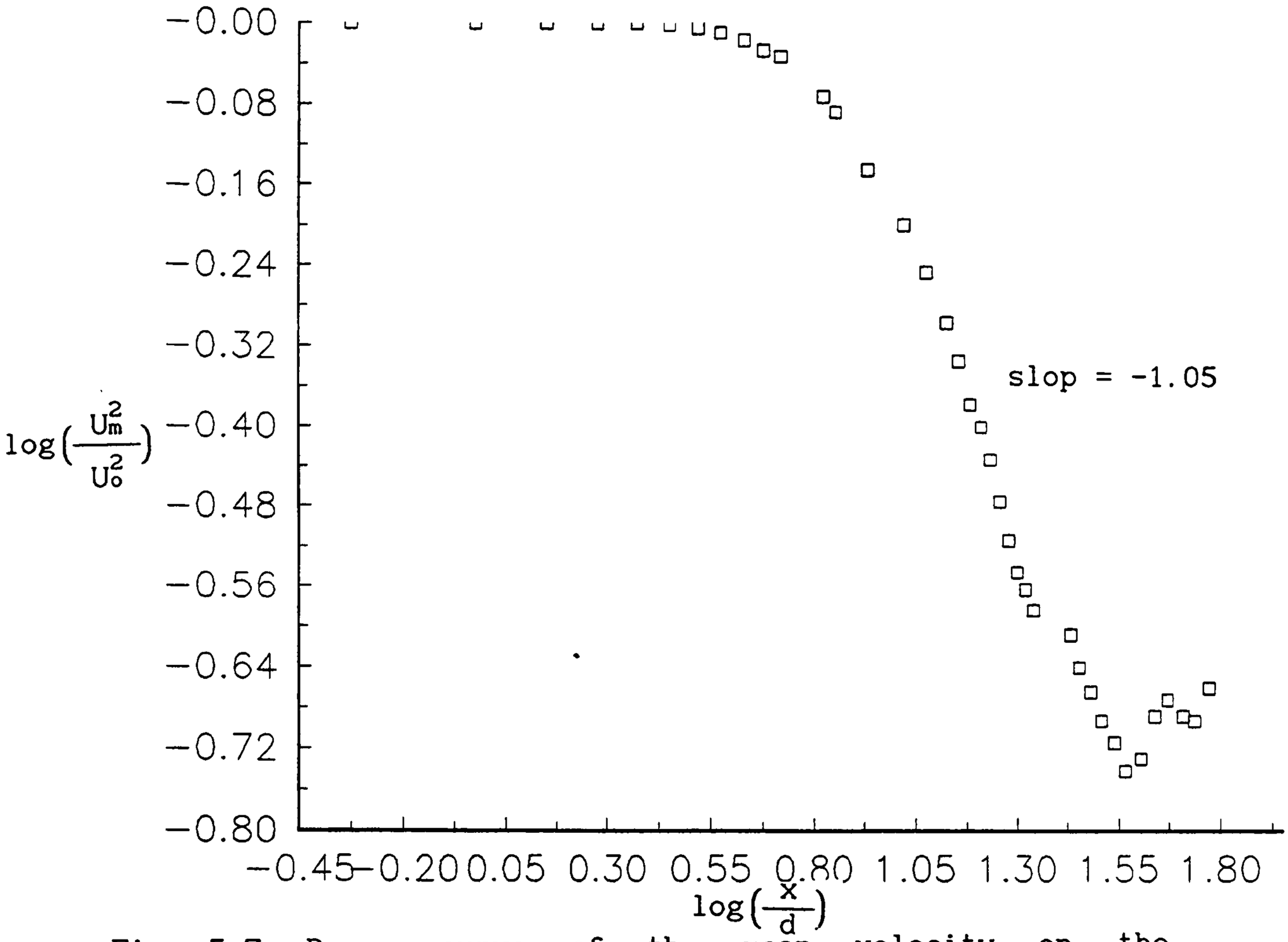

Fig 5.7 Decay curve of the mean velocity on the centreline from the simulation.

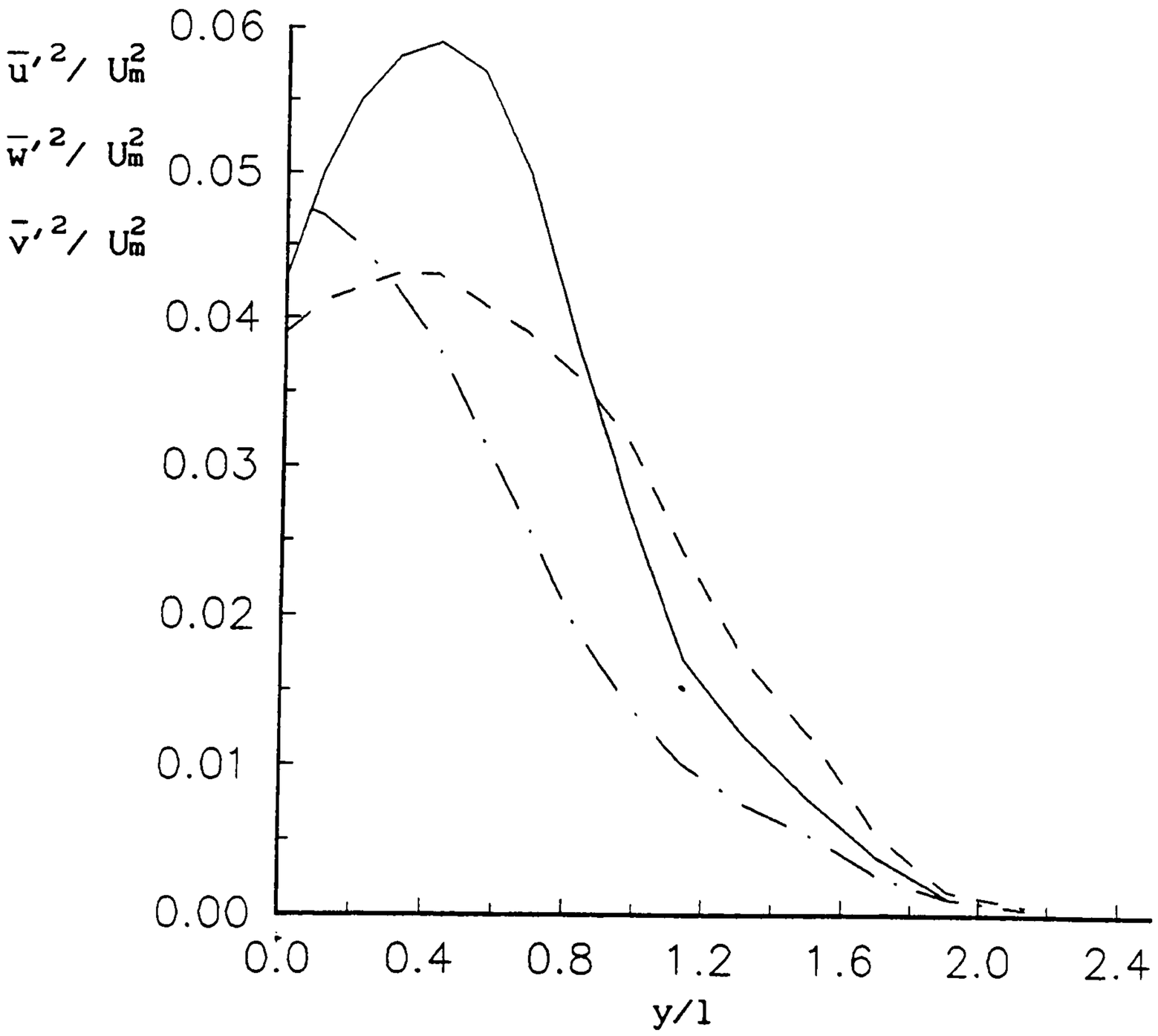

Fig 5.8 Profiles of the turbulence intensities from numerical simulation at x/d = 17.5. Solid line: $\overline{u}'^2/ U_m^2$; dash dot line: $\overline{w}'^2/ U_m^2$; dash line: $\overline{v}'^2/ U_m^2$.

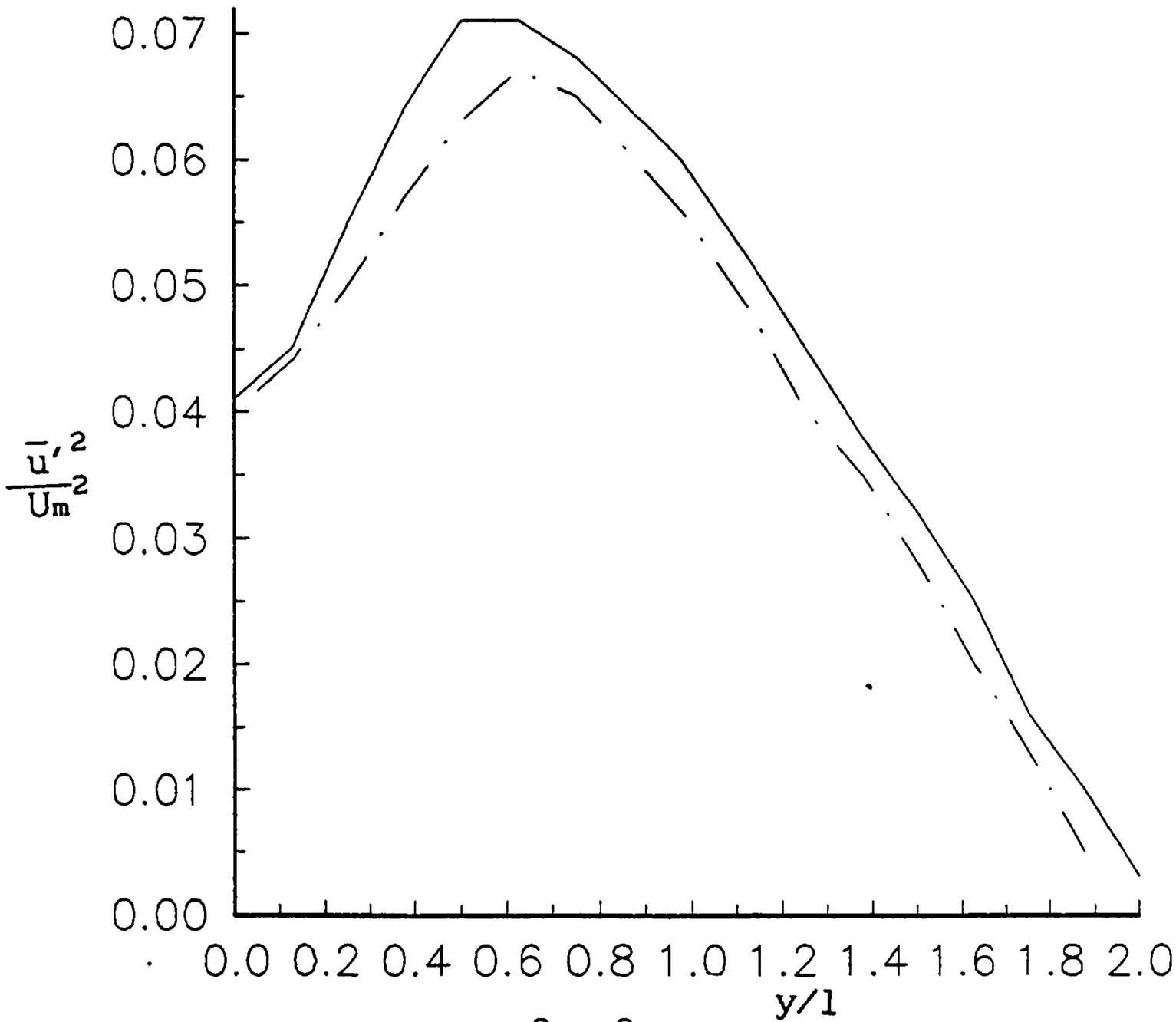

Fig 5.9 Profiles of $\overline{u'^2}/U_m^2$. Solid line: simulation at x/d = 21.7; Dash dot line: Bradbury (1965), empirical fit at 22 ≤ x/d ≤ 70.

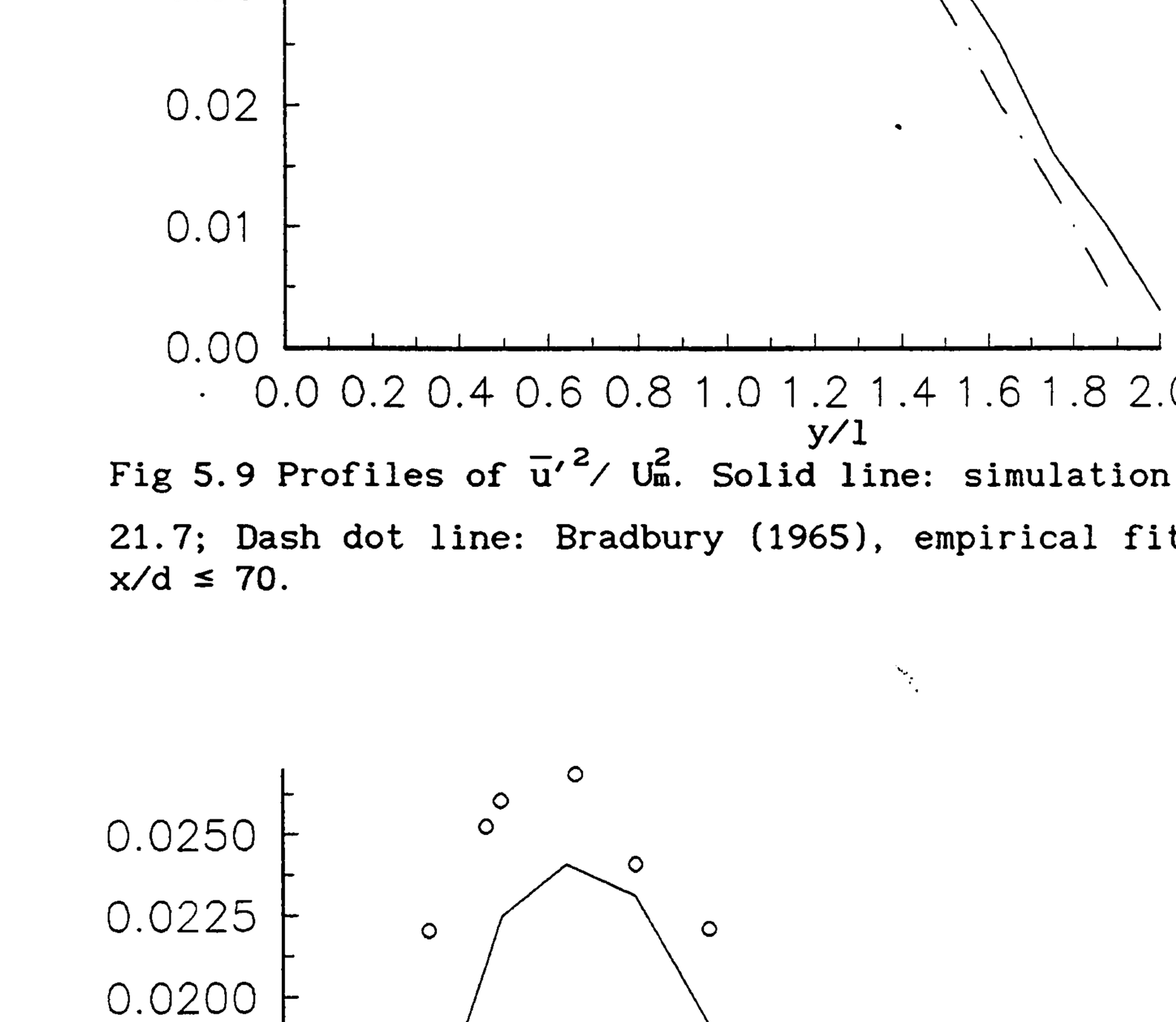

Fig 5.10 Profiles of the Reynolds shear-stress. Line, simulation at x/d = 21.7; symbols, Bradbury(1965) at x/d = 51.

Fig. 6.1(a) Noise test. $\zeta = 0.5$.

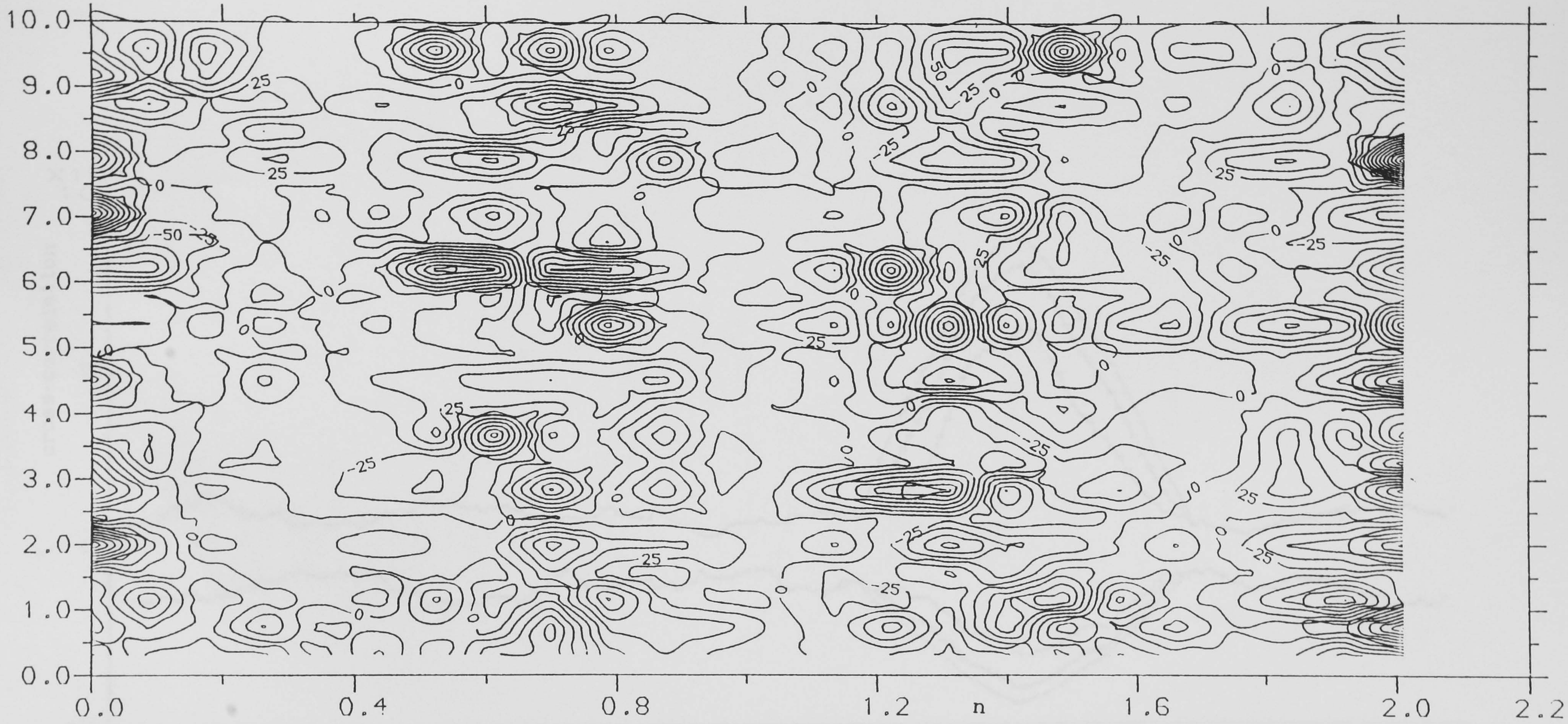

Fig. 6.1(b) Noise test. $\zeta = 2.0$

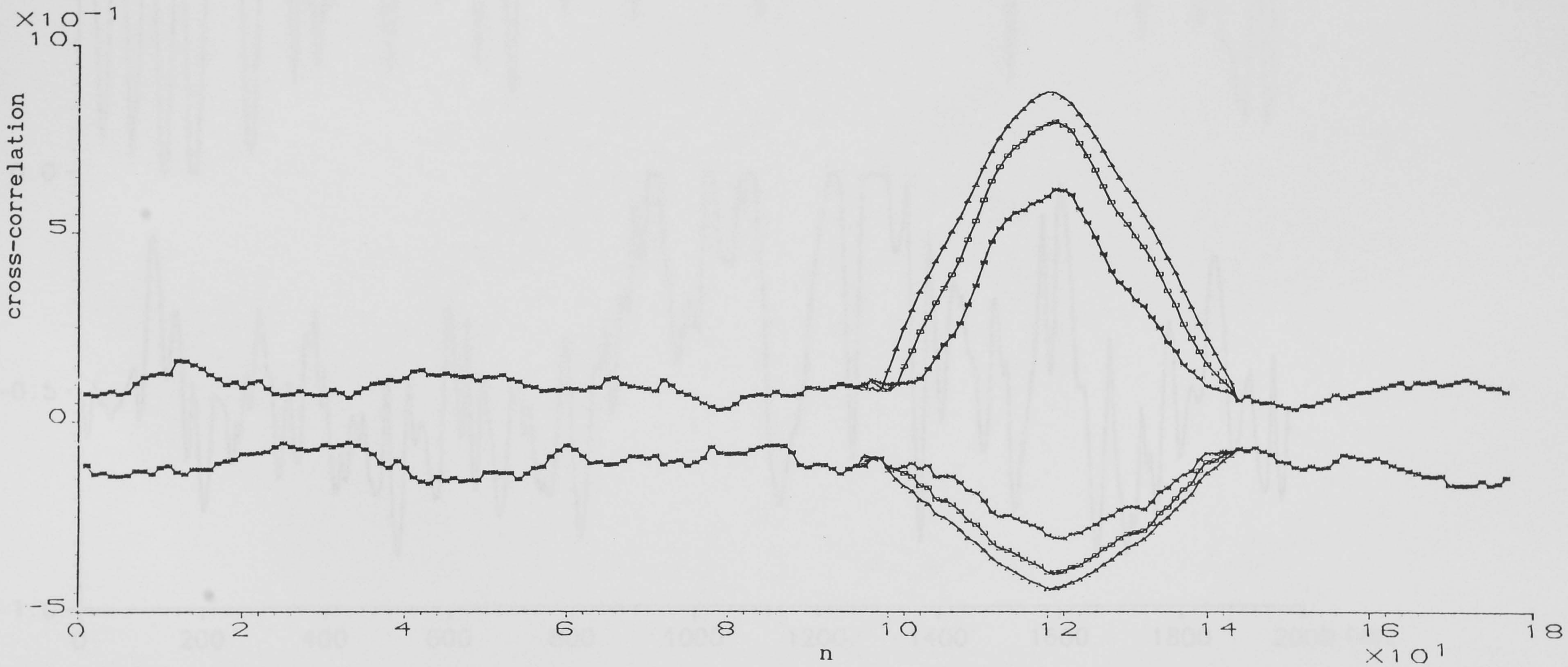

Fig. 6.1(c) Variation of the cross-correlation with noise-to-signal amplitude ratio. $\zeta = 0.5$, $\zeta = 1.0$, $\zeta = 2.0$.

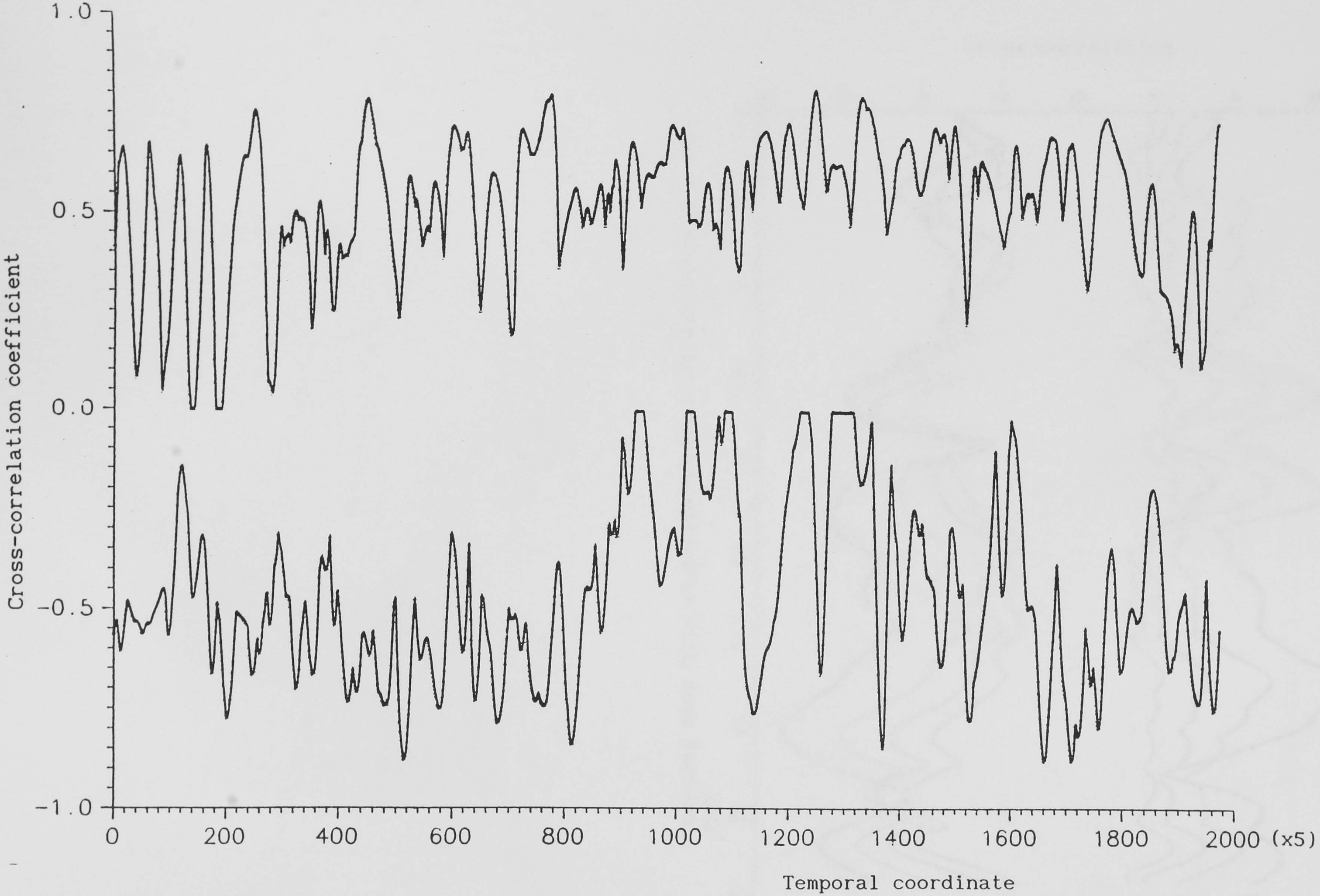

Fig. 6.2 Spanwise max. and min. cross-correlation.

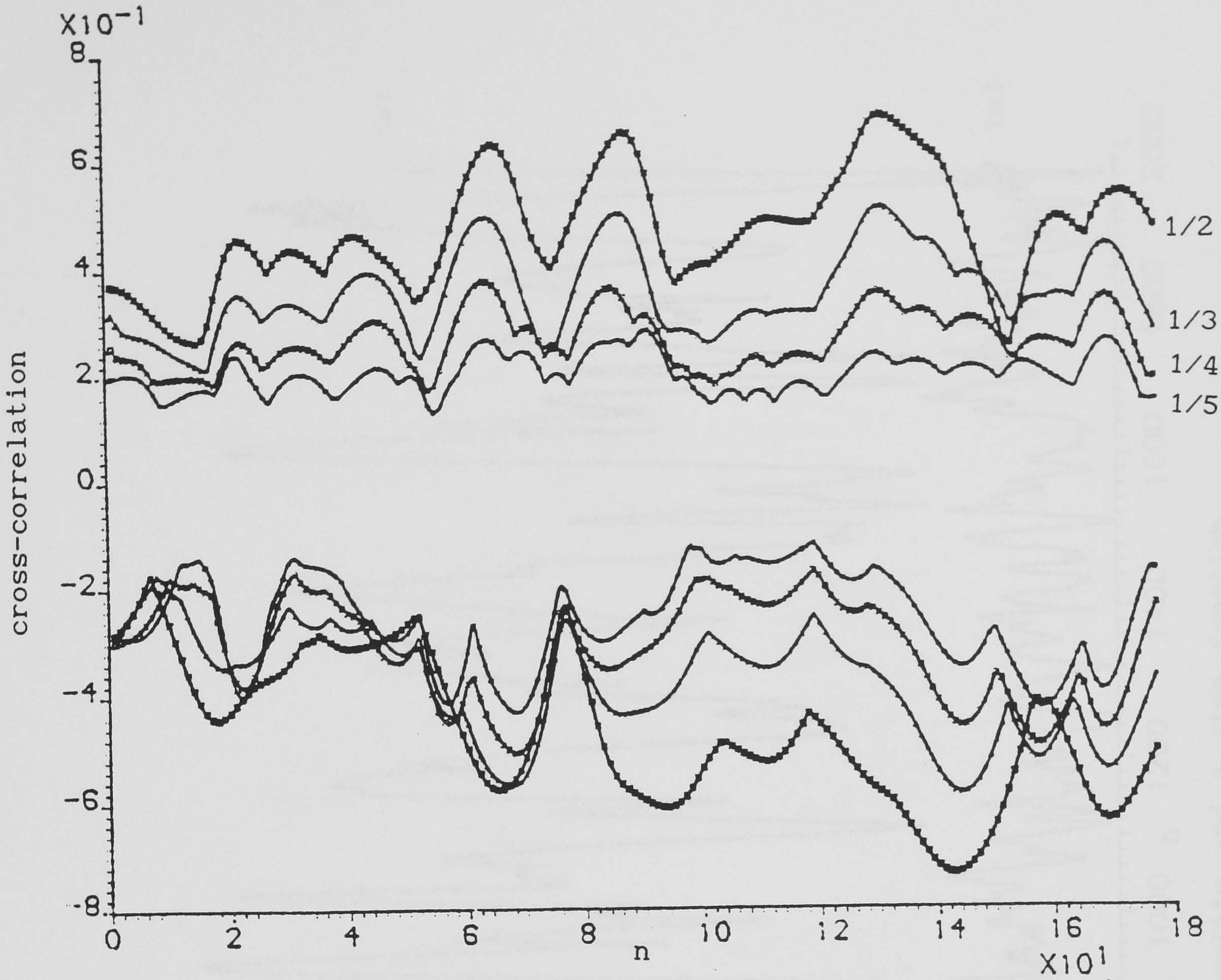

Fig. 6.3 Variation of cross-correlations with zoom factors.

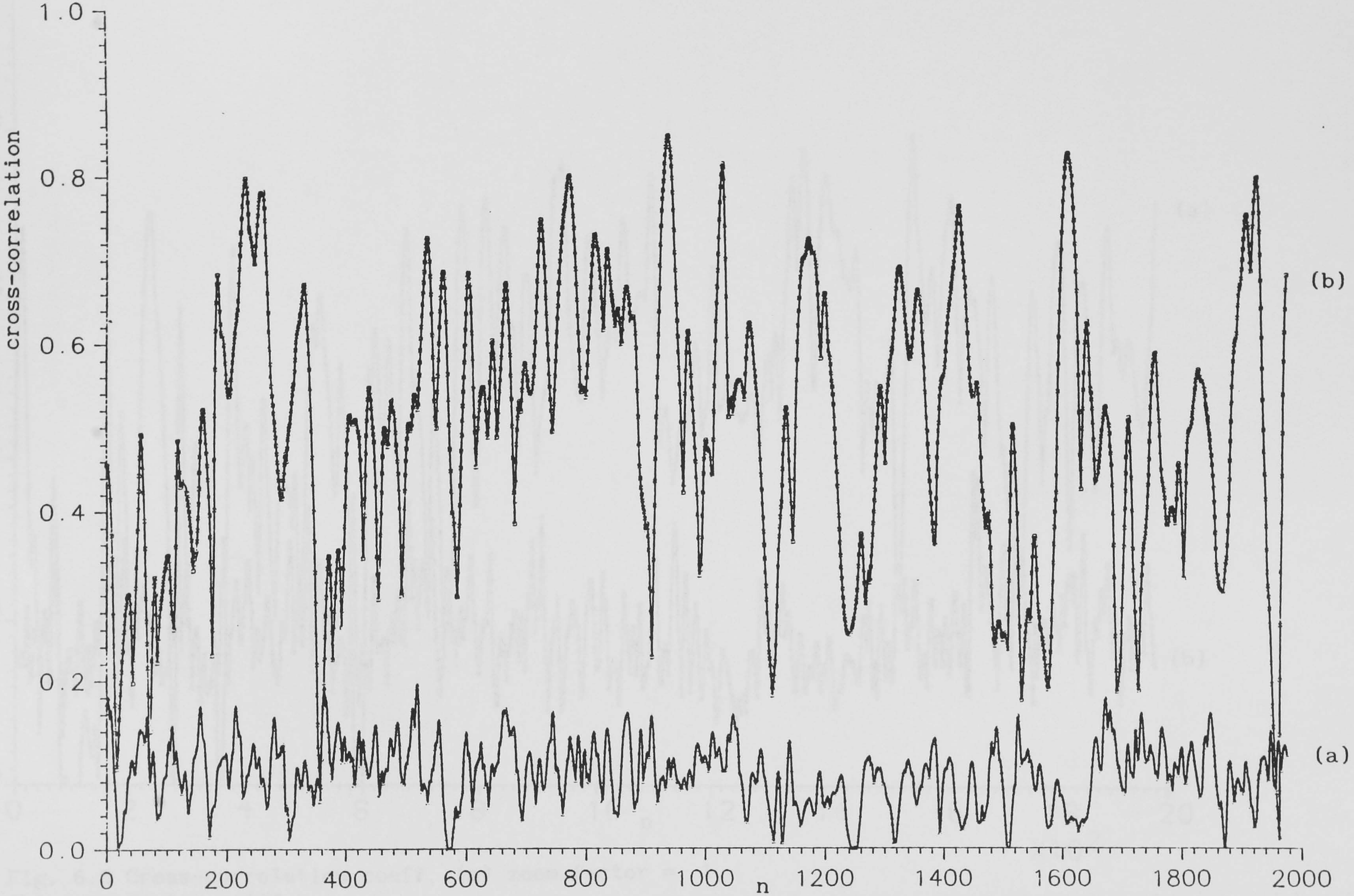

Fig. 6.4 Comparison between a random template and a step function template. (a) random template, (b) step function template.

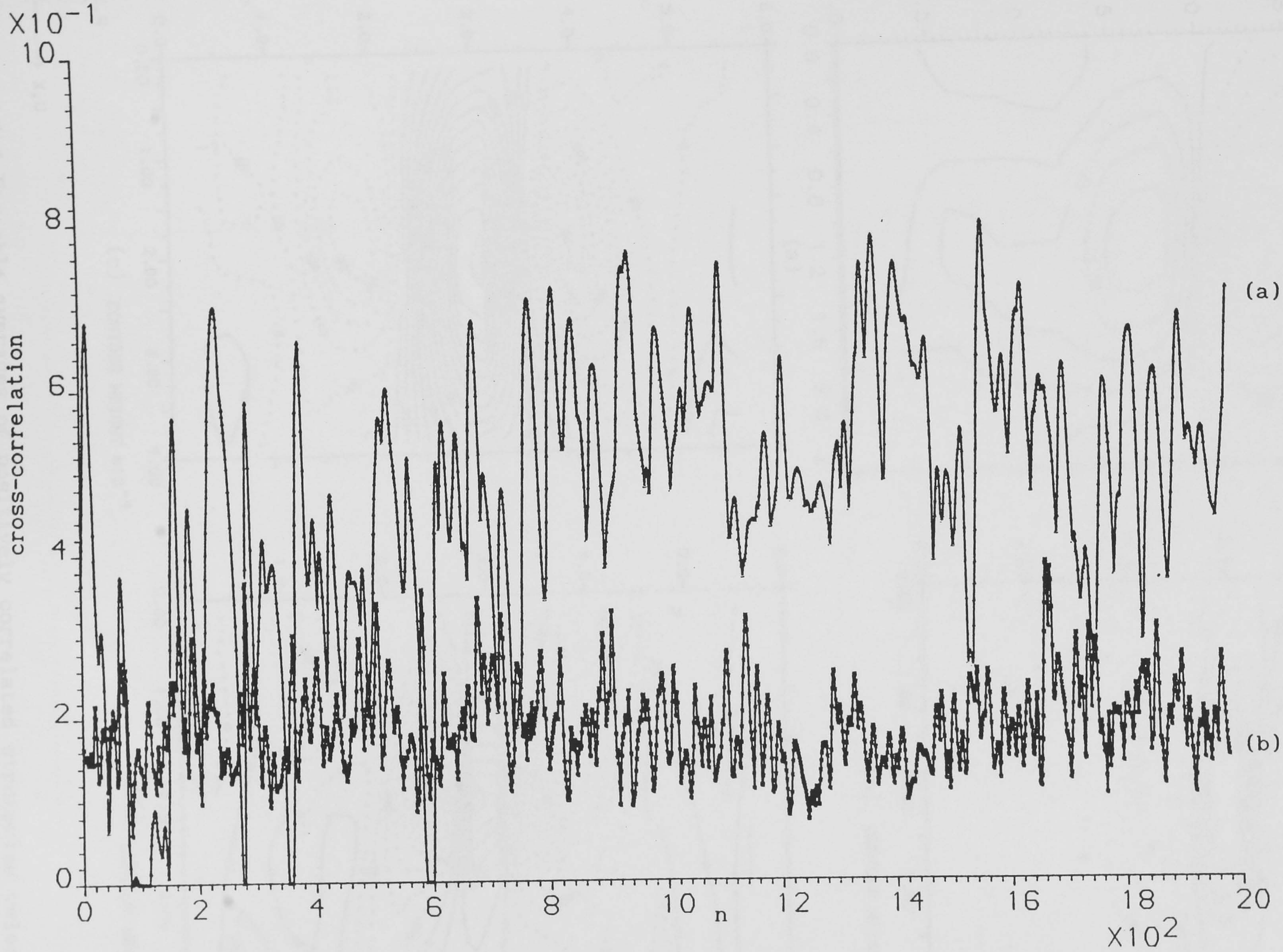

Fig. 6.5 Cross-correlation coeff. (a) zoom factor = 1,
(b) zoom factor = 1/4.

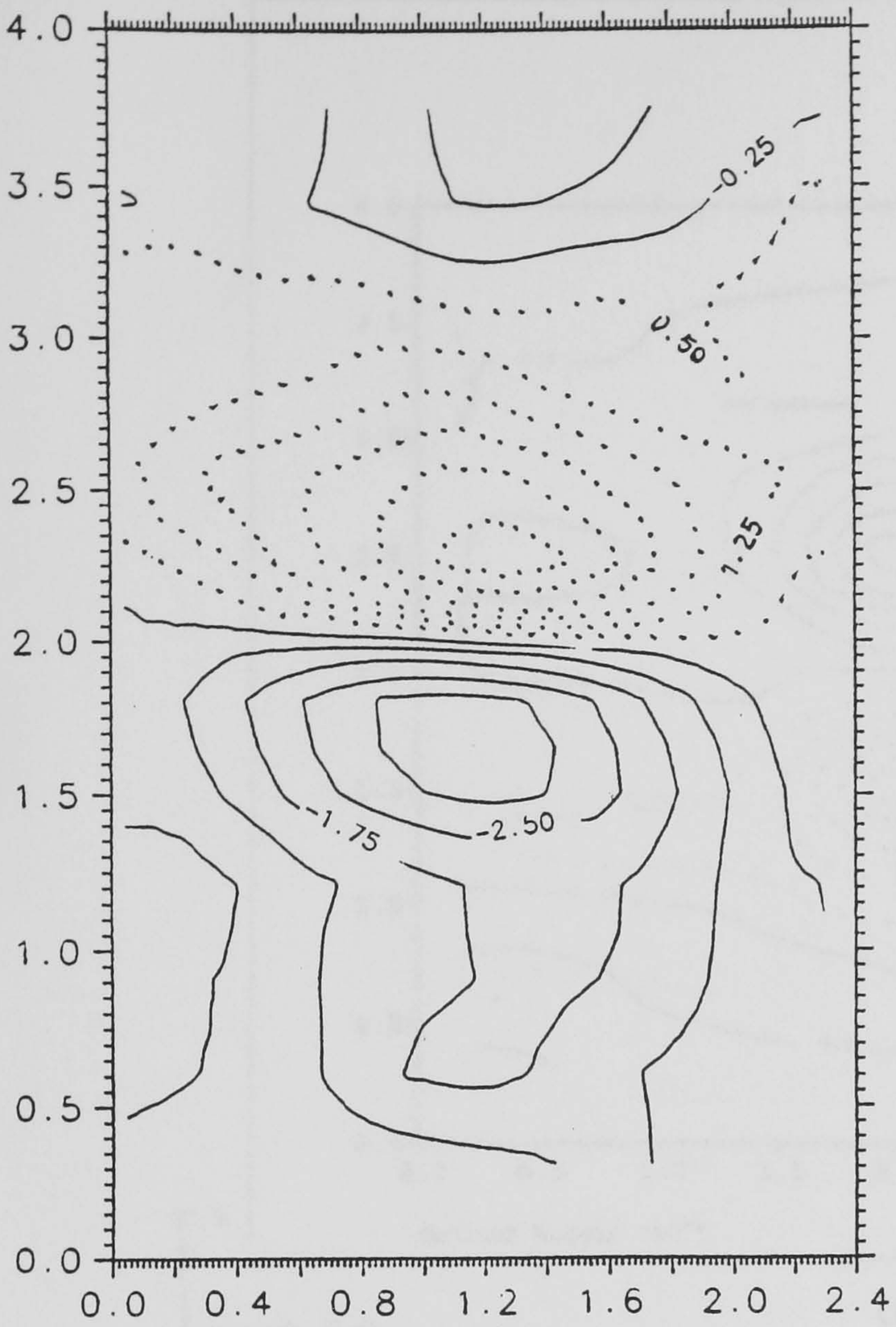

(a)

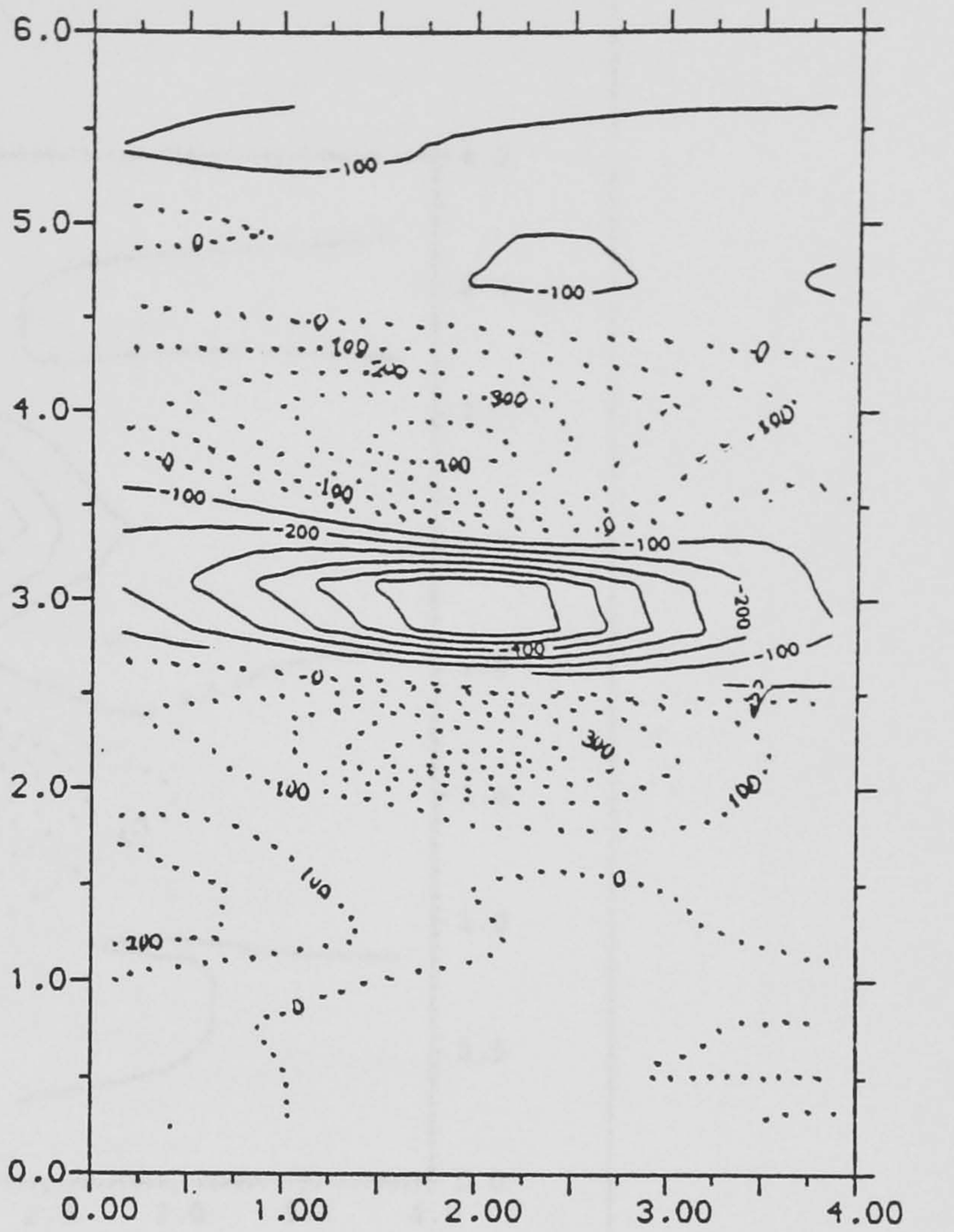

(b) CONTOUR HEIGHT $*10^{-4}$

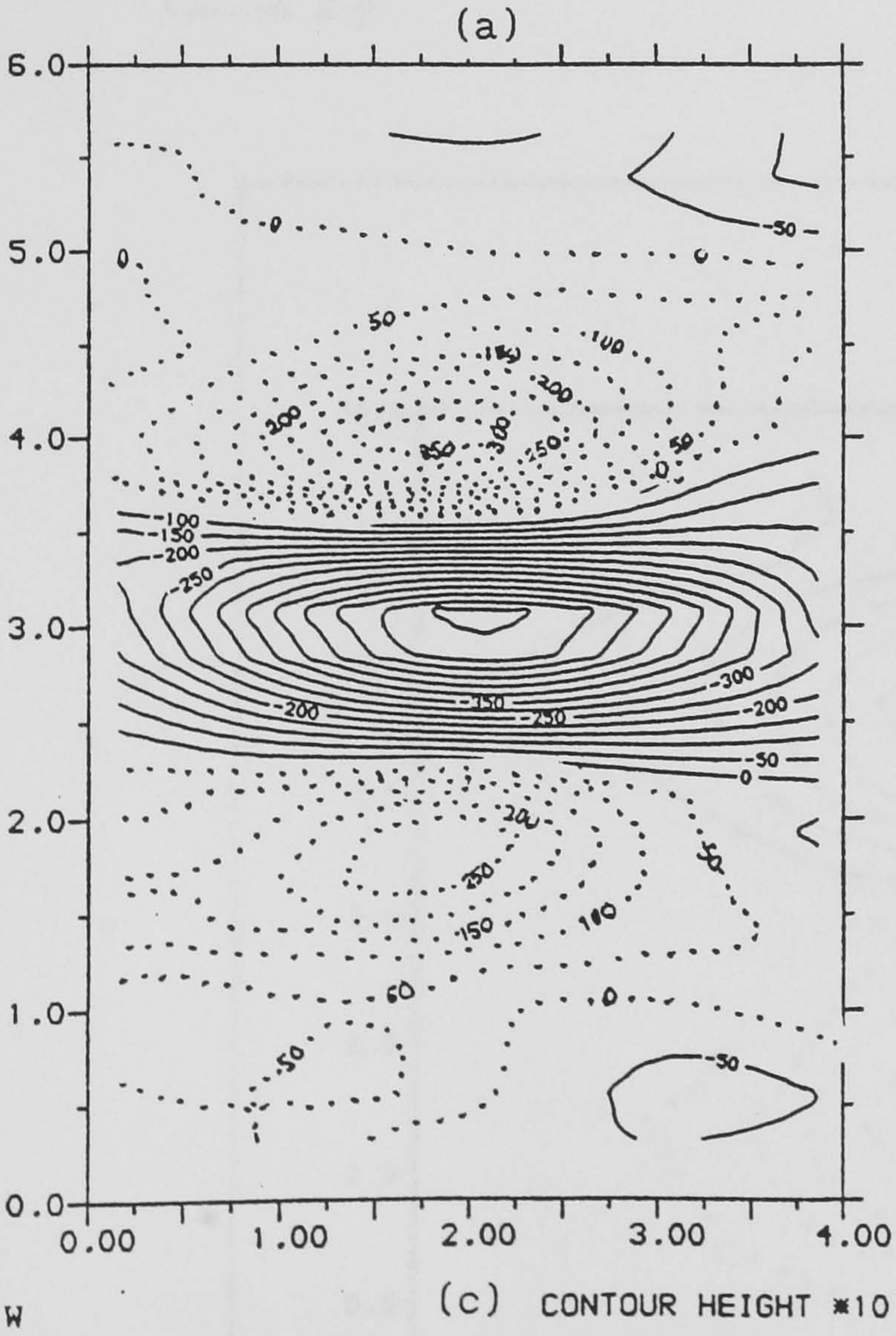

(c) CONTOUR HEIGHT $*10^{-4}$

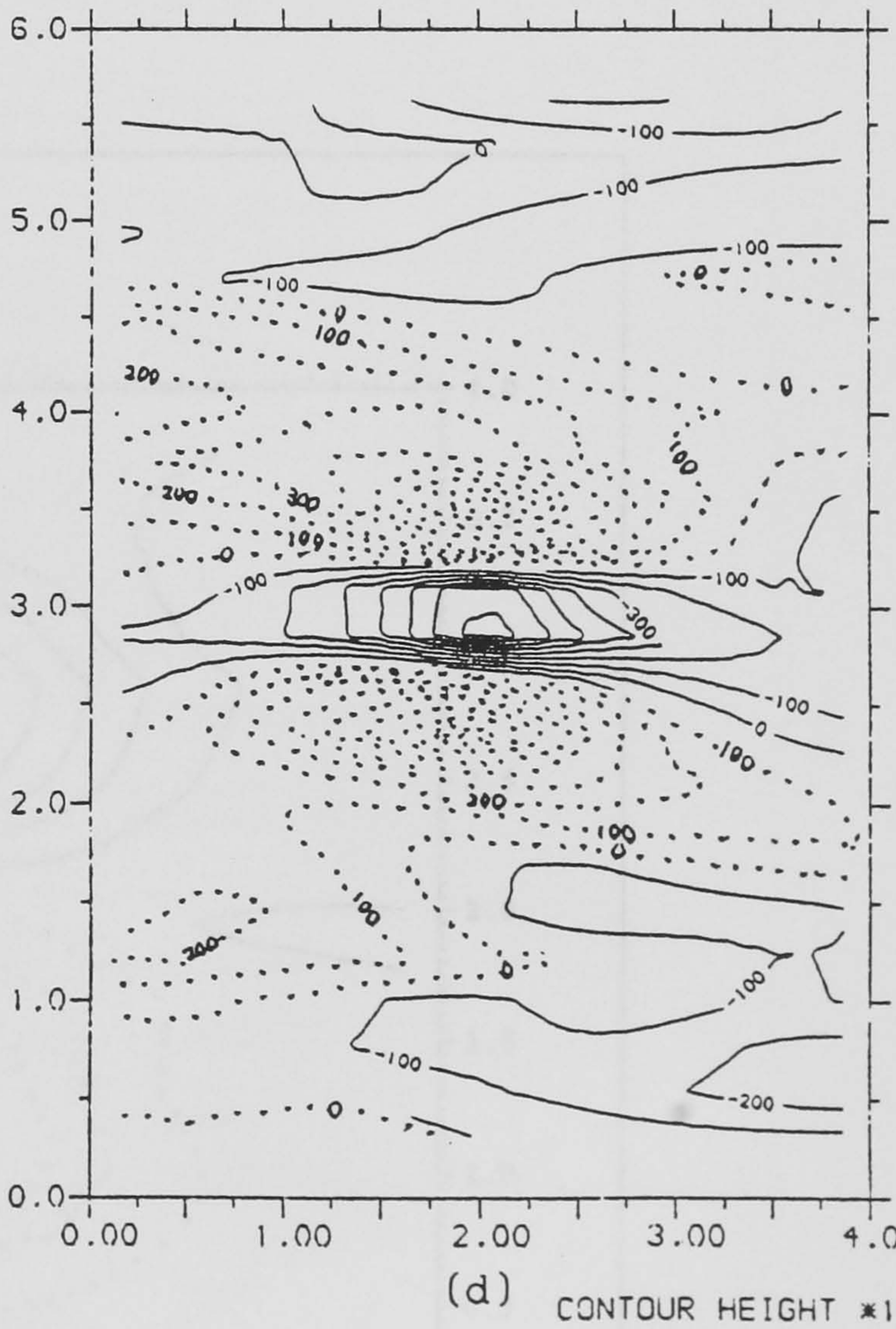

(d) CONTOUR HEIGHT $*10^{-4}$

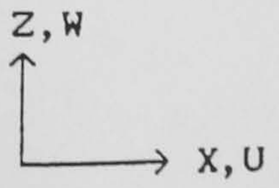

Fig. 6.6 Ensemble averages of positively correlated streamwise velocity fields, (a) single eddy pattern with 12x28 template; (b) vortex pair, zoom factor = 1 (c) zoom factor = 1.5 (d) zoom factor = 0.5 with a 18x48 template at y/l = 0.3, x/d = 18.

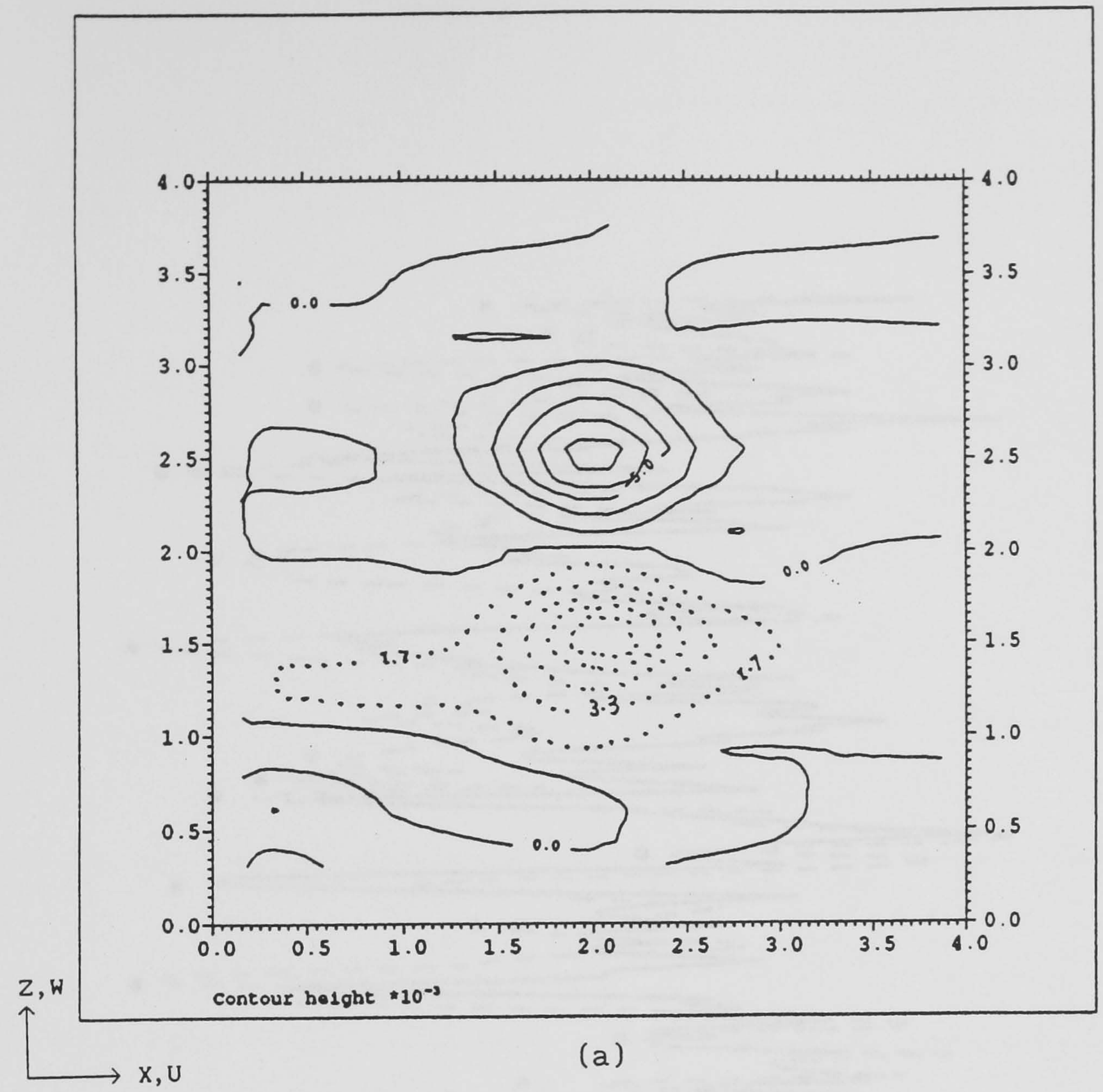

(a)

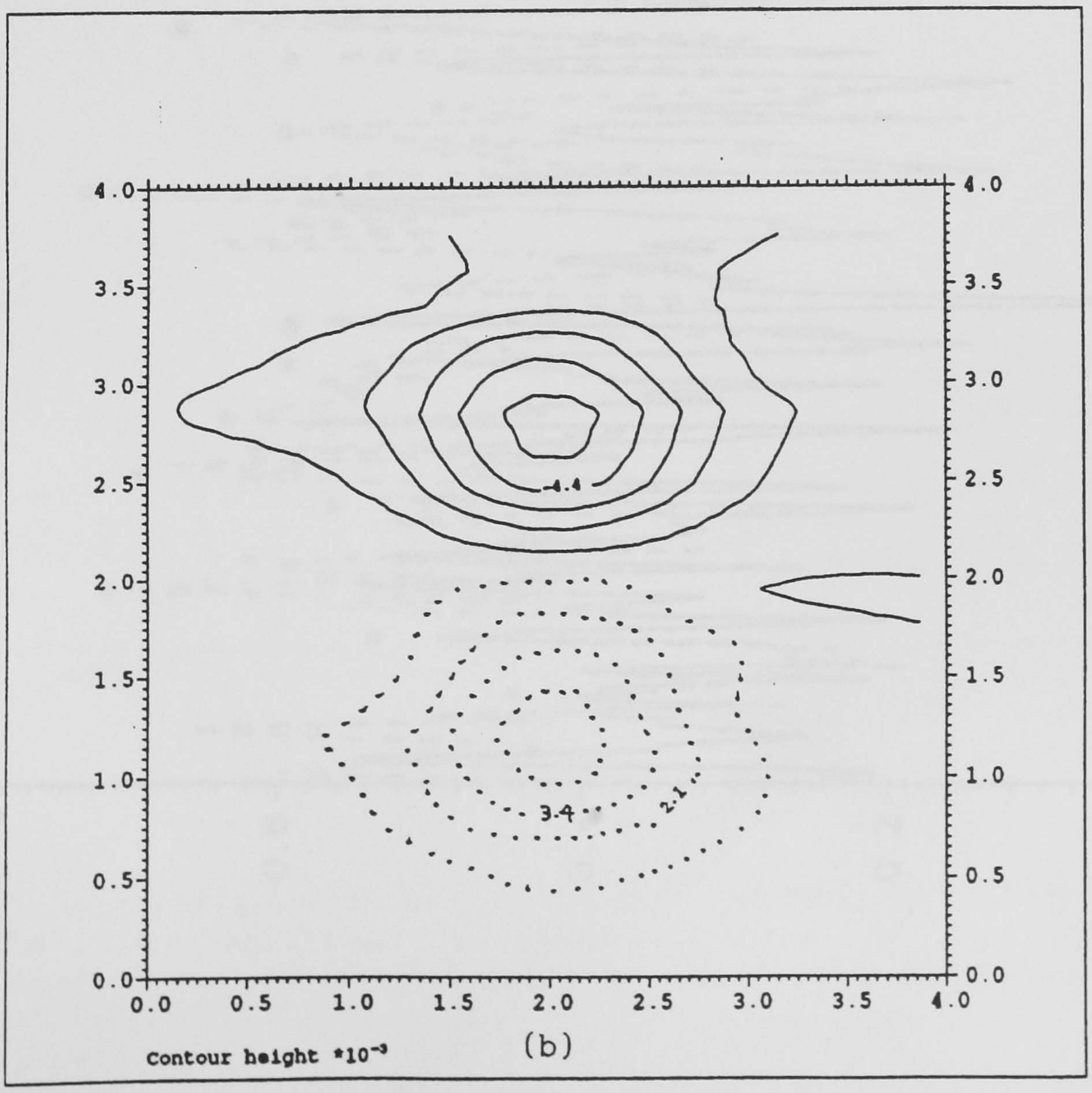

(b)

Fig. 6.7 Ensemble averages of vorticity $\langle\omega\rangle_{xz}$, (a) zoom factor = 1, (b) zoom factor = 1.5 with a 12x48 vorticity template at y/l = 0.3, x/d =18.

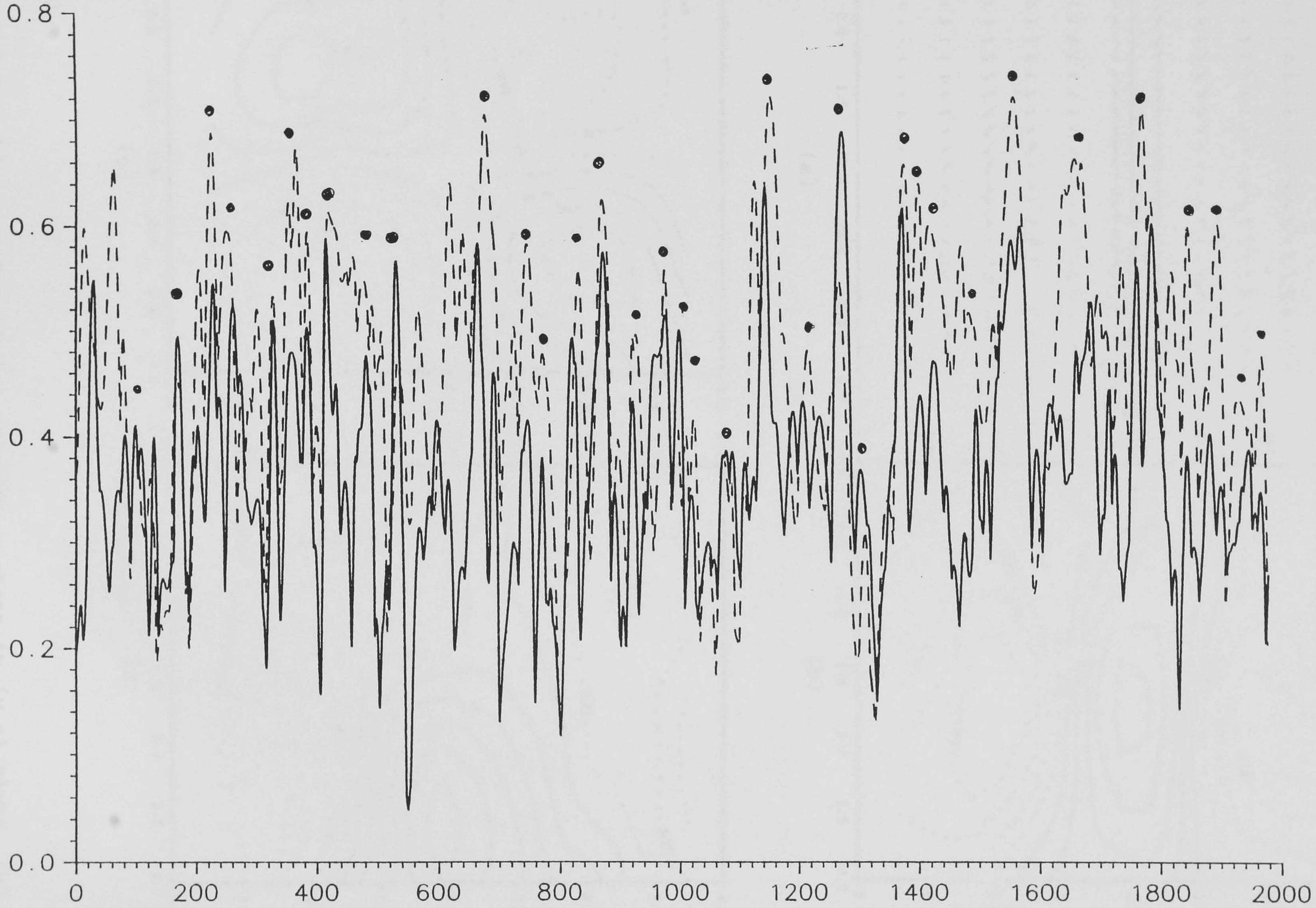

Fig. 6.8 Cross-correlation curves of (a) ——— vorticity, (b) ------ streamwise velocity; ∘ the peaks are in phase.

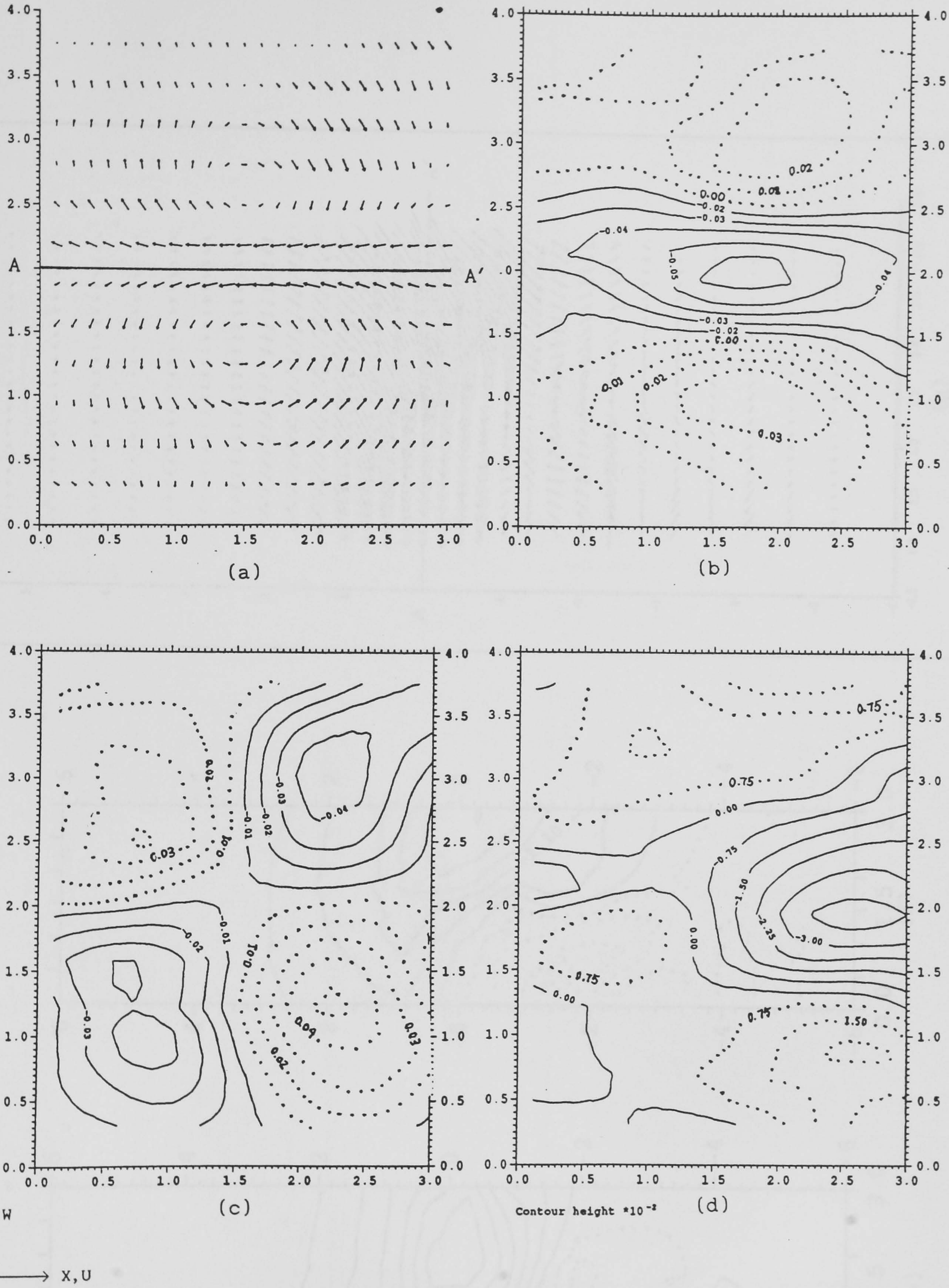

Fig. 6.9 Ensemble averages of (a) velocity vectors in (x,z) plane, (b) <u>xz, (c) <w>xz, (d) <v>xz, (e) <u>xy, (f) <v>xy, (g) velocity vectors in the (x,y) plane, at y/l = 0, x/d = 18. Positively correlated velocity vector fields.

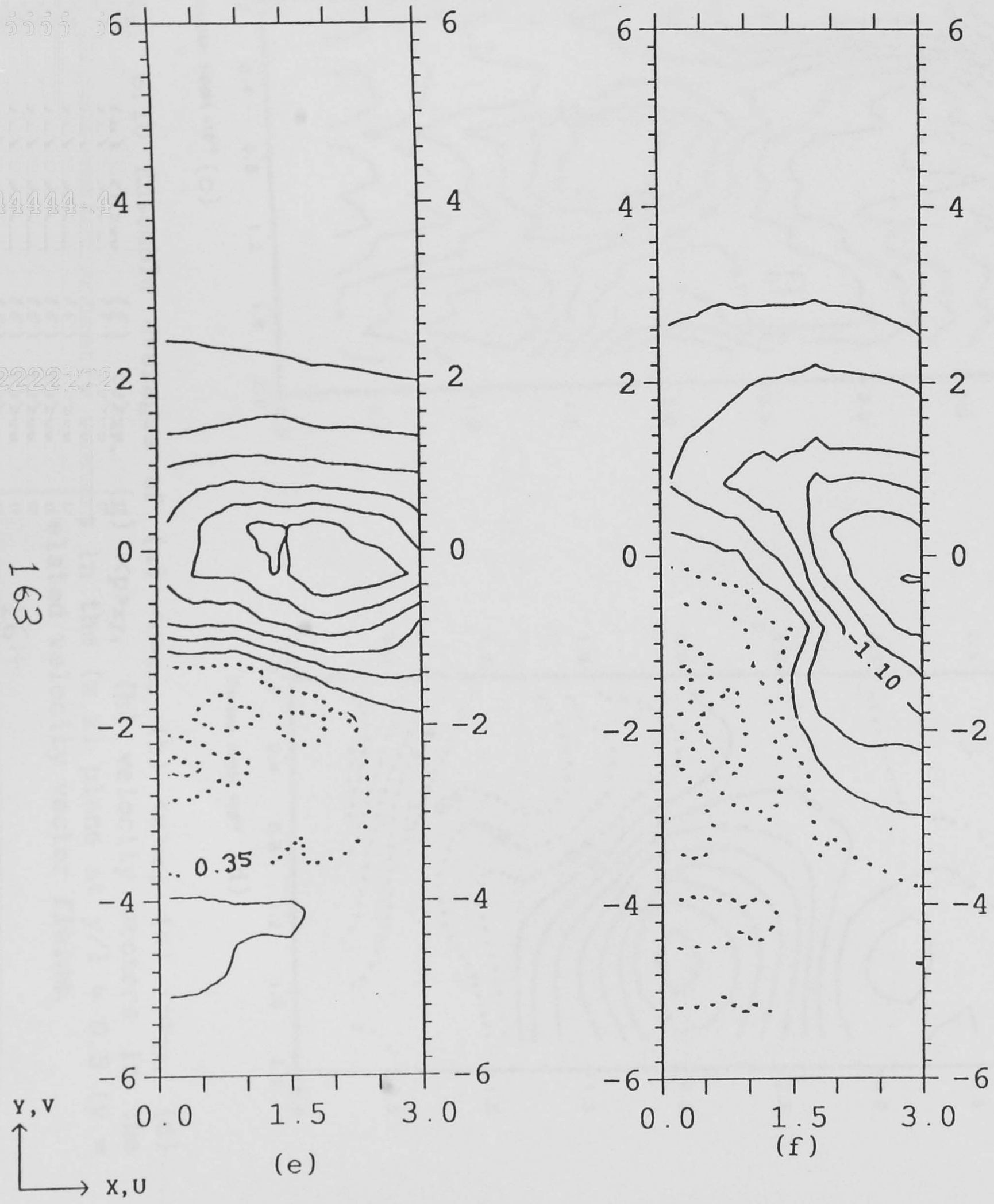

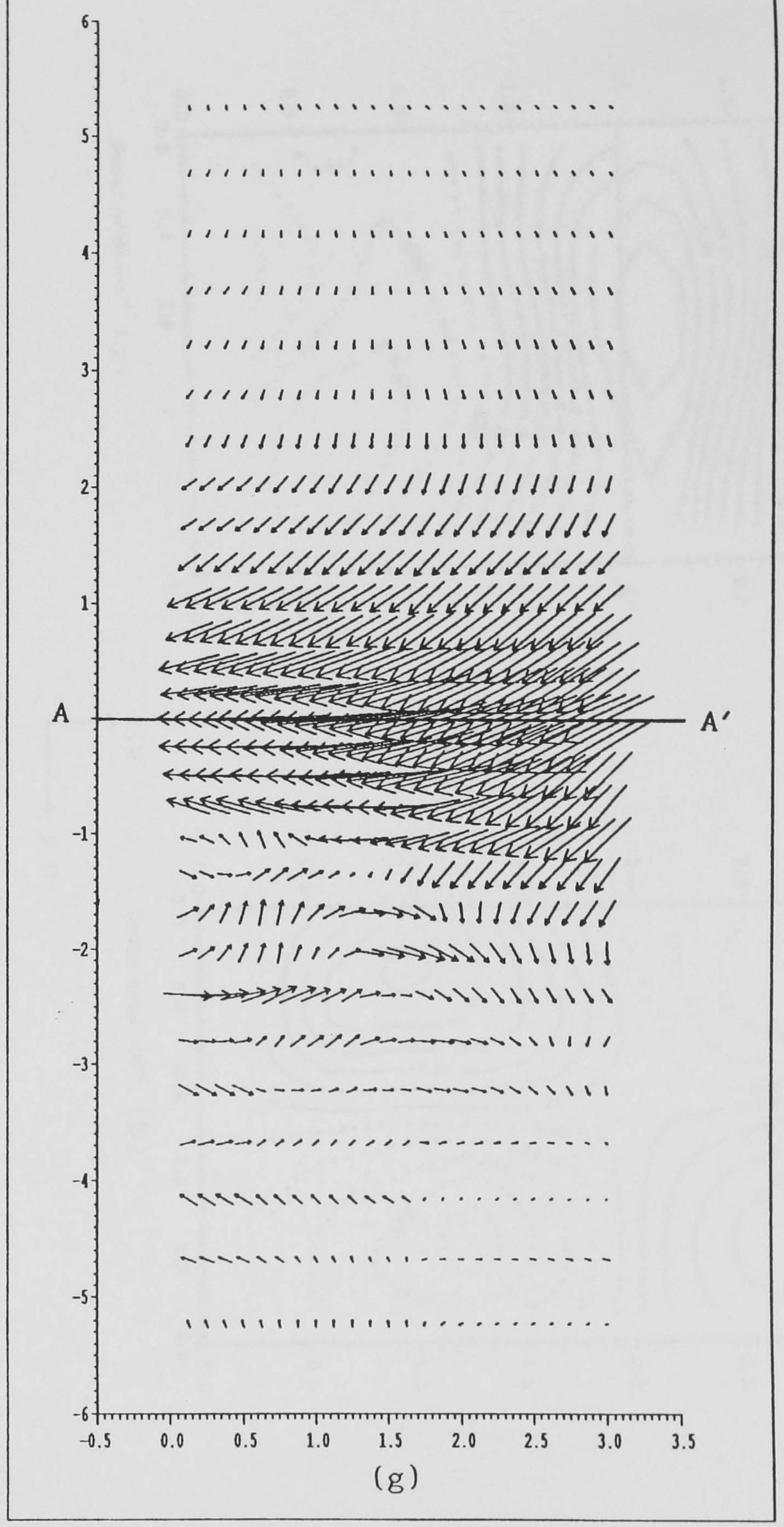

Fig. 6.9 (continued)

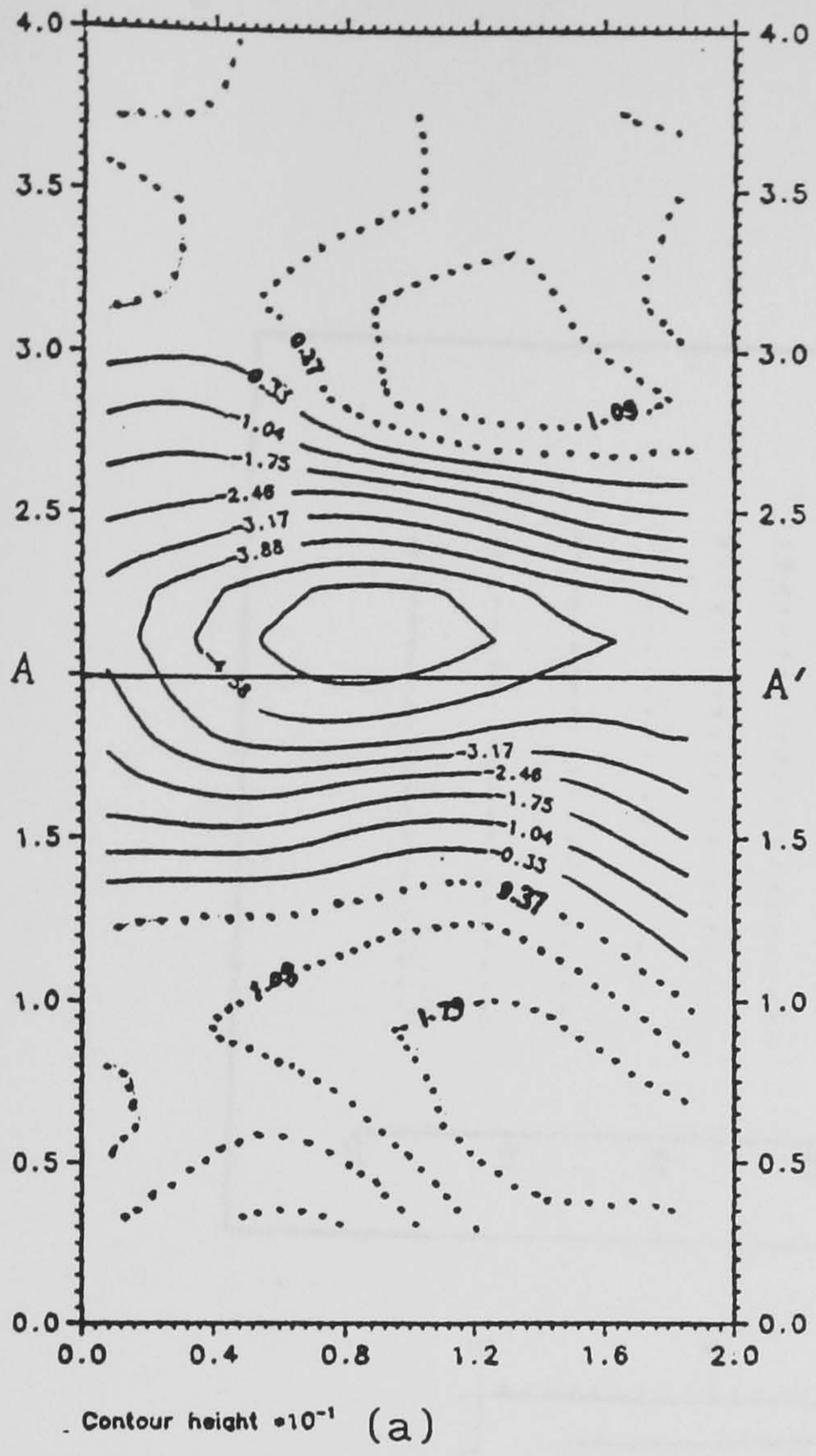

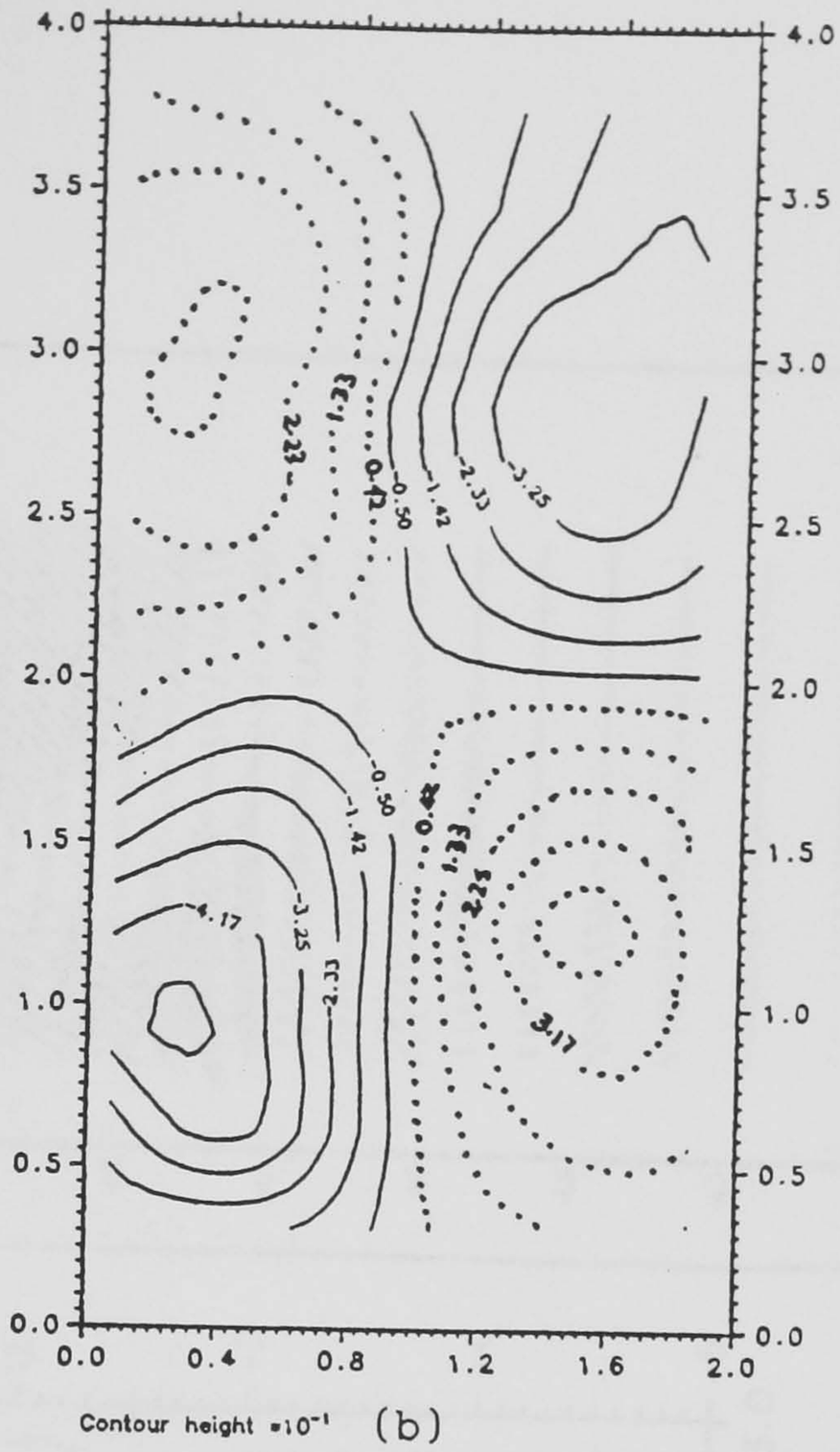

Z, W

X, U

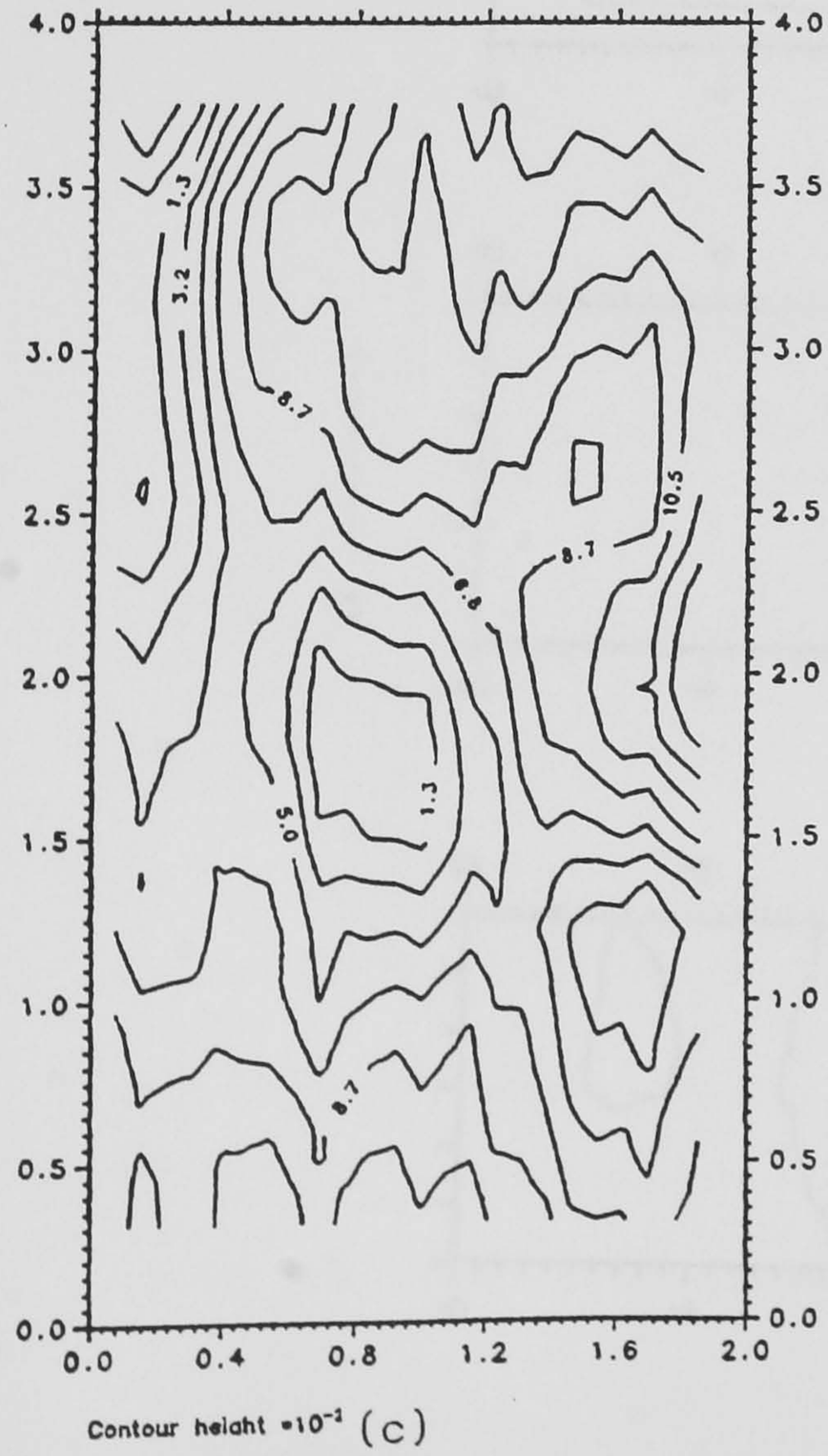

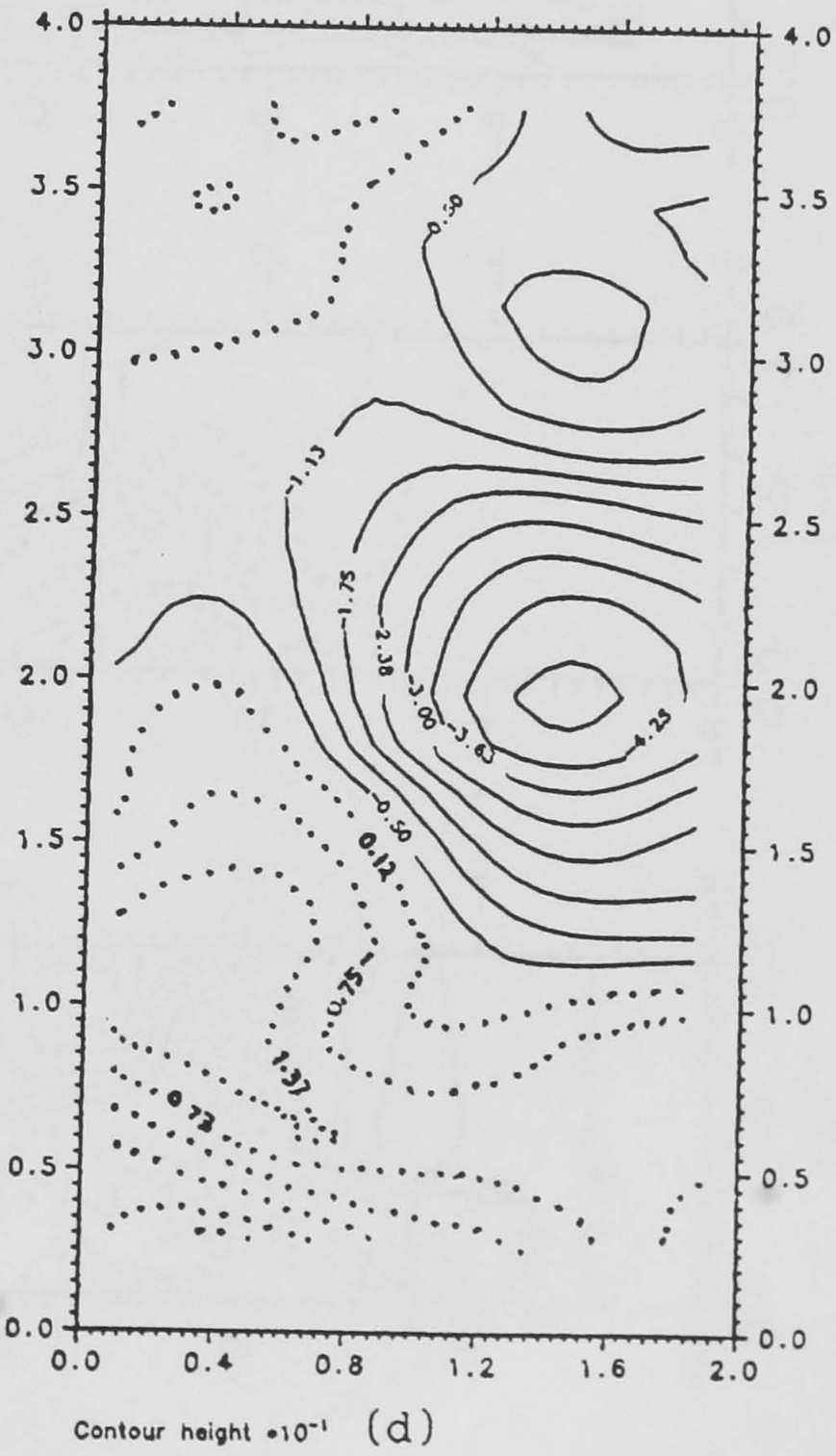

Fig. 6.10 Ensemble averages of (a) <u>xz, (b) <w>xz, (c) <p>xz, (d) <v>xz, (e) <u>xy, (f) <v>xy, (g) <p>xy, (h) velocity vectors in the (x, y) plane, (i) velocity vectors in the (x, z) plane at y/l = 0.3 (y = 0.767). x/d = 18. Positively correlated velocity vector fields.

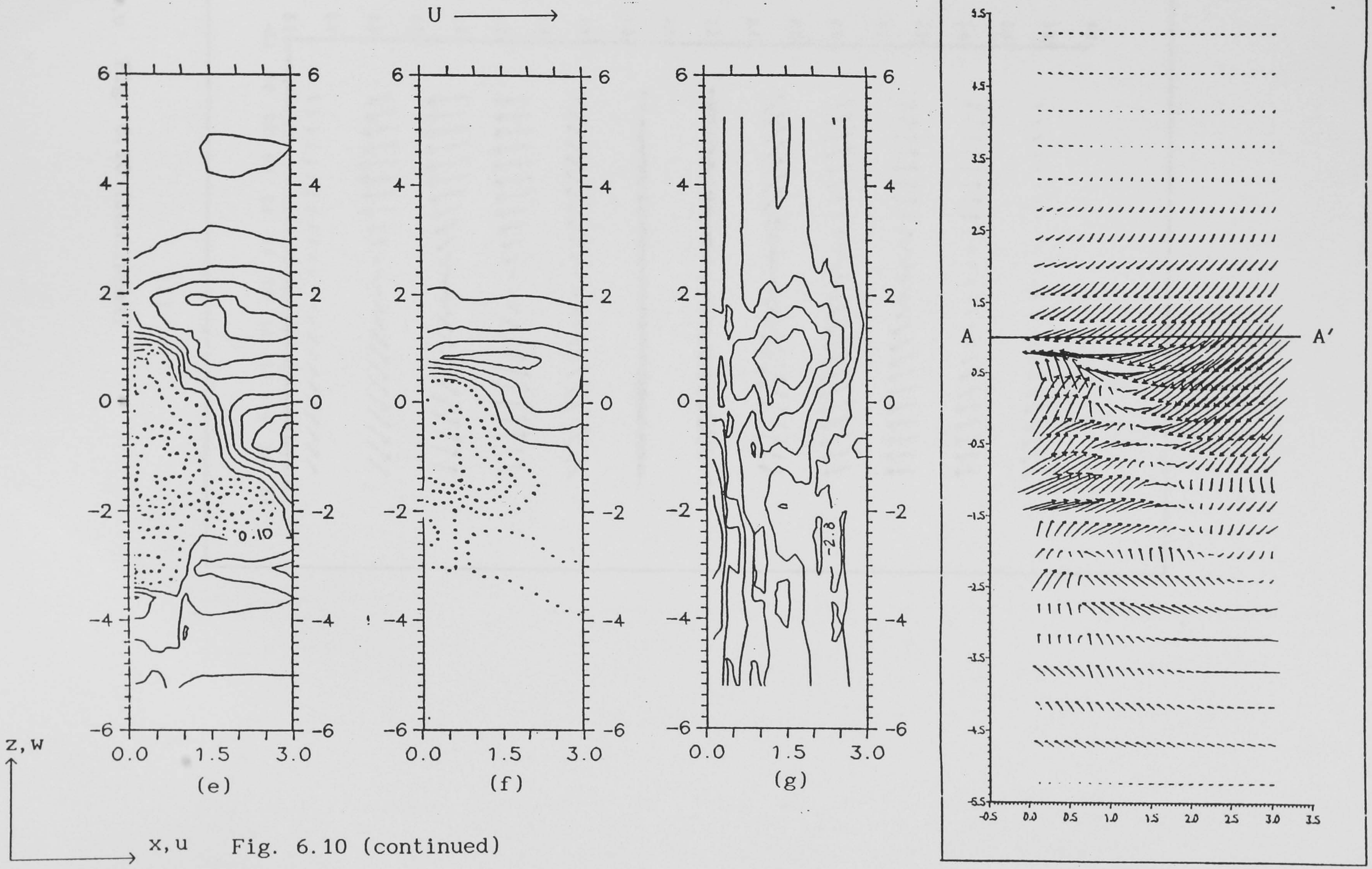

Fig. 6.10 (continued)

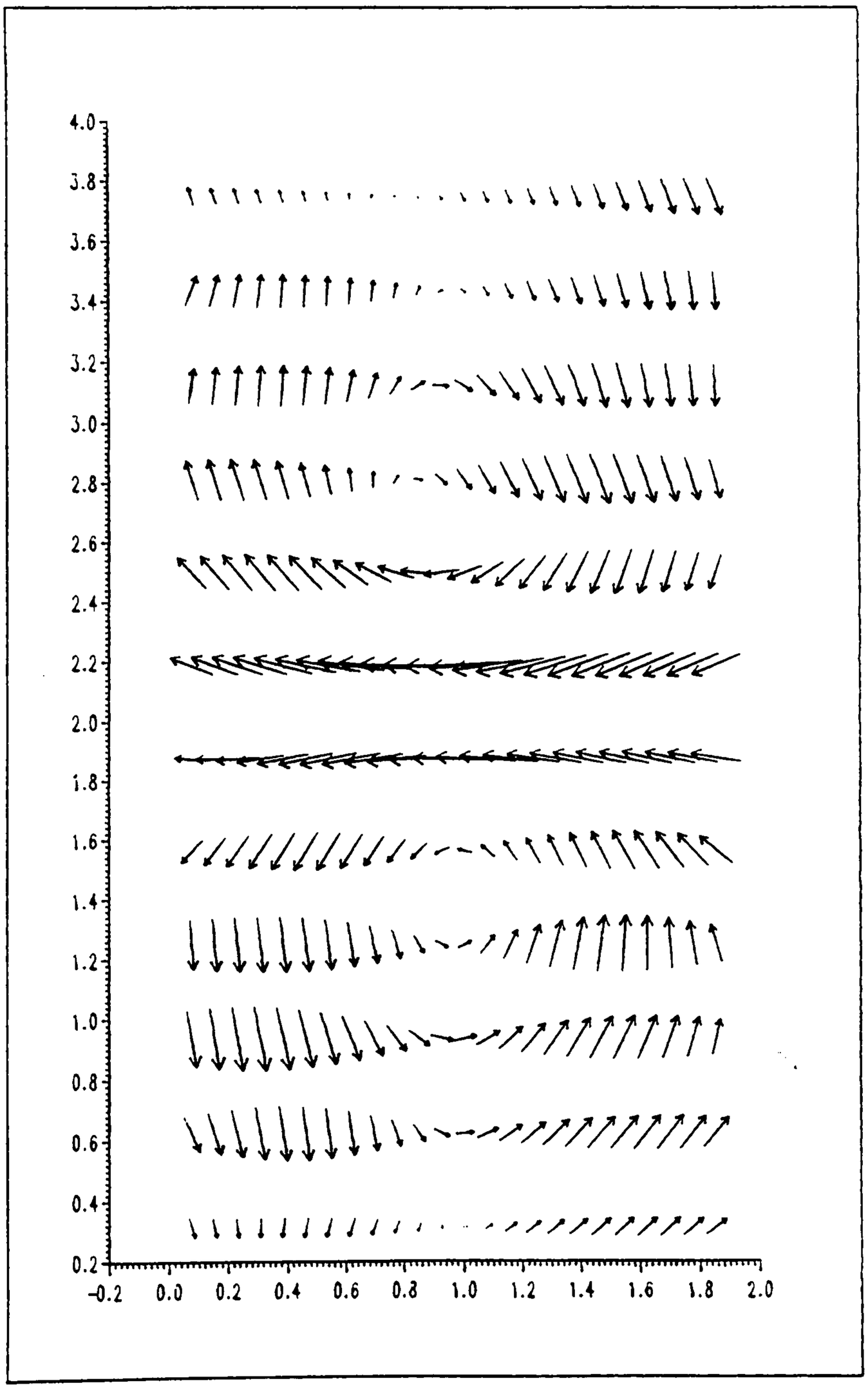

(i)

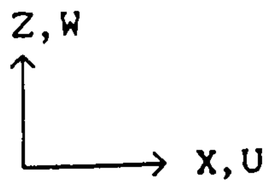

Fig. 6.10 (continued)

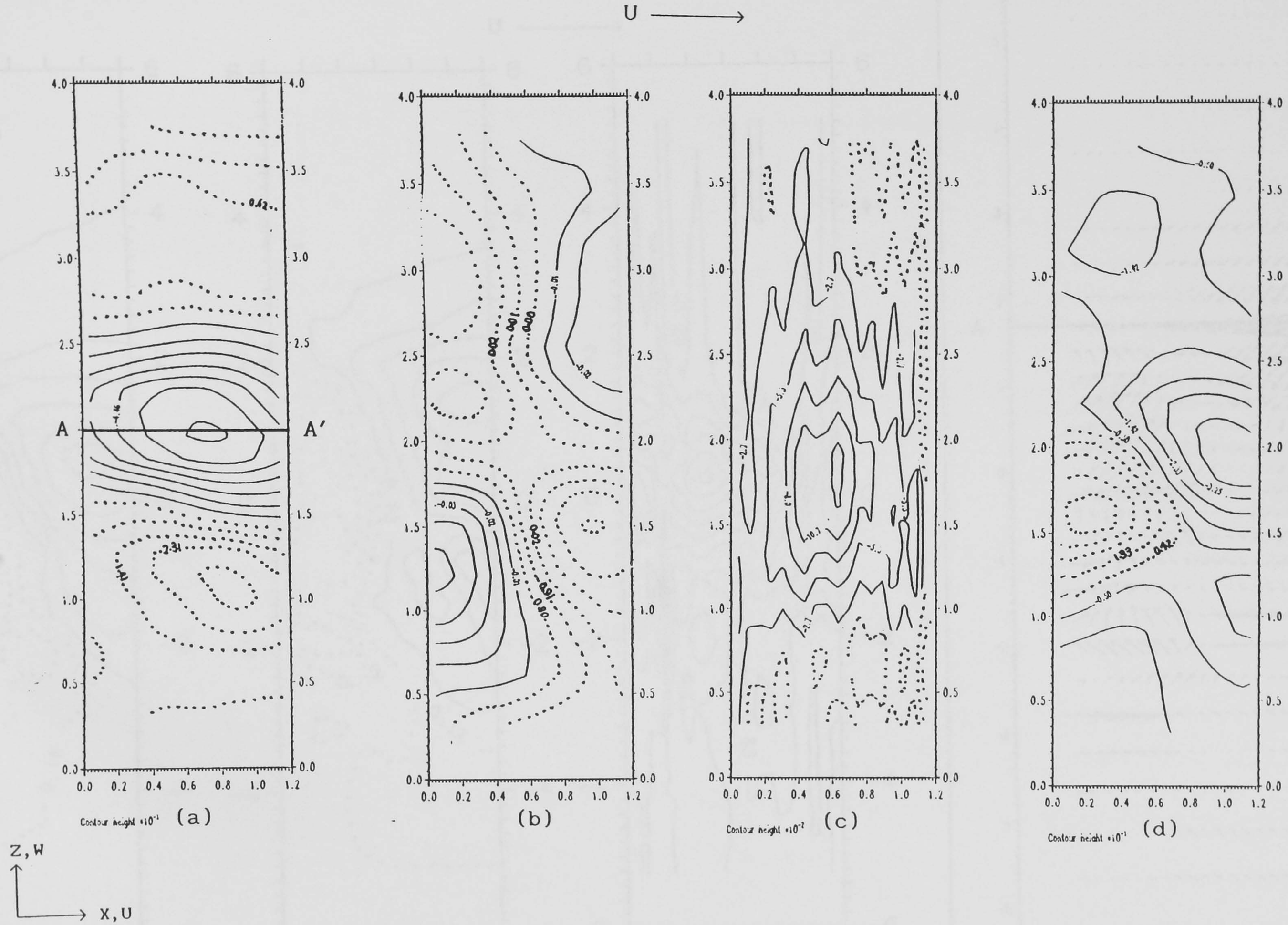

Fig. 6.11 Ensemble averages of (a) <u>xz, (b) <w>xz, (c) <p>xz, (d) <v>xz, (e) <u>xy, (f) <v>xy, (g) <p>xy, (h) velocity vectors in the (x,y) plane at y/l = 0.67 (y = 1.68). Positively correlated velocity vector fields.

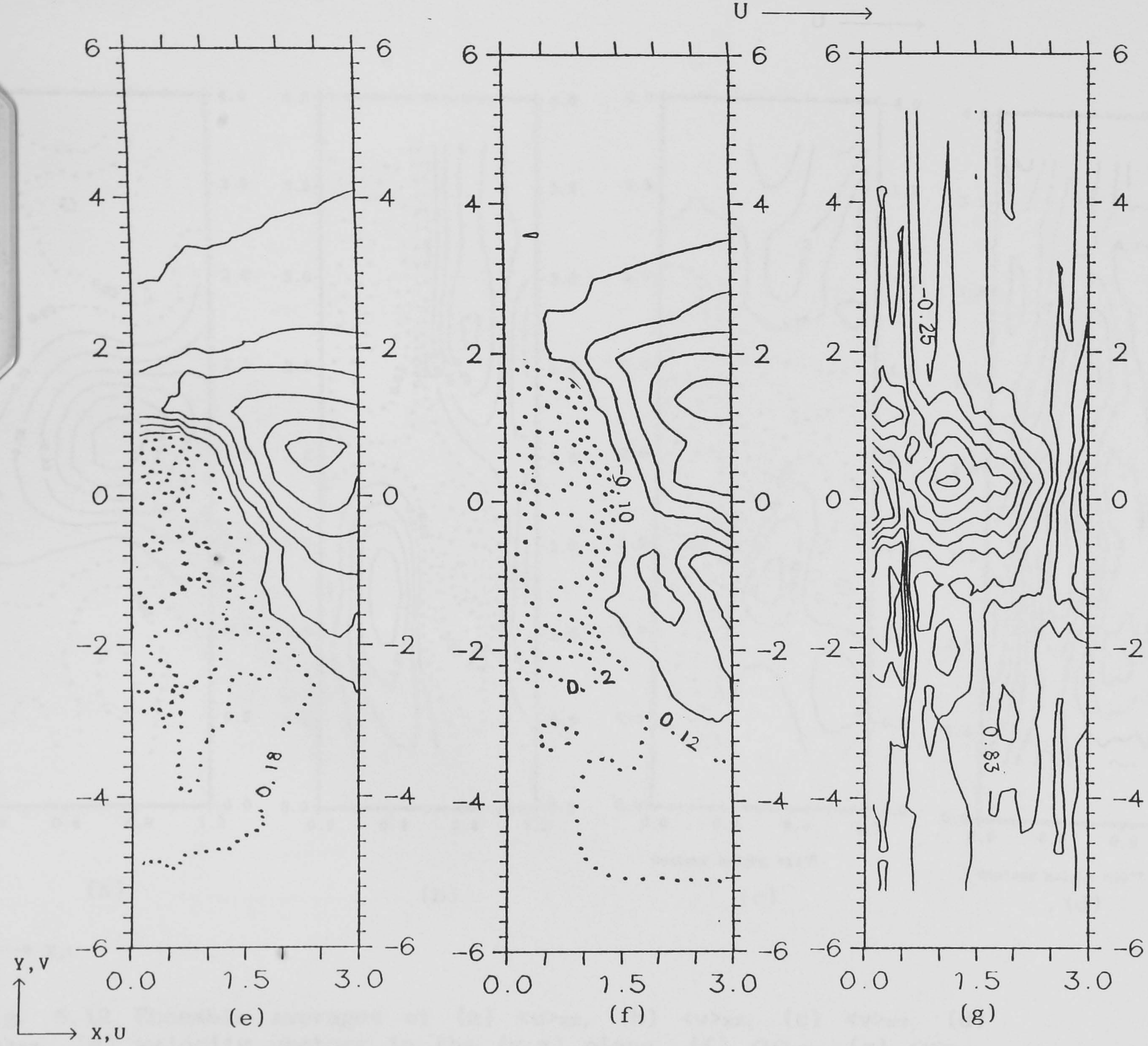

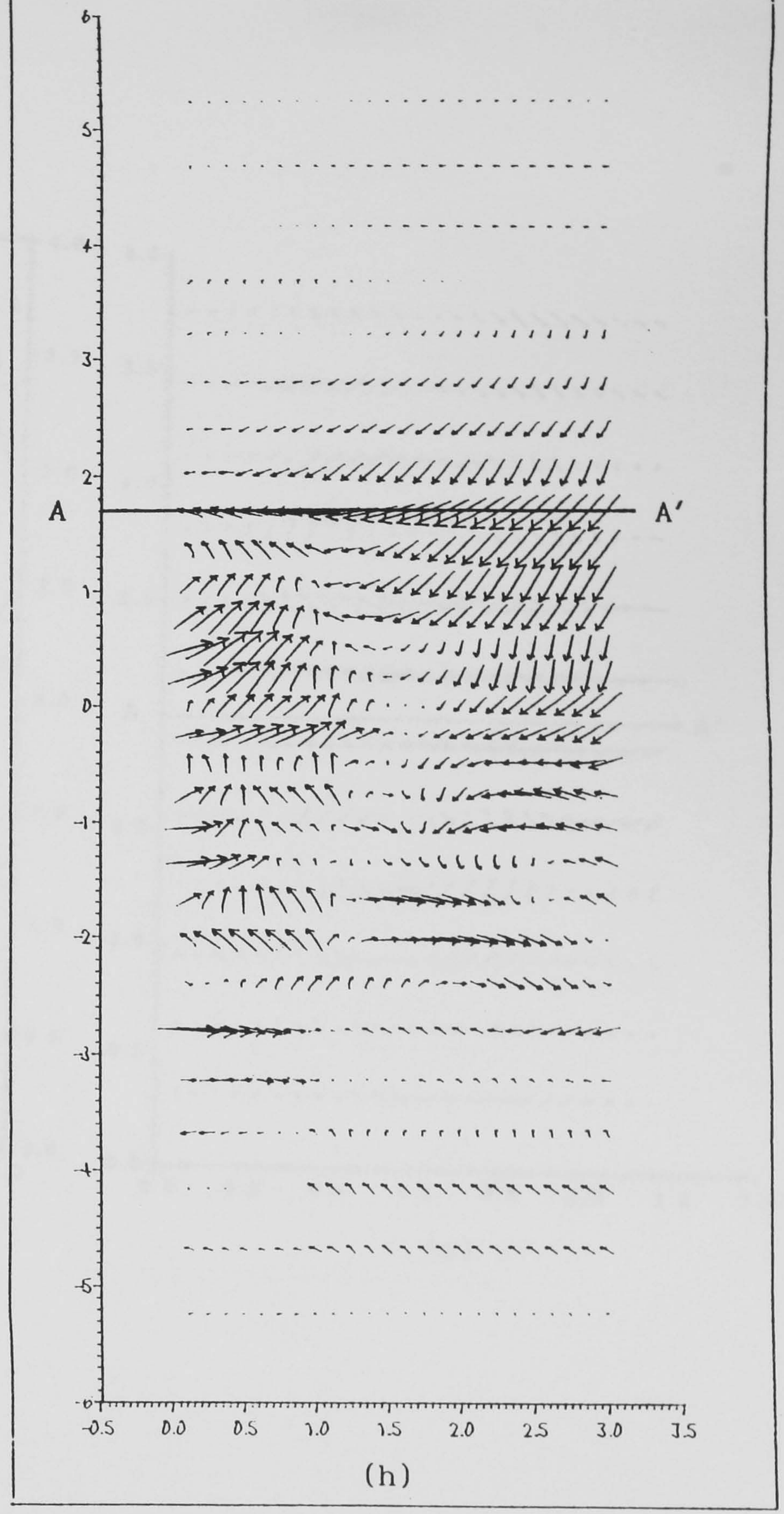

Fig. 6.11 (continued)

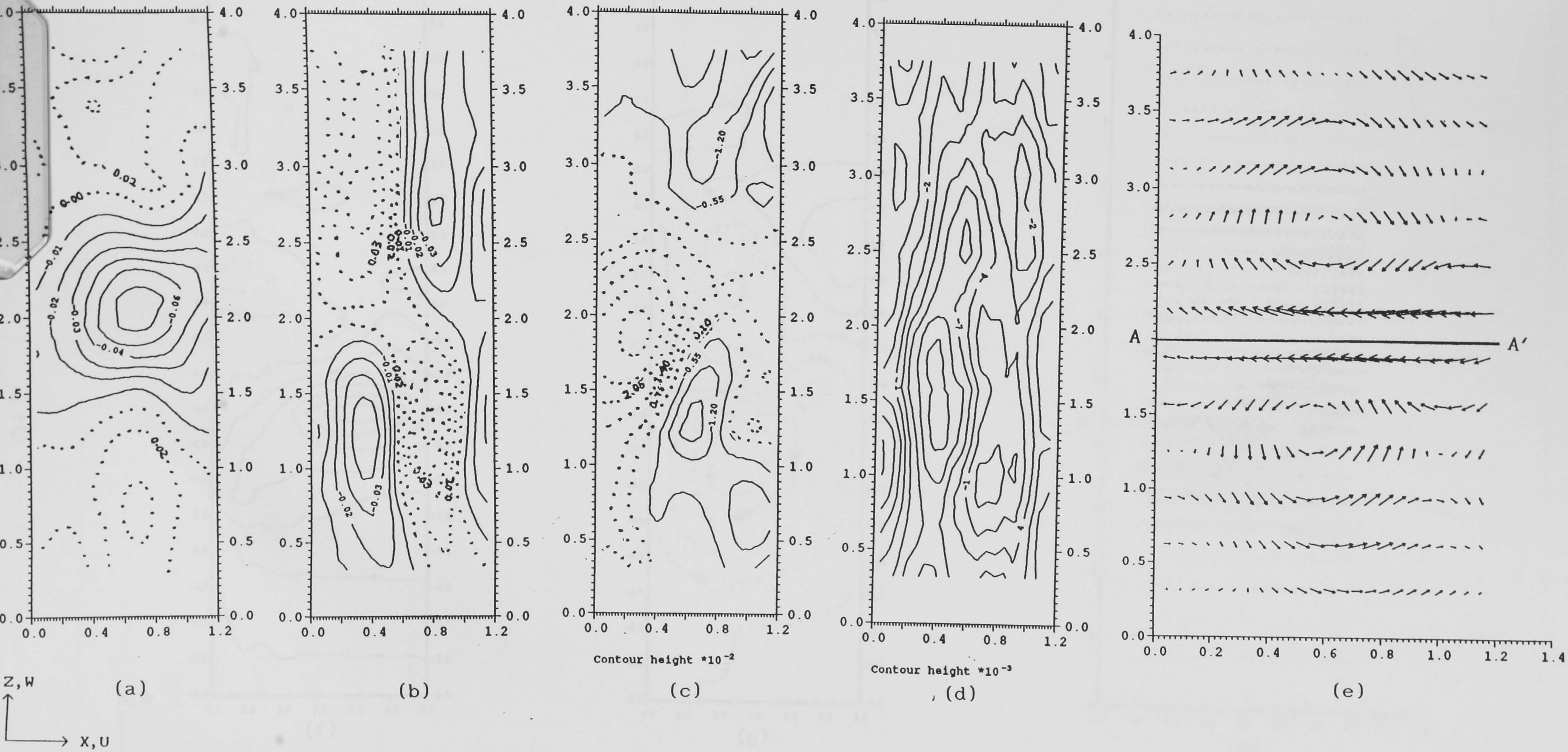

Fig. 6.12 Ensemble averages of (a) <u>xz, (b) <w>xz, (c) <v>xz, (d) <p>xz, (e) velocity vectors in the (x,z) plane, (f) <u>xy, (g) <v>xy, (h) velocity vectors in the (x,y) plane at y/l = -0.67 (y = -1.68). Positively correlated vector fields.

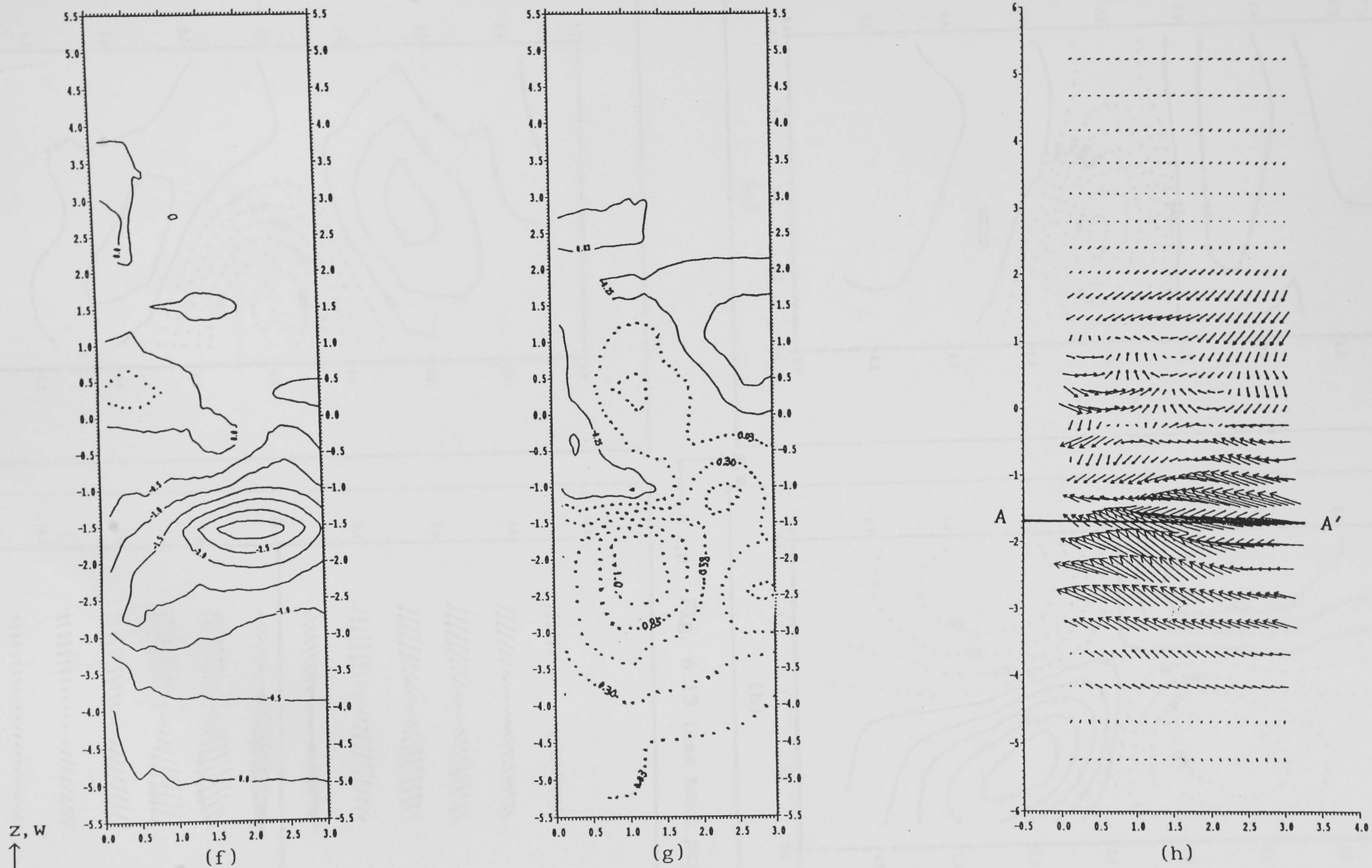

Fig. 6.12 (continued)

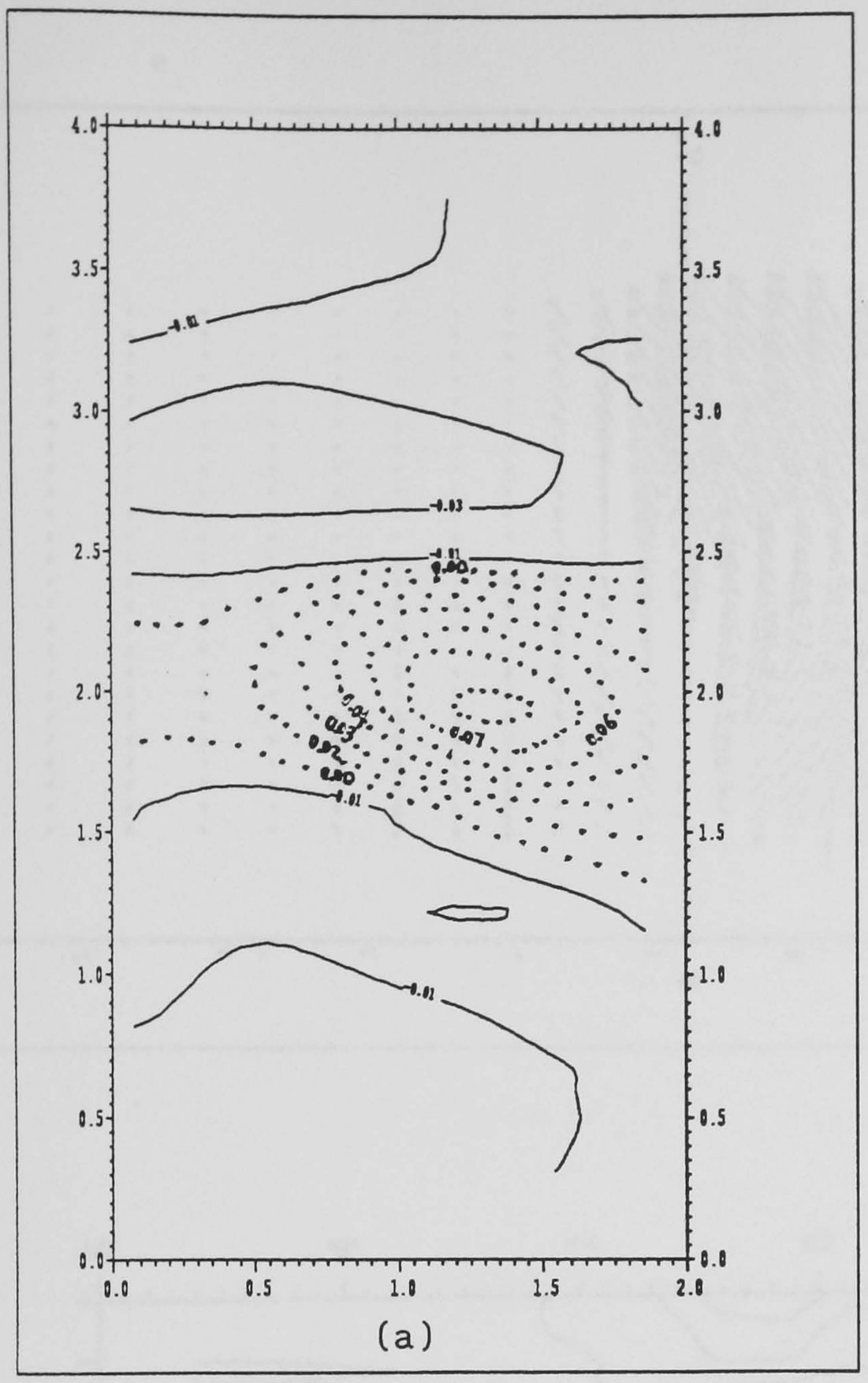

Fig. 6.13 (see next page)

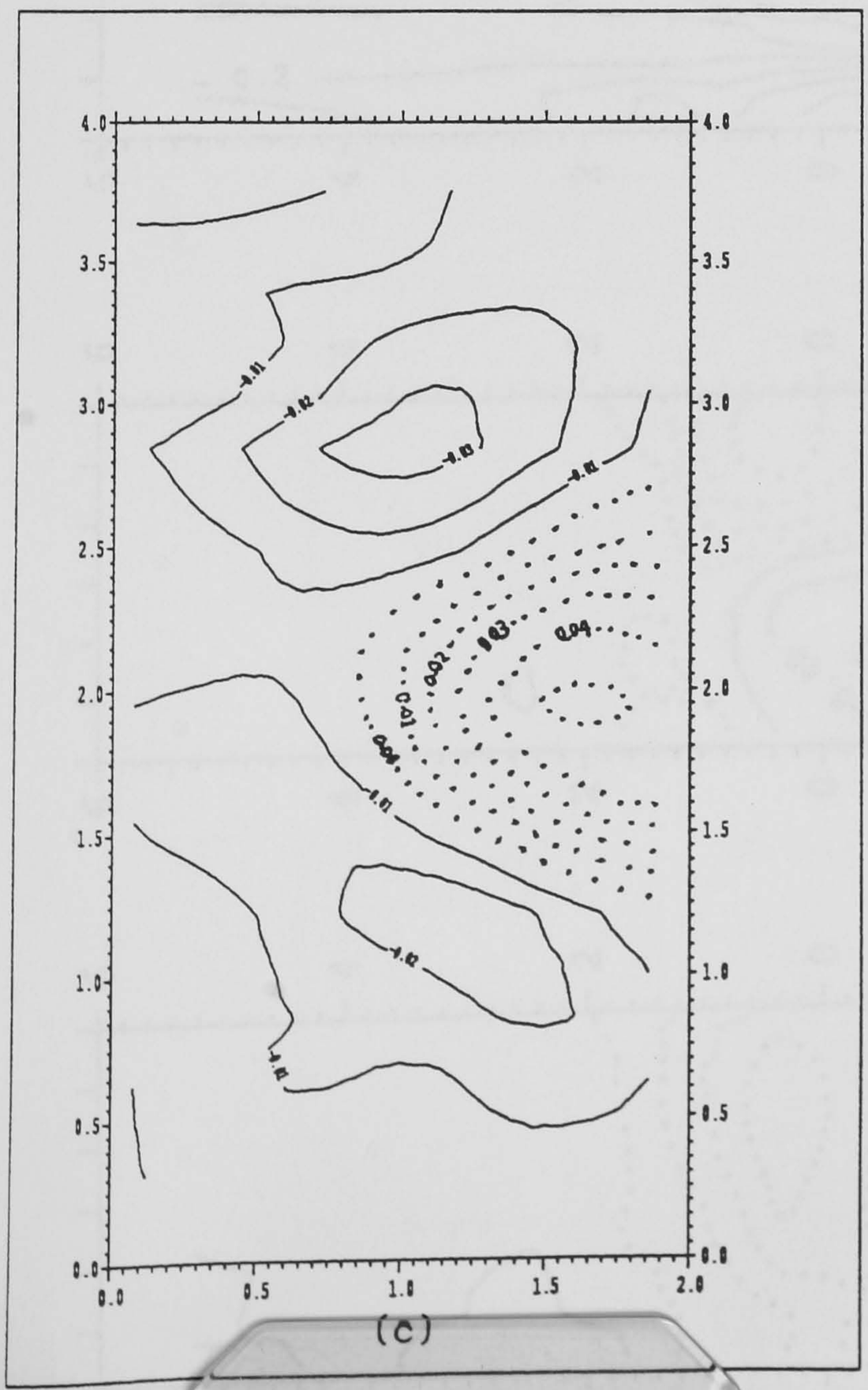

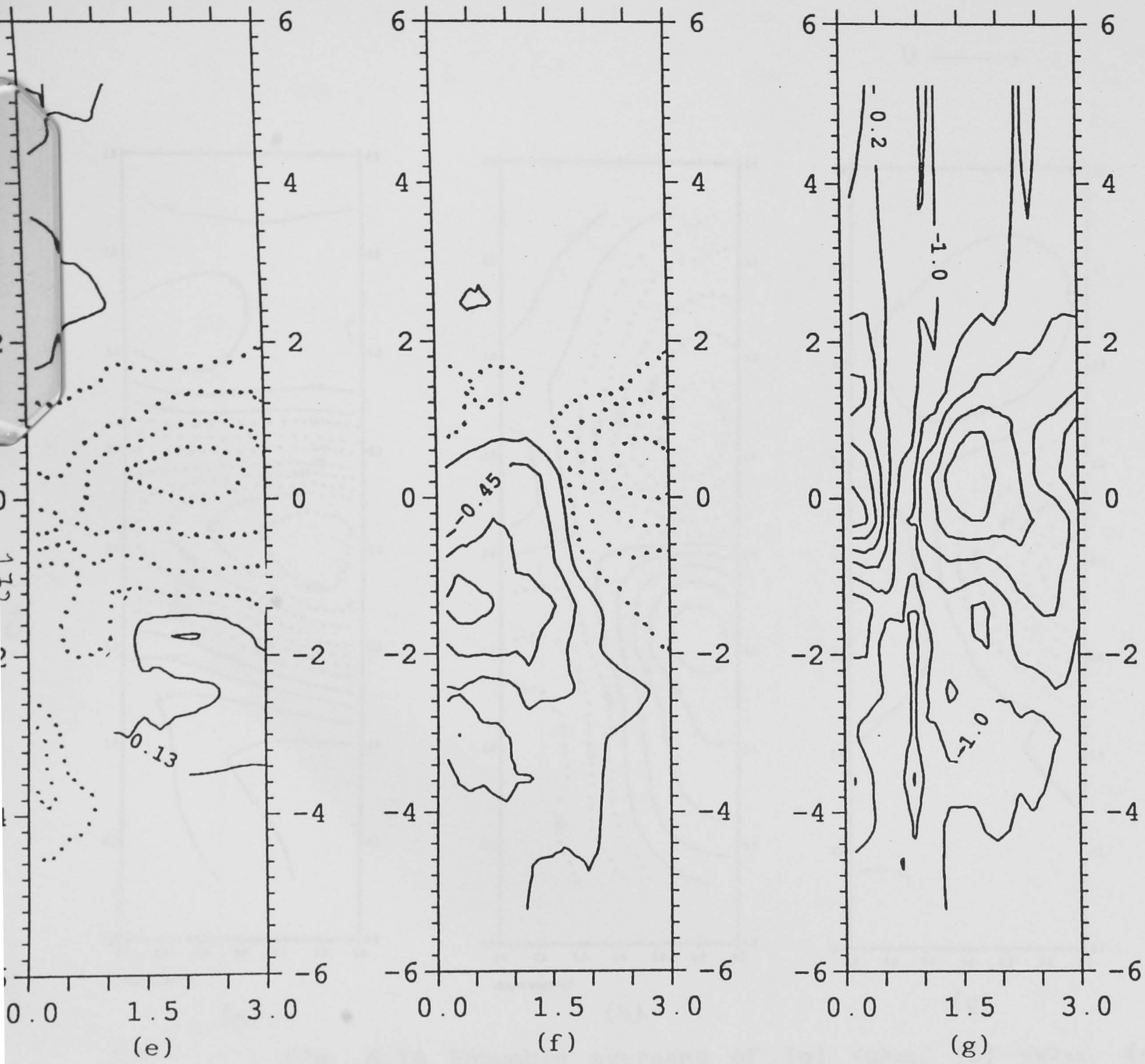

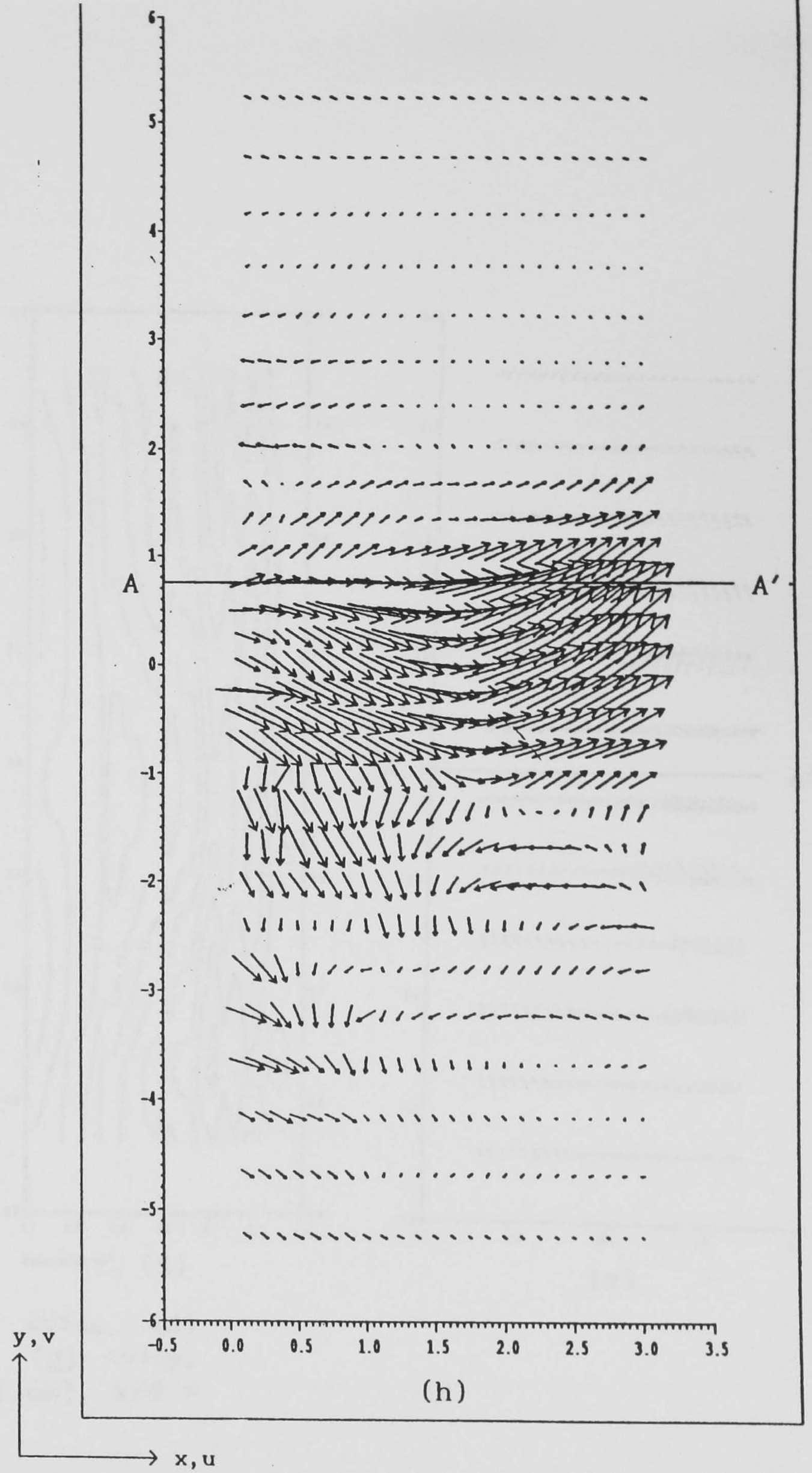

Fig. 6.13 Ensemble averages of (a) <u>xz, (b) <w>xz, (c) <v>xz, (d) velocity vectors in the (x,z) plane, (e) <u>xy, (f) <v>xy, (g) <p>xy, (h) velocity vectors in the (x,y) plane at y/l = 0.3 (y = 0.767), x/d = 18. Negatively correlated velocity vector fields.

U ⟶

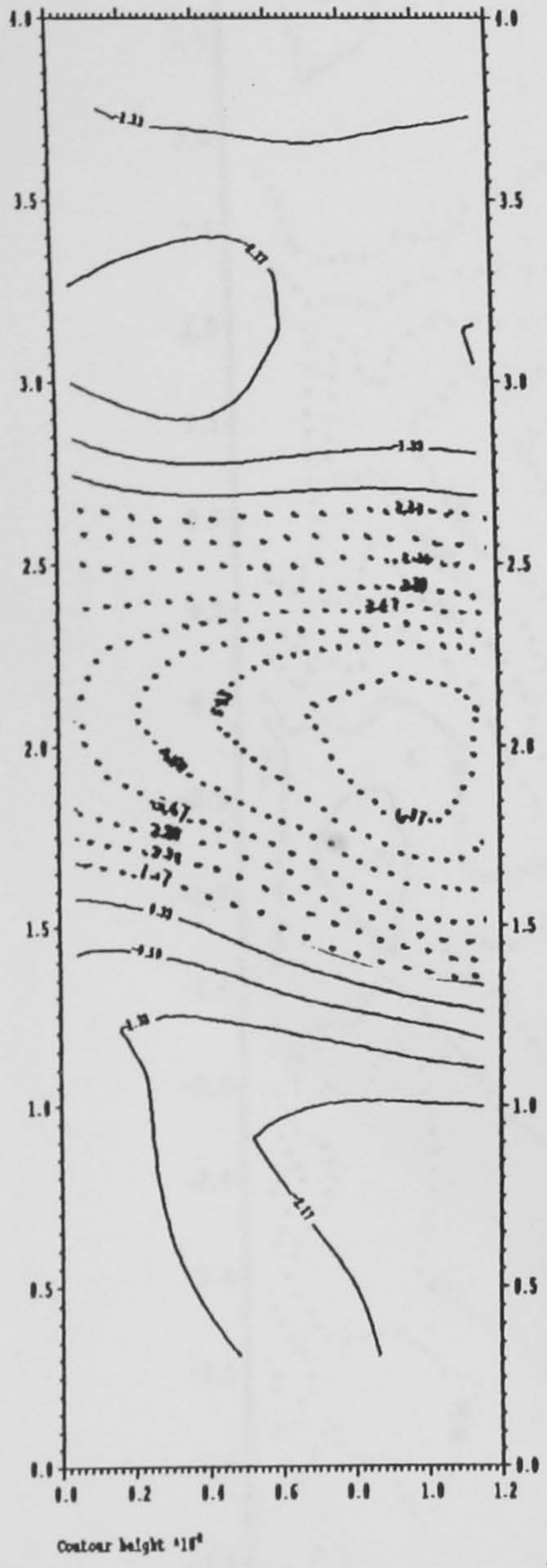

(a)

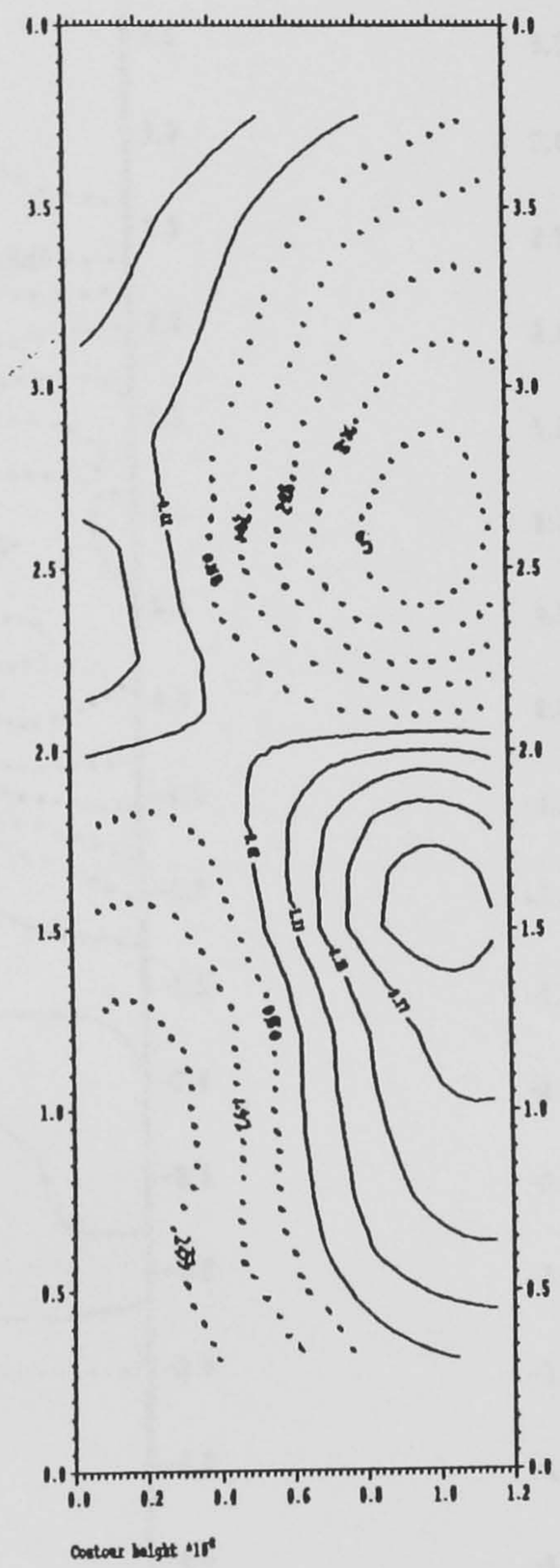

(b)

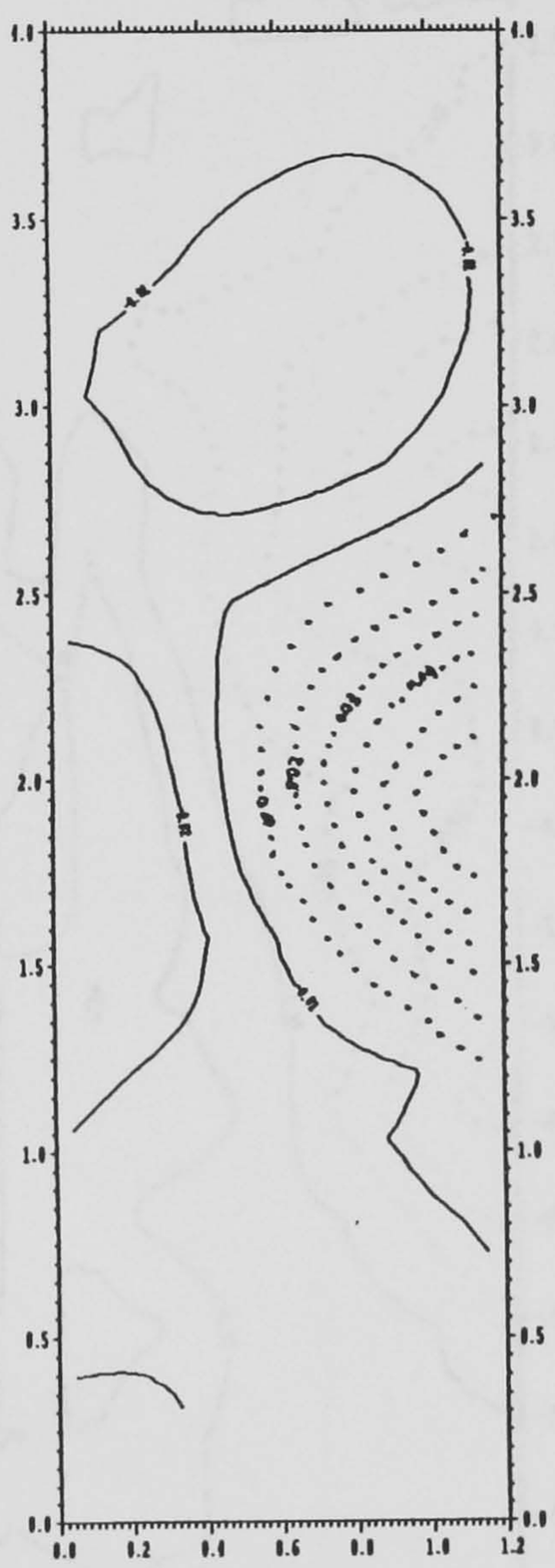

(c)

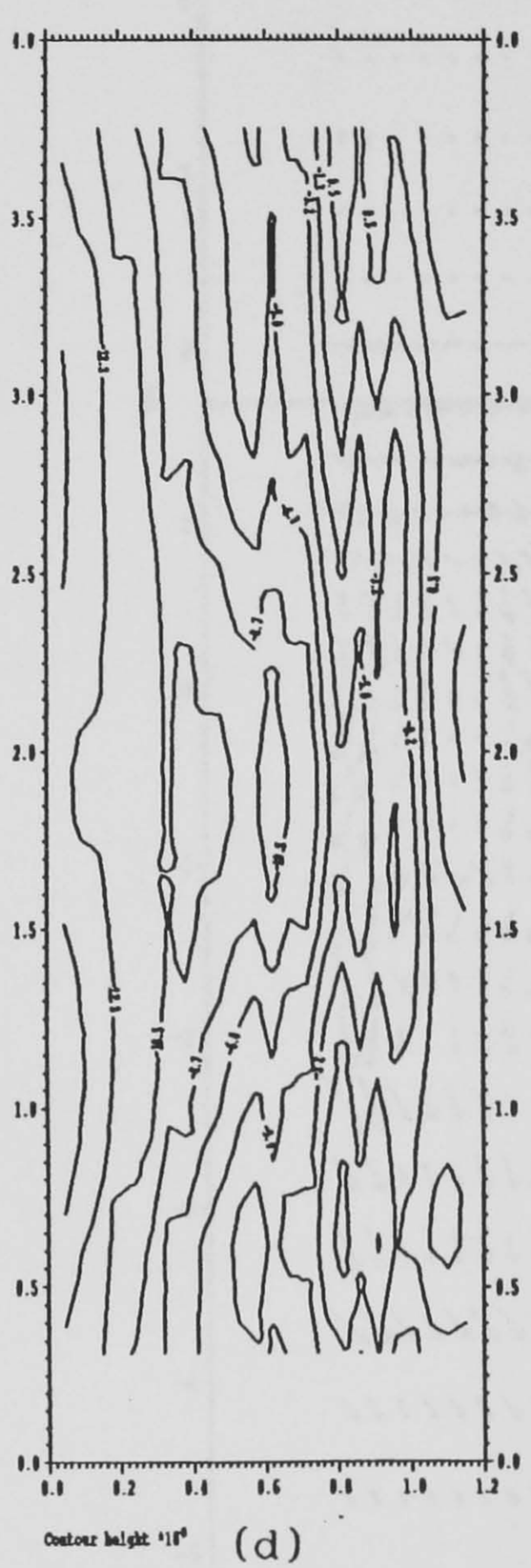

(d)

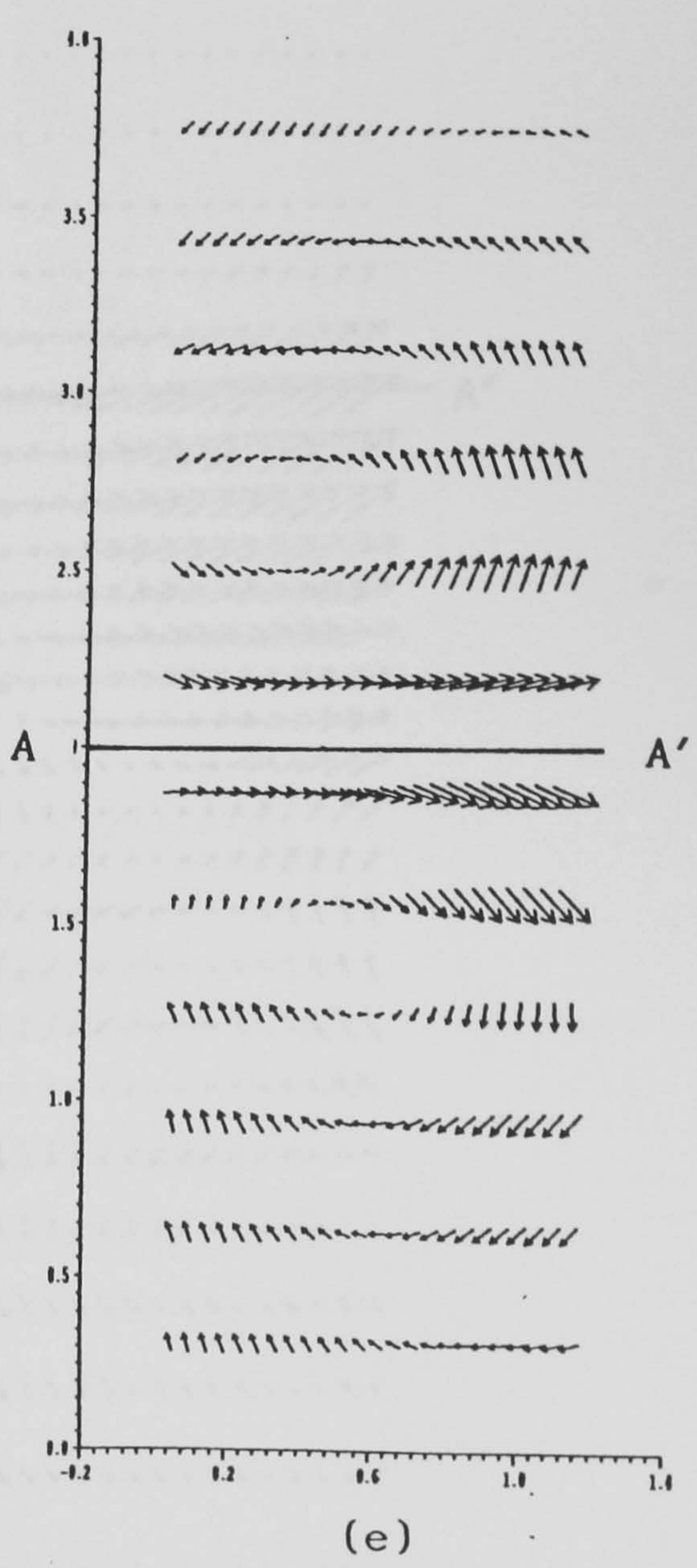

(e)

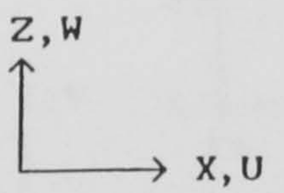

Fig. 6.14 Ensemble averages of (a) <u>xz, (b) <w>xz, (c) <v>xz, (d) <p>xz, (e) velocity vectors in the (x,z) plane, (f) <u>xy, (g) <v>xy, (h) velocity vectors in the (x,y) plane at y/l = 0.67 (y = 1.68), x/d = 18. x/d = 18. Negatively correlated velocity vector fields.

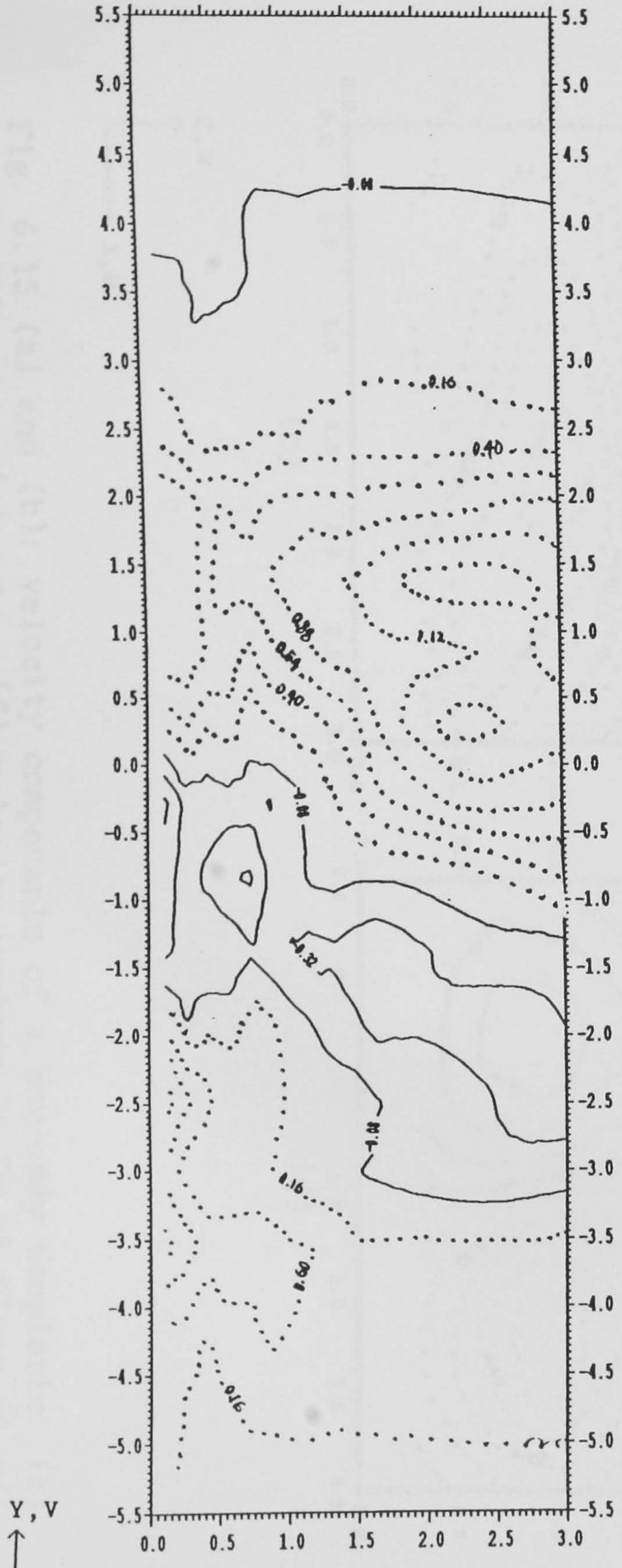

(f)

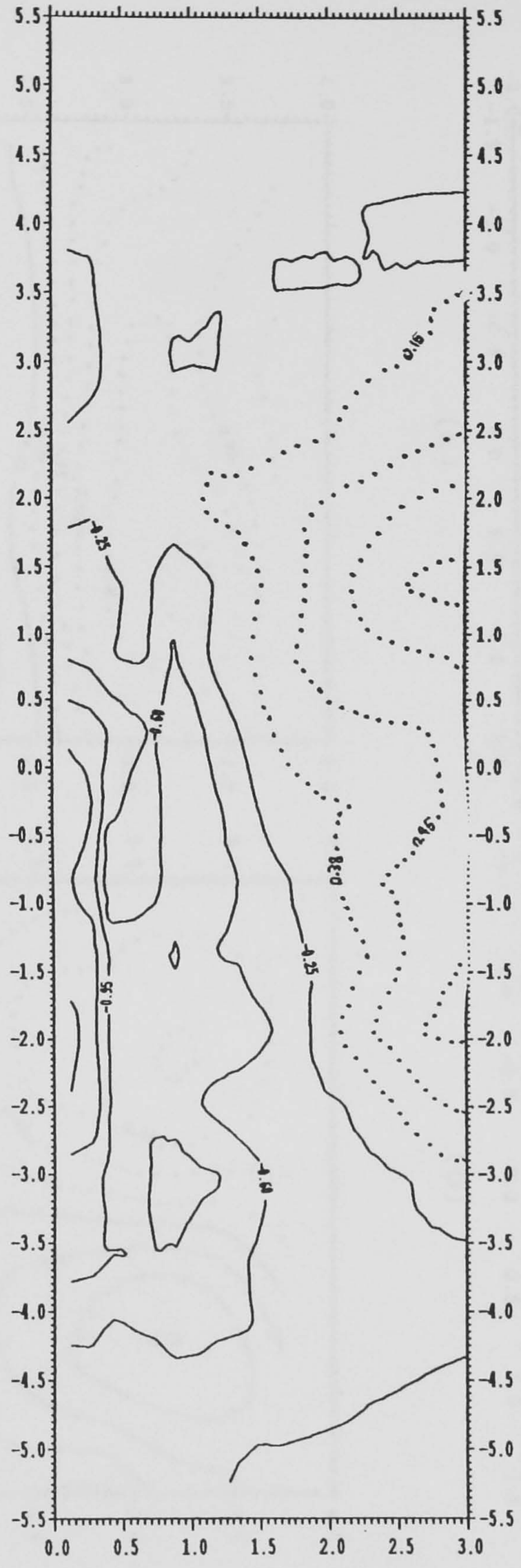

(g)

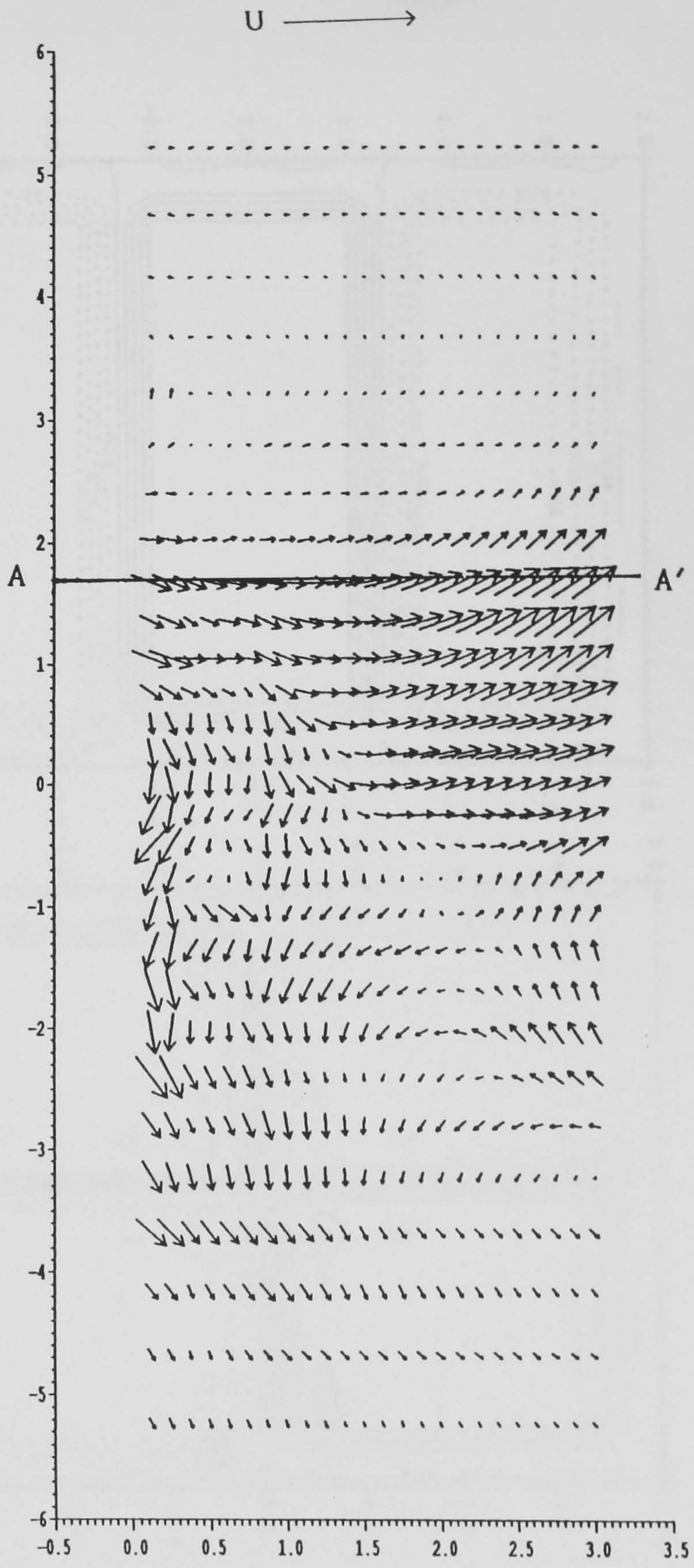

(h)

Fig. 6.14 (continued)

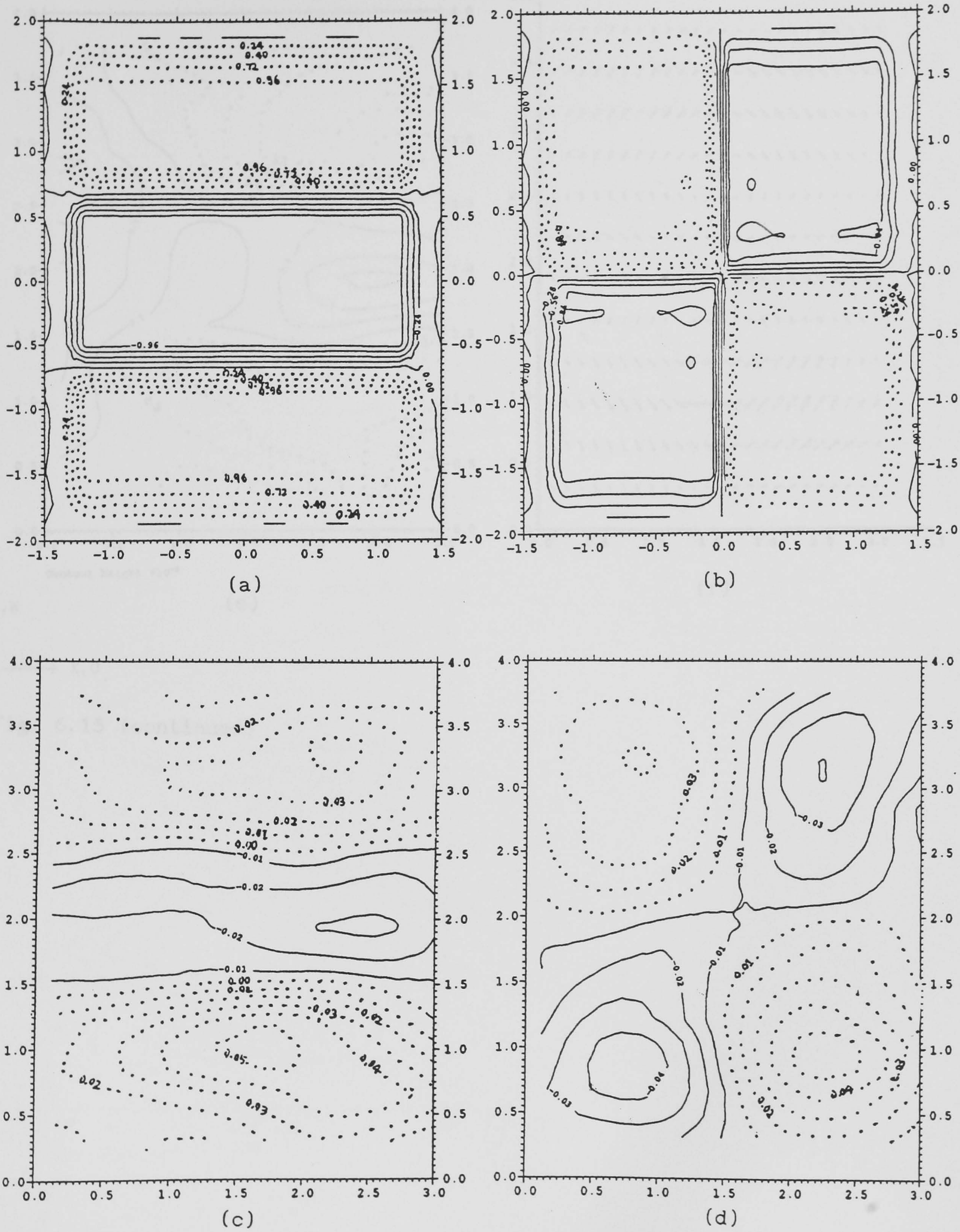

Fig. 6.15 (a) and (b): velocity components of a box-eddy templarte. (c) <u>xz, (d) <w>xz, (e) <v>xz, (f) velocity vectors in (x,z) plane at y/l = 0, a/d = 18. Positively correlated velocity vector fields.

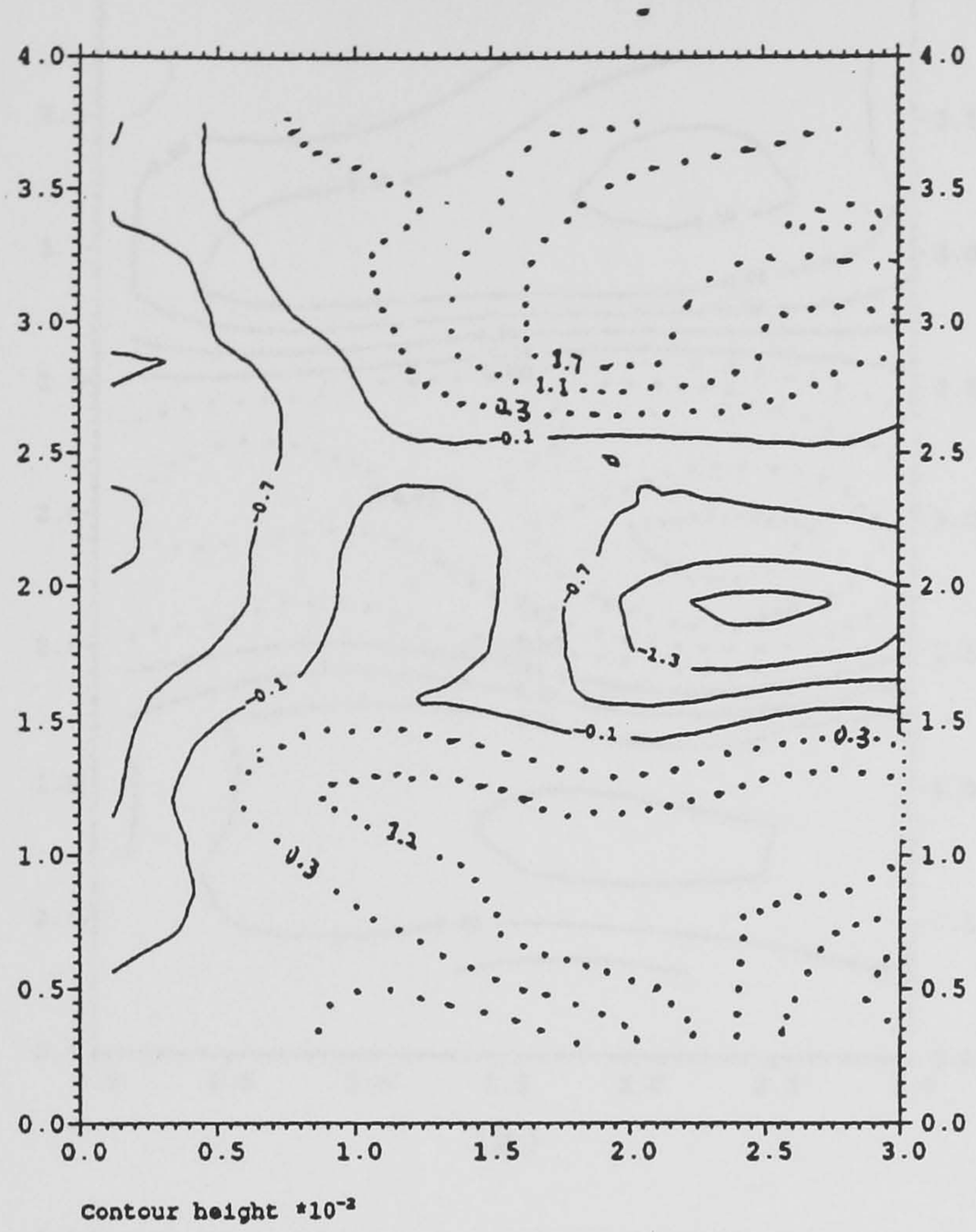

(e)

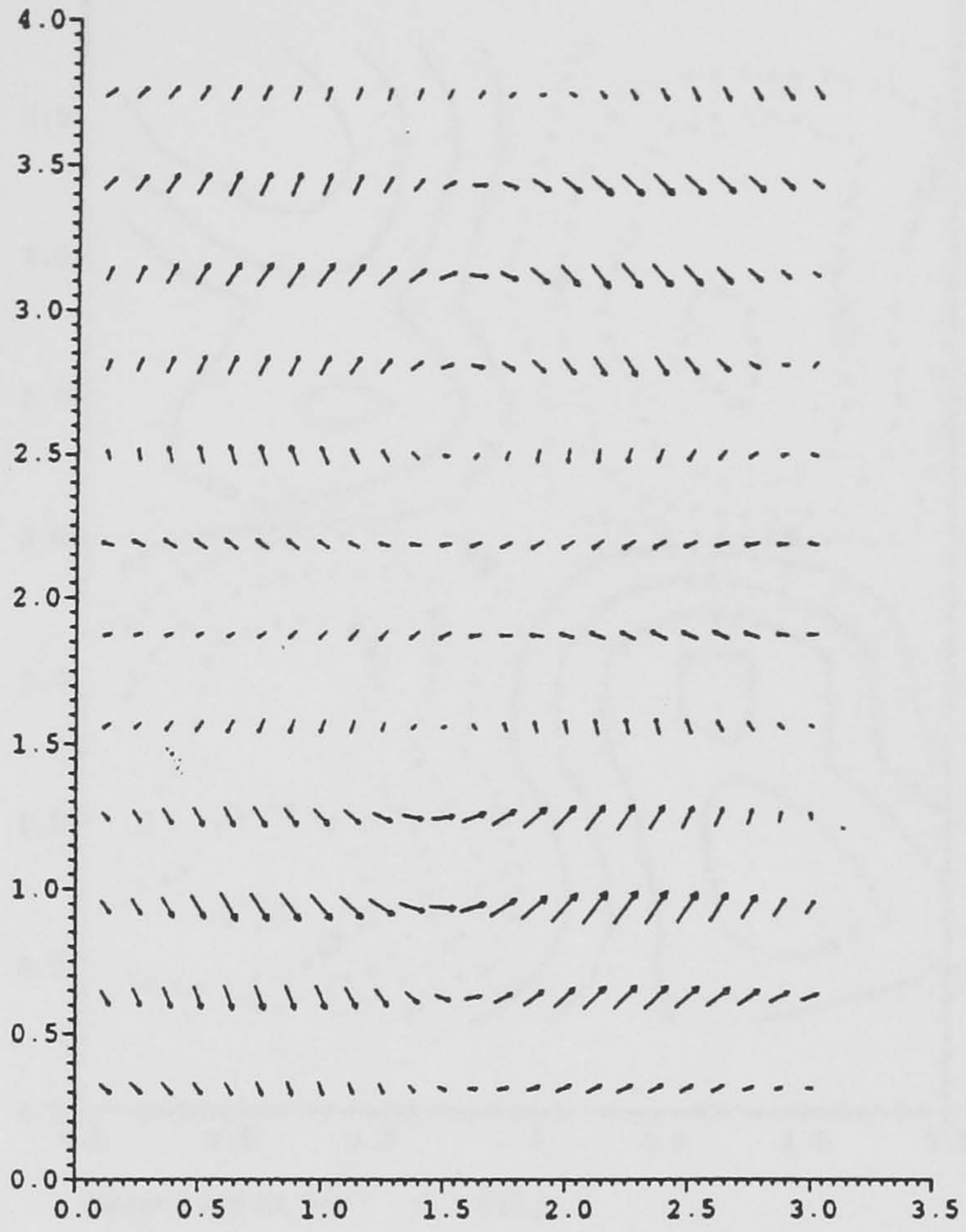

(f)

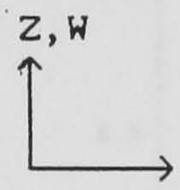

Fig. 6.15 (continued)

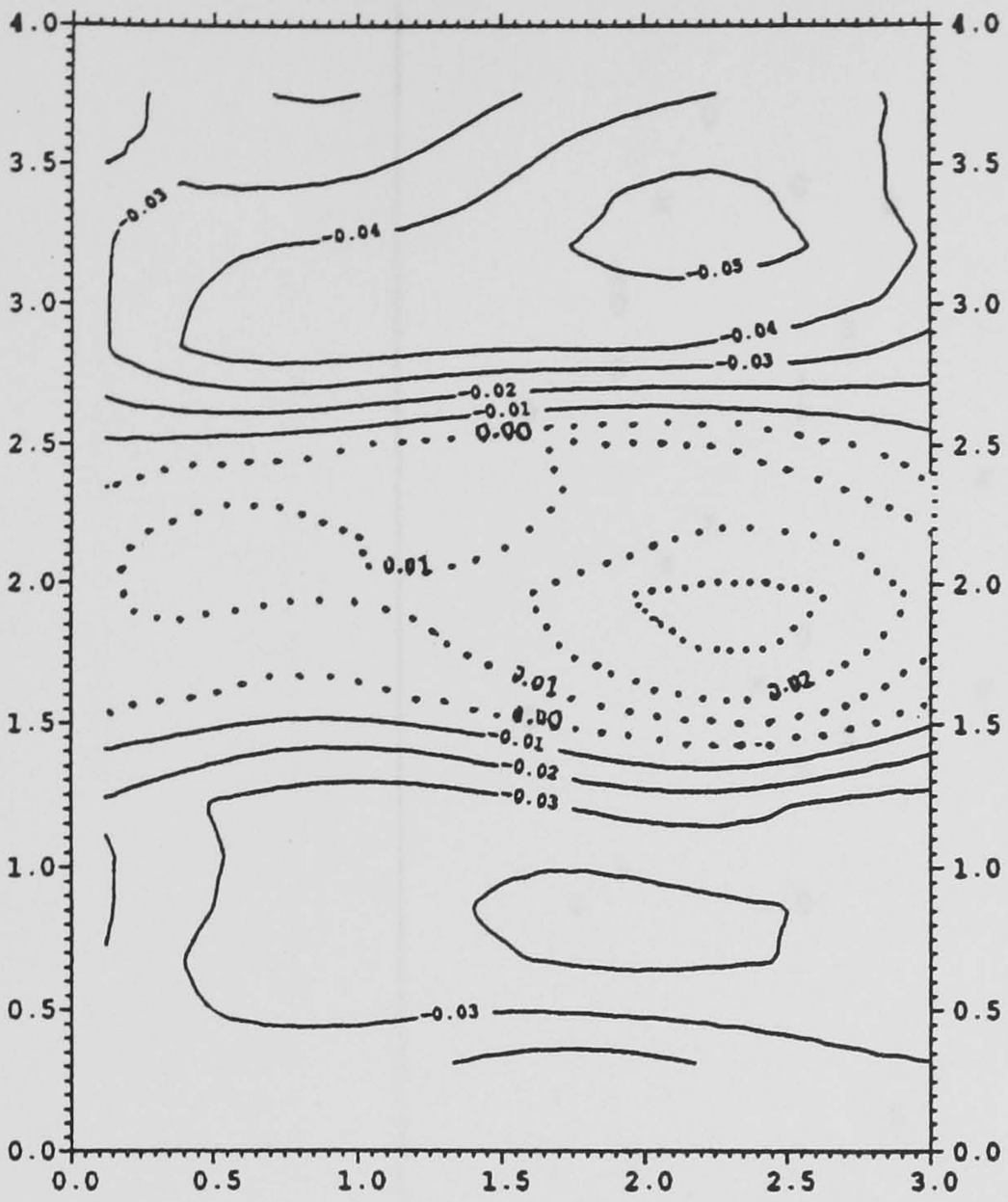

(a)

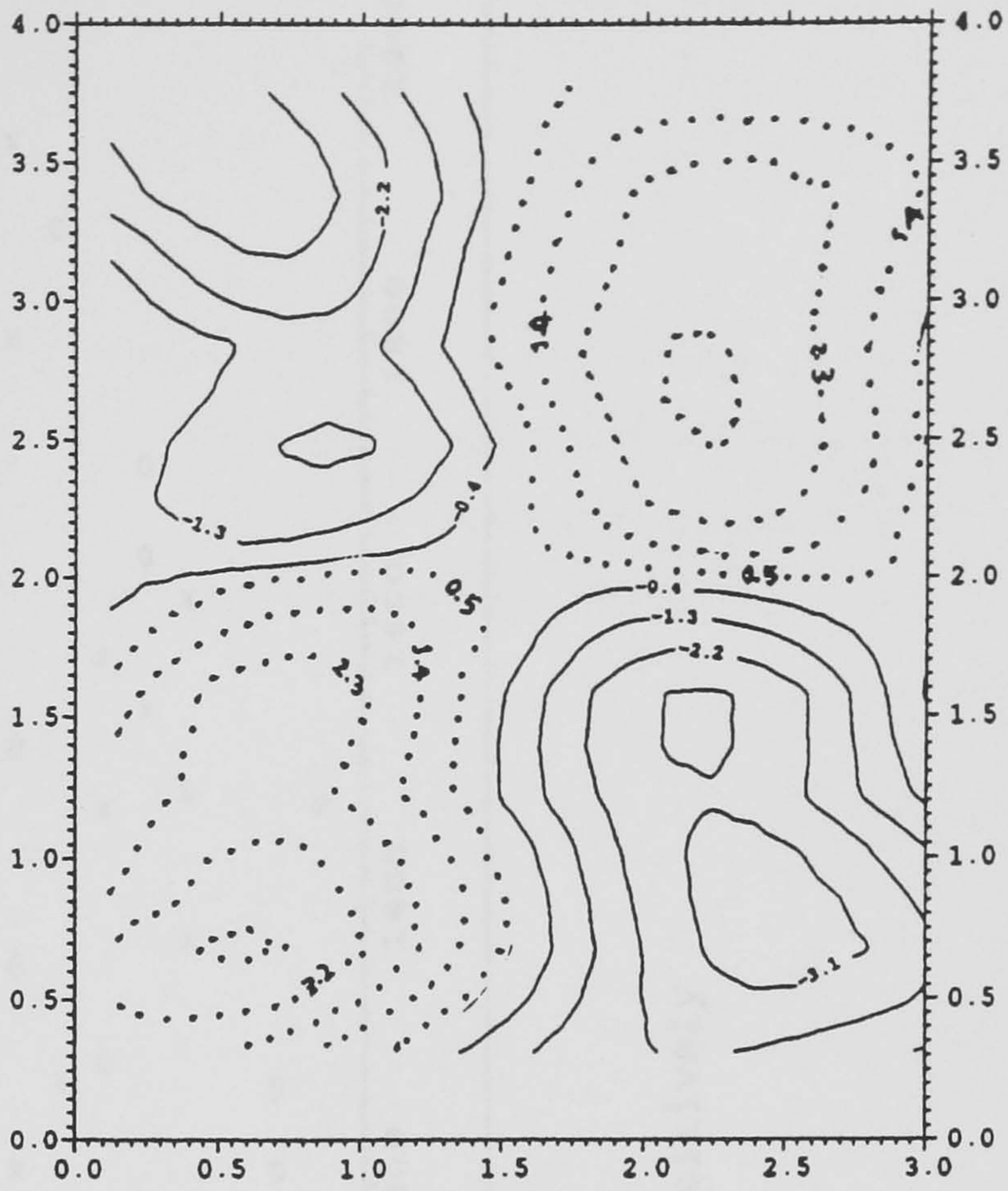

Contour height $*10^{-2}$ (b)

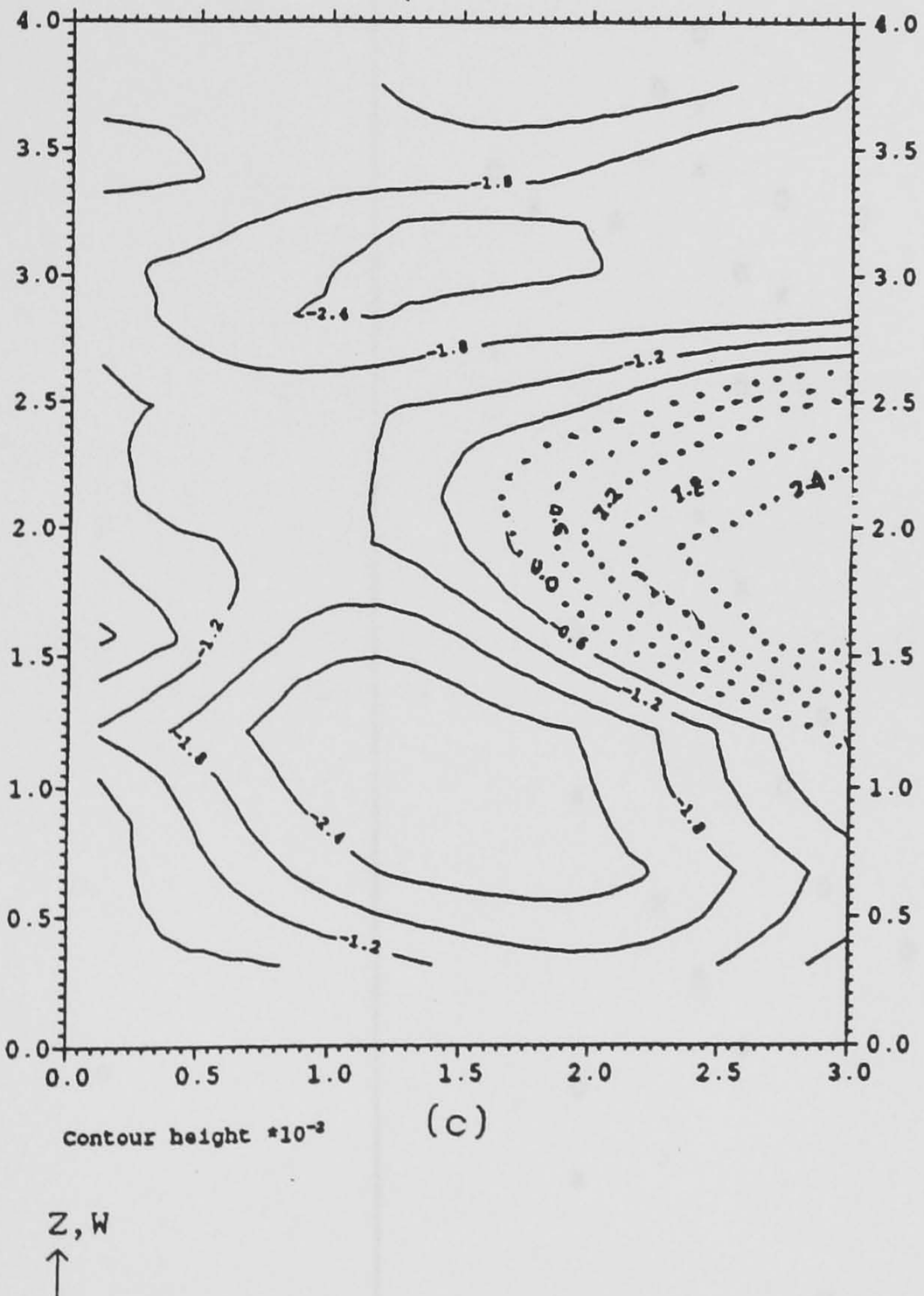

Contour height $*10^{-3}$ (c)

Fig. 6.16 (a) <u>xz, (b) <w>xz, (c) <v>xz at y/l = 0, x/d = 18. Negatively correlated velocity vector fields with a box-eddy template.

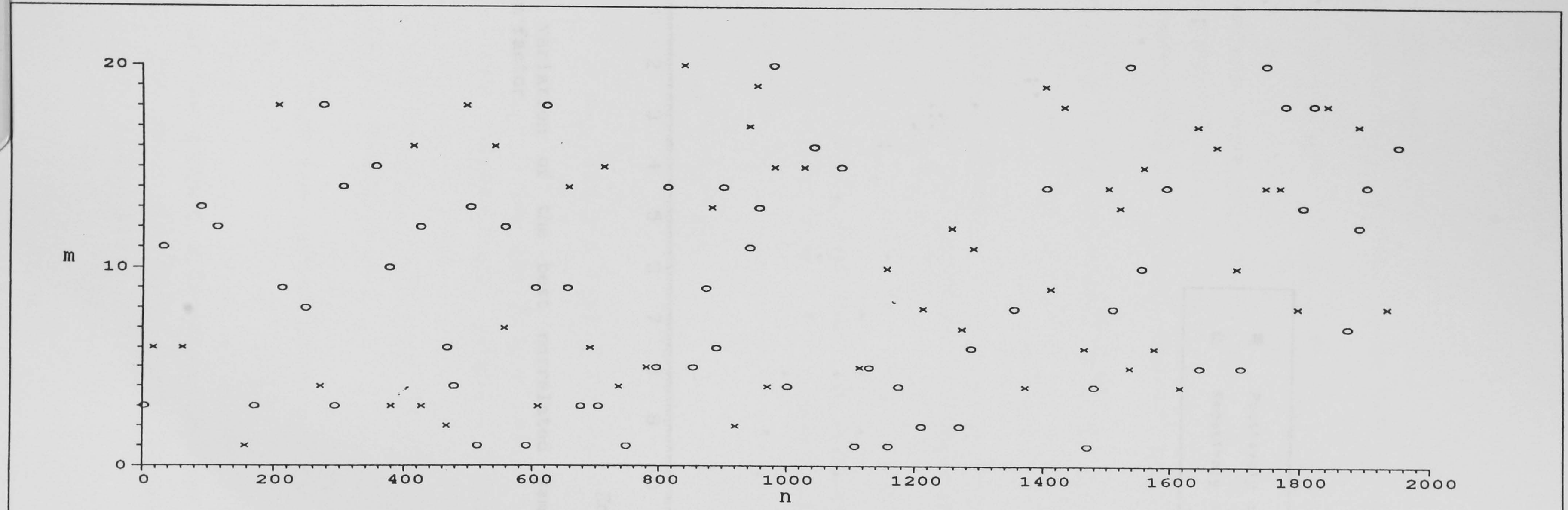

Fig. 6.17 Spatial-temporal locations of the events. × positively correlated samples, o negatively correlated samples.

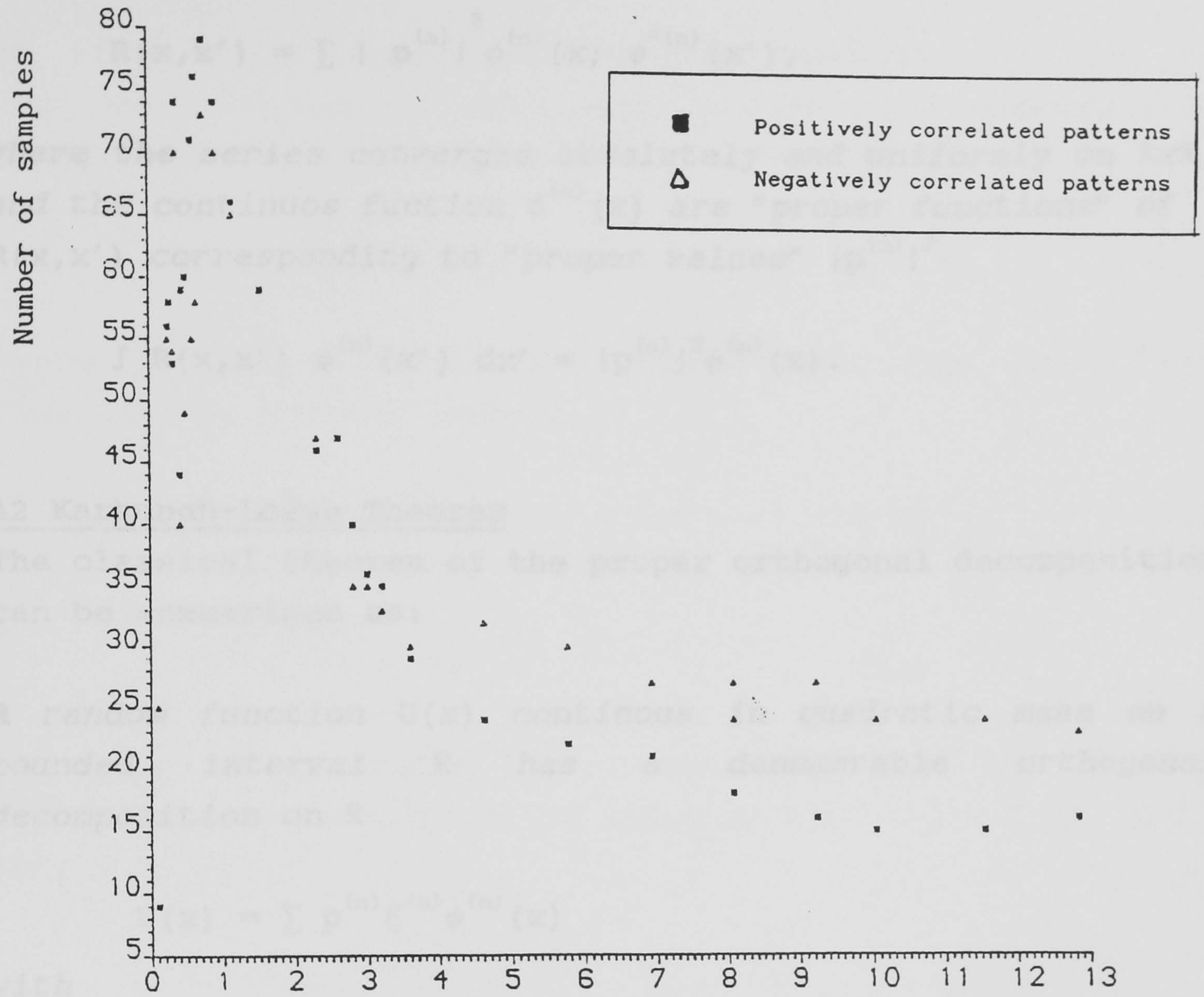

Fig. 6.18 The variation of the best correlated samples with the zoom factor.

Appendix

A1 Mercer's Theorem:

If the covariance $R(x,x')$ *defined on* $\Re x\Re$ *is continous, then*

$$R(x,x') = \sum |p^{(n)}|^2 \phi^{(n)}(x)\ \phi^{*(n)}(x'),$$

where the series converges absolutely and uniformly on $\Re x\Re$, *and the continuos fuction* $\phi^{(n)}(x)$ *are "proper functions" of* $R(x,x')$ *corresponding to "proper values"* $|p^{(n)}|^2$:

$$\int R(x,x')\ \phi^{(n)}(x')\ dx' = |p^{(n)}|^2 \phi^{(n)}(x).$$

A2 Karhunen-Loéve Theorem

The classical theorem of the proper orthogonal decomposition can be summarised as:

A random function $U(x)$ *continous in quadratic mean on a bounded interval* $\Re$ *has a denumerable orthogonal decomposition on* $\Re$

$$U(x) = \sum p^{(n)} \xi^{(n)} \phi^{(n)}(x)$$

with

$$\overline{\xi^{(m)} \zeta^{*(n)}} = \delta_{mn} \quad \text{and} \quad \int \phi^{(m)}(x)\ \phi^{*(n)}(x)dx = \delta_{mn}$$

if and only if, $|p^{(n)}|^2$ *are the proper values and* $\phi^{(n)}(x)$ *are the orthonormal proper functions of its covariance*

$$R(x,x') = u(x)\ u^*(x')$$

defined on $\Re x\Re$. *Then the series converges in quadratic mean uniformly on* $\Re$.

Discussions of the proper orthogonal theorem were given by Loéve (1955), Davenport and Root(1958), Papoulis(1965), and Lumley(1967, 1970, 1980, 1981)

A3 Proof of the Theorem

Proof of the "If" part:

If u(x) is a non-periodic random function, it can be expanded in terms of orthogonal series with uncorrelated coefficients on the interval $x \in [a,b]$:

$$u(x) = \sum_n p^{(n)} \zeta^{(n)} \phi^{(n)}(x) \qquad \text{(A1)}$$

where $\zeta^{(n)}$ are uncorrelated random coefficients and $p^{(n)}$ are some real or complex numbers,

$$\int_b^a \phi^{(n)}(x)\ \phi^{*(m)}(x)\ dx = \delta_{mn} \qquad \text{(A2)}$$

$$\overline{(\zeta^{(n)} \zeta^{*(m)})} = \delta_{mn} \qquad \text{(A3)}$$

In order to determine the functions $\phi^{(n)}$ and the numbers $P^{(n)}$, consider the correlation function with $[x] \in [a,b]$ and $[x'] \in [a,b]$

$$R(x,x') = \overline{u(x)\ u^*(x')}$$

$$= \overline{\sum_n p^{(n)} \zeta^{(n)} \phi^{(n)}(x) \sum_n p^{*(n)} \zeta^{*(n)} \phi^{*(n)}(x')}$$

$$= \sum_n |p^{(n)}|^2 \phi^{(n)}(x)\ \phi^{*(n)}(x') \qquad \text{(A4)}$$

By using equation (A4) and integrating $R(x,x')\ \phi^{(k)}(x')$ over the interval [a,b], we have,

$$\int_a^b R(x,x')\ \phi^{(k)}(x')\ dx' = \sum_n |p^{(n)}|^2 \phi^{(n)}(x) \int_a^b \phi^{*(n)}(x') \phi^{(k)}(x')\ dx'$$

From equation (A2) the non-zero terms of the series are those with n = k. Then,

$$\int_a^b R(x,x')\ \phi^{(k)}(x')\ dx' = |p^{(k)}|^2 \phi^{(k)}(x) \qquad \text{(A5)}.$$

According to Mercer's theorem, $\phi^{(k)}(x)$ are the characteristic functions and $|p^{(k)}|^2$ are the characteristic values of the integral equation:

$$\int_a^b R(x,x')\ \phi(x')\ dx' = \lambda\ \phi(x). \qquad \text{(A6)}$$

Proof of "only if" part:

Let $|p^{(n)}|^2$ be non-zero characteristic values of (A6) with the assumption

$$p^{(n)} = +\sqrt{|p^{(n)}|^2}$$

and $\{\ \phi^{(n)}(x)\ \}$ be a set of orthonormal characteristic functions of (A6) with $\phi^{(n)}(x)$ corresponding to $|p^{(n)}|^2$. Therefore, equation (A2) is automatically satisfied. Let the random coefficients $\zeta^{(n)}$ be given by

$$p^{(n)}\zeta^{(n)} = \int_a^b u(x)\ \phi^{*(n)}(x)\ dx \qquad \text{(A7)}$$

Then

$$\overline{p^{(n)}\zeta^{(n)}\ (\ p^{(m)}\ \zeta^{(m)})^*}$$

$$= p^{(n)}p^{(m)}\ \overline{\zeta^{(n)}\zeta^{*(m)}}$$

$$= \int_a^b u(x)\ \phi^{(n)}(x)\ dx \int_a^b u^*(x')\ \phi^{(m)}(x')\ dx'$$

$$= \int_a^b \int_a^b R(x,x')\ \phi^{*(n)}(x)\ \phi^{(m)}(x')\ dx\ dx'$$

$$= \int_a^b \phi^{*(n)}(x) \; | \; p^{(m)} |^2 \; \phi^{(m)}(x) \; dx \text{ (by eq.(A6))}$$

$$= 0 \qquad \text{if } n \neq m$$

$$= (p^{(n)})^2 \quad \text{if } n = m$$

Hence, equation (A3) is satisfied.

A4 Principal Axes of Strain Rate

Consider a simple parallel shear flow defined by:

$$U_1 = U_o x_2.$$

The strain rate matrix can be written as,

$$S = \begin{pmatrix} \frac{\partial u_1}{\partial x_1} & \frac{1}{2}\left(\frac{\partial u_1}{\partial x_2} + \frac{\partial u_2}{\partial x_1}\right) \\ \frac{1}{2}\left(\frac{\partial u_2}{\partial x_1} + \frac{\partial u_1}{\partial x_2}\right) & \frac{\partial u_2}{\partial x_2} \end{pmatrix}$$

$$= \begin{pmatrix} 0 & \frac{1}{2} U_o \\ \frac{1}{2} U_o & 0 \end{pmatrix}$$

The principal axes can be determined by the rotation transformation of the basis:

$$\frac{1}{2} U_o \begin{pmatrix} \cos\theta & -\sin\theta \\ \sin\theta & \cos\theta \end{pmatrix} \begin{pmatrix} 0 & 1 \\ 1 & 0 \end{pmatrix} \begin{pmatrix} \cos\theta & -\sin\theta \\ \sin\theta & \cos\theta \end{pmatrix}^T$$

$$= \begin{pmatrix} \lambda_1 & 0 \\ 0 & \lambda_2 \end{pmatrix}.$$

$$\frac{1}{2} U_o \begin{pmatrix} -2\sin\theta\cos\theta & \cos^2\theta - \sin^2\theta \\ -(\cos^2\theta - \sin^2\theta) & 2\sin\theta\cos\theta \end{pmatrix} = \begin{pmatrix} \lambda_1 & 0 \\ 0 & \lambda_2 \end{pmatrix}.$$

Hence,

$\cos\theta = \pm \sin\theta$

$\theta = \pm 45^\circ$

These are the directions of maximum and minimum strain rate, which are at right angle to each other (see figure A1).The flow is stretched for a positive eigenvalue and compressed

for a negative eigenvalue:

$\lambda_1 = \pm 1/2U_o$ and $\lambda_2 = \mp 1/2U_o$.

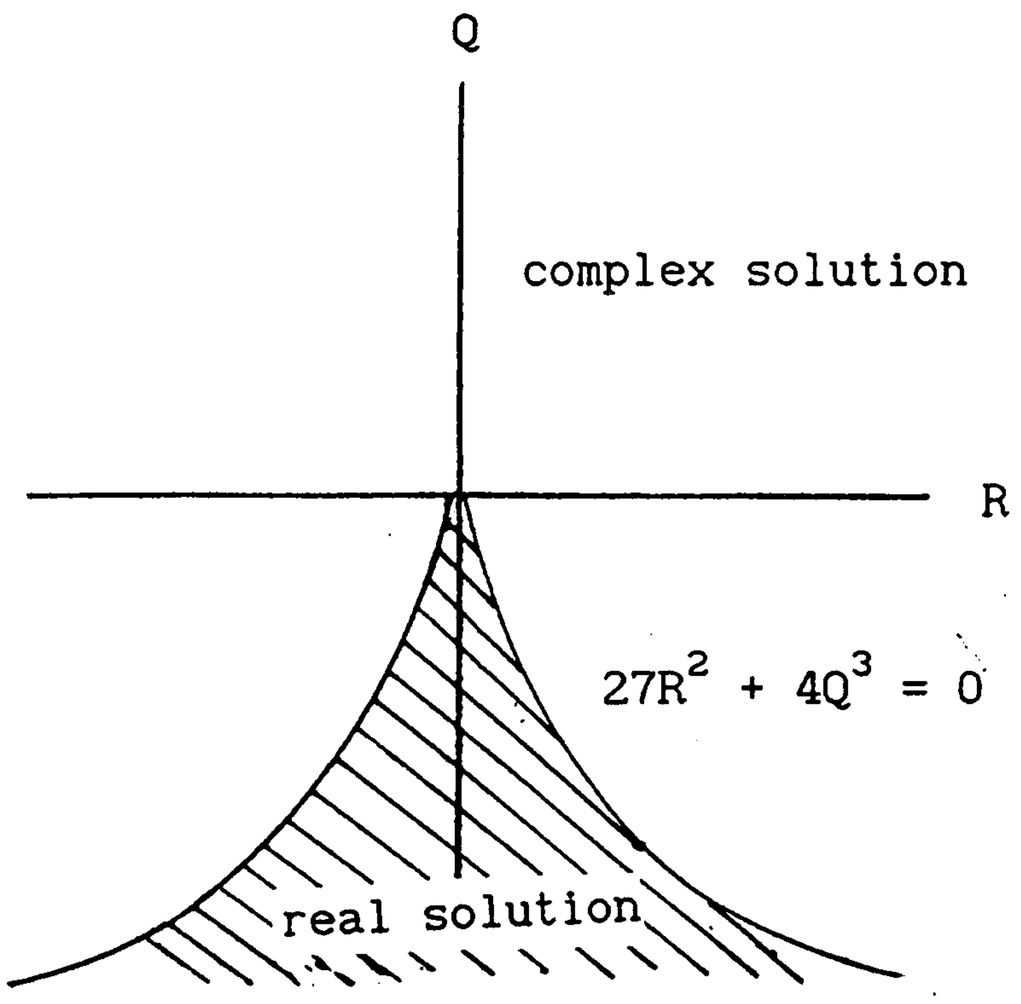

Fig A1 Q-R state-space.

There is a more elegant proof by considering the second-rank strain tensor $\underline{\underline{S}}$. If s is the distance between two points very close together, joined by a line l along the unit vector $\underline{\hat{\lambda}}$, it can be shown that

$$\frac{1}{s}\frac{ds}{dl} = \underline{\hat{\lambda}} \cdot \underline{\underline{S}} \cdot \underline{\hat{\lambda}}$$

We seek for the affine transformation of the coordinates, at which the magnitude of the system is unchanged, making the vectors only stretched and not rotated.

$$S_{ij} - \sum_{\alpha} \lambda^{\alpha} n_i^{\alpha} n_j^{\alpha} = 0$$

or equivalently,

$$n_i^{\alpha} S_{ij} n_j^{\beta} = \lambda^{\alpha} \delta^{\alpha,\beta}$$

where $\delta^{\alpha,\beta}$ denotes the Kronecker delta symbol. If $\underline{n}_i^{\alpha}$, $\underline{n}_j^{\beta}$ are orthonormal vectors, then

$$\underline{n}^{\alpha} \cdot \underline{n}^{\beta} = \delta^{\alpha,\beta} = \begin{cases} 1: \alpha = \beta \\ 0: \alpha \neq \beta \end{cases}.$$

By choosing the orthonormal vectors

$$\underline{n}^1 = \begin{pmatrix} \cos\theta \\ -\sin\theta \end{pmatrix} \text{ and } \underline{n}^2 = \begin{pmatrix} \sin\theta \\ \cos\theta \end{pmatrix},$$

we can obtain the equation which is identical to the rotation tranformation previously described.

A5 Topological Classification of Flow Patterns

Perry and Fairly (1984) introduced the critical point theory or phase-space theory which is a powerful tool for the topological description of the flow patterns. Phase-space theory is a very well-established branch of mathematics, and the readers should be referred to the textbooks on linear differential equations and dynamical systems.

The velocity field is expanded in terms of the Taylor's series above an arbitary point in the flow (Perry and Chong 1990):

$$u_i = \frac{dX_i}{dt} = A_i + A_{ij}X_j + A_{ijk}X_jX_k + \ldots\ldots \quad .$$

For the free slip critical point, the velocity is zero and the slope of the streamline is indeterminate:

$$\frac{u_i}{u_j} = \frac{0}{0} \quad .$$

The higher order terms in the expansion are truncated (with $A_i = 0$),

$$\frac{dX_i}{dt} = A_{ij}X_j$$

If the Taylor series are expanded above the point (0,0,0), then we have three linear first order differential equations:

$$\dot{X}_1 = \frac{\partial u_1}{\partial X_1} X_1 + \frac{\partial u_1}{\partial X_2} X_2 + \frac{\partial u_1}{\partial X_3} X_3$$

$$\dot{X}_2 = \frac{\partial u_2}{\partial X_1} X_1 + \frac{\partial u_2}{\partial X_2} X_2 + \frac{\partial u_2}{\partial X_3} X_3$$

$$\dot{X}_3 = \frac{\partial u_3}{\partial X_1} X_1 + \frac{\partial u_3}{\partial X_2} X_2 + \frac{\partial u_3}{\partial X_3} X_3 \ .$$

The matrix form of the three differential equations can be written as:

$$\dot{\mathbf{X}} = \mathbf{A} \cdot \mathbf{X}$$

where $\dot{\mathbf{X}} = \begin{pmatrix} \dot{X}_1 \\ \dot{X}_2 \\ \dot{X}_3 \end{pmatrix}$, $\mathbf{A} = \begin{pmatrix} a_{11} & a_{12} & a_{13} \\ a_{21} & a_{22} & a_{23} \\ a_{31} & a_{32} & a_{33} \end{pmatrix}$

and $a_{ij} = \frac{\partial u_i}{\partial x_j}$.

The three invariants of a Jacobian matrix are sufficient to classify the three-dimensional patterns. The velocity gradient tensor can be split into symmetric and anti-symmetric parts,

$$\frac{\partial u_i}{\partial x_j} = S_{ij} + \Omega_{ij} \ .$$

If e_1, e_2 and e_3 are the eigenvectors, then

$$\mathbf{A}e = \lambda e.$$

The eigenvalues λ_1, λ_2 and λ_3 can be determined by the characteristic equation:

$$\det[\ \mathbf{A} - \lambda \mathbf{I}\ ] = 0$$

which gives a third-order polynomial:

$$\lambda^3 + P\lambda^2 + Q\lambda + R = 0$$

$$P = -\ \mathrm{trace}[\mathbf{A}] = -S_{ii} = \partial_i u_i .$$

If the flow is incompressible, then P = 0.

$$Q = \frac{1}{2} \left(-S_{ij}S_{ji} - \Omega_{ij}\,\Omega_{ji} \right)$$

$$R = -\det[A] = \frac{1}{3} \left(-S_{ij}S_{jk}S_{ki} - 3\Omega_{ij}\Omega_{jk}\Omega_{ki} \right)$$

In a compressible flow ($P \neq 0$), the solution trajectories can be described by the P-Q-R state-space (see Perry and Chong 1990).

In a two dimensional phase portrait or the Q-R state-space (as shown in figure A2), it can be shown that the real solutions are divided from the complex solutions by the following line (derivation is not shown here):

$$R = \pm \frac{2\sqrt{3}}{9} \cdot (-Q)^{3/2} .$$

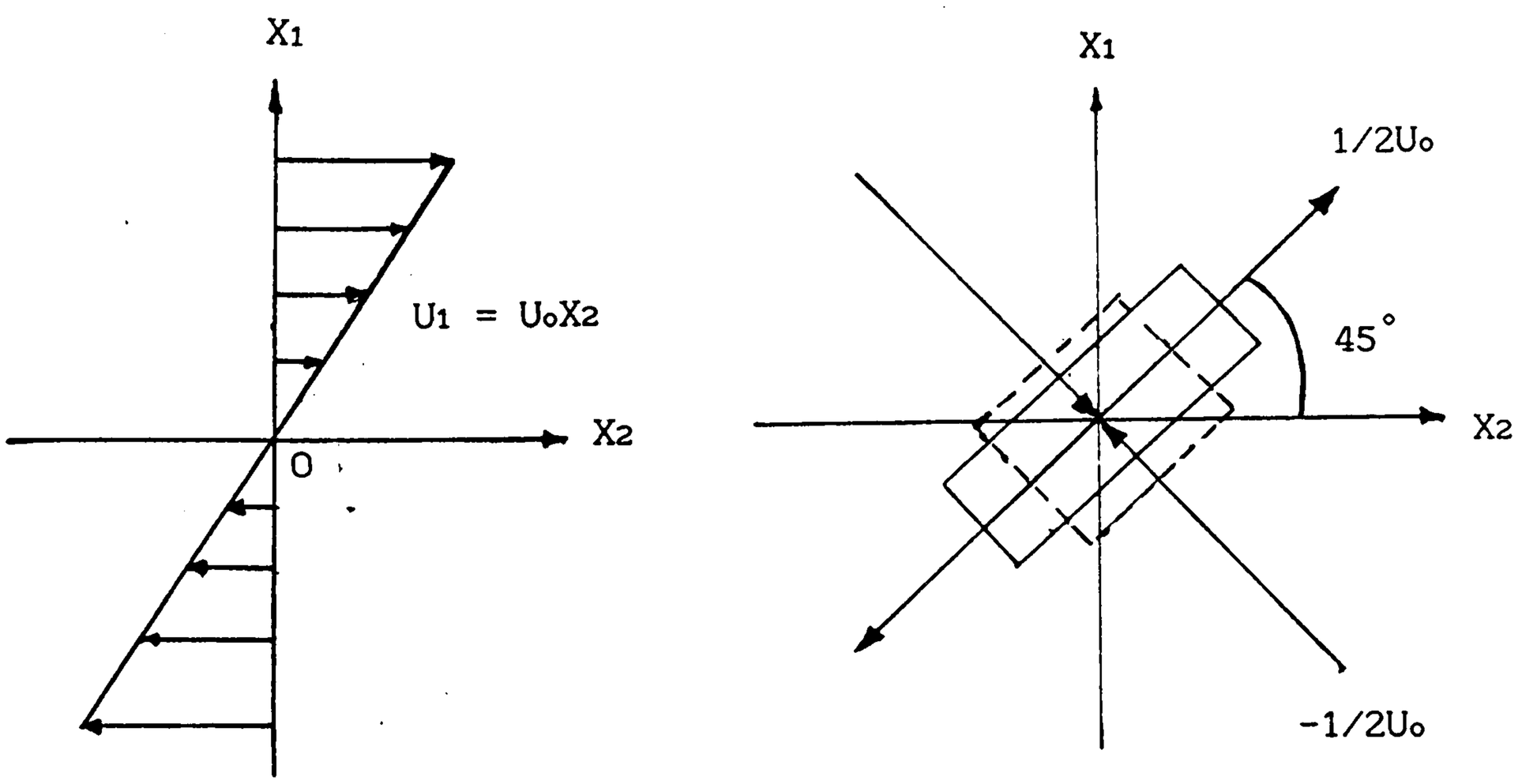

Fig A2 Principal axes of strain rate.

It can be shown that the solution trajactories in two dimensions can be classified as:

If the eigenvalues are complex conjugate with

(1) negative real part; stable focus.

(2) positive real part; unstable focus.

If the eigenvalues are real and

(3) negative; stable node.

(4) positive; unstable node.

(5) of opposite sign; saddle point.

The topological elements are shown in figure A3.

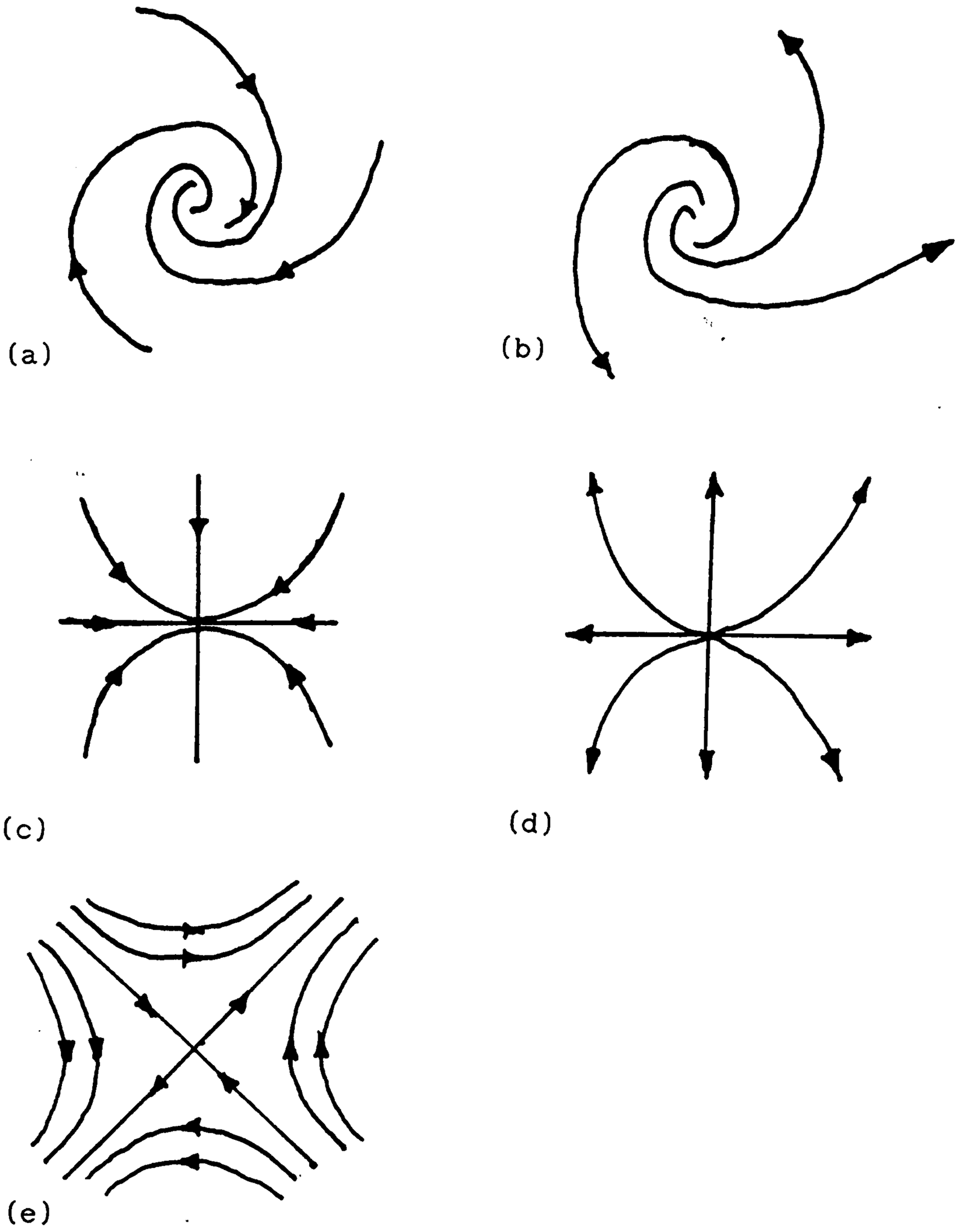

Fig A3 Classification of the solution trajactories: (a) stable focus, (b) unstable focus, (c) stable node, (d) unstable node, (e) saddle point.

REFERENCES

Adrian, R.J., *Linking Correlations and Structure: Stochastic Estimation and Conditional Averaging.* Zoran Zaric Memorial Conference, Near Wall Turbulence, Hemisphere 420-436 (1988).

Adrian, R.J., *Stochastic Estimation of Conditional Structure.* IUTAM Symposium on Eddy Structure Identification in Free Turbulent Shear Flows, Poitiers, III.1.1-1.7 (1992).

Aleksander, I. and Morton, H. *An Introduction to Neural Computing.* Chapman and Hill (1990).

Altmann H. and Reitböck, H.J.P., *A Fast Correlation Method for Scale- and Translation-invariant Pattern Recognition.* IEEE Trans Pattern Analysis and Machine Intelligence. PAMI-6 **1** (1984).

Andrade, E.N., *The Velocity Distribution in a Liquid-into-liquid Jet. Part 2: The Plane Jet.* Physical Soc. **51**, 11.5:784-793 (1939).

Anton, H. *Elementary Linear Algebra* John Wiley and Sons. (1973).

Antonia, R.A., *Conditional Sampling in Turbulence Measurement,* Ann. Rev. Fluid Mech., **13**:131-156, (1981).

Antonia, R.A., Browne, L.W.B., Rajagopalan, S. and Chambers, A.J. *On the Organised Motion of a Turbulent Plane Jet.* J. Fluid Mech. **134**:49-66 (1983).

Antonia, R.A., Browne, L.W.B, Britz, D. and Chambers, A.J., *Organised Structures in a Turbulent Plane Jet: Topology and Contribution to Momentum and Heat Transport.* J. Fluid Mech. **172**:221-229 (1986).

Antonia, R.A. and Zhou, Y., *A Study of Flow Properties Near Critical Points.* IUTAM Symposium Symposium on Eddy Structure

Identification in Free Turbulent Shear Flows, Poitiers, IX.2.1-2.3 (1992).

Aris, R., *Vectors, Tensors, and the Basic Equations of Fluid Mechanics,* Prentice-Hall Inc. (1962).

Aubry, N., Holmes, P. Lumley, J.L. and Stone, E., *The Dynamics of Coherent structures in the Near Wall Region of a Turbulent Boundary Layer.* J. Fluid Mech. **192**; 115-173 (1988).

Batchelor, G.K., *The Theory of Homogeneous Turbulence,* Cambridge University Press, (1953).

Batchelor, G.K., *An Introduction to Fluid Mechanics.* Cambridge University Press (1967).

Berkooz, G. and Holmes, P. and Lumley, J.L., *The Proper Orthogonal Decomposition in the Analysis of Turbulent Flows,* Annu. Rev. Fluid Mech. **25**:539-575, (1993).

Beale, R.and Jackson, T., *Neural Computing* IOP Publishing Ltd (1990).

Bradbury, L.J.S., *The Structure of a Self-preserving Jet.* J. Fluid Mech., **23**:31-64 (1965).

Breidenthal, R., *Response of Plane Shear Layers and Wakes to Strong Three-dimensional Disturbances.* Phys. Fluids **23**(10) (1980).

Brown, G.B., *On Vortex Motion in Gaseous Jets and the Origin of Their Sensitivity to Sound,* Physical Society, **47**:703-733, (1935).

Cantwell, B., *Organized Motion in Turbulent Flow.* Ann. Rev. Mech. **13**:457-515, (1981).

Cantwell, B. and Coles, D., *An Experimental Study of*

Entrainment and Transport in Turbulent Near Wake of a Circular Cylinder. J. Fluid Mech. **136**:321-374 (1983).

Cimbala, J.M., Nagib, H.M., and Roshko, A., *Large Structure in the Wakes of Two-dimensional Bluff Bodies.* J.Fluid Mech. **190**:265-298 (1988).

Corrsin, S. and Kistler, A.L., *The Free-stream Boundaries of Turbulent Flows.* NACA, Technical Note. TN 3133 (1954).

Davenport, W.B. and Root, W.L., *An Introduction to the Theory of Random Signals and Noise.* McGraw-Hill (1958).

Deardorff, J.W., *Three-dimensional Numerical Investigation of the Idealised Planetary Boundary Layer,.* Geophys. Fluid Dyn. **1**:377-410 (1970).

Doob, J.L., *Stochastic Process* Wiley, New York (1953).

Farge, M., *Wavelet Transforms and their Applications to Turbulence* Ann. Rev. Fluid Mech. **24**:395-457 (1992).

Ferré. J.A.. *PhD Thesis, Aplicacio D'Algorithmes D'intelligencia Artificial* (In Catalan), University of Barcelona (1986).

Ferré, J.A. and Giralt, F. *Pattern Recognition Analysis of the Velocity Field in Plane Wakes.* J. Fluid Mech., **198**:27-64 (1989a).

Ferré, J.A. and Giralt, F., *Some Topological Features of the Entrainment Process in a Heated Turbulent Wake.* J. Fluid Mech. **198**:65-78 (1989b).

Ferré, J.A., Giralt, F. and Antonia, R.A., *Evidence for Double-Roller Eddies in a Turbulent Wake from Two-Component Velocity Measurements,* Proc TSF7, Stanford University.

Ferré, J.A., Giralt, F., Mumford, J.C., Savill, A.M.

Three-dimensional Large Eddy Motions and Fine-scale Activity in Plane Turbulent Wakes. J.Fluid Mech., **210**:371-414 (1990).

Fiedler, H.E., *Coherent Structures in Turbulent Flows.* Prog. Aerospace Sci. **25**:231-269 (1988).

Frost, w., Moulden, T.H., *Handbook of Turbulence.* Plenum Press (1977).

Fletcher, C.A.J., *Computational Techniques for Fluid Dynamics* vol 1 and vol 2. Springer-Verlag (1988).

Glauser, M.N., Cole, D.R.and Ukeiley, L.S., *An Examination of the Axisymmetric Jet Mixing Layer using Coherent Structure Detection Techniques.* IUTAM Symposium on Eddy Structure Identification in Free Turbulent Shear Flows, Poitiers, VI.2.1-2.5 (1992).

Gavrilakis, S., Tsai, H.M., Voke, P.R. and Leslie, D.C. *Large Eddy Simulation of Low Reynolds Number Channel Flow by Spectral and Finite Difference Methods.* Proc. of EUROMECH **199**, (1985).

Goshtasby, A.,Gage, S.H. and Bartholic, J.F., *A Two-Stage Cross Correlation Approach to Template Matching* IEEE Trans PAMI-6:3 (1984).

Grant, H.L. *The Large Eddies of Turbulent Motion*, J. Fluid Mech., **18**:239-273 (1958).

Guezennec, Y.G., and Choi, W.C., *Stochastic Estimation of Coherent Structures in Turbulent Boundary Layers.* Zoran Zaric Memorial Conference, Near Wall Turbulence, Hemisphere 453-468 (1988).

Guezennec, Y.G. and Gieseke, T.C. *Stochastic Estimation of Multipoint Conditional Averages and their Spatio-Temporal Evolution* IUTAM Symposium on Eddy Structure Identification in Free Turbulent Shear Flows, Poitiers, III.2.1-2.5 (1992).

Head, M.R. and Brandyopadhyay, P., *New Aspects of Turbulent Boundary-layer Structures.* J. Fluid Mech., **107** :297-338 (1981).

Hilberg, D. W., Lazik, W., Fiedler, H.E., *The Application Of Classical POD and Snapshot POD in a Turbulent Shear Layer with Periodic Structures.* IUTAM Symposium on Eddy Structure Identification in Free Turbulent Shear Flows, Poitiers, II.4.1-4.6 (1992).

Hinze, E., *Turbulence.* McGraw-Hill, New York (1951).

Hussian, F., *Coherent Structures and Turbulence.* J, Fluid Mech. **173**:303-356, (1986).

Husain, H.S. and Hussain, F., *Dynamics of Coherent Structures: Pairing Elliptic Jets. Part 2.*J. Fluid Mech. **233**: 439-482, (1991).

Hussain, F., and Hayakawa, M., *Three-dimensionality of Organised Structures in a Plane Turbulent Wake.* J. Fluid Mech. **206**:375-402 (1989).

Hussain, F., and Hayakawa, M., *Eduction of Large-scale Oraganised Structures in a Turbulent Plane Wake.* J. Fluid Mech. **180**:193-229 (1987).

Hussain, F., *Study of Coherent Structures via Vortex Dynamics: Core Dynamics, Helical Waves, and Interaction with Fine Scale Turbulence*. Eddy Structure Identification in Free Turbulent Shear Flows. Poitiers. V.1.1-V.1.8 (1992).

James, M., *Pattern Recognition* BSP Professional Books. Oxford (1987).

Jiménez, J. and Moin, P., *The Minimal Flow in Near-wall Turbulence*, J. Fluid Mech. **225**:213-240, (1991).

Kim, J., Moin, P., Moser, R. *Turbulence Statistics in Fully Developed Channel Flow at Low Renolds Number.* J. Fluid Mech. 177:133-166 (1987).

Kim, J. and Moin, P., *The Structure of the Vorticity Field in Turbulent Channel Flow.* J. Fluid Mech., 162: 339-363, (1986).

Kline, S.J., Reynolds, W.C., Schraub, F.A. and Runstadler, P.W., *The Structure of Turbulent Boundary Layers.* J. Fluid Mech., 30:741-773, (1967).

Kolmogorov, A.M. *A Refinement of Previous Hypothesis Concerning the Local Structure of Turbulence in Viscous Incompressible Flows at High Reynolds Number.* J. Fluid Mech. 177 133-166 (1961).

LaRue and Libby,. *Temperature and Intermittency in the Turbulent Wake of a Heated Cylinder.* Physics of Fluids. 17 No.5 873-878 (1974).

Leslie, D.C. *Developments in the Theory of Turbulence,* Clarendon Press, Oxford (1973).

Leslie, D.C. and Love, M.D. *Studies of Subgrid Modelling with Classical Closures aand Burgers Equation.* Proc. Symp. on Turbulent Shear Flows, Penn. State Univ. (1976).

List, E.J., *Turbulent Jets and Plumes.* Ann. Rev. Fluid Mech. 14:189-212, (1982).

Loeve, M. *Probability Theory,* Van Nostrand, New York, (1955).

Lovitt, W.V., *Linear Integral Equation.* New York, Dover, (1950).

Low, A. *Introductory Computer Vision and Image Processing.* McGraw-Hill Book Co. (1991).

Lumley, J.L., *Large Eddy Structure of the Turbulent Wake behind a Circular Cylinder.* Physics of Fluids Supp. S194 (1967).

Lumley, J.L. *The Structure of Homogeneous Turbulence Flows.* Proceedings of Int Col on Fine Scale structure of the Atmosphere and its Influence On Radio Wave Propagation. Doklady Akadamia Nank USSR Moscow (1967).

Lumley, J.L. *Stochastic Tools in Turbulence,* Academic Press, New York, San Francisco, London (1970).

Lumley, J.L. and Tennekes, H. *A First Course in Turbulence.* The MIT Press (1972).

Lumley, J.L. and Panofsky, H.A., *The Structure of Atmospheric Turbulence.* Interscience. New York (1964).

Lumley, J.L. *Coherent Structures in Turbulence. In Transition and Turbulence* ed. R.E. Meyer, pp215-241. New York. Academic (1981).

Manhart, M. and Wengle, H., *Turbulent Free Shear Layers above 2D and 3D Obstacles: An Evaluation of Large-eddy Simulations by Proper Orthogonal Decomposition.* IUTAM Symposium on Eddy Structure Identification in Free Turbulent Shear Flows. Poitiers, XI.12.1-12.5 (1992).

McComb, W.D. *The Physics of Fluid Turbulence* Clarendon Press, Oxford (1990).

Meibury, E. and Lasheras, J.C. *Experimental and Numerical Investigation of the Three-dimensional Transition in Plane Wakes*. J. Fluid Mech. **190**:1-37 (1988).

Miller, D.R. and Comings, E.W., *Static Pressure in the Free Turbulent Jet,*. J. Fluid Mech. **3**:1-16 (1957).

Moin, P. and Kim, J. *Numerical Investigation of Turbulent*

Channel Flow. J. Fluid Mech. **118**:341-377 (1982).

Moin, P. and Moser, R.D., *Characteristic-Eddy Decomposition of Turbulence in a Channel*, J. Fluid Mech. **200**:471-509 (1989).

Morton, B.R., *The Generation and Decay of Vorticity,* Geophys. Astrophys. Fluid Dynamics, **28**:277-308 (1984).

Mumford, J.C., *The Structure of Large Eddies in Fully Developed Turbulent Shear Flows. Part I The Plane Jet.* J. Fluid Mech., **118**:241-268 (1982).

Mumford, J.C., *The Structure of Large Eddies in Fully Developed Turbulent Shear Flows. Part II. The Plane Wake.* J. Fluid Mech., **137**:447-456 (1983).

Obled, C.H. and Creutin, J.D., *Some Developments in the Use of Empirical Orthogonal Functions for Mapping Meteorlogical Fields.* J. of Climate and Meteorology, **25** NO.9 (1986).

Offen, G.R., *A Proposed Model of the Bursting Process in Turbulent Boundary Layers.* J. Fluid Mech., **70**:209-228, (1975).

Oler, W., *Coherent Structures in the Similarity Region of a Two-dimensional Turbulent Jet.* Ph.D thesis, Purdue University (1980).

Orszag, S.A., and Pao, Y.H., *Numerical Computation of Turbulent Shear Flows.* Phys. Fluid, Suppl. **2**:250-257 (1974).

Papoulis, A., *Probability, Random Variables, and Stochastic Process.* McGraw-Hill (1965).

Perry, A.E. and Tim, T.T. *Coherent Structures in Coflowing Jets and Wakes.* J. Fluid Mech. 1978, **88**:451-463 (1978).

Perry, A.E., and Chong, M.S., *A Description of Eddying*

Motions and Flow Patterns Using Critical-points Concept. Annual Review of Fluid Mechanics 19:125-155 (1987).

Perry, A.E. and Chong, M.S., *A General Classification Of Three-Dimensional Flow Fields.* Phys. Fluids A 2(5):765-777 (1990).

Perry, A.E., *Topology of Flow Patterns in Vortex Motions and Turbulence.* IUTAM Symposium on Eddy Structure Identification in Free Turbulent Shear Flows, Poitiers, IX.1.1-1.6 (1992).

Poa, Y.H., *Adaptive Pattern Recognition and Neural Networks* Addison Wesley (1989).

Potamitis, S.G., Voke, P.R. *Numerical Simulation of a Plane Wake.* University of Surrey. ME-FD/9204 (1992).

Robinson, S.K., *Coherent Motions in the Turbulent Boundary Layer.* Annu. Rev. Fluid Mech. 23:601-639 (1991).

Robinson, S.K., Kline, S.J., Spalart, P.R., *Quasi-Coherent Structures in Turbulent Boundary Layer: Part II. Verification and New Information from a Numerically Simulated Flat-Plate Layer.* Zoran Zaric Memorial Conference, Near Wall Turbulence, Hemisphere. 218-247 (1988).

Rodi, W., *Turbulent Buoyant Jets and Plumes.* Pergamon press. Heat Mon. Transf. 6 (1982).

Rogallo, R.S. and Moin, P., *Numerical Simulations of Turbulent Flows.* Ann. Rev. Fluid Mech. 16:99-137 (1984).

Roshko, A., *Structure of Turbulent Shear Flows: A New Look.* 14, No10 Oct. AIAA Journal (1976).

Savill, A.M., *Effects on Turbulence of Curved or Distorting Mean Flow.* Ph.D thesis University of Cambridge, (1979).

Savill, A.M., Klein, H. and Friedrich, R. *Pattern*

Recognition of Structure in Manipulated Channel Flow. IUTAM Symposium on Eddy Structure Identification in Free Turbulent Shear Flows, Poitiers, IV.3.1-3.5 (Ed. J-P Bonnet, Kluwer Academic Publishers & to appear in Applied Scientific Research) (1992).

Savill, A.M. and Ferré, J.A. *Extension of Pattern Recognition Analysis Technique to Distorted and Manipulated Flows.* Fluid Mech Australasian Conf. (1989).

Savill, A.M. *Effects on Turbulence of Curved or Distorting Mean Flow.* Ph.D thesis University of Cambridge (1979).

Savill, A.M. *Recent Developments in Rapid-Distortion Theory.* Annual Review of Fluid Mechanics **19**: 531-575 (1987).

Schlichting, H. 1979. *Boundary Layer Theory.* McGraw-Hill Book Company.

Schumann, U., *Subgrid Scale Model for Finite Difference Simulations of Turbulent Flows in Plane Channels and Annuli.* J. Comp. Physics. **18**:376-404 (1975).

Shtilman, L. and Polifke, W., *On the Mechanism of the Reduction of Nonlinearity in the Incompressible Navier-Stokes Equation.* Phys. Fluids **A1** (5):778-780, (1989).

Sirovich, T.J., Winter, M., Eversion, R.M. and Barber, T.J., *Eigenfunction Analysis of Turbulent Mixing Phenomena.* AIAA Journal **30**:1681-1688, (1992).

Smagorinsky, J., Manaba, S. and Holloway, J.L., *Numerical Results from a Nine-level General Circulation Model of the Atmosphere.* Mon Weather Rev. 95:727-768. (1965).

Smagorinsky, J., *General Circulation Experiments with the Primitive Equations,* Monthly Weather Review. 93, No3 p99 (1963).

Smith, C.R. and Lu, L.J., *The Use of a Template -Matching Technique to Identify Hairpin Vortex Flow Structures in Turbulent Boundary Layers.* Zoran Zaric Memorial Conference, 248-267 (1988).

Smith, C.R. and Acalar, M.S., *A Study of Hairpin Vortices in a Laminar Boundary Layer. Part 1. Hairpin Vortices Generated by a Hemisphere Protuberance.* J. Fluid Mech., **175**:1-41, (1987).

Smith, C.R. and Acalar, M.S., *A Study of Hairpin Vortices in a Laminar Boundary Layer. Part 2. Hairpin Vortices Generated by Fluid Injection.* J. Fluid Mech. **175**:43-83, (1987).

Smith, C.R. and Walker, J.D.A., *Turbulent Wall-Layer Vortices.* submitted to 'Fluid Vortices' (1993).

Soria, J. and Cantwell, B.J., *The Identification and Classification of Topological Structures in Free Shear Flows.* IUTAM Symposium on Eddy Structure Identification in Free Turbulent Shear Flows, Poitiers, VII.12.2-12.5 (1992).

Soria, J., Wu, J., *Identification of Vortex Structures in Plane Wakes Using Digital Image Methods.* IUTAM Symposium on Eddy Structure Identification in Free Turbulent Shear Flows, Poitiers, XI.10.1-XI.10.5 (1992).

Spalart, P., *Direct Simulation of a Turbulent Boundary Layer up to* R_θ *= 1410,* J. Fluid Mech. **7**:61-98 (1988).

Stretch, D. *Patterns in Simulated Turbulent Channel Flow,* Draft Report for CRT Annual Research Brief. NASA Ames, Stanford University (1991).

Swarztrauber, P.N., *A Direct Method for the Discrete Solution of Separable Elliptic Equations.* SIAM. J.Numerical Analysis. **11**:6:1136-1150 (1974).

Townsend, A.A., *The Eddy Viscosity in Turbulent Shear Flow.* Phil. Magazine 890-906 (1950).

Townsend, A.A. *Flow Patterns of Large Eddies in a Wake and in a Boundary Layer.* J.Fluid Mech., **95**:515-537 (1979).

Townsend, A.A., *The Structure of Turbulent Shear Flow.* The Cambridge University Press, (1956).

Townsend, A.A., *Entrainment and the Structure of Turbulent Shear Flow.* J. Fluid Mech., **41**:13-46 (1970).

Tsinober, A. and Levich, E., *On the Helical Nature of Three-Dimensional Coherent Structures in Turbulent Flows.* Physics Letters, **99A**, no. 6,7 (1983).

Tsinober, A., *On the Property of Lamb Vector in Isotropic Turbulent Flow.* Phys. Fluids **A2** (4):484-486, (1990).

Voke, P.R. *Multiple Mesh Simulation of Turbulence.* Dept. of Aero. Eng. report EP-1082, QMW University of London, U.K. (1990).

Voke, P.R., Gao, S. *Further Large-Eddy Simulation of a Thermal Impinging Jet.* Dept. of Mech. Eng. University of Surrey. ME-FD/92.05 (1992).

Voke, P. R., *The Characterisation of Variation of Eddy Structures by Affine Matching,* IUTAM Symposium on Eddy Structure Identification in Free Turbulent Shear Flows, Poitiers, X.4.1-4.5 (1992).

Voke, P. R., *Affine Matching Pattern Recognition Analysis of Eddy Structures in a Numerically Simulated Boundary Layer,* submitted to Theoretical and Computational Fluid Dynamics, (1993).

Wallace, J.M., Brodkey, R.S., and Eckelmann, H., *Pattern-recognized Structures in Bounded Turbulent Shear*

Flows. Fluid Mech., 83:673-693 (1977).

Williamson, C.H.K., *The Existence of Two stages in the Transition to Three-dimensionality of a Cylinder Wake.* Phys. Fluids 31(11) p3165 (1988).

Zilberman, M., Wygnanski, I. and Kaplan, R.E., *Transitional Boundary Layer in a Fully Turbulent Environment.* J. Fluid Mech 224:133-158 (1991).